Aerodynamics of insect flight

Wouter G. van Veen

Aerodynamics of insect flight

Wouter G. van Veen

Propositions

1. Systematic parametric studies are vital for understanding the aerodynamics of insect flight. (this thesis)

2. The quasi-steady aerodynamic model for insect flight has an explanatory and a predictive role. (this thesis)

3. Ranking indoor rowers based on power output is incorrect if their mass is not taken into account.

4. Stimulating the innate immunity might be a good addition to the development of vaccines against emerging diseases, for both humans and animals.

5. The university should focus only on education and research, monetizing of research should be left to the companies.

6. To get more women active in science and education a fundamental change in social culture is needed, but until then using a quota is the best option we have.

7. Working on a PhD whilst receiving unemployment benefits should no longer be the standard.

Propositions belonging to the thesis, entitled
Aerodynamics of insect flight
Wouter Gerben van Veen

Wageningen, 5 October 2020

Aerodynamics of insect flight

Wouter G. van Veen

Thesis Committee

Promotor
Prof. Dr J. L. van Leeuwen
Professor of Experimental Zoology
Wageningen University & Research

Co-promotor
Dr F. T. Muijres
Assistant professor, Experimental Zoology Group
Wageningen University & Research

Other members
Prof. Dr A. J. F. Hoitink, Wageningen University & Research
Prof. Dr G. J. F van Heijst, Eindhoven University of Technology
Dr B. W. van Oudheusden, Technical University of Delft
Prof. Dr F. O. Lehmann, University of Rostock Germany

This research was conducted under the auspices of the Graduate School Wageningen Institute of Animal Sciences (WIAS)

Aerodynamics of insect flight

Wouter G. van Veen

Thesis
submitted in fulfilment of the requirements for the degree of doctor
at Wageningen University
by the authority of the Rector Magnificus,
Prof. Dr A. P. J. Mol
in the presence of the
Thesis Committee appointed by the Academic Board
to be defended in public
on Monday 5 October 2020
at 4 p.m. in the Aula

Wouter G. van Veen

Aerodynamics of insect flight, 264 pages

PhD thesis, Wageningen University, Wageningen, the Netherlands (2020)
With references, with summaries in English and Dutch

ISBN: 978-94-6395-479-2
DOI: 10.18174/528044

For my mother & sister who have always supported me

For Annelieke who kept me sane

Contents

Chapter 1

General introduction

Wouter G. van Veen

When the skis of the first man-made aircraft left the ground at Kitty Hawk [1] probably billions of insects where flying world wide at the same time. After this first flight, it would take several decades before high-speed camera's would be able to capture the wing movement of a flying locust. By then the world was already flying regularly around the world, and much was known about aircraft, and the aerodynamics involved to keep them aloft. Yet the aerodynamics involved in flapping flight remained a mystery.

In the 1930's an engineer applied the knowledge of this "aircraft" aerodynamics to the flight of a bumblebee and proved that it should not be able to fly [2]. Obviously, bumblebees are able to fly, but this story does illustrate that the knowledge gained on aircraft cannot be readily applied to flying insects.

So, "*How do insects fly?*". Because the methods of insect flight found in nature is huge, I will focus on the flight of diptera, which is an order of two-winged flying insects [3]. Nonetheless, the aerodynamics that explain the flight of a dipteran might be used to explain the flight of other insects alike.

Throughout this thesis I will keep referring back to the fruit fly (*Drosophila hydei*) and the malaria mosquito (*Anopheles coluzzii*) as my model species. I chose these two insects because their average size [4] , and their different methods of flying: low-frequency high-amplitude vs high-frequency, low-amplitude. Both of these insects operate in an intermediate Reynolds number regime ($Re = \mathcal{O}(100)$).

In this chapter, I will give some background on insect flight. I will start out with a description of the movement of the wings of the mosquito and fruit fly in section 1.1. In section 1.2, I will outline how this movement of the wings results in the generation of force with the use of aerodynamic mechanism. Throughout this section, I will also highlight where the open questions remain in the current knowledge of insect flight. In the final section 1.3, I will briefly summarize the open questions I highlighted in the section before and give an outline of my thesis.

1.1 How do insects move their wings?

Unlike an aircraft, an insect generates forces from the movement of its wings relative to its body. Rightfully the pioneering scientist stated that the movement of the wings should be known before an explanation for the involved aerodynamics can be found

[5]. Insects flap their wings incredibly fast, when observed with the naked eye it is often impossible to see more than the blur of the wings. For instance, the humble fruit fly moves its wings about 200 times back and forth in a second [6]. Even more extreme, the mosquito that zooms around our heads during warm summer nights moves its wings back and forth about 500 to 1000 times a second [7, 8].

Because insects flap their wings so fast, high-speed camera's are often used to extract the exact movement of the wings and body. Several synchronized high-speed cameras are used from different angles. The filmed body and wing movements are then used to reconstruct the three-dimensional movement of the wings [9].

The wing is assumed to rotate around a fixed point (the hinge) on the body of the insect. Therefore it is convenient to express the orientation of the wing with respect to the body with three Euler angles: the stroke angle, the deviation angle and the pitch angle (figure 1.1 *e*).

An insect flaps its wings back and forth, contrary to for instance most birds that flap their wings up and down (figure 1.1 *a–d*). The angle that describes the arc over which the wing moves is the stroke angle (figure 1.1 *e*, blue lines). I will withhold a formal description of the Euler angles for later chapters in this thesis. Often a plane is defined which is parallel to the average motion of the wing, this plane is known as the stroke plane. For the fruit fly and the mosquito, the stroke-plane is almost parallel to the ground surface. The amount of out of plane motion is described by the deviation angle (figure 1.1 *e*, red lines). Finally, the rotation of the wing around its span-wise axis is described by the pitch-angle.

The movement of the wings can be divided in two parts: the forward stroke and the backward stroke. The forward stroke starts with the wings at the dorsal side of the animal (figure 1.1 *a*, *c*) with the wing almost upright. At the start of the forward stroke, the wing will pitch down and increase the stroke rate. For the fruit fly, the wing is pitched-down to an angle-of-attack of about $\alpha = 45°$, for the mosquito the angle-of-attack keeps decreasing throughout the forward stroke. At the end of the forward stroke, the wing rotates around its span in order to attain a positive angle-of-attack for the backward stroke. The point where the wing changes its stroke direction is known as the stroke-reversal. At stroke-reversal the wing rotates around its span-wise axis, which is known as pronation and supination. The backward stroke is similar to the forward stroke, only the wing is moving towards the dorsal side.

The angle that the wing describes between the minimum and maximum stroke angle is known as the wing-stroke amplitude. For the two examples, I discussed

earlier, the fruit fly and the mosquito, this amplitude is 131° and 40° respectively (based on the kinematics in figure 1.1). Thus, the fruit fly represents an insect with a low frequency (188 Hz) and high amplitude (131°) and the mosquito resembles an insect with a high frequency (500 Hz to 1000 Hz) and low amplitude (40°). Because, these two insects represent two different methods of flying, I chose them as my model species for my thesis.

1.2 How are forces generated with flapping wings?

Turning back to the early pioneers in the field, we need to address how the aforementioned wing movement leads to the generation of forces. Due to huge variety of flying insects, this question turns from an apparent innocent one into a complex one. Luckily one of the suggested methods for dissecting insect flight leads to a more universal understanding of insect flight: the aerodynamic mechanism [10]. Throughout this section, I will use figure 1.2 as a guideline. In this figure, I depicted all the different aerodynamic mechanisms schematically.

An aerodynamic mechanism is a link of a part of the motion of the wing to the aerodynamic force generation. These aerodynamic mechanisms are captured in a model, which can be combined into a model for predicting the aerodynamic forces, known as the quasi-steady model. The quasi-steady model assumes that for each point in time the forces can be determined independent of the flow history [10].

The subdivision of the aerodynamics into several aerodynamic mechanisms is not always straight-forward, because where does one mechanisms stop and another begin? And do the aerodynamic mechanisms interact with each other, or are they independent? To overcome this issue, I based each aerodynamic mechanism on the least possible number of kinematic parameters. For instance, when looking at the forces that depend on the stroke rate of the wing, I only studied the effect of the stroke rate and the angle-of-attack, but removed all effects of the history of the flow, and startup effects. I consider these two unsteady effects as a separate entity.

In the sections below, I choose to name the aerodynamic mechanisms after the associated kinematics. I did this to easily identify the underlying kinematics of a certain aerodynamic mechanisms. With this choice, I will sometimes have to deviate from the naming most common in literature, but I will mention this when it occurs.

1.2.1 Stroke rate forces & the leading edge vortex

Arguably the biggest advancement in the past three decades in insect flight was made with the discovery of the leading edge vortex (LEV) [11]. The LEV is formed on top of the wing during the forward and backward stroke (see figure 1.2 *a* for a schematic representation). Due to the high angle-of-attack of an insect wing, the flow separates at the leading edge of the wing. However, the flow reattaches before the trailing edge forming a stable separated region.

Due to the angular motion of the wing, the separated region does not fully detach from the wing surface [12]. This results in the ability of the insect to fly at high angles-of-attack and produce high lift forces. The stability of LEV can be ascribed to the rotational accelerations of the wing [13].

I call the forces based on the stroke motion and the presence of the LEV: the stroke rate forces. In literature, these forces are often named "translational forces". The stroke rate forces depend on the stroke rate and the angle-of-attack, similar to how the drag and lift of a helicopter blade depend on the angle-of-attack and rotation rate of the propeller system. The stroke rate forces can be derived from the conventional lift and drag in three consecutive steps as

$$F_{sr} = \frac{1}{2}\rho \int_0^R V_\infty^2 C_{sr}\left(\alpha\right) c dr \tag{1.1}$$

$$= \frac{1}{2}\rho \int_0^R \left(\omega_s r\right)^2 C_{sr}\left(\alpha\right) c dr \tag{1.2}$$

$$= \frac{1}{2}\rho \omega_s^2 C_{sr}\left(\alpha\right) \int_0^R r^2 c dr, \tag{1.3}$$

where V_∞ is the far-field fluid velocity relative to the wing, α the angle-of-attack, $C_{sr}\left(\alpha\right)$ the stroke rate force coefficient as a function of the angle-of-attack, c the local chord length, r the distance from the root of the wing (rotation point) and finally R the distance from the tip of the wing to the rotation point.

In the last step (equation (1.3)), the movement and position of the wing are separated from a geometrical scaling parameter (the integral). This integral is the second moment of area S_{yy}, and is a measure of how much surface area of the wing is placed away from the root of the wing. Due to the rotational nature of the wing movement during flapping flight, the second moment of area will play an important role for numerous aerodynamic mechanisms.

The relation between the angle-of-attack, the stroke rate, and the force coefficient C_{sr} describes the force production of the wing. This relation is often determined by an experiment with a revolving wing. A wing is placed under a fixed angle-of-attack and the angular rate is increased. This experiment is repeated for different angles of attack until the relation is known [14, 15, 16, 17, 7]. In a recent study, a wide range of different aerodynamic models have been compared to experimental results [18]. Here they found that the model based on the velocity component normal to the surface of the wing performed the best.

1.2.2 Stroke-pitch interaction forces

Around stroke reversal, the wing is rotating rapidly around its span-wise axis. This pitch rotation, in combination with the aforementioned stroke motion, generates stroke pitch interaction forces. In literature, these forces are often named "rotational lift", however I think this naming is misleading, because the "rotational" part is unclear about what rotation (for instance the stroke motion is also a rotation), and the "lift" part actually includes both a lift and a drag component. Therefore, I will refer to the "rotational lift" as the stroke-pitch interaction forces, because that removes these problems.

The stroke-pitch interaction forces are based on the Kramer effect. When a wing is pitching up, while moving forward, the relative velocity to the wing at the trailing edge is decreased, and at the leading edge is increased. This change in local relative velocity caused a pressure difference between the bottom and top surface of the wing, which in turn generates an aerodynamic force. This forces acts normal to the surface of the wing and is often derived from a two dimensional model, based on thin airfoil theory [4]. I integrate this two-dimensional model over the surface of the wing, which results in

$$F_{sr-pr} = \rho \int_0^R C_{sr-pr} V_\infty \Gamma c dr \tag{1.4}$$

$$= \rho \int_0^R C_{sr-pr} \omega_s r \omega_p c c dr \tag{1.5}$$

$$= \rho C_{sr-pr} \omega_s \omega_p \int_o^R r c^2 dr, \tag{1.6}$$

where Γ is the bound circulation, C_{sr-pr} the stroke-pitch interaction force coefficient independent of the motion of the wing and wing morphology, and ω_p the pitch rate of

the wing.

Here, the stroke-pitch interaction forces are modeled with the change in bound circulation due to the pitching motion. This bound circulation is simply modeled as: $\Gamma = \omega_p c$. Although it is valid to make a predictive model based on the circulation, caution should be taken to see this as an explanation of the stroke-pitch interaction forces. To illustrate my point, I will quote the textbook "Fundamentals of Aerodynamics"[19] "Keep in mind that the true physical sources of aerodynamic force on a body are the pressure and shear stress distributions exerted on the surface of the body".

The inclusion of the stroke-pitch interaction model in the quasi-steady model led to a good prediction of the lift forces of a fruit fly [14, 4]. Even though, there was still a significant variation in the parameter C_{sr-pr} when the kinematics and the pitch-axis where changed. This suggests that C_{sr-pr} is still dependent on the kinematics and the wing morphology, even though it should not be.

Despite these open questions, the model was widely adopted [14, 6, 20, 21]. Furthermore, the model assumes that a wing that is pitching up generates the same forces as a wing that pitches down, only mirrored. This assumption was never tested explicitly, nor is the assumption that there is no interaction between other aerodynamic mechanisms and this mechanism.

1.2.3 Pitch rate forces

Forces around stroke-reversal are often associated with wake-capture (see section 1.2.5), forces associated with wing-acceleration ("added mass", see section 1.2.4) and stroke-pitch interaction forces (see section 1.2.2). However, the pitch rate forces (rotational drag) could also be an explanation of the forces around stroke-reversal [22, 21]. These forces are even thought to be the main driving mechanism behind mosquito flight [7].

For the same reasons as with the naming of the "rotational lift", I think that the naming of "rotational drag" is misleading. The "rotational drag" consists of both a lift and drag component, however the name suggests that it is a pure drag component. Furthermore, it is again unclear to what the "rotational" part is referring to. Therefore, I chose to name the "rotational drag" component as the pitch rate forces.

Like the stroke-pitch interaction forces, the pitch rate forces are assumed to be independent on the angle-of-attack. Furthermore, they only act normal to the wing

surface. This means that the pitch rate forces are assumed to only comprise of pressure forces. The pitch rate forces can be modeled as a function of the change in angle-of-attack $\dot{\alpha}$ and a constant coefficient as [21]

$$F_{pr} = \frac{1}{2}\rho \int_{c_{te}}^{c_{le}} r c^2 dc C_{pr} \dot{\alpha}|\dot{\alpha}|. \tag{1.7}$$

The coefficient C_{pr} is assumed to equal the coefficient of drag at an angle-of-attack of 90° [21], which can be obtained as $C_{pr} = 3.2$ [23]. The integral in equation (1.7) represents the geometrical scaling parameter.

Even though the model for the pitch rate forces (equation (1.7)) is indeed capable of predicting forces around stroke-reversal no direct validation is presented. The dependence of equation (1.7) on the derivative of the angle-of-attack $\dot{\alpha}$ means that a wing that is plunging, without changing its pitch angle, also generates pitch rate forces. This definition is troublesome, because the pitch rate forces provide an explanation for the forces when no stroke rate is presented, which means that the angle-of-attack at that point is undefined.

1.2.4 Stroke & pitch acceleration forces

Due to the constant change of direction of the wing, large accelerations are present in the wingbeat kinematics of flapping insects (figure 1.1 *i*, *j*, example for the fruit fly and mosquito). As a result of the wing accelerations the fluid around the wing has to be accelerated as well. The mass of this fluid is often seen as "added-mass" [24]. In its most simple form, added mass can be visualized by a volume of fluid that is attached to the wing (figure 1.2 *d*). This fluid has a mass and a force is required to accelerate this fluid, hence the name "added mass". In equation form we can write this idea as

$$\vec{F}_{am} = \rho V \frac{\mathrm{d}\vec{v}}{\mathrm{d}t}, \tag{1.8}$$

where V is the volume of the "added mass" and $\mathrm{d}v/\mathrm{d}t$ the acceleration of the wing (and therefore, the acceleration of the added mass). Obviously, equation (1.8) leaves a lot of open questions, for instance, how large is the volume of fluid that is accelerated? Does it change over time? Is there a gradient in the acceleration of the fluid around the wing?

Before continuing with the investigation of different models for the added mass

forces, it is wise to look at what kind of accelerations are present in insect flight. The wing is changing direction at the end of each stroke, this introduces stroke accelerations (e.g. changes in the stroke rate). At the same time, the wing is pitching around its span, introducing pitch accelerations. Therefore, I will split the added mass forces into two components directly related to the kinematics: the stroke acceleration forces and the pitch acceleration forces.

Both the stroke acceleration forces and pitch acceleration forces can be approximated using a two dimensional model based on inviscid flow. This model assumes that the fluid that is accelerated with the wing equals that of a cylinder around the wing with a diameter equal to the chord length of the wing. Therefore the volume of the cylinder in the two dimensional model equals $\pi c^2/4$. This results in a two-dimensional model written as [25, 26]

$$F_{2D} = \rho \frac{\pi}{4} c^2 \left(\frac{\mathrm{d}v_{\text{wing}}}{\mathrm{d}t} + \Delta x \dot{\omega}_p \right), \tag{1.9}$$

where Δx is the offset between the pitch axis and the symmetry axis of the chord. The first term in equation (1.9) describes the stroke acceleration forces, and the second term the pitch acceleration forces. Integrating equation (1.9) over the span of the wing gives two three dimensional models for the stroke acceleration forces and pitch acceleration forces, which can be written as

$$F_{sa} = \rho \frac{\pi}{4} \sin(\alpha) \dot{\omega}_s \int_0^R r c^2 dr \tag{1.10}$$

$$F_{pa} = \rho \frac{\pi}{4} \dot{\omega}_p \int_0^R \Delta x c^2 dr. \tag{1.11}$$

In both equations, the right side integral represents the dependence of the forces on the wing morphology. The left side of the equation shows the dependence of the forces on the wing kinematics.

Interestingly, both the stroke acceleration forces and the pitch acceleration forces are linearly dependent on their respective acceleration. This means that for a fully symmetrical periodic wingbeat kinematics the average of these forces equate to zero [27]. However, even for a completely symmetric wingbeat the average of the drag is non-zero.

1.2.5 Unsteady effects

In the previous sections, I described a relation between part of the movement of the insect and the forces associated with that movement. This direct relation between the movement of the wing and the forces implies that the forces are not influenced by the history of the flow-field around the wing. I mean with this that each point in time and space can be seen completely isolated from the rest of the movement. This assumption is known as the quasi-steady assumption [28, 29], and is often used as assumption to form a quasi-steady model.

One reasoning behind this assumption is the ”proof by contradiction”, which simply states that if the predicted forces are below the real forces produced by the animal the quasi-steady is insufficient. If the predicted forces are larger, than the quasi-steady model cannot be discounted [10, 29]. The reason why I put this rather old thought experiment here is that it illustrates the connection between the predictive and explanatory roles of the quasi-steady model. Or turning it around, if the model predicts the forces correctly then the model must explain these forces.

Besides this quasi-steady assumption, which simply removes all unsteady effects, some mechanisms are identified that explicitly model the aerodynamic forces that are the result of unsteady effects. The first model is known as the Wagner effect [30], which takes into account the time-history by considering the development of the flow. Another mechanism is the wake-capture effect, which includes the interaction between the wake and the wing [31, 32, 33].

The naming of the wake-capture effect suggests that this mechanism particularly plays a role around stroke-reversal, where the wing meets its own wake. However, all insects flap their wings at subsonic speeds, meaning that the entire wake influences the forces on the wing, not only the wake in front of the wing.

1.3 Outline of this thesis

In the previous section, I summarized the known aerodynamic mechanisms that are responsible for force generation in insect flight. In the last chapter of this thesis (chapter 6), I highlighted the double role that the quasi-steady model has in explaining insect flight: predictive and explanatory. In this thesis, I revised some of the known aerodynamic mechanisms with systematic parametric studies to uncover their physical principles and their dependence on the kinematics and wing morphology.

In **chapter 2**, I revised the two aerodynamic mechanisms that are based on the pitch rate motion of the wing: stroke-pitch interaction forces and pitch rate forces. With the use of large parametric study based on computational fluid dynamics I related the wing kinematics to the generation of aerodynamic forces. Furthermore, I included seven different wing morphologies to explicitly test the dependence of the stroke-pitch interaction forces and the pitch rate forces on the wing morphology.

In **chapter 3**, I studied the added mass effects with a similar systematic parametric study I used in **chapter 2**. This method enabled me to validate the two-dimensional model often used to explain the stroke acceleration forces in insect flight. First, I systematically varied the kinematics to find the relation between the stroke acceleration and the change in aerodynamic forces. Furthermore, I used this parametric study to study how the stroke acceleration aerodynamic mechanism interacts with the stroke rate aerodynamic mechanism. Second, I varied the wing morphology systematically to test the dependence of the stroke acceleration forces and its interactions on the wing morphology. At the end of this chapter, I applied the model on the kinematics of the fruit fly and the mosquito.

In **chapter 4**, I turned my attention back to the pitching movement of the wing. Again based on a systematic parametric study, I related the generation of aerodynamic forces to a pitch motion with non constant pitch rate. In this chapter, I was able to explicitly test the validity of the two-dimensional model for a pitching wing. Furthermore, in this chapter I tested the assumption that the aerodynamic forces behave similarly for a wing that is pitching up or down, only opposite in sign. At the end of this chapter, I applied the newly found models to the kinematics of the fruit fly and mosquito.

In **chapter 5**, I seemingly took a detour from the study into the different aerodynamic mechanisms, by studying the take-off of malaria mosquitoes. In this chapter, I tested if the surroundings of the insect influenced the aerodynamic forces with the inclusion of the ground effect. Apart from the ground effect, the study in this chapter enabled me to see how the mosquito uses the substrate, from which it takes off.

Finally, in **chapter 6**, I used the models I found in the previous chapters to make a single quasi-steady model. This quasi-steady model not only verified the predictive capabilities of the aerodynamic mechanisms found in this thesis, but also reviewed their importance for the fruit fly and mosquito as model organisms for low-frequency high-amplitude, and high-frequency low-amplitude flight. At the end of the general discussion, I took the take-off of the mosquito and tested the quasi-steady model in

maneuvering flight. Again, I used the model here to see how the insect uses the adaption of its kinematics to generate the required forces for the take-off.

1.4 References

[1] J. D. Jr. Anderson. *Introduction to Flight*. Mc Graw-Hill, 2005.

[2] Antoine Magnan. *Le vol des insectes Volume 1 van Locomotion chez les animaux*. Vol. 1. Hermann, 1934.

[3] *The Biomechanics of Insect Flight Form, Function, Evolution*. Princeton University Press, 2000.

[4] S. P. Sane and M. H. Dickinson. "The aerodynamic effects of wing rotation and a revised quasi-steady model of flapping flight". In: *The Journal of Experimental Biology* 205.8 (2002), pp. 1087–1096.

[5] T. Weis-Fogh. "Biology and physics of locust flight II. Flight performance of the desert locust (Schistocera Gregaria)". In: *Philosophical Transactions of the Royal Society B* 239.667 (1956). DOI: 10.1098/rstb.1956.0008.

[6] M. H. Dickinson and F. T. Muijres. "The aerodynamics and control of free flight manoeuvres in Drosophila". In: *Philosophical Transactions B* 371.1704 (2016). DOI: 10.1098/rstb.2015.0388.

[7] R. J. Bomphrey, T. Nakata, N. Phillips, and S. M. Walker. "Smart wing rotation and trailing-edge vortices enable high frequency mosquito flight". In: *Nature* 554 (2017), pp. 92–95. DOI: 10.1038/nature21727.

[8] F.T. Muijres, S.W. Chang, W.G. Veen, J. Spitzen, B.T. Biemans, M.A.R. Koehl, and R. Dudley. "Escaping blood-fed malaria mosqtuitoes minimize tactile detection without compromising on take-off speed". In: *Journal of Experimental Biology* 220.20 (2017), pp. 3751–3762. DOI: 10.1242/jeb.163402.

[9] E. I. Fontaine, F. Zabala, M. H. Dickinson, and J. W. Burdick. "Wing and body motion during flight initiation in *Drosophila* revealed by automated visual tracking". In: *The Journal of Experimental Biology* 212 (2009), pp. 1307–1323. DOI: 10.1242/jeb.025379.

[10] C. P. Ellington. "The aerodynamics of hovering insect flight. IV. aerodynamic mechanisms". In: *Philosophical transaction royal society London* 305 (1984), pp. 79–113. DOI: 10.1098/rstb.1984.0052.

[11] C. P. Ellington, C. van den Berg, A. P. Willmott, and A. L. R. Thomas. "Leading-edge vortices in insect flight". In: *Nature* 384.6610 (1996), pp. 626–630. DOI: 10.1038/384626a0.

[12] M. H. Dickinson. "The effects of wing rotation on unsteady aerodynamic performance at low Reynolds numbers". In: *The Journal of Experimental Biology* 192 (1994), pp. 179–206. ISSN: 0022-0949.

[13] D. Lentink and M. H. Dickinson. "Rotational accelerations stabilize leading edge vortices on revolving fly wings". In: *The Journal of Experimental Biology* (2009). DOI: 10.1242/jeb.022269.

[14] M. H. Dickinson, F. Lehmann, and S. P. Sane. "Wing rotation and the aerodynamic basis of insect flight". In: *Science* 284.5422 (June 1999), pp. 1954–1960. DOI: 10.1126/science.284.5422.1954.

[15] Z. J. Wang, J. M. Birch, and M. H. Dickinson. "Unsteady forces and flows in low Reynolds number hovering flight: two-dimensional computations vs robotic wing experiments". In: *The Journal of Experimental Biology* 207 (2003), pp. 449–460. DOI: 10.1242/jeb.00739.

[16] Z. J. Wang. "Dissecting Insect Flight". In: *Annual Reviews in Fluid Mechanics* 37 (2005), pp. 183–210. DOI: 10.1146/annurev.fluid.36.050802.121940.

[17] P. S. Sane and M. H. Dickinson. "The control of flight force by a flapping wing: lift and drag production". In: *The journal of experimental biology* 204 (2001), pp. 2607–2626. ISSN: 0022-0949.

[18] M. R. A. Nabawy and W. J. Crowther. "The role of the leading edge vortex in lift augmentation of steadily revolving wings: a change in perspective". In: *Journal of the Royal Society Interfact* 14 (2017), pp. 1–9. DOI: 10.1098/rsif.2017.0159.

[19] J. D. Jr. Anderson. *Fundamentals of Aerodynamics*. Fourth. McGraw-Hill, 2007.

[20] L. Zheng, T. L. Hedrick, and R. Mittal. "A multi-fidelity modelling approach for evalutation and optimization of wing stroke aerodynamics in flapping flight". In: *The Journal of Fluid Mechanics* 721 (2013), pp. 118–154. DOI: 10.1017/jfm.2013.46.

[21] T. Nakata, H. Liu, and R. J. Bomphrey. “A CFD-informed quasi-steady model of flapping-wing aerodynamics”. In: *Journal of Fluid Mechanics* 783 (Nov. 2015), pp. 323–343. DOI: 10.1017/jfm.2015.537.

[22] J.P. Whitney and R.J. Wood. “Aeromechanics of passive rotation in flapping flight”. In: *Journal of Fluid Mechanics* 660 (2010). DOI: 10.1017/S002211201000265X.

[23] J. R. Usherwood and C. P. Ellington. “The aerodynamcis of revolving wings”. In: *The Journal of Experimental Biology* 205.11 (2002), pp. 1547–1564. ISSN: 0022-0949.

[24] T. L. Daniel. “Unsteady aspects of aquatic locomotion”. In: *American Zoologist* (1984).

[25] L. I. Sedov. *Two-Dimensional Problems in Hydrodynamics and Aerodynamics*. Interscience Publishers, 1965.

[26] L. Liu and M. Sun. “The added mass forces in insect flapping wings”. In: *Journal of theoretical biology* 437 (Jan. 2017), pp. 45–50. DOI: 10.1016/j.jtbi.2017.10.014.

[27] C. Zhang, T. L. Hedrick, and R. Mittal. “Centripetal acceleration reaction: An effective and robust mechanism for flapping flight in insects”. In: *Plos One* (2015). DOI: 10.1371/journal.pone.0132093.

[28] C. P. Ellington. “The aerodynamics of hovering insect flight. III. kinematics”. In: *Philosophical Transactions B* 305.1122 (1983), pp. 41–78. ISSN: 0080-4622.

[29] S. P. Sane. “The aerodynamics of insect flight”. In: *The Journal of Experimental Biology* 206 (2003), pp. 4191–4208. DOI: 10.1242/jeb.00663.

[30] H. Wagner. “Flight performance and visual control of flight of the free-flying housefly”. In: *Philosphical transactions Royal Society of London* (1980).

[31] J. M. Birch and M. H. Dickinson. “The influence of wing–wake interactions on the production of aerodynamic forces in flapping flight”. In: *The Journal of Experimental Biology* 206 (2003), pp. 2257–2272. DOI: 10.1242/jeb.00381.

[32] D. Lentink, F. T. Muijres, F. J. Donker-Duyvis, and J. L. van Leeuwen. “Vortex-wake interactions of a flapping foil that models animal swimming and flight”. In: *The Journal of Experimental Biology* 211 (2007), pp. 267–273. DOI: 10.1242/jeb.006155.

[33] F. Lehman. “When wings touch wakes: understanding locomotor force control by wake–wing interference in insect wings”. In: *The Journal of Experimental Biology* 211 (2008), pp. 224–233. DOI: 10.1242/jeb.007575.

1.5 Figures

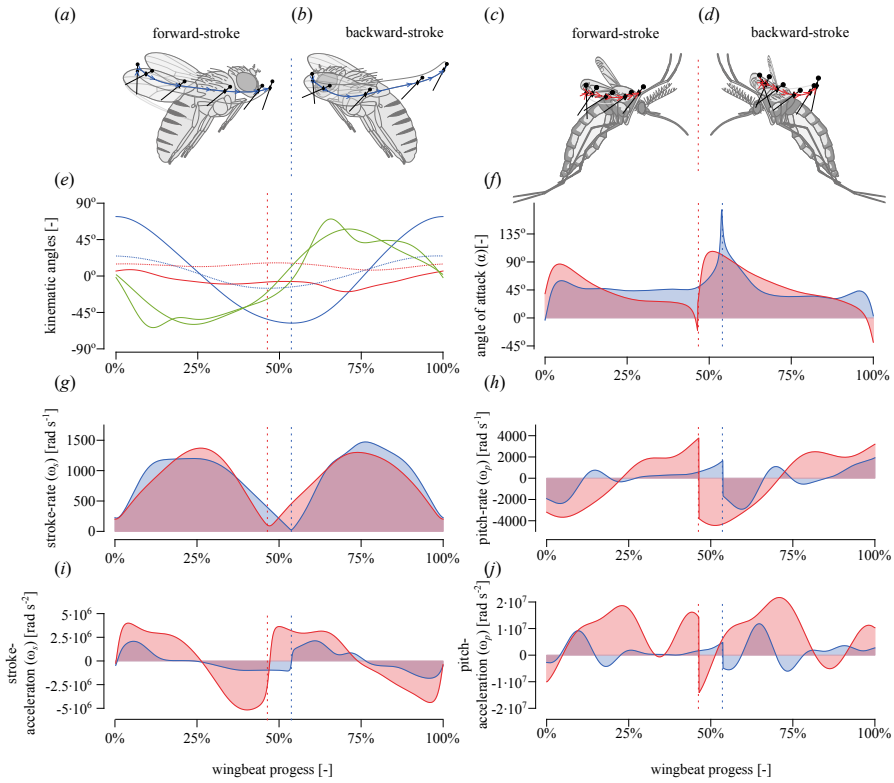

Figure 1.1: Kinematics of a fruit fly [6] and a mosquito [8]. (*a* – *d*) Schematic representation of the flapping motion of the fruit fly (*a*, *b*) and mosquito (*c*, *d*) respectively. The left and right panel show the forward and backward stroke respectively, black lines indicate the location of the chord at 2 mm from the wing root, the black dot the leading edge and the diamond the rotation axis. (*e*) The three Euler angles for the fruit fly (solid) and the mosquito (dashed), stroke angle (blue), deviation angle (red), pitch angle (green). (*f*) The angle-of-attack for the fruit fly (blue) and the mosquito (red). (*g*) The stroke rate for the fruit fly (blue) and mosquito (red). (*h*) The pitch rate for the fruit fly (blue) and mosquito (red). (*i*) The stroke acceleration for the fruit fly (blue) and the mosquito (red). (*j*) The pitch acceleration for the fruit fly (blue) and the mosquito (red).

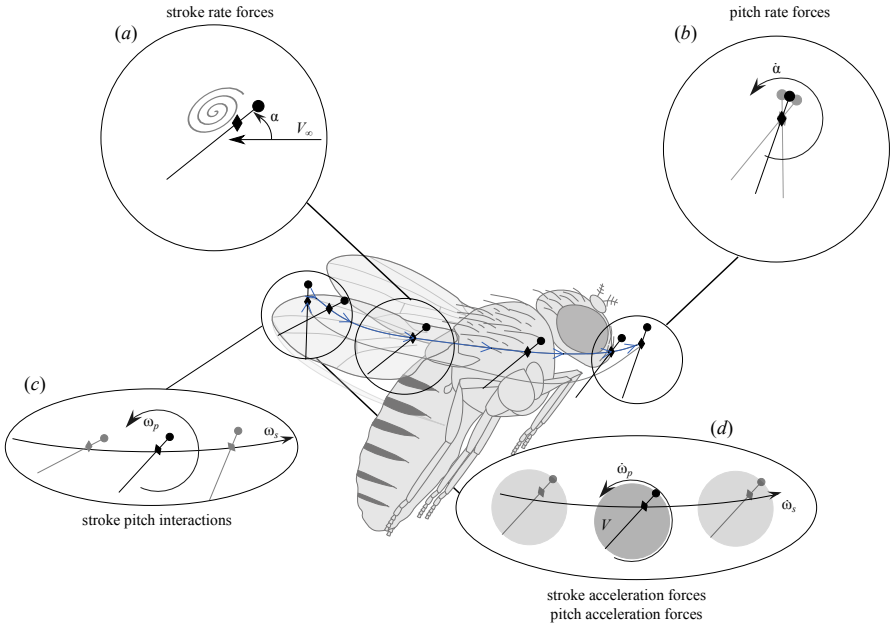

Figure 1.2: Schematic representation of aerodynamic mechanisms, black line indicates the cross-section of the wing at 2 mm from the root of the wing, the diamond the location of the wing pitch axis, and the dot the location of the leading edge. (*a*) Schematic representation of the stroke rate forces, which are related to the presence of the leading edge vortex on top of the wing, and to the free-stream velocity V_∞ and the angle-of-attack α. (*b*) Schematic representation of the pitch rate forces, which are only related to the change in angle-of-attack $\dot{\alpha}$. (*c*) Schematic representation of the stroke-pitch interaction forces, which are related to the stroke rate and pitch rate. (*d*) Schematic represenation of the stroke acceleration forces and pitch acceleration forces, which are a function of their respective accelerations; circle indicates the assumed volume of fluid attached to the accelerating wing.

Chapter 2

A chordwise offset of the wing-pitch axis enhances rotational aerodynamic forces on insect wings: a numerical study

Wouter G. van Veen, Johan L. van Leeuwen, Florian T. Muijres

Journal of The Royal Society Interface (2019) Volume 16 Issue 155

Abstract

Most flying animals produce aerodynamic forces by flapping their wings back and forth with a complex wingbeat pattern. The fluid dynamics that underlies this motion has been divided into separate aerodynamic mechanisms of which rotational lift, that results from fast wing pitch rotations, is particularly important for flight control and maneuverability. This rotational force mechanism has been modelled using Kutta-Joukowski theory, which combines the forward stroke motion of the wing with the fast pitch motion to compute forces. Recent studies, however, suggest that hovering insects can produce rotational forces at stroke reversal, without a forward motion of the wing. We have conducted a broad numerical parametric study over a range of wing morphologies and wing kinematics to show that rotational force production depends on two mechanisms: 1) conventional Kutta-Joukowski-based rotational forces, and 2) a rotational force mechanism that enables insects with an offset of the pitch-axis relative to the wing's chordwise symmetry axis to generate rotational forces in the absence of forward wing motion. Because flying animals produce control actions frequently near stroke reversal, this pitch-axis-offset dependent aerodynamic mechanism may be particularly important for understanding control and maneuverability in natural flyers.

2.1 Introduction

Most flying animals flap their wings to produce the aerodynamic forces required for flight. These rapid oscillatory wing movements cause a complex unsteady airflow over the wing, resulting in unsteady aerodynamic force production. To explain how aerodynamic forces are related to the complex wing motion of flapping flight, distinct unsteady aerodynamic mechanisms have been defined and modelled [1]. Arguably the most important aerodynamic mechanisms currently identified for flapping flight are delayed stall and the linked leading-edge-vortex-based lift [2], rotational lift resulting from rapid wing pitch rotations [3], acceleration reaction forces or added mass forces [1], clap-and-fling [4], and wake capture [5].

Models of the separate unsteady aerodynamics mechanisms are often combined to

form a single quasi-steady model, where the aerodynamic forces produced by a beating wing can be estimated as the sum of the forces resulting from the separate aerodynamic mechanisms [1]. For hovering fruit flies, a quasi-steady model based on only leading-edge-vortex-based forces and rotational forces predicts the total aerodynamic forces rather well, suggesting that these are two essential aerodynamic mechanisms [6, 7].

The leading-edge-vortex-based forces scale with wing stroke rate and the angle-of-attack of the wing (figure 2.1 *a*) [3]. Insect wings tend to operate at remarkably high angles-of-attack (in the order of 45°) [3], which results in high aerodynamic force production. The ability to operate at high-angles-of-attack without stalling the airflow over the wing is linked to the presence of a leading-edge vortex (LEV) on the wing [8], which is stabilized due the accelerations acting on the flow caused by the revolving wing movement [9]. Despite the importance of the revolving wing movement on force production, leading-edge-vortex-based forces are often called the translational forces [6, 7]. Here, we will refrain from using this erroneous nomenclature, and call leading-edge-vortex-based forces the stroke-rate related forces.

The second aerodynamic mechanism, the rotational force mechanism, is schematically represented in figure 2.1*b,c*. In flapping flight, an insect wing beats back and forth, and in order to keep a positive angle-of-attack during both the forward and backward stroke, the animal needs to rapidly pitch its wing up and down at stroke reversal (figure 2.1*d*). This rapid pitch rotation generates aerodynamic forces in addition to the stroke-rate related force mechanism described earlier [10, 11, 12], and adjusting the phase of the pitch movement relative to stroke reversal allows an animal to rapidly adjust this rotational aerodynamic force [3]. For this reason, it was suggested that rotational force production might be particularly important for flight control and manoeuvrability [3], which was confirmed in later studies [7, 13, 14].

The previously proposed rotational force mechanism in fruit flies is based on the Kramer effect and modelled using Kutta-Joukowski theory [11]. The Kramer effect describes the force production of an aerofoil that both translates and pitches up at the same time. The rotational velocity causes an increase in the circulation bound to the aerofoil, which causes an increase in force production on the translating wing. For hovering fruit flies, this Kutta-Joukowski based model predicts rotational forces rather well, but there are several issues associated with this approach.

Firstly, as described above, an insect wing in hovering flight does not produce a pure translating motion; the back and forth wing stroke movements are in fact rota-

tional movements around the wing root. Secondly, the rotational force coefficient of the Kutta-Joukowski-based model remains depended on the wing-pitch rate and the chordwise location of the pitch axis [3, 11]. By using an alternative force normalization, one may develop a rotational force model of which the coefficient is independent of wing-pitch rate and pitch-axis placement. Finally, the Kutta-Joukowski model predicts zero rotational force at zero stroke rate, which occurs at stroke reversal. In contrast, wing-pitch rates are highest during stroke reversal, and a recent study on the aerodynamics of mosquito flight showed that these insects produce relatively high aerodynamic forces near stroke reversal [15]. As these forces correlated strongly with wing-pitch rate, the authors suggested that mosquitoes produce these forces by using additional novel aerodynamic mechanisms called rotational drag and trailing-edge-vortex-based lift, by smart positioning of the wing pitch axis relative to the wing chord [15].

The model developed to predict the rotational drag forces works well when applied to a hovering hawkmoth [16]. However, the effect of the geometrical scaling on the rotational drag coefficient is not tested directly, as only a single wing was tested [16]. For example, the rotational drag model suggests that a fully symmetrical wing pitching about the symmetry axis would produce finite rotational drag. Such wing would produce an aerodynamic torque about the pitch axis, but not a drag force because aerodynamic forces near the leading edge would be canceled by equal and oppositely directed aerodynamic forces near the trailing edge.

Based on computational fluid dynamics simulations with systematically varying wing morphology and wing movement kinematics, we tested how wing morphology and kinematics affect rotational force production. Using the outcomes, we propose an improved rotational force model. To isolate the rotational force mechanism from other aerodynamic mechanisms, such as the added mass, wake capture and leading-edge-vortex-based force mechanisms, we used a study design inspired by previous studies on the topic [3, 11], whereby we simulated wings moving at constant stroke rates and pitch rates. But unlike these previous studies, we tested a range of wing shapes and kinematics that encompassed two extremes within the dipteran insect family, the fruit fly and the malaria mosquito. In addition, we simulated generic wing shapes and varied the kinematics in a systematic way. Together, these simulations led to the development of a new rotational force model that can predict rotational forces at stroke reversal due to an offset between the wing-pitch axis and the chordwise symmetry axis of the wing.

2.2 Methodology

We conducted a systematic computational fluid dynamics (CFD) study within a parametric space based on eight different wing morphologies and a range of different kinematic parameters, using the IBAMR CFD solver based on the immersed boundary method [17]. See the Supplementary Methods in the Electronic Supplementary Material (ESM) for more detail.

2.2.1 Wing morphology

To systematically test the effect of wing shape on rotational force production, we designed a set of six rigid elliptical wings with a systematically varying chordwise position of the pitch axis (figure 2.2*a*, right-hand side). Each generic elliptical wing had a span of 3 mm and maximum chord length of 0.65 mm; for the six wings, the rotational axis relative to the centre of the wing varied with a step size of 0.1 mm from 0 mm for the symmetric wing to 0.5 mm for the most asymmetric wing, that thus pitches around an axis close to the leading edge. Next to these six geometries, we tested both the wing geometry of a fruit fly *Drosophila hydei* [13] and a malaria mosquito *Anopheles coluzzii* [18]. Both wings were scaled to also have a wing span (from root to wing tip) of 3 mm, and the wing-pitch axis was set to go through the centre of the wing root (figure 2.2*a*).

2.2.2 Kinematic design

The kinematics for these simulations were designed such that at a pitch angle of 45° the wing was moving at a constant pitch-rate ω_{pitch} and stroke-rate ω_{stroke} (figure 2.1*f–h*). At the point where the pitch angle is 45°, the forces were extracted. The extraction point was at a maximum stroke angle of 107°, to avoid wake interaction. As a consequence, at the point of extraction only the forces of two aerodynamic mechanisms are present: the stroke-rate related forces F_{stroke} and the rotational forces $F_{\text{rotational}}$. In line with previous studies into the rotational force mechanism [3,7], we estimated the rotational force ($F_{\text{rotational}}$) as the difference between the forces on a wing that is rapidly pitching up and the forces on the same wing with equal orientation, but with a zero pitch rate (figure 2.1*i*, movie S1), as

$$F_{\text{rotational}} = F_{\text{total}} - F_{\text{stroke}}. \tag{2.1}$$

Here F_{total} is the total force on the wing with a pitch angle of 45° and moving with both a constant stroke rate and pitch rate, and F_{stroke} is the stroke-rate related force of a wing with a constant pitch angle of 45° and the same stroke rate. Also in line with previous studies [3], we assumed that rotational forces are the result of a pressure difference above and below the wing, and therefore we measured and modelled the rotational forces normal to the flat wing surface.

We performed these simulations for a range of constant pitch rates ω_{pitch} and stroke rates ω_{stroke}. The (ω_{pitch}, ω_{stroke}) parametric space was designed such that it spans the range of stroke rates and pitch rates employed by a fruit fly *Drosophila hydei* [14] and malaria mosquito *Anopheles coluzzii* [18] during hovering flight (figure 2.1*j*). The resulting simulations spanned a Reynolds-number range of 25 to 500 (equation S1 in ESM), which is re presentable for small to average-sized insects [3]. Our method implies that the rotational forces are not depending on the pitch angle. To test the validity of this assumption, we repeated all the simulations in the (ω_{pitch}, ω_{stroke}) parametric space of the most asymmetric elliptical wing, at a pitch angle of 30° and 60° (figure S4).

2.2.3 Flow-field analysis

To study how changes in air movement and pressure distributions result in rotational forces, we visualized airflow dynamics at the wing surface and within two planes positioned perpendicular to the wing-pitch axis, placed at one-third and two-third of the wing span (i.e. $y = 1\,\text{mm}$ and $2\,\text{mm}$, respectively). On the wing surface, we visualized the pressure difference across the top and bottom surface of the wing, and within a selection of planes perpendicular to the wing-pitch axis we visualized the air-pressure distribution and distribution of the air-speed vectors.

2.2.4 Definition of our rotational model

We propose an aerodynamic rotational force model that captures the forces produced by an insect wing making simultaneous stroke and pitch movements, by combining a Kutta-Jakouwski-based model [3] with the rotational drag model [16]. The Kutta-Jakouwski-based model predicts forces based on stroke and pitch movement of the

wing; therefore, we will call these forces the stroke-pitch coupled forces $F_{\text{stroke-pitch}}$. The rotational drag term is only depended on the wing-pitch-rate and therefore we will call these forces the pitch-rate related forces F_{pitch} [16]. Thus, the total rotational force is defined as

$$F_{\text{rotational}} = F_{\text{stroke-pitch}} + F_{\text{pitch}}. \tag{2.2}$$

The stroke-pitch coupled force per unit span $F'_{\text{stroke-pitch}}$ can be modelled using Kutta-Joukowski theory [11] as (figure 2.1*b*)

$$F'_{\text{stroke-pitch}} = \rho U_\infty \Gamma, \tag{2.3}$$

where U_∞ is the free-stream velocity and Γ is bound circulation caused by the rotational pitch movement [11]. The conventional rotational force model for insect wings expresses the bound circulation as a function of both pitch rate and a wing-geometry metric, and U_∞ was characterized using wing-tip speed [11]. But as discussed above, this model has the caveat that an insect wing has a rotational stroke movement rather than a purely translational movement. To solve this issue, we propose to model U_∞ as a function of ω_{stroke} and the second-moment-of-area S_{yy}, similar to the case of stroke-rate related forces [18]. Likewise, we propose to express the pitch-rate related bound circulation as a function of ω_{pitch} and the second-moment-of-area relative to the pitch-axis S_{xx}. Thus, stroke-pitch coupled aerodynamic forces can be expressed based on Kutta-Joukowski theory (equation (2.3)) as

$$F_{\text{stroke-pitch}} = C_{F,\text{stroke-pitch}} \rho \sqrt{S_{xx} S_{yy}} \omega_{\text{pitch}} \omega_{\text{stroke}}, \tag{2.4}$$

where we call $\sqrt{S_{xx} S_{yy}}$ the pitch-stroke coupled second-moment-of-area, and $C_{F,\text{stroke-pitch}}$ is the non-dimensional force coefficient for stroke-pitch coupled force production (figure 2.1*b*). The second rotational force component (F_{pitch}, equation (2.2)) expresses the forces produced by a pitching wing in absence of a stroke movement (figure 2.1*c*). Here, we suggest modelling these pitch-rate related forces similar to the rotational drag [16], but with a different geometrical scaling. We propose that the offset between the pitch axis and the chord-wise centreline of the wing, called wing-pitch asymmetry ($b_{\text{asymmetry}}$, figure 2.1*c*), primarily affects the magnitude of pitch-rate related forces (figure 2.1*c*). The explanation of this is as follows. A fully symmetric wing, where the pitch axis is positioned at the wing centreline (figure 2.1*b*), will not

produce a net aerodynamic force when only pitching up. In contrast, an asymmetric pitching wing, where the pitch axis is shifted towards the leading edge, will produce a net aerodynamic force due to the asymmetry in effective airspeed near the leading edge and trailing edge of the wing (figure 2.1*c*). The effect of pitch axis offset on the second-moment-of-area relative to the pitch axis can be quantified by the asymmetric second-moment-of-area defined as

$$S_{x|x|} = \int_{c_1}^{c_2} x|x|\mathrm{d}A, \tag{2.5}$$

where x is the chordwise wing axis, $\mathrm{d}A$ is an infinitesimal wing surface area, and c_1 and c_2 are the locations of the wing trailing edge and leading edge, relative to the pitch axis, respectively (figure 2.1*e*). Based on the here proposed scaling, we pose to express pitch-rate related rotational aerodynamic forces as

$$F_{\text{pitch}} = C_{F,\text{pitch}}\rho S_{x|x|}\omega_{\text{pitch}}^2, \tag{2.6}$$

where $C_{F,\text{pitch}}$ is the force coefficient for pitch-rate related force production. Note that equation (2.6) does not include the factor $\frac{1}{2}$, because this results in the same scaling for F_{pitch} and $F_{\text{stroke-pitch}}$ (equation (2.4)), with $C_{F,\text{pitch}}$ and $C_{F,\text{stroke-pitch}}$ as non-dimensional parameters, respectively.

2.3 Results

2.3.1 Numerical simulations

We performed numerical experiments for 312 combinations of stroke rate, pitch rate and wing geometry (figure 2.1*j*, database S1). Each experiment took on average 25 000 time steps and the mesh size (after adaptive refinement) was on average four million cells. These simulations required 0.5 million CPU hours on our computer cluster with 176 CPU's.

2.3.2 Rotational force model

For our rotational force model, we focused on the forces normal to the wing surface, as we assumed rotational forces to primarily consist of pressure forces. We tested this assumption by comparing the normal and tangential components of the rotational

forces. The tangential force component was 11 % ± 6 % (mean ± standard deviation) of the total rotational forces, showing that tangential forces were small but not negligible. The full three-dimensional rotational forces for all simulations are provided in ESM, database S1. The rotational forces for all simulations of the most asymmetric elliptic wing, the fruit fly wing, the malaria mosquito wing, and the symmetric elliptic wing are shown in figure 2.2*b–e*, respectively. For each combination of pitch-rate and wing type, the rotational force varies linearly with stroke rate, allowing a fit with the linear function $F_{\text{rotational}} = A_{\text{stroke}}\omega_{\text{stroke}} + B_{\text{no-stroke}}$, where A_{stroke} is the stroke-rate slope, and $B_{\text{no-stroke}}$ is the intercept, i.e. the rotational force without a stroke rate. The fits for the different wings and pitch rates, figure 2.2 *b–e* shows that both the slope and intercept vary with pitch rate. Comparing this with our rotational model (equation (2)–(6)) suggests that slope of the fits (figure 2.2*b–e*) multiplied with the stroke rate are the stroke-pitch coupled forces ($A_{\text{stroke}}\omega_{\text{stroke}} = F_{\text{stroke-pitch}}$) and that the intercept are the pitch-rate related forces $B_{\text{no-stroke}} = F_{\text{pitch}}$. Combining this with equation (2.4) and (6) results in

$$\begin{aligned} A_{\text{stroke}} &= C_{F,\text{stroke-pitch}}\rho\sqrt{S_{xx}S_{yy}}\omega_{\text{pitch}} \\ B_{\text{no-stroke}} &= C_{F,\text{pitch}}\rho S_{x|x|}\omega_{\text{pitch}}^2. \end{aligned} \tag{2.7}$$

2.3.3 Stroke-pitch coupled rotational force model

We tested the relationship between $F_{\text{stroke-pitch}}$ and both ω_{pitch} and $\sqrt{S_{xx}S_{yy}}$ in three consecutive steps (figure 2.3*a–c*). First, we tested how A_{stroke} varied with pitch rate (figure 2.3*a*), confirming that this relationship is also approximately linear, and can thus be expressed as

$$A_{\text{stroke}} = A_{\text{pitch}}\omega_{\text{pitch}}. \tag{2.8}$$

Here, A_{pitch} is the linear fit coefficient that quantifies the pitch-rate slope for stroke-pitch coupled forces. Secondly, we tested how A_{pitch} depends on wing geometry, expressed as $\sqrt{S_{xx}S_{yy}}$ (figure 2.3*b*). This test revealed that A_{pitch} scales approximately linearly with $\sqrt{S_{xx}S_{yy}}$, and that the intercept of the linear fit equals zero. Finally, to estimate the magnitude of the corresponding force coefficient $C_{F,\text{stroke-pitch}}$,

we normalized the stroke-pitch couple force as

$$F^*_{\text{stroke-pitch}} = \frac{F_{\text{stroke-pitch}}}{\sqrt{S_{xx}S_{yy}}} \tag{2.9}$$

and plotted this against ω_{pitch} for all our simulations (figure 2.3*c*). The linear fit for each wing geometry has a slope equal to $C_{F,\text{stroke-pitch}}$, which is similar among the eight tested wings (figure 2.3*c*). Thus, we estimated the stroke-pitch-couple force coefficient for all eight wing geometries combined as $C_{F,\text{stroke-pitch}} = 2.08 \pm 0.15$ (mean $\pm$ standard deviation, $n = 8$).

2.3.4 Pitch-rate related rotational force model

We tested our pitch-rate related rotational force model using the same three-step approach as used for $F_{\text{stroke-pitch}}$ scaling above (figure 2.3*e*–*g*). First, we tested how F_{pitch} ($= B_{\text{no-stroke}}$) varied with pitch rate for the different wings (figure 2.3*e*), confirming that F_{pitch} scales quadratic with pitch rate as

$$F_{\text{pitch}} = D_{\text{pitch}}\omega^2_{\text{pitch}}, \tag{2.10}$$

where D_{pitch} is the quadratic growth factor of pitch-rate related forces. The intercept is set to zero, because no rotational forces are produced by a non-moving wing ($F_{\text{pitch}} = 0\,\text{N}$ at $\omega_{\text{stroke}} = 0\,\text{rad}\,\text{s}^{-1}$ and $\omega_{\text{pitch}} = 0\,\text{rad}\,\text{s}^{-1}$). Secondly, we tested how D_{pitch} depends on the asymmetry of the wing, expressed by $S_{x|x|}$, showing that this relationship is linear (figure 2.3*f*). We have omitted the symmetric elliptic wing from this analysis, because for this wing $F_{\text{pitch}} = 0\,\text{N}$ for all simulations with $\omega_{\text{stroke}} = 0\,\text{rad}\,\text{s}^{-1}$ (figure 2.2*e*). Thirdly, to determine the magnitude of the pitch-rate related rotational force coefficient we normalized the pitch-rate related force with $S_{x|x|}$ as

$$F^*_{\text{pitch}} = \frac{F_{\text{pitch}}}{S_{x|x|}}, \tag{2.11}$$

and plotted this against the pitch rate (figure 2.3*g*), for all simulations except those of the symmetric wing with $S_{x|x|} = 0\,\text{m}^4$. As expected, F^*_{pitch} scales quadratic with pitch rate, and thus we fitted quadratic functions through the data of each tested wing, where the quadratic growth factor of each fit equals $C_{F,\text{pitch}}$ of that wing. The val-

ues of $C_{F,\text{pitch}}$ of the different wings are similar, showing that the pitch-rate related rotational force coefficient is approximately independent of wing shape and kinematics. Therefore, we expressed this coefficient for the seven asymmetric wings combined as $C_{F,\text{pitch}} = 2.08 \pm 0.11$ ($n = 7$). Surprisingly, this coefficient is nearly identical to $C_{F,\text{stroke-pitch}}$ discussed in the previous section. In fact, the two coefficients are not significantly different from each other (paired t-test, t-value(degrees-of-freedom=13)=−0.89, p-value=0.41), and thus we suggest to use a single rotational force coefficient for both mechanisms, being $C_{F,\text{rotational}} = 2.08 \pm 0.13$ ($n = 15$). This results in our new rotational force model for a generic insect wing that moves at both a constant stroke-rate and pitch-rate of

$$F_{\text{rotational}} = C_{F,\text{rotational}}\rho\left(\sqrt{S_{xx}S_{yy}}\omega_{\text{stroke}}\omega_{\text{pitch}} + S_{x|x|}\omega_{\text{pitch}}^2\right). \tag{2.12}$$

2.3.5 Effect of pitch angle on rotational force production

To test whether our rotational force model is independent of the pitch angle, we estimated the rotational force coefficient for the most asymmetric elliptical wing at pitch angles of both 30° and 60° (figure S4). These coefficients were not significant different from the those of the 45° pitch angle simulations ($C_{F,\text{pitch}}$: independent t-test, t-value(5)= 2.28, p-value=0.057; $C_{F,\text{stroke-pitch}}$: independent t-test, t-value(6)= 0.52, p-value=0.62), showing that rotational force magnitude is not significantly dependent on pitch angle.

2.3.6 Aerodynamics of the combined stroke and pitch wing movement

The aerodynamic pressure forces produced by a wing moving with a combined stroke and pitch movement (F_{total}) act on the wing at its centre of pressure. The location of this centre of pressure is found by integrating the pressure distribution over the wing surface. We performed this analysis for the symmetric elliptic wing, the fruit fly wing, the mosquito wing, and the most asymmetric elliptic wings, moving with a stroke-rate and pitch-rate of both 1000 rad s^{-1} (figure 2.4*a–d*, respectively). For all wings, the centre of pressure is located close to the chordwise centre of the wing, suggesting that it is nearly independent of the location of the pitch-axis.

To illustrate the nature of the distribution of pressure differences, we showed the pressure differences across the wing surfaces (figure 2.4*e–h*), and flow field and air pressures around the wings within two planes perpendicular to the pitch-axis, at 1 mm

and 2 mm from the root (figure 2.4*i*-*l* and figure 2.4*m*-–*p*, respectively). These flow fields and air-pressure distributions are similar between all tested wing geometries: for all wings, the pressure differences across the wing surface is highest near the tip and leading edge of the wing (figure 2.4*e*–-*h*), and along the complete lower side of each wing a high-pressure region is present (figure 2.4*m*-*l*). The magnitude of this high-pressure region is higher at the location 2 mm from the root (figure 2.4*m*-*p*) than at the 1 mm location (figure 2.4*i*–*l*). On the upper side of each wing, a low-pressure region is formed close to the leading edge, which coincides with the expected location of the leading-edge-vortex (LEV). Both the low- and high-pressure regions intensify with increasing wing asymmetry, which is most apparent for the low-pressure region present near the trailing edge (figure 2.4*i*–*p*).

2.3.7 Aerodynamics of pitch-rate related rotational force production

The pitch-rate related aerodynamic forces on a wing (F_{pitch}, equation (2.6)) were isolated by analyzing the simulations of wings moving only with a non-zero pitch-rate ($\omega_{\text{stroke}} = 0\,\text{rad}\,\text{s}^{-1}$ and $\omega_{\text{pitch}} = 1000\,\text{rad}\,\text{s}^{-1}$, figure 2.5). We again analyzed the results of the symmetric elliptic wing, the most asymmetric elliptic wing, the mosquito wing and the fruit fly wing. Comparing these results with those of the same wings moving with both a stroke and pitch movement (figure 2.4), highlights several interesting aspects.

The center of pressure of the pitch-rate related forces (F_{pitch}, figure 2.5*a*–*d*) lies closer to the trailing edge than that of the total aerodynamic force (F_{total}, figure 2.4*a*–*d*). For all wings, the distribution of the pressure difference across the wing surface does not vary along the span of the wing (figure 2.5*e*–*h*). In contrast, the pressure difference varies strongly in chordwise direction, where it increases with the chordwise distance from the pitch axis. In front of the pitch axis (i.e. towards leading edge), these pressure differences are positive, whereas behind the pitch axis (i.e. towards the trailing edge) they are negative. Because negative pressure differences are associated with a positive force production, the wing area in front of the pitch axes contributes to negative pitch-rate related force production, and areas behind the pitch axis produce positive forces.

These dynamics explain why pitch-rate related aerodynamic forces increase with wing pitch asymmetry (as expressed by $S_{x|x|}$), and why the center of pressure of F_{pitch} is located relatively close to the trailing edge (figure 2.5*a*–*d*): for the symmetric

wing ($S_{x|x|} = 0$), the same amount of surface area is located in front and behind the pitch axis, and thus the positive and negative contributions to force production exactly balance each other (figure 2.5*e*), resulting in a zero net pitch-rate related force (figure 2.5*a*). For the asymmetric wings, the wing area behind the pitch axis is larger than the area in front of the pitch axis, resulting in a larger positive contribution to F_{pitch} near the trailing edge than the negative F_{pitch} production near the leading edge (figure 2.5*b–d*). As a result, the net pitch-rate related forces are positive and located behind the chordwise centre of the wing.

To illustrate the nature of these pressure differences across the wing surface, we show the flow field and air pressures around the wings within a plane perpendicular to the pitch axis and at 2 mm from the root of the wing for the four examined cases (figure 2.5*i–p*). The flow fields are shown in two reference frames, in the wing reference frame as defined above (figure 2.5*i–l*) and the wing reference frame without the subtraction of the wing velocity (figure 2.5*m–p*).

For the symmetric wing (figure 2.5*i,m*), the air pressure and flow fields are perfectly two-fold rotational symmetric relative to the center of the wing, explaining why no net pressure force is produced. For all asymmetric wings, there are large pressure variations near the trailing edge of the wing (figure 2.5*j–l*, *n–p*): underneath each wing there is a high-pressure region and above the wing a low-pressure region. Thus, the large pressure differences across the asymmetric wings, near the trailing edge, are due to both a high-pressure region below the wings and a low-pressure region above the wings.

To find the origin of the high-pressure region, we used the flow fields in the wing reference frame (figure 2.5*j–l*), showing that for all asymmetric wings, there is a stagnation point in the middle of the high-pressure region. To find the origin of the low-pressure region above the wing, we used the flow fields in the wing reference frame, but without subtracting of the wing velocity (figure 2.5*m–p*). These flow fields show that the air behind the stagnation point (towards the trailing edge) curls around the trailing edge, forming a vortex near the trailing edge on the top surface of the wing. The location of this trailing edge vortex coincides with a low-pressure region found above the wing near the trailing edge.

2.3.8 Aerodynamics of stroke-pitch coupled force production

Unlike for the pitch-rate related forces, there are no simulations at which only stroke-pitch coupled forces were produced. Therefore, to isolate the aerodynamics underlying the stroke-pitch coupled rotational forces ($F_{\text{stroke-pitch}}$) we used a method similar to the method for estimating rotational forces (equations (1)–(2)). When assuming that the pressure field around a wing that has a stroke and pitch movement (p_{total}) consists of the linear summation of the pressure field resulting from the stroke movement (p_{stroke}), the pitch movement (p_{pitch}) and the stroke-pitch coupling ($p_{\text{stroke-pitch}}$), then we can estimate $p_{\text{stroke-pitch}}$ as

$$p_{\text{stroke-pitch}} = p_{\text{total}} - p_{\text{pitch}} - p_{\text{stroke}} \tag{2.13}$$

where the pressure fields p_{total}, p_{pitch} and p_{stroke} come from separate simulations.

We performed this analysis for the four wing geometries described earlier, moving at $\omega_{\text{stroke}} = 1000\,\text{rad}\,\text{s}^{-1}$ and $\omega_{\text{pitch}} = 1000\,\text{rad}\,\text{s}^{-1}$ (figure 2.6). Thus, to estimate $p_{\text{stroke-pitch}}$ for a wing moving at $\omega_{\text{stroke}} = 1000\,\text{rad}\,\text{s}^{-1}$ and $\omega_{\text{pitch}} = 1000\,\text{rad}\,\text{s}^{-1}$, we subtracted both the pressure field p_{stroke} around a wing moving at $\omega_{\text{stroke}} = 1000\,\text{rad}\,\text{s}^{-1}$ and $\omega_{\text{pitch}} = 0\,\text{rad}\,\text{s}^{-1}$, and pressure field p_{pitch} of a wing moving at $\omega_{\text{stroke}} = 0\,\text{rad}\,\text{s}^{-1}$, $\omega_{\text{pitch}} = 1000\,\text{rad}\,\text{s}^{-1}$, from pressure field p_{total} around a wing moving at $\omega_{\text{stroke}} = 1000\,\text{rad}\,\text{s}^{-1}$ and $\omega_{\text{pitch}} = 1000\,\text{rad}\,\text{s}^{-1}$ (equation (2.13)). We did not apply this subtraction for the velocity field due to their non-linear relation with the pressure field.

The comparison of the derived pressure fields that result in $F_{\text{stroke-pitch}}$ (figure 2.6) with the pressure fields resulting in F_{total} and F_{pitch} (figure 2.4 and 2.5, respectively) highlights several interesting aspects. For all wings, both the magnitude and the location of $F_{\text{stroke-pitch}}$ (figure 2.6*a–d*) lie in between those of F_{total} and F_{pitch} (figure 2.4*a–d* and 2.5*a–d*, respectively).

The pressure differences across the wing surface that causes $F_{\text{stroke-pitch}}$ (figure 2.6*e–h*) is similarly distributed along the wing as for that of F_{total} (figure 2.4*e–h*), with a low-pressure region near the wing tip and trailing edge. Unlike for the F_{total} case, for $F_{\text{stroke-pitch}}$ a secondary low-pressure is present close to the trailing edge at approximately $2/3^{\text{rd}}$ span (figure 2.6*e–h*).

The pressure in the two planes perpendicular to the pitch-axis (figure 2.6*i–p*) reveal a high-pressure region at the bottom surface of all tested wings, which is slightly shifted towards the trailing edge. In the plane 1 mm from the wing root (figure 2.6*i–l*),

a low-pressure region is distributed over a large area on top of each wing, whereas in the plane closer to the wing tip (2 mm from root) the low-pressure region is mostly concentrated near the leading edge. Particularly the intensity of the low-pressure region near the leading edge increases towards the wing tip (figure 2.6*m–p*), explaining the large pressure difference across the wing near the tip and leading edge.

2.4 Discussion

2.4.1 The rotational force model

In our study, we showed that the rotational aerodynamic force ($F_{\text{rotational}}$) produced by an insect wing moving at a constant stroke rate and pitch rate is composed of a pitch-rate related force component (F_{pitch}) and a stroke-pitch coupled force component ($F_{\text{stroke-pitch}}$) (equation (2.12)). The relation between $F_{\text{rotational}}$ and the stroke rate, captured in the stroke-pitch coupled force component ($F_{\text{stroke-pitch}}$), is linear, which is in line with previous research [11]. Unlike these previous models, our stroke-pitch coupled force model explicitly quantifies the effect of wing morphology on stroke-pitch coupled force production.

Our pitch-rate related rotational force model is also similar to models described in previous studies [16, 19]. But unlike these previous models, our model is able to accurately capture the effect of wing-pitch asymmetry on the pitch-rate related force, allowing us to show how flying insects can generate forces without making a stroke movement.

Our rotational model is based on CFD simulations on rigid insect wings and elliptical wings rotating at constant stroke rates and pitch rates. This approach isolates the rotational forces from the forces resulting from other aerodynamic mechanisms, which enabled us to model the rotational forces. This also removed the effect of the interaction between the rotational force mechanism and the other aerodynamic mechanism. Thus, how all these aerodynamic mechanisms interact remains an open question.

In addition, the proposed model assumes that the forces are all fully developed, while it is known that the flow over the wing needs time to develop [12], meaning that at rapid changing pitch rates the force estimates of our model might overestimate the forces found in real insects. We consider these transient effects part of a separate aerodynamic mechanism that should be investigated further in a future study.

Despite these limitations, our new rotational force model captures the full dynamics between rotational force production and wing morphology and motion, yet the model remains remarkable simple. Strikingly, the force coefficients of the stroke-pitch coupled force model and pitch-rate related force model do not differ significantly from each other suggesting that both components form a single rotational mechanism (equation (2.12)).

2.4.2 Stroke-pitch coupled rotational forces

The stroke-pitch coupled rotational force model resembles the conventional rotational models based on Kutta-Joukowski theory [11, 16], but we use a different geometrical scaling (equation (2.4)). After applying geometrical scaling, the previously-defined conventional rotational lift model continues to show a dependency on wing pitch rate, as its force coefficient increases with pitch rate [11]. In contrast, our stroke-pitch coupled rotational force model removes the dependency of its force coefficient on the wing pitch rate completely (figure 2.3*a–c*).

In addition, due to the applied geometrical scaling (equation (2.4)), the coefficient of our stroke-pitch coupled rotational force model is also independent of wing geometry, at least for the eight tested wings (figure 2.3*a–c*), whereas for previous models this is ambiguous. This geometrical scaling shows equal effects of spanwise and chordwise wing size on force production, as shown by the equal contribution of S_{yy} and S_{xx}, respectively (equation (2.4)). This means that an insect wing with a large span (high aspect ratio) is equally able to generate pitch-stroke coupled rotational forces as an insect wing with a large chord width (low aspect ratio).

The distribution of the pressure differences across the wing surface that underlie the stroke-pitch coupled rotational forces also shows a dependence on both the span and the chord. This demonstrates the physical basis of the scaling used in our model: flapping-induced velocities further away from both the wing root and the pitch-axis are higher, leading to larger pressure differences across the wing surface, which in turn leads to a larger net aerodynamic force.

2.4.3 Pitch-rate related rotational forces

Contrary to the stroke-pitch coupled forces, the pitch-rate related rotational forces are not dependent on the stroke-rate, and can thus result in significant aerodynamic force production at stroke reversal of a beating insect wing. Such forces around stroke re-

versal were observed in flying mosquitoes, and ascribed to a new aerodynamic mechanism called rotational drag [15, 16]. Our pitch-rate related rotational force model resembles the model previously developed for this rotational drag mechanism [16], but similar to the pitch-stroke coupled rotational force model, our geometrical scaling is crucially different. We have chosen a geometrical scaling that quantifies asymmetry in the wing, which is a vital basis for pitch-rate related rotational force production.

The geometrical scaling of our pitch-rate related rotational force model reveals that the offset of the pitch-axis with respect to the wing symmetry axis determines the magnitude of the pitch-rate related rotational forces (figure 2.3*e–g*). Hence, a wing of which the pitch axis coincides with the symmetry axis cannot produce pitch-rate related forces, something that was not captured by previous models [3, 16, 19]. This suggests that an insect wing with a pitch axis located close to the chordwise symmetry axis cannot generate high forces around stroke-reversal, using the rotational force mechanism.

The flow dynamics associated with pitch-rate related rotational force production shows that the low-pressure region is correlated to the presence of a trailing-edge vortex (figure 2.5). This trailing-edge vortex has been identified previously near the stroke reversal of a flapping mosquito wing, and which was proposed to result from wake-capture [15]. In our study, wake-capture was absent and we still found a trailing edge vortex; this suggests that the trailing edge vortex of the flapping mosquito wing might be related to rotational force production instead of wake capture.

2.4.4 Rotational forces in the fruit fly and malaria mosquito

Our rotational model is not a complete model for flapping insect flight because other important aerodynamic mechanisms such as added mass, wake capture, and stroke-based forces are not modelled. Therefore, a remaining question is: how important are the stroke-pitch coupled and pitch-rate related rotational forces for flying insects?

To investigate this, we applied our model to the full parametric space of stroke rates and pitch rates found within the wingbeat kinematics of a hovering fruit fly (figure 2.7*a–d*) [13] and a hovering malaria mosquito (figure 2.7*e–h*) [20]. Throughout each parametric space, we estimated the rotational forces $F_{\text{stroke-pitch}}$ and F_{pitch} using our rotational force model (equation (2.12)), which we then normalized using the approximate body weight of these fruit flies and mosquitoes (mg, with mass $m = 1\,\text{mg}$ and gravitational acceleration $g = 9.8\,\text{m}\,\text{s}^{-2}$).

Both the stroke-pitch coupled rotational forces and pitch-rate related rotational forces were on average higher for the mosquito than for the fruit fly (figure 2.7), which is explained by the higher pitch-rates throughout the mosquito wingbeat caused by their extremely high-frequency wingbeat (580 Hz for the mosquito compared to 190 Hz for the fruit fly) [13, 20]. These results agree with previous studies that showed that high-frequency flappers rely more on rotational forces for weight support [15, 21].

In contrast, our results suggest that the differences in rotational force production between the fruit fly and mosquito might be smaller than previously reported based on the wingbeat kinematics alone. The low aspect ratio wing of the fruit fly has a relatively high second-moment-of-area about the pitch axis, and as a result both and $S_{x|x|}$ are higher for the fruit fly than for the mosquito (figure 2.2*a*). Hence, compared to the mosquito, the fruit fly has a wing shape that is better adapted for high rotational force production. This shows that to assess the relative contribution of rotational forces to total aerodynamic force production in flying insects, both wing kinematics and wing morphology should be considered. To maximize its rotational force production, an insect can employ a low-aspect-ratio wing in combination with high pitch rates and stroke rates. Furthermore, placing the pitch-axis closer to the wing leading edge increases the asymmetric second-moment-of-area of the wing and consequently increases the pitch-rate related rotational forces.

For both the mosquito and fruit fly, pitch-rate related rotational forces dominate at low stroke-rates, whereas at higher stroke-rates the stroke-pitch coupled rotational forces are higher (figure 2.7*d, h*). This suggests that near stroke reversal our newly-defined pitch-rate related rotational forces are the primary aerodynamic force mechanism at play. Several studies have shown that insects primarily use this phase of the wingbeat to produce aerodynamic roll and pitch torques for flight control [7], suggesting that the here-introduced pitch-rate related rotational forces might be relatively important for animal flight control and manoeuvrability.

The CFD simulations that we based our rotational lift model on encompasses a Reynolds-number regime ranging from 25 to 500 (as defined by ESM equation S1). Most insects fly within this Reynolds-number range [3, 22], suggesting that the model might be relevant for the majority of flying insects; more research is needed to test whether our model is also valid for natural flyers that operate at significantly higher Reynolds numbers, such as large insects, birds and bats.

2.5 References

[1] C. P. Ellington. “The aerodynamics of hovering insect flight. IV. aerodynamic mechanisms”. In: *Philosophical transaction royal society London* 305 (1984), pp. 79–113. DOI: 10.1098/rstb.1984.0052.

[2] C. van den Berg and C. P. Ellington. “The three-dimensional leading-edge vortex of a ’hovering’ model hawkmoth”. In: *Philosophical transactions B* (1997). DOI: 10.1098/rstb.1997.0024.

[3] M. H. Dickinson, F. Lehmann, and S. P. Sane. “Wing rotation and the aerodynamic basis of insect flight”. In: *Science* 284.5422 (June 1999), pp. 1954–1960. DOI: 10.1126/science.284.5422.1954.

[4] G. R. Spedding and T. Maxworthy. “The generation of circulation and lift in a rigid two-dimensional fling”. In: *Journal of Fluid Mecahnics* 165 (1986), pp. 247–272. DOI: 10.1017/S0022112086003087.

[5] J. M. Birch and M. H. Dickinson. “The influence of wing–wake interactions on the production of aerodynamic forces in flapping flight”. In: *The Journal of Experimental Biology* 206 (2003), pp. 2257–2272. DOI: 10.1242/jeb.00381.

[6] W. B. Dickson, A. D. Straw, and M. H. Dickinson. “Integrative Model of *Drosophila* flight”. In: *AIAA Journal* 46.9 (2008), pp. 2150–2164.

[7] M. H. Dickinson and F. T. Muijres. “The aerodynamics and control of free flight manoeuvres in Drosophila”. In: *Philosophical Transactions B* 371.1704 (2016). DOI: 10.1098/rstb.2015.0388.

[8] C. Poelma, W. B. Dickson, and M. H. Dickinson. “Time-resolved reconstruction of the full velocity field around a dynamically-scaled flapping wing”. In: *Experiments in fluids* 41 (2006), pp. 213–225.

[9] D. Lentink and M. H. Dickinson. “Rotational accelerations stabilize leading edge vortices on revolving fly wings”. In: *The Journal of Experimental Biology* (2009). DOI: 10.1242/jeb.022269.

[10] C. P. Ellington. “The aerodynamics of hovering insect flight. III. kinematics”. In: *Philosophical Transactions B* 305.1122 (1983), pp. 41–78. ISSN: 0080-4622.

[11] S. P. Sane and M. H. Dickinson. “The aerodynamic effects of wing rotation and a revised quasi-steady model of flapping flight”. In: *The Journal of Experimental Biology* 205.8 (2002), pp. 1087–1096.

[12] S. P. Sane. “The aerodynamics of insect flight”. In: *The Journal of Experimental Biology* 206 (2003), pp. 4191–4208. DOI: 10.1242/jeb.00663.

[13] F. T. Muijres, M. J. Elzinga, J. M. Melis, and M. H. Dickinson. “Flies evade looming targets by executing rapid visually directed banked turns”. In: *Science* 344 (2014), pp. 172–177. DOI: 10.1126/science.1248955.

[14] F. T. Muijres, J. Elzinga, N. A. Iwasaki, and M. H. Dickinson. “Body saccades of Drosophila consist of stereotyped banked turns”. In: *The Journal of Experimental Biology* 218 (2015), pp. 864–875. DOI: 10.1242/jeb.114280.

[15] R. J. Bomphrey, T. Nakata, N. Phillips, and S. M. Walker. “Smart wing rotation and trailing-edge vortices enable high frequency mosquito flight”. In: *Nature* 554 (2017), pp. 92–95. DOI: 10.1038/nature21727.

[16] T. Nakata, H. Liu, and R. J. Bomphrey. “A CFD-informed quasi-steady model of flapping-wing aerodynamics”. In: *Journal of Fluid Mechanics* 783 (Nov. 2015), pp. 323–343. DOI: 10.1017/jfm.2015.537.

[17] A. P. S. Bhalla, R. Bale, B. E. Griffith, and N. A. Patankar. “A unified mathematical framework and an adaptive numerical method for fluid–structure interaction with rigid, deforming, and elastic bodies”. In: *Journal of Computational Physics* 250 (2013), pp. 446–476. DOI: 10.1016/j.jcp.2013.04.033.

[18] C. P. Ellington. “The aerodynamics of hovering insect flight. I. The quasi-steady analysis”. In: *Philosophical transactions of the Royal Society B* 305 (1984), pp. 1–15. DOI: 10.1098/rstb.1984.0049.

[19] Jeffrey A. Walker. “Rotational lift: something different or more of the same?” In: *The Journal of Experimental Biology* 205 (2002), pp. 3783–3792.

[20] F.T. Muijres, S.W. Chang, W.G. Veen, J. Spitzen, B.T. Biemans, M.A.R. Koehl, and R. Dudley. “Escaping blood-fed malaria mosqtuitoes minimize tactile detection without compromising on take-off speed”. In: *Journal of Experimental Biology* 220.20 (2017), pp. 3751–3762. DOI: 10.1242/jeb.163402.

[21] D. L. Altshuler, W. B. Dickson, J. T. Vance, S. P. Roberts, and M. H. Dickinson. "Short-amplitude high-frequency wing strokes determine the aerodynamics of honeybee flight". In: *PNAS* 102.50 (2005), pp. 18213–18218.

[22] R. Dudley. *The biomechanics of insect flight: form, function, evolution*. Princeton University Press, 2002.

[23] Pauli Virtanen, Ralf Gommers, Travis E. Oliphant, Matt Haberland, Tyler Reddy, David Cournapeau, Evgeni Burovski, Pearu Peterson, Warren Weckesser, Jonathan Bright, Stéfan J. van der Walt, Matthew Brett, Joshua Wilson, K. Jarrod Millman, Nikolay Mayorov, Andrew R. J. Nelson, Eric Jones, Robert Kern, Eric Larson, CJ Carey, İlhan Polat, Yu Feng, Eric W. Moore, Jake Vand erPlas, Denis Laxalde, Josef Perktold, Robert Cimrman, Ian Henriksen, E. A. Quintero, Charles R Harris, Anne M. Archibald, Antônio H. Ribeiro, Fabian Pedregosa, Paul van Mulbregt, and SciPy 1. 0 Contributors. "SciPy 1.0: Fundamental Algorithms for Scientific Computing in Python". In: *Nature Methods* 17 (2020), pp. 261–272. DOI: `https://doi.org/10.1038/s41592-019-0686-2`.

2.6 Figures

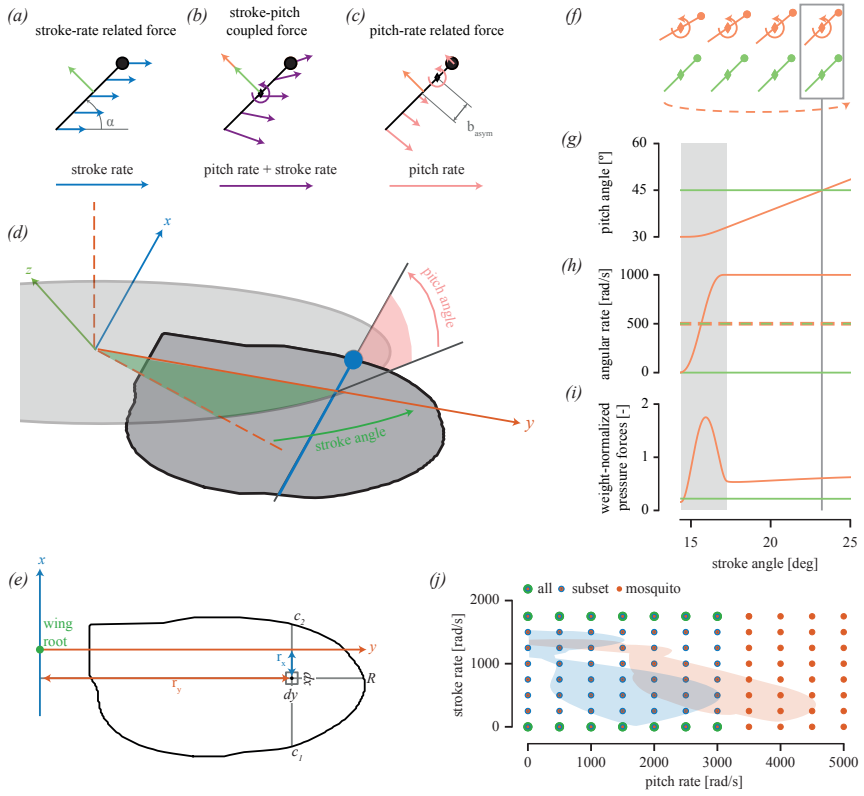

Figure 2.1: (*a*–*c*) A two-dimensional schematic representation of the stroke-rate related force, the stroke-pitch coupled force, and the pitch-rate related force on a wing, respectively (equations (1)–(2)). The circle and diamond indicate the leading edge and pitch-axis location, respectively. The green and orange arrows show stroke-rate related force and rotational force, respectively. (*a*) Blue arrows show wing velocity due to stroke movement. (*b*) Purple arrows show the wing-velocity distribution due to the combined stroke-pitch movement. (*c*) Pink arrows show the wing velocity due to the pitch movement; $b_{asymmetry}$ is pitch asymmetry. (*d*) The fruit fly wing in the world reference frame, including the wing reference frame axes (attached to the wing), the stroke plane (in light grey), stroke angle, and pitch angle (angle between the stroke plane and the wing surface). (*e*) wing geometry parameters for calculating the second-moment-of-area parameters S_{xx}, S_{yy} and $S_{x|x|}$. (*f*–*i*) the kinematics and forces used to estimate rotational force production, where data in orange are for the pitching wing, and the green data are of a non-pitching wing ($\omega_{\text{pitch}} = 0\,\text{rad}\,\text{s}^{-1}$); grey area is where the wing is still accelerating around its pitch axis; box with line indicates the stroke angle at which forces are extracted. (*f*) schematic representation of the two wings; the curved dashed line indicates the direction of (revolving) stroke motion; (*g*) pitch angle versus stroke angle throughout the simulation, (*h*) pitch rate (solid) and stroke rate (dashed) versus stroke angle, and (*i*) forces normal to the wing surface versus stroke angle. (*j*) Parametric space of stroke rate and pitch rate for an average wingbeat of a hovering fruit fly (blue surface)[13] and of a hovering mosquito (red surface)[18]. Dots indicate the stroke rate and pitch rate of all simulations conducted with the mosquito wing (red dots), the fruit-fly wing and the symmetric and most asymmetric elliptic wings (blue dots), and all eight tested wings (green dots).

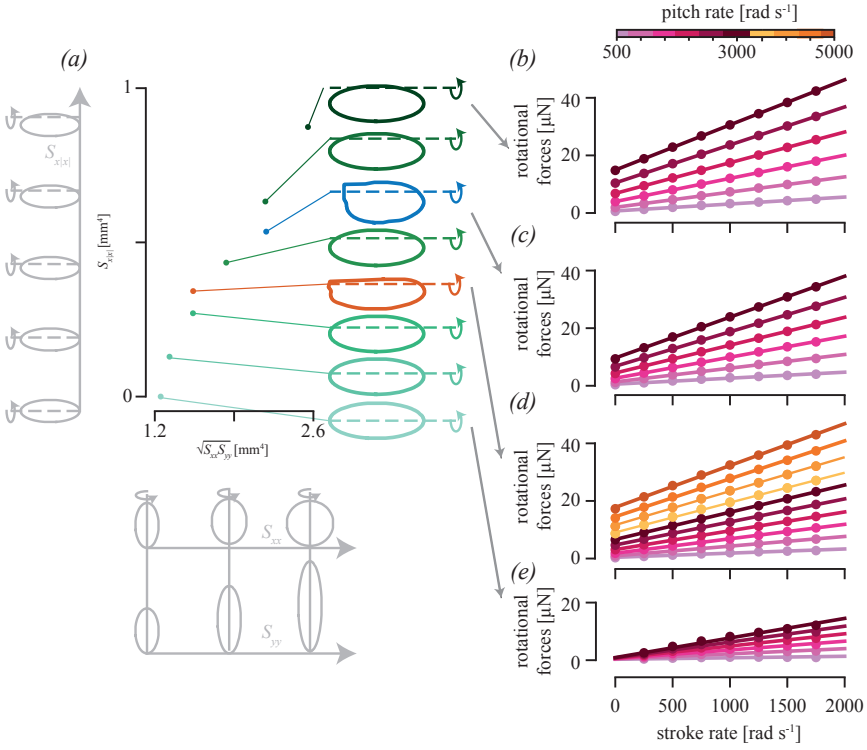

Figure 2.2: (*a*) The geometry parameters, the stroke-pitch coupled second-moment-of-area $\sqrt{S_{xx}S_{yy}}$ and the asymmetrical second-moment-of-area $S_{x|x|}$, of the six elliptic wings (green), the fruit-fly wing (blue), and the mosquito wing (red). In light-grey along the $\sqrt{S_{xx}S_{yy}}$ y-axis are examples of wings with both increasing S_{xx} and S_{yy}; in light-grey along the $S_{x|x|}$ -axis is an example of wings with increasing $S_{x|x|}$. (*b–e*) The rotational forces (difference between total forces and stroke-rate related forces at an angle of attack of 45°) (ordinate) versus the stroke-rate (abscissa) and pitch-rate (colour-bar above (*b*)), for the most asymmetric elliptic wing, the fruit-fly wing, the mosquito wing, and the symmetric wing, respectively. A linear function was fitted through the dataset at each simulated pitch rate.

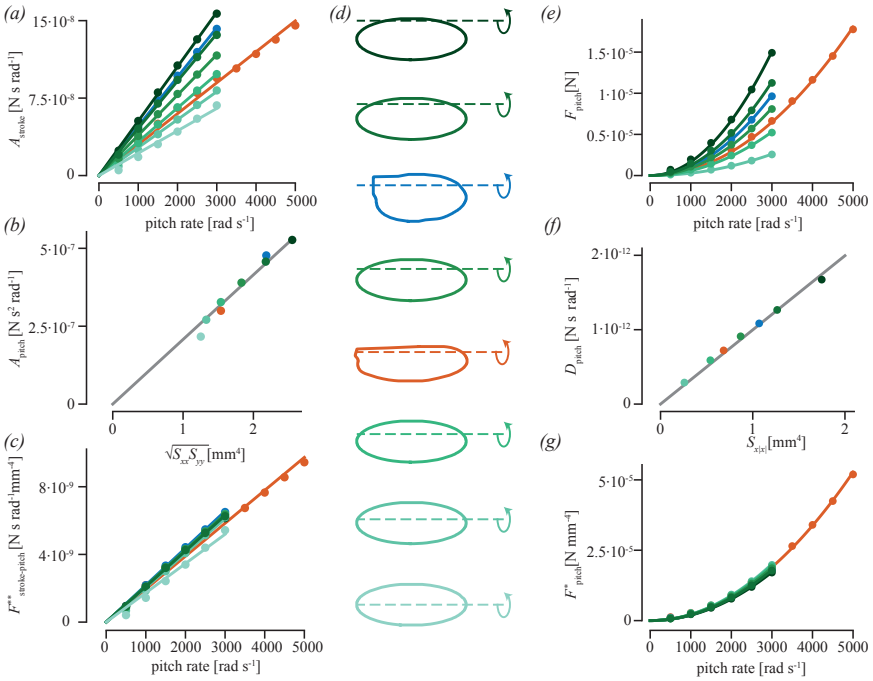

Figure 2.3: Testing of the stroke-pitch coupled force model (*a*–*c*) and the pitch-rate related force model (*e*–*g*) using our CFD simulations. All data was color-coded with wing geometry as defined in (*d*). (*a*) Stroke-rate slope of stroke-pitch coupled forces A_{stroke} (as defined by equation (2.7)) versus pitch-rate, for the eight wing geometries (color coded). Linear functions were fitted through the data for each separate wing. (*b*) Pitch-rate slope for stroke-pitch coupled forces A_{pitch} (equation (2.8)) versus $\sqrt{S_{xx}S_{yy}}$, including a linear fit with intercept fixed at zero. (*c*) Normalized stroke-pitch coupled forces $F^{**}_{\text{stroke-pitch}}$ (equation (2.9)) versus pitch-rate. The linear fit for each wing has a slope equal to its force coefficient CF,stroke-pitch (equation (2.4)). (*e*) Pitch-rate related rotational forces Fpitch versus pitch rate, including quadratic fits. (*f*) Growth factor of these quadratic fits D_{pitch} (equation (2.10)) versus $S_{x|x|}$, including a linear fit. (*g*) Normalized pitch-rate related forces F^{*}_{pitch} (equation (2.11)) versus pitch rate. The growth factor of the quadratic fit for each wing equals its force coefficient, $C_{F,\text{pitch}}$ (equation (2.6)).

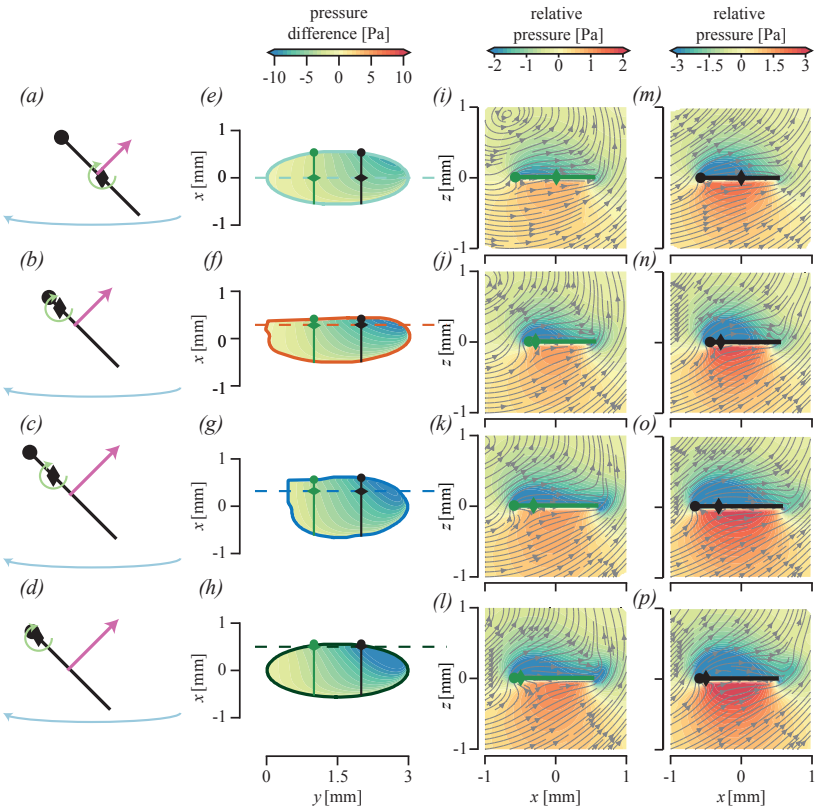

Figure 2.4: The aerodynamics of the sub-set of four wings moving at a stroke rate and pitch rate of both 1000 rad s^{-1}. (*a–d*) Schematic representation of the aerofoil, where the dot indicates the leading edge and the diamond the rotation axis. Pink arrow illustrates the resultant force, F_{total}, blue arrow shows stroke direction, and green arrow indicates the direction of the wing pitch. The forces and their location were obtained by integration of the pressure differences across the wing surface. (*e–h*) The distribution of pressure differences across the wing surface. Dashed line indicates pitch-axis location; green and black lollipops indicate the location of the extraction planes shown in (*i–l*) and (*m–p*), respectively. (*i–p*) Pressure and flow field relative to the wing surface extracted from the planes indicated in (*e–h*).

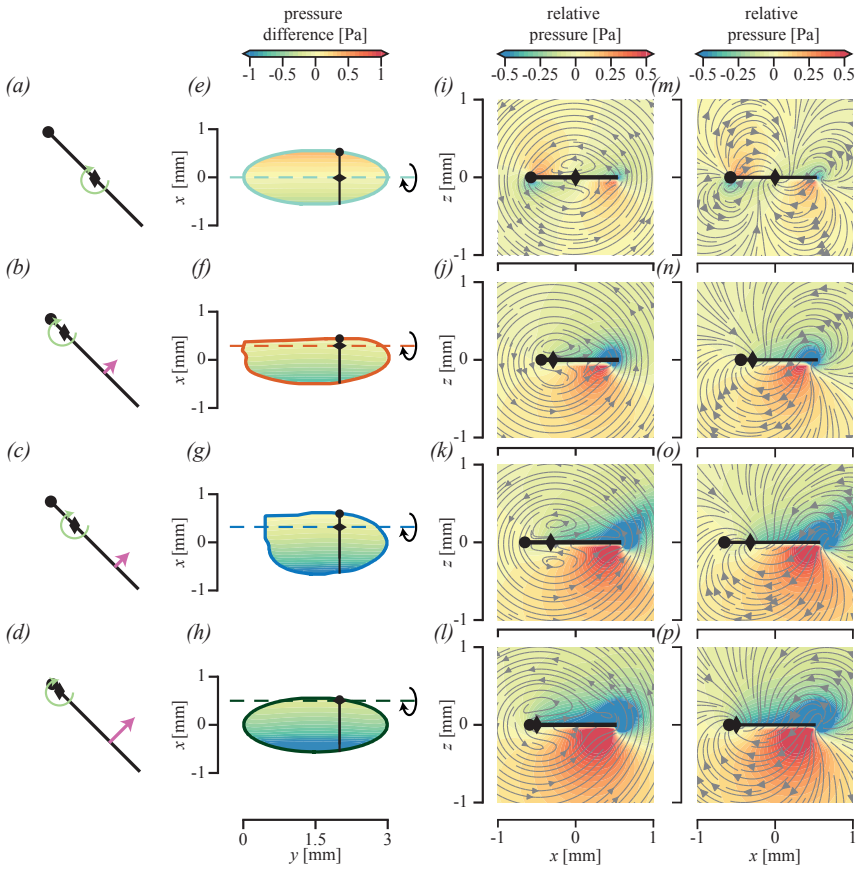

Figure 2.5: The aerodynamics of pitch-rate related force production by the sub-set of four wings moving at a pitch rate of 1000 rad s^{-1} and a zero stroke rate. (*a–d*) Schematic representation of the aerofoil (dot indicates leading edge; diamond indicates rotation axis). Pink arrow indicates the pitch-rate related force F_{pitch}, and green arrow shows the direction of wing pitch. The forces and their location were obtained by integration of the pressure differences across the wing surface. (*e–h*) The distribution of pressure difference across the wing surface. Dashed line shows the pitch-axis; black lollipop indicates the location of the extraction plane shown in (*i–p*). (*i–p*) Pressure and flow field in respectively the wing reference frame with subtraction of wing velocity (*i–l*) and the wing reference frame without subtraction of wing velocity (*m–p*).

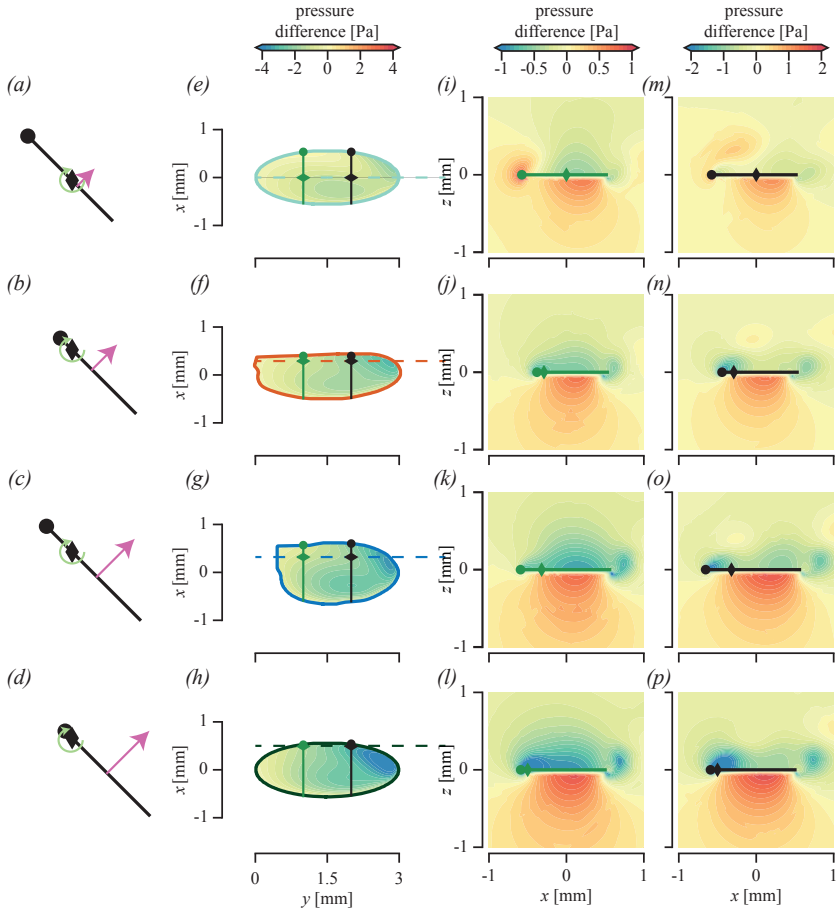

Figure 2.6: The aerodynamics of stroke-pitch coupled force production by the subset of four wings moving at both pitch rates and stroke rates of 1000 rad s^{-1}. (*a–d*) Schematic representation of the aerofoil (dot indicates leading edge; diamond indicates rotation axis). Pink arrow indicates the resultant stroke-pitch coupled force $F_{\text{stroke-pitch}}$, and green arrow indicates the wing pitch direction. The forces and their location were obtained by integration of the pressure differences across the wing surface. (*e–h*) Distribution of pressure differences across the wing surface. Dashed line indicates the location of the pitch-axis; green and black lollipops indicate the location of the extraction planes visualized in (*i–l*) and (*m–p*), respectively. (*i–p*) Pressure distributions throughout the planes defined in (*e–h*). All pressures were computed using equation (2.13).

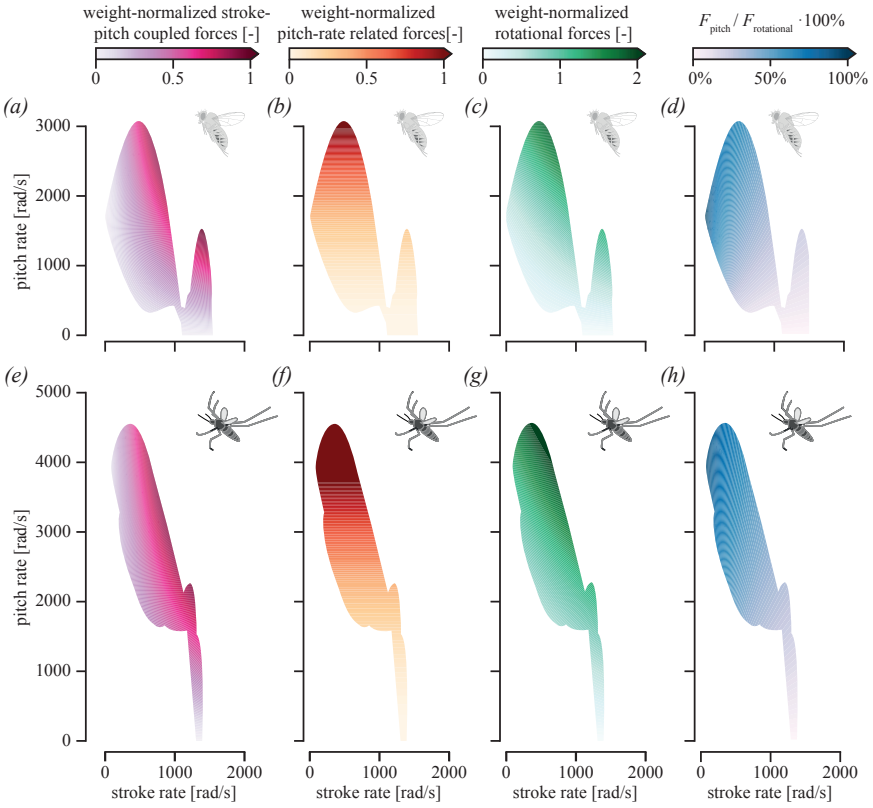

Figure 2.7: Weight-normalized rotational forces throughout the parametric space of stroke rates and pitch rates, for the wingbeat of a hovering fruit fly (*a–d*) and a hovering malaria mosquito (*e–h*). The different components are: (*a, e*) weight-normalized stroke-pitch coupled rotational forces; (*b, f*) weight-normalized pitch-rate related forces; (*c, g*) weight-normalized total rotational forces; (*d, h*) percentage of pitch-rate related forces relative to the total rotational forces. All forces were estimated using our rotational force model (equation (2.12)).

Supplementary methods

2.7 Pre-processing

2.7.1 Kinematic design

Each numeric experiment consisted of two simulations. A simulation where the wing had a set stroke rate and a constant pitch angle, and a wing moving at the same stroke rate but that was also pitching up at a constant pitch rate (figure 2.8*f–h*).

For the simulation with constant pitch angle, the wing was placed in the numerical domain at a pitch angle of 45°, and the stroke rate ω_{stroke} was increased to the required value using a smooth acceleration. The pitching wing was started at a pitch angle of 30°, and ω_{stroke} was increased using the same smooth acceleration. As soon as this wing reached its constant stroke rate, a smooth acceleration around the pitch axis was started until it reached the desired pitch rate (figure 2.9*g*). We determined the forces acting on both wings at the point in time at which the pitching wing reached a pitch angle of 45°. We then estimated the rotational forces on the pitching wing as the difference in forces normal to the wing surface between the pitching and non-pitching wing (figure 2.8*i*).

For the set of eight wing shapes, a parametric study of different combinations of stroke rate ω_{stroke} and pitch rate ω_{pitch} was conducted. The parametric space completely encloses the parametric space of the hovering wingbeat of the fruit fly [13] and the mosquito [20] (figure 2.8*j*). For the fruit fly wing and the symmetric and most asymmetric elliptic wings, we simulated a stroke-rate range of $0 < \omega_{\text{stroke}} < 1750\,\text{rad}\,\text{s}^{-1}$ with steps of $250\,\text{rad}\,\text{s}^{-1}$ and a pitch-rate range of $0 < \omega_{\text{pitch}} < 3000\,\text{rad}\,\text{s}^{-1}$ in steps of $500\,\text{rad}\,\text{s}^{-1}$. To completely enclose the parametric space occupied by the mosquito, the range for the mosquito wing was increased by adding pitch rates of up to $5000\,\text{rad}\,\text{s}^{-1}$(figure 2.8*j*). Finally, for the four remaining elliptic wings we performed simulations at a pitch rates of both $0 < \omega_{\text{pitch}} < 3000$ rad/second in steps of $500\,\text{rad}\,\text{s}^{-1}$, for the stroke rates of both $0\,\text{rad}\,\text{s}^{-1}$ and $1750\,\text{rad}\,\text{s}^{-1}$ (figure 2.8*j*). The resulting parametric space spanned a Reynolds number range from 25 to 500, based on the definition of the Reynolds number of

$$Re = \frac{\rho c \sqrt{(\omega_{\text{stroke}} l)^2 + (\omega_{\text{pitch}} c)^2}}{\mu}, \tag{2.14}$$

where ρ is the air density, μ is the dynamic viscosity, c is the maximum chord length, and l is the wing length.

2.8 Solver

2.8.1 Numerical setup

The simulations were performed on a domain of 14 mm × 14 mm × 14 mm (figure 2.8*a*), where a periodic boundary condition was applied on all external boundaries and a no-slip boundary condition at the wing surface.

At the centre of the domain, we placed a single wing model with prescribed wing movement kinematics (figure 2.8*d*). All tested wings had a span of 3 mm and wing thickness of 0.03 mm (1 % of the span). The domain was optimized to have no interference of the flow with the domain boundaries but kept as small as possible to reduce mesh size and therefore computation time. To minimize the number of cells used in the mesh, and to simultaneously optimize the quality of the results, we used the adaptive local refinement method of the CFD solver [17]. This method automatically refines the mesh in regions with high vorticity (figure 2.8*d*).

2.8.2 Mesh and time-step study

The spatial and time resolutions were chosen after performing a mesh and time-step study. The mesh-study was performed first using a wing that pitches up ($\omega_{\text{pitch}} = 3000\,\text{rad}\,\text{s}^{-1}$) whilst moving forward ($\omega_{\text{stroke}} = 1750\,\text{rad}\,\text{s}^{-1}$), for a range of mesh sizes (figure 2.9*c*) with a time-step of $\Delta t = 1 \cdot 10^{-7}$ s. The effect of the mesh size on the force at the extraction point (figure 2.9*a,c*) is small but decreasing mesh size comes at a vast increase in the amount of cells. We have chosen the mesh-size of $\Delta x = 1.09 \cdot 10^{-5}$ m, which is at the boundary where a further refinement has little effect on the solution; in contrast the computation time increases steeply due to the large number of cells needed. Choosing this mesh-size led to an average use of four million cells for each simulation. After choosing the mesh-size, the time-step was chosen in a similar fashion. For the same simulation as used for the mesh study ($\omega_{\text{pitch}} =$

3000 rad s^{-1}, $\omega_{\text{stroke}} = 1750$ rad s^{-1}), a range of time-steps where tested (figure 2.9*d*). The effect of the time-step (figure 2.9*b,d*) is larger than that of the mesh-size. We chose a time step $\Delta t = 1 \cdot 10^{-7}$ s, because further refinement has little effect on the solution, but the number of steps needed does increase drastically.

2.8.3 Solver validation

After performing the mesh-size and time-step study, the solver was validated by using the known forces for hovering flight of the Drosophila hydei from robotic experiments [7]. The forces produced by the numerical simulations [17] show the same overall dynamics and magnitude in forces as the robotic experiment (figure 2.9*f*).

2.9 Post-processing

2.9.1 Plane extraction

To study how changes in air movement and pressure distributions result in rotational forces, we calculated airflow dynamics within four planes fixed in the wing reference. Two planes were positioned parallel to the wing, at a distance of 0.06 mm above and below the wing surface. Two additional planes were positioned perpendicular to the wing pitch axis at one-third and two-third of the wing span (i.e. $y = 1$ mm and $y = 2$ mm, respectively). In the planes parallel to the wing, we computed the air pressure distributions, from which we estimated the pressure difference across the top and bottom surface of the wing. Within the planes perpendicular to the wing pitch axis, we computed, next to the air pressure distribution, also the air velocity distribution using a three-dimensional linear interpolator method [23].

In this study, we report air velocities in the wing reference frame, both relative to the earth and relative to the wing. The air speeds relative to the wing were determined as $\boldsymbol{U}_{\text{rel,world}} = \boldsymbol{U}_{\text{air,world}} - \boldsymbol{U}_{\text{world}}$, whereby $\boldsymbol{U}_{\text{air,world}}$ is the air velocity vector in the world reference frame, and $\boldsymbol{U}_{\text{world}}$ is the wing velocity in the world reference frame. The resulting air velocities relative to the wing, $\boldsymbol{U}_{\text{rel,world}}$, were then converted to velocities in the wing reference frame, $\boldsymbol{U}_{\text{rel,wing}}$, using the method described earlier for forces.

2.9.2 Sensitivity analysis

The pressure differences across the wing surface were of particular interest because these cause the aerodynamic pressure forces on the wing. We therefore performed a sensitivity analysis to determine the correct offset of the extraction planes relative to the wing surface. An offset for the planes relative to the wing was needed because the cell height was in the same order of magnitude as the wing thickness, and therefore pressure changed over several cells was not captured correctly if the planes would be directly fixed to the wing surface.

To determine what the offset between wing surface and extraction plane needed to be, we conducted a sensitivity study (figure 2.10), in which we systematically increased the offset from the wing surface to the extraction plane (figure 2.10*c*). The force resulting from integrating the pressure difference across the wing was compared with the force computed by the solver (figure 2.10*b*). Based on this, we chose to give all the planes an offset of 0.06 mm from the wing surface, as this gives the smallest error (figure 2.10*b*).

The effect of the offset on the computation of the centre of pressure is minimal (figure 2.10*a, d*), meaning that the distribution of the pressure difference over the wing is probably similar for all offsets.

2.9.3 Pitch angle variation

As discussed in section 2.2.4 of the main manuscript we performed additional simulations. These simulations are similar in setup as the other simulations discussed in section 2.2.2 with the exception that the pitch angles at which the rotational forces were extracted were 30° and 60°. Figure 2.11 shows the results for these additional simulations with the most asymmetric elliptic wing. This shows that also these rotational forces have a linear relation with stroke rate ω_{stroke} (figure 2.11*a, b*). A similar analysis as discussed in section 2.3.3 and 2.3.4 is performed on these new simulations, which yielded the same relation between stroke-pitch coupled rotational forces and pitch rate ω_{pitch} (figure 2.11*c*), and pitch-rate related forces and pitch rate (figure 2.11*d*).

2.10 Supplementary figures

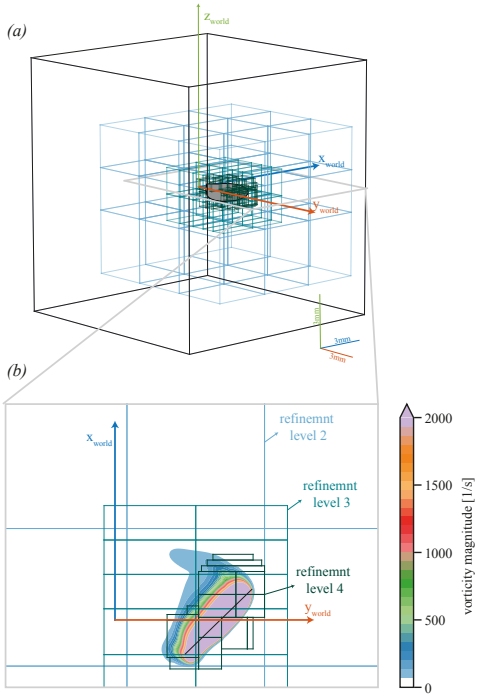

Figure 2.8: Domain setup. (*a*) domain of 14 mm x 14 mm x 14 mm with in the center the fruit fly wing geometry, boxes indicate local refinement defined by the adaptive mesh refinement algorithm. (*b*) Slice of the domain (*a*) with the vorticity magnitude added, the adaptive mesh refinement algorithm uses the vorticity to determine where to refine.

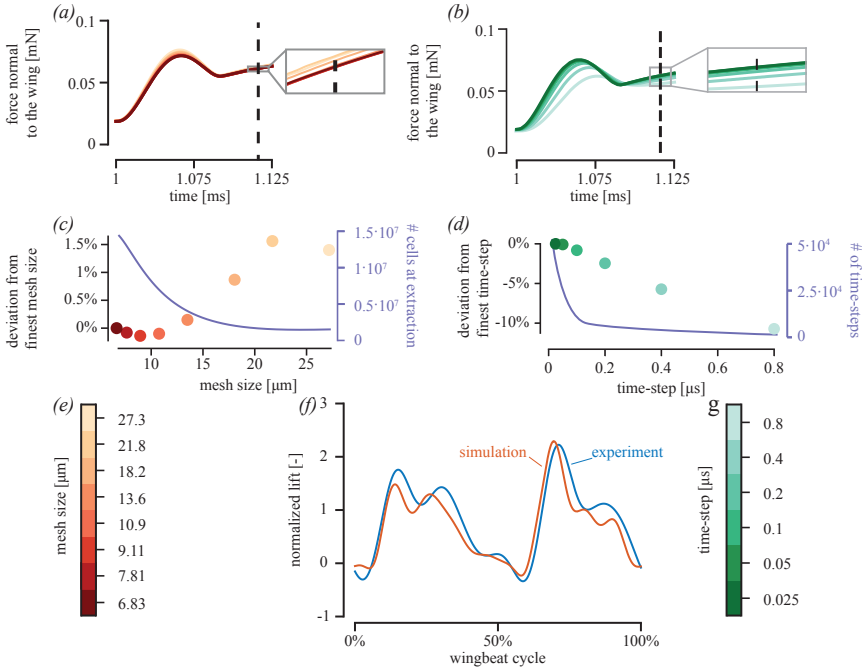

Figure 2.9: Mesh-study, time-step study and solver validation. (*a*) Forces for a pitching fruit fly wing ($\omega_{\text{pitch}} = 3000\,\text{rad}\,\text{s}^{-1}$, $\omega_{\text{stroke}} = 1750\,\text{rad}\,\text{s}^{-1}$) for several mesh sizes (see figure S2e). (*b*) Forces for a pitching fruit fly wing ($\omega_{\text{pitch}} = 3000\,\text{rad}\,\text{s}^{-1}$, $\omega_{\text{stroke}} = 1750\,\text{rad}\,\text{s}^{-1}$) for several time-steps (see figure S2g). (*c*) Force deviation from finest mesh at extraction point (pitch angle=45°) for several mesh sizes (see figure S2e), in purple an estimate of the number of cells at extraction. (*d*) Force deviation from finest time-step at extraction point ($\omega_{\text{pitch}} = 45°$) for several time-steps (see figure S2g). (*e*) Colour-legend for all the mesh sizes used in panel (*a*) and (*c*). (*f*) Solver validation using the kinematics of a hovering fruit fly [7], red shows simulation results, and blue shows robotic experiment results [7]. (*g*) Colour-legend for all time-steps used in panel (*b*) and (*d*)

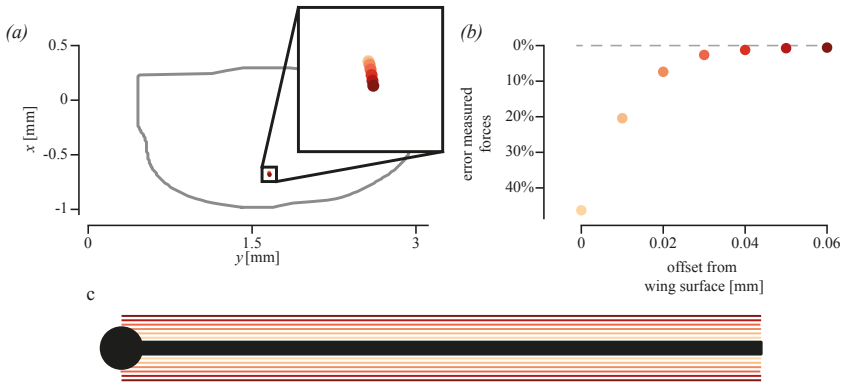

Figure 2.10: Sensitivity study of the extraction plane offset relative to the wing-surface. (*a*) change of the centre of pressure with increasing offset (see panel (*b*) and (*c*) for colour coding) for a pitching fruit fly wing with pitch rate $\omega_{\text{pitch}} = 1000\,\text{rad}\,\text{s}^{-1}$ (*b*) Comparison between the forces computed by the solver and the result of integrating the pressure difference across the wing surface. (*c*) Schematic representation of the wing chord at 2 mm from the root with the extraction planes increasing in distance with darkening colour.

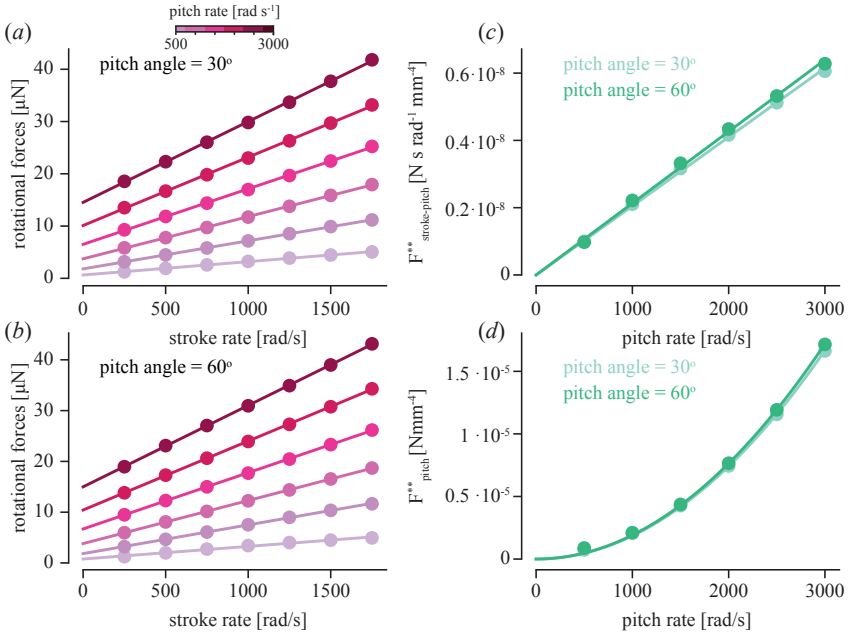

Figure 2.11: Additional simulations with extraction points at 30° and 60°. (*a*) The rotational forces (difference between total force and stroke-related force) at an pitch angle of 30° (*a*) and 60° (*b*) (ordinate) versus the stroke rate (abscissa) and pitch rate (colour-bar above (*a*)), for the most asymmetric elliptic wing, the fruit fly wing, the mosquito wing, and the symmetric wing, respectively. A linear function was fitted through the dataset at each simulated pitch rate. (*c*) Normalized stroke-pitch coupled forces $F^{**}_{\text{stroke-pitch}}$ (equation (2.9)) versus pitch rate, for the most asymmetric elliptic wing at a pitch angle of 30° and 60°. The linear fit for each pitch angle has a slope equal to its force coefficient $C_{F,\text{stroke-pitch}}$ (equation (2.4)). (*d*) Normalized pitch rate related forces F^{*}_{pitch} (equation (2.11)) versus pitch rate, for the most asymmetric elliptic wing at a pitch angle of 30° and 60°. The growth factor of the quadratic fit for each pitch angle equals its force coefficient $C_{F,\text{pitch}}$ (equation (2.6))

2.11 Supplementary tables

Table 2.1: List of symbols

Symbol	unit	Description
A_{pitch}	N	Pitch-rate slope for stroke-pitch coupled forces
A_{stroke}	N s rad^{-1}	Stroke-rate slope for stroke-pitch coupled forces

Continued on next page

Continued from previous page

Symbol	unit	Description
$B_{\text{no-stroke}}$	N	Pitch rate related forces
$b_{\text{asymmetry}}$	mm	Wing pitch asymmetry
$C_{F,\text{pitch}}$	-	Force coefficient of the pitch-rate related aerodynamic mechanism
$C_{F,\text{rotational}}$	-	Force coefficient of the rotational aerodynamic mechanism
$C_{F,\text{stroke}}$	-	Force coefficient of the stroke-rate related aerodynamic mechanism
$C_{F,\text{stroke-pitch}}$	-	Force coefficient of the stroke-pitch coupled aerodynamic mechanism
c_1	mm	Chordwise location of the trailing edge (figure 2.1*e*)
c_2	mm	Chordwise location of the leading edge (figure 2.1*e*)
$\mathrm{d}A$	mm^2	Infinitesimal wing surface area
D_{pitch}	N s rad^{-1}	Quadratic growth factor of pitch-rate related forces
F_{pitch}	N	Pitch-rate related forces
$F_{\text{rotational}}$	N	Rotational aerodynamic forces
F_{stroke}	N	Stroke related forces
$F_{\text{stroke-pitch}}$	N	Stroke-pitch related forces
F_{total}	N	Total aerodynamic forces
$F'_{\text{stroke-pitch}}$	N mm^{-1}	Stroke-pitch coupled forces per unit span
F^{*}_{pitch}	N/mm^4	Pitch-rate related forces on a wing, normalized with the asymmetric second-moment-of-area of the wing
$F^{**}_{\text{stroke-pitch}}$	Ns/radmm^4	Stroke-pitch coupled forces, normalized with stroke rate and pitch-stroke coupled second-moment-of-area
p	N m^{-2}	Air pressure
p_{pitch}	N m^{-2}	Air pressure of a simulation with a wing moving with a constant pitch rate
p_{stroke}	N m^{-2}	Air pressure of a simulation with a wing moving with a constant stroke rate
$p_{\text{stroke-pitch}}$	N m^{-2}	Air pressure related to the stroke-pitch forces
p_{total}	N m^{-2}	Air pressure of a simulation with a wing moving with constant stroke rate and pitch rate
Re	-	Reynolds number, as defined by equation (2.14)
S_{xx}	mm^4	Second moment of area along the chord
$S_{x\lvert x\rvert}$	mm^4	Asymmetric second moment of area (equation (2.5))
S_{yy}	mm^4	Second moment of area along the chord
t	s	Time relative to the start of the simulation
$\boldsymbol{U}$	m s^{-1}	Air velocity vector
U_∞	m s^{-1}	Free stream air speed
$[x, y, z]$	m	Coordinates in the wing reference frame
$[x_{\text{world}}, y_{\text{world}}, z_{\text{world}}]$	m	Coordinates in the world reference frame
α	rad	Angle-of-attack
Γ	m^2 /s	Air circulation
Δt	s	Simulation time step
Δx	m	Grid mesh size
ρ	kg m^{-3}	Air density
ω_{pitch}	rad s^{-1}	Pitch rate
ω_{stroke}	rad s^{-1}	Stroke rate

Chapter 3

A numerical analysis of wing-stroke related acceleration-based forces in insect flight

Wouter G. van Veen, Johan L. van Leeuwen, Florian T. Muijres

Abstract

To produce the aerodynamic forces required for flight, dipteran insects beat their wings back and forth at high frequencies. Because the angular accelerations of this oscillating wing system scales quadratic with the wingbeat frequency, wing stroke-acceleration based forces are expected to be particularly high for these two-winged fliers. Here, we used computational fluid dynamics (CFD) simulations to study systematically how stroke-acceleration based forces and flow dynamics depend on wing morphology, wing-stroke rate, and wing-stroke acceleration. Based on these results, we developed an aerodynamic model that captures the stroke-acceleration forces based on the wingbeat kinematics and wing morphology. Furthermore, we explicitly modeled the interaction of the stroke-acceleration with a selection of other known aerodynamic mechanisms. Our analysis shows that especially for high-frequency flapping flight the stroke-acceleration forces contribute substantially to the forces on the wing.

3.1 Introduction

Dipteran insects fly by moving their wings rapidly back and fort in a complex motion pattern. With this wing motion, they generate the aerodynamic forces required for flight. Due to the unsteady nature of the involved aerodynamics and the complex wing motion, the interaction between the wings and the surrounding air has been difficult to model. To solve this problem, a common approach is to use aerodynamic mechanisms [1], also known as phenomenology-based models [2]. These models link the aerodynamic forces directly to the morphology and motion of the wing. Each aerodynamic mechanism is able to predict the aerodynamic forces based on part of the motion and orientation characteristics of the wing, for example the angular rate of the wing and the angle-of-attack. Several of such aerodynamic mechanism have been identified: translational lift (stroke-based forces) [3, 4, 5, 6], rotational lift (rotational forces) [4, 7, 8, 9], wake-capture (forces owing to wing interaction with a previously generated wake) [10, 11, 12, 13] and added-mass (acceleration-reaction forces) [12, 14, 15, 16, 7]

Dipteran fliers exhibit a large range of wingbeat patterns, but common is that they

move their wings mostly back and forth at a high angle-of-attack ($\approx 45°$) (figure 3.1*a*, *b*). The wing motion can be divided into two parts: the forward stroke and backward stroke (figure 3.1*a* and *b* respectively). During the forward-stroke, the wing is moving from the dorsal side of the insect towards the ventral side, and visa-versa for the backward-stroke. Stroke-reversal is defined as the point where the wing moves from the forward- to the backward-stroke, or visa-versa. Around stroke-reversal the wing first has to decelerate and then accelerate rapidly in the opposite direction. Furthermore, the wing has to rotate around its span with an angle of around 90° such that the angle-of-attack during the next stroke is again close to 45° (figure 3.1*c*). Due to the high flapping frequency (in the order of 100 Hz), this all has to happen in an incredibly short time [17, 18].

The stroke-based forces are related to the angular stroke velocity of the wing and the angle-of-attack. The stroke-based forces are often linked to the presence of a leading edge vortex (LEV), which is a stable separated region above the wing and behind the leading edge. This separated region reattaches before the trailing edge and is often identified as the reason that insects can fly at such high angles of attack without experiencing stall, and consequently produce the high-lift forces required for flight [19, 4, 3, 20]. The stroke-based forces are most prominent during mid-stroke, where the stroke-rate is highest (figure 3.1*d*). The stroke-based forces can be modeled with knowledge of the kinematics and the wing geometry as [4]

$$\vec{F}_{sr} = \rho \vec{C}_{sr}\left(\alpha\right) \omega_s^2 \int_0^R y^2 c dy, \tag{3.1}$$

where $\vec{F}_{sr}$ is the stroke-rate force, ρ the air density, $\vec{C}_{sr}$ the stroke-rate force coefficient vector as a function of the angle-of-attack α, ω_s the stroke-rate of the wing, y the position along the span of the wing, and R the length of the wing. The integral in equation (3.1) is responsible for the geometrical scaling known as the span-wise second moment of area (S_{yy}). This aerodynamic mechanism ignores the Wagner effect, which states that at the start of a wingbeat the airflow needs time to develop around the wing, and consequently there is a delay in aerodynamic force build up [14, 21]. However, the model is still able to predict the lift forces of a hovering fruit fly rather well [12, 17], but falls short in predicting the drag forces [12].

The forces related to the pitching motion of the wing (i.e. rotation around the spanwise axis) are a combination of rotational lift [4] and rotational drag [7, 8, 9] and

are most prominent during stroke-reversal. Around stroke-reversal, the pitch-rate of the wing is high, which results in the presence of rotational forces. The rotational forces can also be modeled using a quasi-steady approach, based on wing geometry, wing pitch-rate and the stroke-rate of the wing [9].

The wake-capture aerodynamic mechanism is most prominent at the start of each wing stroke [13, 10, 12]. This mechanisms relates the interaction of the wing with the wake of the previous stroke. Because the wake of the previous stroke is part of the time-history of the flow-field, it is difficult to capture the wake-capture aerodynamic mechanism in a single model based on the kinematics and the wing morphology alone.

The stroke-acceleration forces are the forces caused by a change of the stroke-rate. The stroke-acceleration forces arise because a volume of fluid around the wing is accelerated when the wing accelerates and hence exerts a force on the wing. The force can be modelled as [22]

$$\vec{F}_{sa} = \rho V \frac{d}{dt}\left(\vec{v}\right), \tag{3.2}$$

where V is the volume of air that accelerates with the wing, $\vec{v}$ the velocity of the wing and t is time. For insect flight, the acceleration-reaction forces are often approximated by the model of a two-dimensional flat plate moving through inviscid air [23, 14, 12, 15, 16, 24] rewritten for a rotating wing using blade-element theory as

$$F_{sa,\text{2D}} = \frac{\pi}{4}\rho\dot{\omega}_s \sin\left(\alpha\right) \int_0^R y c^2(y) dy, \tag{3.3}$$

where $\dot{\omega}_s$ is the angular acceleration of the wing, and the integral a geometrical scaling parameter we will define as S_{sedov}.

Apart from the inviscid component of the acceleration-reaction forces an additional component that is related to the non-slip condition parallel to the surface of the wing has been identified [2]. This component generates a non-zero contribution to the overall acceleration-reaction forces, but is not linked to any phenomenology-based model. It can be investigated with the use of force decomposition or the panel method in flapping flight of a fruit fly [2, 25].

The aerodynamic mechanisms defined above are often combined in a quasi-steady model [1], which enables one to predict the forces of an insect based only on the motion and shape of the wing. Most of these models simply use linear summation of only the stroke-rate force mechanism and the rotational force mechanism (e.g. [17],

[18]). Wake capture is often ignored because it is difficult (or maybe even impossible) to capture in a quasi-steady model. The linear relation of stroke-acceleration forces with angular acceleration (equation (3.3)) of the wing means that for a symmetric cyclical wingbeat the net contribution of the stroke-acceleration forces is zero [2], which might partly be the reason why added mass forces are also often ignored when modeling insect flight. However, stroke-acceleration forces still affect instantaneous force production, and thus they can influence the power requirement of flight. Furthermore, the wingbeat kinematics during many flight maneuvers are asymmetric as the wings tend to move further to the back than to the front, and non-cyclic motions occur during torque production in maneuvering flight.

In this study, we used computation fluid dynamics (CFD) modeling to systematically study how wing stroke accelerations affect aerodynamic force production, and how this interacts with stroke-based forces. We designed a set of wing motion pattern that allowed us to isolate the acceleration-reaction forces from forces produced using the other aerodynamic mechanisms. By systematically varying the wing morphology, angle-of-attack, stroke-rate and stroke-acceleration of the wing, we developed an aerodynamic model that captures stroke-acceleration forces, and its interaction with stroke-based forces. We applied our newly found model to the wingbeat kinematics of the fruit fly and mosquito and revealed that the stroke acceleration forces are particular important for high-frequency flappers.

Our new acceleration-reaction force model improves our insight into the fluid dynamics of rapidly oscillating wings, and the evolutionary trade-offs in the flight-apparatus of dipteran insects. Furthermore, these insights may help the pave to path to the application of biological inspired flying machines [26].

3.2 Material and Methods

3.2.1 Nomenclature

We studied how wing stroke-accelerations affect the aerodynamic force production through acceleration-reaction and its interaction with the stroke-rate based aerodynamic mechanism. To differentiate between the various force mechanisms, we based their naming on the underlying kinematics. We defined a general model for stroke-

based aerodynamic force production as

$$\vec{F}_s = \vec{F}_{sr}\left(\alpha, \omega_s, \text{geometry}\right) + \vec{F}_{sr-sa}\left(\alpha, \omega_s, \dot{\omega}_s, \text{geometry}\right) + \vec{F}_{sa}\left(\alpha, \dot{\omega}_s, \text{geometry}\right). \tag{3.4}$$

In this general model, there are three terms defined together with their dependency; $\vec{F}_{sr}$ which are the stroke-rate based forces, $\vec{F}_{sr-sa}$ are the forces caused by the interaction between the stroke-rate and stroke-acceleration of the wing, and $\vec{F}_{sa}$ are the acceleration-reaction forces caused by the stroke-acceleration of the wing (comparable to equation (3.3)).

3.2.2 Numerical setup

We conducted all our simulations with the immersed boundary methods solver IBAMR [27]. A single rigid wing was placed with its root in the center of a domain with the size of 5 cm x 5 cm x 5 cm. A periodic boundary condition was used on the sides of the domain, and a no-slip boundary condition was chosen at the surface of the wing.

The time and space resolutions were chosen based on a previous study as $\Delta t = 1 \cdot 10^{-7}$ s and $\Delta x = 0.01$ mm [9]. The mesh uses adaptive mesh refinement based on the vorticity in the flow-field; we used in total 3 refinement levels with the vorticity thresholds at 50 s^{-1}, 500 s^{-1}, 5000 s^{-1}, from coarsest to finest respectively. This resulted in a mesh size of approximately 4 million cells and a total of 10 000 time-steps per simulation.

The solver was validated by comparing the results of a simulation of hovering kinematics of a fruit fly with forces measured in an experiment with a robotic flapper [17] (see supplementary methods for more detail).

3.2.3 Wing morphology

Different wing morphologies were used during this study to explicitly study the effect of the geometry on the stroke-based forces (equation (3.4)). Each modeled wing was completely rigid with a wing thickness of 1 % of the semi-span of the wing. Two wing morphologies were based on those of the fruit fly and the malaria mosquito. In addition to these two morphologies, we designed 13 elliptical morphologies. The first set of four elliptical wings had a fixed wing length $R = 3$ mm and a varying chord length $c_{max} = 0.5$ mm to 1.5 mm with steps of 0.25 mm (figure 3.2*d*, squares).

The second set of four elliptical wings has a fixed chord length $c_{max} = 1$ mm and a varying wing length $R = 2$ mm to 4 mm in steps of 0.5 mm, figure 3.2*d* circles). For these sets of wings, the Sedov's scaling parameter based on earlier stroke-acceleration models (equation (3.3)) can be analytical be determined as

$$S_{\text{sedov}} = \int_0^R c(y)^2 y dy = \int_{-\frac{1}{2}\theta}^{\frac{1}{2}\pi} \left(c_{max}\cos(\theta)\right)^2 \left(\frac{1}{2}R\sin(\theta) + \frac{1}{2}R\right)\frac{1}{2}R d\theta, \quad (3.5)$$

where c_{max} is the maximum chord length and θ the polar coordinate defined in figure 3.2*c*. Equation (3.5) shows that if the product $c_{max}R$ is kept constant the value S_{sedov} also remains constant, for elliptical-shaped wings. Based on this notion, we designed a set of five elliptical wings with constant S_{sedov} (based on $c_{max} = 1$ mm and $R = 3$ mm with a varying wing length and chord length (figure 3.2*d*, diamonds)).

The value of S_{sedov} increases with increasing value of S_{yy} (figure 3.2*e*) except for the elliptical wings with constant S_{sedov}. The values of S_{yy} and S_{sedov} of both the fruit fly and the mosquito fall within the parametric space spanned by the sets of elliptical wings (figure 3.2*e*).

3.2.4 Reference frames

The position of the wing and the forces computed by the numerical solver were expressed in a right-handed world reference frame with its origin at the root of the wing (see figure 3.1*f*). The position of the wing was computed by first rotating around the z-axis of the world-reference frame with the stroke-angle γ. The wing was then rotated around its span-axis (*y*-axis of the wing-reference frame) with a pitch angle (ϕ). In this study, there is no difference between the pitch-angle and the angle-of-attack and therefor we will only refer to the pitch-angle as the angle-of-attack. If there would have been an additional wing rotation, often described as the deviation angle, or a non-zero velocity field the pitch angle and the angle-of-attack would not coincide.

The forces used to create the model (see section 3.2.1) are all expressed in the wing reference-frame, which is a right-handed reference frame with the origin a the wing hinge, the *x*-axis parallel to the wing surface pointing towards the trailing edge, the *y*-axis parallel to the surface pointing towards the wing-tip and the *z*-axis perpendicular to the wing-surface (figure 3.1*f*).

3.2.5 Kinematic setup: accelerating wings

We designed a set of simulations that allowed us to isolate the effect of the stroke-acceleration on the forces from the other aerodynamic mechanisms present. Each set of wing kinematics could be controlled by three main parameters; the stroke-rate, the stroke-acceleration and the angle-of-attack. The angle-of-attack was kept constant during the simulation, and was only varied between simulations. The stroke-rate and stroke-acceleration varied during the simulation, however we used the stroke-rate and stroke-acceleration at the end of the simulation to classify each simulation. Only the forces at the last time-step of the simulations were used for the analysis.

To explain how the kinematics were designed, we will use the set of simulations at a stroke-rate of $\omega_s = 1000\,\mathrm{rad\,s^{-1}}$ and stroke-accelerations of $\dot{\omega}_s = 1 \cdot 10^6\,\mathrm{rad\,s^{-2}}$ to $4.5 \cdot 10^6\,\mathrm{rad\,s^{-2}}$ as an example (this range is also highlighted in figure 3.2*f*, *g*). In each simulation, the wing was first accelerated to a constant stroke-rate of $\omega_s = 600\,\mathrm{rad\,s^{-1}}$, irrespective of the stroke-acceleration at the end of the simulation (figure 3.1*g*, *h*). We chose this initial stroke rate as 60 % of the maximum stroke rate at the end of the simulation. To reduce the effect of time on the development of the flow, we designed the kinematics such that each simulation took exactly the same time (1 ms). Because the kinematics with a different stroke-acceleration would take a different time to bridge the difference in stroke-rate (in this case $400\,\mathrm{rad\,s^{-1}}$), we started the acceleration of the wing at different times (figure 3.1*g*, *h*). The stroke-acceleration was increased smoothly for each simulation (figure 3.1*h*), and then kept constant until the end of the simulation.

At the end of each simulation, the stroke-rate and angle-of-attack was the same for all simulations, only the stroke-acceleration was different. This means that only the stroke-acceleration parameter can explain the differences in the forces acting on the wing between the simulations.

3.2.6 Kinematic setup: decelerating wings

In addition to wings that were accelerating we designed an additional set that was decelerating. We used the same approach as described for the accelerating wing. However, the stroke rate had to be increased above the stroke rate at the end of the simulation (figure 3.1 *g*). We took this stroke rate at 40 % higher than the stroke rate at the end of the simulation.

3.2.7 Parametric space

The kinematics described in section 3.2.5 has three input parameters; stroke-acceleration, stroke-rate and angle-of-attack. In this study, these parameters were systematically varied to asses there influence on the forces. The range of these parameters was determined based on the range encountered during hovering flight of the fruit fly (*Drosophila hydei*)[17] and mosquito (*Anopheles coluzzii*) [18] (figure 3.2*f–h* blue fruit fly, red mosquito). The set of simulations can roughly be divided into two subsets: a set of simulations based on the fruit fly wing morphology, and a set of simulations with varying wing-morphologies.

The set of simulations based on the fruit fly wing morphology was primarily used to quantify the relation between the kinematics and the stroke-based forces F_s. Based on the observed kinematics, we used a range for the angle-of-attack that varied from 9° to 90° in steps of 9°, the stroke-rate from $500\,\mathrm{rad\,s^{-1}}$ to $2000\,\mathrm{rad\,s^{-1}}$ with steps of $250\,\mathrm{rad\,s^{-1}}$ and the stroke-acceleration from $1 \cdot 10^6\,\mathrm{rad\,s^{-2}}$ to $4.5 \cdot 10^6\,\mathrm{rad\,s^{-2}}$ with steps of $0.5 \cdot 10^6\,\mathrm{rad\,s^{-2}}$ for the fruit fly wing (indicated with the blue dots in figure 3.2*c*, *d*). This resulted in a total of 480 simulations for the fruit fly wing morphology alone (table 3.1).

In addition to the kinematics of an accelerating wing, we included a subset of 56 simulations for a decelerating wing with the angle-of-attack $\alpha = 36°$, the stroke-rate was varied between $250\,\mathrm{rad\,s^{-1}}$ to $1750\,\mathrm{rad\,s^{-1}}$ with steps of $250\,\mathrm{rad\,s^{-1}}$ and the stroke-acceleration varied between $-4.5 \cdot 10^6\,\mathrm{rad\,s^{-2}}$ to $-1 \cdot 10^6\,\mathrm{rad\,s^{-2}}$ with steps of $0.5 \cdot 10^6\,\mathrm{rad\,s^{-2}}$ (table 3.1).

The second set of simulations was primarily used to quantify the dependence of the stroke-based forces F_s on the wing morphology. For this, we added the wing morphology of the mosquito and the 13 elliptical wings (see section 3.2.3). For the mosquito wing and the elliptical wings with constant S_{sedov}, we used a constant angle-of-attack $\alpha = 36°$, varied the stroke-rate $\omega_s = 500\,\mathrm{rad\,s^{-1}}$ to $1750\,\mathrm{rad\,s^{-1}}$ in steps of $250\,\mathrm{rad\,s^{-1}}$, and used two different stroke-accelerations $\dot{\omega}_s = 1 \cdot 10^6\,\mathrm{rad\,s^{-2}}$ and $\dot{\omega}_s = 4.5 \cdot 10^6\,\mathrm{rad\,s^{-2}}$. This resulted in total to 192 simulations for these six wing morphologies (table 3.1)

For the four elliptical wings with varying wing length and the four elliptical wings with varying chord, we used the following kinematics; an angle-of-attack of $\alpha = 36°$, a stroke-rate range of $\omega_s = 500\,\mathrm{rad\,s^{-1}}$ to $1500\,\mathrm{rad\,s^{-1}}$ in steps of $500\,\mathrm{rad\,s^{-1}}$, and two stroke-accelerations $\dot{\omega}_s = 1 \cdot 10^6\,\mathrm{rad\,s^{-2}}$ and $\dot{\omega}_s = 4.5 \cdot 10^6\,\mathrm{rad\,s^{-2}}$. For these 8

wing morphologies this led to a total of 32 simulations. In summary, in this study we included 15 different wing morphologies and carried out a total of 776 simulations (table 3.1).

Table 3.1: Stroke-acceleration kinematics overview. *ff* fruit fly wing morphology, *mo* mosquito wing morphology, *e* S_{sedov} ellipse shaped wing with constant S_{sedov}, *e* R ellipse shaped wing with constant wing length, *e* $c_{\max}$ ellipse shaped wing with constant chord length.

Geometry	α [-]	$\Delta\alpha$[-]	ω_s [rad s^{-1}]	$\Delta\omega_s$ [rad s^{-1}]	$\dot{\omega}_s$ [rad s^{-2}]	$\Delta\dot{\omega}_s$ [rad s^{-2}
ff	9° to 90°	9°	250 to 1750	250	$1 \cdot 10^6$ to $4.5 \cdot 10^6$	$5 \cdot 10^6$
ff	36°	-	250 to 1750	250	$-4.5 \cdot 10^6$ to $-1 \cdot 10^6$	$5 \cdot 10^6$
mo	36°	-	250 to 1750	500	$1 \cdot 10^6$ & $4.5 \cdot 10^6$	$5 \cdot 10^6$
e S_{sedov}	36°	-	250 to 1750	500	$1 \cdot 10^6$ & $4.5 \cdot 10^6$	$5 \cdot 10^6$
e R	36°	-	500 & 1500	-	$1 \cdot 10^6$ & $4.5 \cdot 10^6$	-
e c_{max}	36°	-	500 & 1500	-	$1 \cdot 10^6$ & $4.5 \cdot 10^6$	-

3.3 Results

The result section is divided into five parts. First, the dependence of the forces on the kinematics is discussed in section 3.3.1. Second the dependence on the wing morphology is discussed in section 3.3.2. Third, the flow-field is studied for the two acceleration-based components: the stroke-acceleration component F_{sa} (section 3.3.3) and the interaction component F_{sr-sa} (section 3.3.4). Finally, we apply our newly found model on the kinematics of the fruit fly and mosquito in section 3.3.5.

3.3.1 The forces

The forces as a result of the stroke-accelerations $\dot{\omega}_s$ were assumed to decompose into two terms: an acceleration term $\vec{F}_{sa}$ and an interaction term $\vec{F}_{sr-sa}$. The interaction term consists of the interaction between the previously described stroke-rate forces and the stroke-acceleration forces.

The viscous forces due to the stroke acceleration comprise of 5 % and 9 % of the total forces for the *x*- and *y*-component respectively (taken at $\alpha = 45°$, $\omega_s = 1000\,\text{rad s}^{-1}$ and $\dot{\omega}_s = 2 \cdot 10^6\,\text{rad s}^{-2}$). Here, we focus on the stroke-acceleration induced pressure forces, and ignore the much smaller stroke-acceleration evoked viscous forces (see appendix 3.8). The forces normal to the wing increase with increasing stroke-acceleration $\dot{\omega}_s$, for all angles of attack (figure 3.3*a–k*). We grouped the simulations with the same stroke-rate at the end of the simulation, and approximated the

total force with a linear relation

$$F_{s,z} = \rho \left[A_{sa} \dot{\omega}_s + B_{sr} \right]. \tag{3.6}$$

Parameter A_{sa} models the change in the stroke force $F_{s,z}$ due to stroke-acceleration $\dot{\omega}_s$. This parameter A_{sa} consists of the acceleration term F_{sa} and the interaction term F_{sr-sa} (the last two terms in equation (3.4)). Parameter B_{sr} models the force generated in absence of stroke-acceleration (i.e. due to the stroke-rate).

Acceleration forces & interaction forces

Both A_{sa} and B_{sa} are a function of the stroke-rate ω_s and the angle-of-attack (figure 3.4*a* and *c* respectively). Parameter A_{sa} is almost constant for the lower angles-of-attack (α). However, for the higher angles-of-attack the effect of the stroke-acceleration is reduced with increasing stroke-rate. We modeled A_{sa} with a simple quadratic relation without linear term

$$A_{sa} = c_{sa} \omega_s^2 + d_{sa}. \tag{3.7}$$

The coefficients c_{sa} and d_{sa} in equation (3.7) are both a function of the angle-of-attack. The first part of equation (3.7) models the *interaction* between the stroke-rate and stroke-acceleration on the stroke-based forces, and can be recognized as the interaction term F_{sr-sa} in equation (3.4). The second term models the effect of the stroke-acceleration on the stroke-based forces, independent of the stroke rate. Thus, d_{sa} is equal to the acceleration term F_{sa} in equation (3.4). The coefficient c_{sa} that modulates the interaction decreases with the angle-of-attack (figure 3.4*c*), although the change is limited for higher angles of attack $\alpha = 54°$. The acceleration term d_{sa} increases with increasing angle-of-attack (figure 3.4*e*). Both terms were approximated by a quadratic relation

$$c_{sa} = c_{sa-\alpha a} \alpha^2 + c_{sa-\alpha b} \alpha \tag{3.8}$$

$$d_{sa} = d_{sa-\alpha a} \alpha^2 + d_{sa-\alpha b} \alpha. \tag{3.9}$$

For the fruit fly wing, the coefficients were estimated as $c_{sa-\alpha a} = 2.01 \cdot 10^{-13}$ µNs^6, $c_{sa-\alpha b} = -4.89 \cdot 10^{-13}$ µNs^6, $d_{sa-\alpha a} = -1.29 \cdot 10^{-6}$ µN s^2 and $d_{sa-\alpha b} = 4.5 \cdot 10^{-6}$ µN s^2.

Stroke-rate forces

The forces in absence of stroke-acceleration (B_{sr}) are also a function of the stroke-rate (ω_s) and the angle-of-attack (α) (figure 3.4*b*). These forces should coincide with the *stroke-rate* forces (F_{sr}, equation (3.4) and (3.21)), because without any stroke-acceleration the stroke-acceleration forces and the interaction forces are equal to zero (see equation (3.6)). Therefore the same relation to model B_{sr} is used as for the stroke-rate forces (equation (3.21))

$$B_{sr} = h_{sr}\omega_s^2, \tag{3.10}$$

where the coefficient h_{sr} increases with angle-of-attack (figure 3.4*e*) similar to the stroke-rate forces. Therefore, again a simple quadratic relation is used to model the dependence of h_{sa} on the angle-of-attack α as

$$h_{sr} = h_{sa-\alpha a}\alpha^2 + h_{sa-\alpha b}\alpha. \tag{3.11}$$

For the fruit fly wing, the values of these coefficients are $h_{sa-\alpha a} = -1.25 \cdot 10^{-9}$ µN s^2 and $h_{sa-\alpha b} = 2.41 \cdot 10^{-7}$ µN^2. These forces only depend on the stroke-rate, and therefore are expected to coincide with the stroke-rate forces F_{sr} described earlier. However, the forces estimated by equation (3.10), are slightly lower than the forces estimated by equation (3.21)). This difference is caused by a non-linear behavior for low stroke-accelerations (below $5 \cdot 10^5$ rad s^{-2}) as explained the following section.

Deceleration

For the simulations with a negative stroke-acceleration, we repeated the steps as for the accelerating wings. The total stroke-based forces F_s are again approximated by a linear relation (3.6) (figure 3.5*a*). The slope of this linear approximation A_{sa} shows a similar relation with the stroke-rate ω_s (figure 3.5*b*). The forces that only depend on the stroke-rate B_{sr} are now estimated to be higher than the stroke-rate forces F_{sr} from equation (3.21). Directly comparing the model for acceleration and deceleration show that there is an offset, suggesting a non linear effect at very low stroke accelerations. This non-linearity can be modeled using some form of a mixing function. However, in the current study we only included the deceleration for a single angle-of-attack, meaning that we were unable to determine this non-linear mixing function.

3.3.2 Geometrical scaling

For the 14 different wing morphologies, we computed the two coefficients A_{sa} and B_{sr} (figure 3.6*a*, *d*). We then estimated their dependence on the stroke-rate using the same equations as for the fruit fly wing morphology (equations (3.7), (3.10)). After this last step, the stroke-based forces F_s can be approximated by three coefficients c_{sa}, d_{sa} and h_{sa}. The first two coefficients show a linear relation with the scaling proposed in equation (3.5) (figure 3.6*b*, *c* respectively). The last coefficient (h_{sr}) depends on the second moment of area along the span S_{yy} (figure 3.6*e*). The final model for the stroke-acceleration forces F_{sa} and interaction forces F_{sr-sa} becomes:

$$F_{sr-sa} = \rho \left[\left(c^*_{sa-\alpha a}\alpha^2 + c^*_{sa-\alpha b}\alpha \right) \dot{\omega}_s \omega_s \sqrt{S_{yy} S_{\text{sedov}},} \right] \tag{3.12}$$

$$F_{sa} = \rho \left[\left(d^*_{sa-\alpha a}\alpha^2 + d^*_{sa-\alpha b}\alpha \right) \dot{\omega}_s \sqrt{S_{yy} S_{\text{sedov}}} \right], \tag{3.13}$$

where we assume that the fractions $c^*_{sa-\alpha a}/c^*_{sa-\alpha b}$ and $d^*_{sa-\alpha a}/d^*_{sa-\alpha b}$ are the same for each geometry. From that assumption we derived the coefficients based on $N = 15$ wing geometries as: $c^*_{sa-\alpha a} = 3.02 \cdot 10^{-8} \pm 6.13 \cdot 10^{-9}$ s^4, $c^*_{sa-\alpha b} = -7.35 \cdot 10^{-8} \pm 1.49 \cdot 10^{-8}$ [-], $d^*_{sa-\alpha a} = -1.98 \cdot 10^{11} \pm 2.01 \cdot 10^{9}$[-] and $d^*_{sa-\alpha b} = 6.92 \cdot 10^{11} \pm 7.05 \cdot 10^{9}$ [-], which are the coefficients independent of the wing morphology.

3.3.3 Aerodynamics of the stroke-acceleration forces

The pressure distribution p_{sa} on the wing surface due to the stroke-acceleration $\dot{\omega}_s$ is approximated in two consecutive steps; First, the total pressure distribution p_s for a wing with high stroke-acceleration $\dot{\omega}_s = 4.5 \cdot 10^6$ rad s^{-2}) and low stroke-rate $\omega_s = 500$ rad s^{-1} is extracted (figure 3.10*a*, *b*). Secondly, the pressure distribution p_{sr} of a wing moving at the same stroke-rate (figure 3.10*c*, *d*); $\omega_s = 500$ rad s^{-1}), but without a stroke-acceleration is extracted. The pressure distribution resulting form stroke acceleration is estimated as

$$p_{sa} \approx p_s - p_{sr}. \tag{3.14}$$

Here, we have assumed that the effect of the interaction term is limited at these low stroke-rates. The pressure distribution p_{sa} (figure 3.10*e*, *f*) is a result of the wing acceleration, and the stroke-acceleration interaction term (F_{sa} and F_{sr-sa} in equation (3.4) respectively).

Effect of the stroke-acceleration

We estimated the pressure distribution p_{sa} (equation (3.14)) on the top, bottom and in a plane perpendicular to the span of the wing (figure 3.7*a*) for a wing moving at different stroke-accelerations (figure 3.7). A low pressure region is formed on the top surface of the wing and a high-pressure region on the bottom of the wing. The low pressure region appears to develop slower (figure 3.7*b* vs *d*) than the high pressure region on the bottom of the wing. A similar pattern is observed when comparing the top surface with the bottom surface (figure 3.7*f–i*, *j–m*).

The pressure region on top of the wing shows a small asymmetry along the chord, where the lower pressure region is located more towards the trailing edge of the wing. This might be the result of the pressure distribution of the interaction forces (see section 3.3.4), or an interaction with the leading-edge vortex on the top surface of the wing. The pressure region on top of the wing is symmetrical with the chord of the wing and has its maximum around 2 mm from the base of the wing.

Angle-of-attack effect

The change of the angle-of-attack α shows a similar pattern as the change of the stroke-acceleration $\dot{\omega}_s$ (figure 3.8). The development of the high-pressure region on the bottom surface is slowly followed by the development of a low-pressure region on the top surface with an increasing angle-of-attack (figure 3.8*a–d*). On the bottom surface, the maximum pressure is again located close to the center of the chord and 2 mm from the root along the span (figure 3.8*e–h*). On the top surface, the low pressure region is formed closer to the trailing edge. Interestingly, the low pressure region moves further away from the root for an increase in angle-of-attack (figure 3.8*i–l*).

Aerodynamics of deceleration

The pressure distribution due to the wing deceleration (p_{sa}) shows that the low-pressure region is now located on the bottom of the wing and the high-pressure region on top of the wing (figure 3.9*a–d*). Interestingly, the high-pressure region that is now located on top of the wing shows a shift towards the trailing edge. This shift towards the trailing edge is similar to the shift of the low-pressure region of the accelerating wing (figures 3.7 and 3.8). This further strengthens the notion that this shift is due to the interaction with the leading-edge vortex.

Geometrical scaling

We estimated the thickness of the accelerated fluid layer (δ_{sa}) from the pressure distribution on the wing-surface due to the stroke-acceleration. We first assumed that this pressure distribution was caused only by the acceleration of a volume of fluid V. The acceleration of the wing at any given location along the span y

$$a = \dot{\omega}_s y. \tag{3.15}$$

With the use of the second law from Newton we can use this local acceleration a to compute the local force (dF) acting on the surface of the wing

$$m \cdot a = \rho V \dot{\omega}_s y = dF. \tag{3.16}$$

The local force acting on the surface of the wing dF can also be derived from the pressure distribution

$$dF = p_{sa} dA, \tag{3.17}$$

where dA is the surface of an infinitesimal part of the wing. The volume of air that is acceleration (V, equation (3.16)) can be written in terms of this same surface $V = \delta_{sa} dA$. Combining this with equation (3.16) and (3.17)

$$\rho \delta_{sa} dA \dot{\omega}_s y = p_{sa} dA \tag{3.18}$$

$$\delta_{sa} = \frac{p_{sa}}{\rho \dot{\omega}_s y}. \tag{3.19}$$

A schematic representation of the shape of the fluid-layer (figure 3.10*g*) shows an elliptical shape of the fluid-layer across the chord. We computed the thickness of the fluid-layer for the elliptical wings with a changing chord length (figure 3.10*h–l*), which shows that the chord length influences the thickness of the fluid-layer. The thickness of the fluid-layer decreases over the span, which was not predicted by the blade-element model (equation (3.3)). This aerodynamic effect explains why a geometrical scaling parameter that includes the influence along the span and chord was needed to normalize the forces $\left(\sqrt{S_{yy} S_{\text{sedov}}}\right)$.

3.3.4 Aerodynamics of the interaction forces

The pressure distribution due to the interaction p_{sr-sa} was estimated by taking the difference between two wings moving at the same stroke-acceleration $\dot{\omega}_s$, but different stroke-rates ω_s, which results in

$$p_{sr-sa} \approx \left[p_s\left(\dot{\omega}_s, \omega_1\right) - p_{sr}\left(\omega_1\right)\right] - \left[p_s\left(\dot{\omega}_s, \omega_2\right) - p_{sr}\left(\omega_2\right)\right], \tag{3.20}$$

where we took the baseline stroke rate at $\omega_2 = 750\,\mathrm{rad\,s^{-1}}$ and the first stroke rate at $\omega_1 = 1750\,\mathrm{rad\,s^{-1}}$. We computed the pressure distribution due to the interaction p_{sr-sa} for four different stroke accelerations (figure 3.11). The pressure on the bottom of the wing (figure 3.11*a–d*) is almost unaffected by the stroke-interaction. However, the pressure distribution on top of the wing (figure 3.11*e–h*) is increased over a large portion of the wing surface. Only near the tip of the wing, a negative region is formed. This increase in the pressure on top of the wing causes a reduction of the net pressure distribution (figure 3.11*i–l*), which is in line with the reduction of the forces due to the interaction mechanism (see section 3.3.1).

This same pattern of reduction persists with different angles of attack (figure 3.12*i–l*). The reduction of net pressure does move from the tip of the wing closer to the root of the wing. The span-wise vorticity is reduced for a wing moving with a stroke-acceleration (figure 3.12*e–h*) when compared with a wing moving without a stroke-acceleration (figure 3.12*a–d*). This reduction of the span-wise vorticity hints at a reduction of the leading-edge vortex when the wing is accelerating.

3.3.5 Application of the model

The model we found for the forces on a wing moving at a non-constant stroke rate (equation (3.12) and equation (3.13)) was applied to the kinematics of a fruit fly [17] and a malaria mosquito [18] (figure 3.13*a* and *b* respectively). A full definition of the model can be found in the appendix section 3.10.

The stroke-rate forces for the fruit fly are dominant for both drag and lift (100 % and 95 % of the total forces respectively 3.13*g*, *i*). The maximum of these stroke rate forces is reached around mid-stroke for both the forward-stroke and backward-stroke. For the mosquito, the stroke-rate forces also reaches a maximum around mid-stroke (figure 3.13*h*, *j*). However, the dominance of the stroke-rate forces for the mosquito wing motion is less pronounced than for the fruit fly (drag 71 % lift 87 % of the total

forces).

The stroke-acceleration forces are around zero during mid-stroke of both the fruit fly (figure 3.13*e*, *g* and *i*) and the mosquito (figure 3.13*f*,*h* and *j*), when the stroke acceleration is zero. Before mid-stroke the stroke-acceleration forces have a positive contribution to both lift and drag. At the start of the stroke, the stroke-accelerations are positive (figure 3.1*e*). After mid-stroke, the wing is decelerating, preparing to change direction at stroke-reversal. This leads to a negative contribution of the acceleration-reaction forces to both lift and drag. The latter is interesting, because a negative drag means that the wing is actually propelled by the stroke-acceleration forces.

Finally, the interaction forces do not appear to play any significant role in either the fruit fly (lift 0.3 %, drag −0.2 %) or the mosquito (lift 0.8 %, drag 0.5 %). This means that the interaction between the stroke-rate forces and the stroke acceleration forces can be neglected when modeling the forces of flapping flight for the considered medium-sized insects.

3.4 Discussion

3.4.1 The stroke-acceleration model

In this study, we showed that the stroke-based forces F_s comprises of three terms: the stroke-rate forces F_{sr}, the interaction forces F_{sr-sa} and the stroke-acceleration forces F_{sa}. For the last two forces, we developed a model that links the stroke-rate ω_s, stroke-acceleration $\dot{\omega}_s$, the angle-of-attack α and the wing morphology to the generation of forces.

Other models were based on a two-dimensional model for an accelerating flat plate in inviscid flow [7, 12, 14, 15, 23, 16]. Our model is the first that used fully three-dimensional viscous flow as a basis for a model of the stroke-acceleration forces. Furthermore, we explicitly tested if the stroke-acceleration forces F_{sa} where influenced by the stroke-rate forces F_{sr}, through the inclusion of the interaction forces F_{sr-sa}.

To isolate the stroke-based forces F_s from other possible aerodynamic mechanisms, we kept the angle-of-attack α constant within a single simulation. This means that the wing was not undergoing any pitch-motion, and that the aerodynamic mechanisms associated with this motion where not present [7, 9]. Thus, possible interactions with pitch motions have not been tested.

Furthermore, insects flap their wings back and forth; hence they flap back through

their own wake [10, 11, 12]. In our study, we eliminated the effect of this wake-capture mechanism by excluding a reciprocal wing movement. This also meant that we could not study the effect of wake-capture on the stroke-acceleration forces.

It takes time for the flow around a moving wing to develop [21]. To remove the dependence of this development time, we made sure that each simulation took exactly 1 ms. However, it is unclear if the development time of the flow is not influenced by the wing motion and angle-of-attack.

3.4.2 The stroke-acceleration forces

The model for the stroke-acceleration forces (equation (3.13)) resembles the model based on two-dimensional inviscid flow (equation (3.3)). Here we showed that the previous two-dimensional model over-predicts the stroke-acceleration forces slightly F_{sa} based on an angle-of-attack of $\alpha = 45°$ and the "old" geometrical scaling [16, 14, 7, 12, 15]. This force difference can be explained by the volume of fluid that is accelerated by the wing. In the two-dimensional model, it was assumed that a cylinder of fluid is accelerated with the wing [23]. However, our flow-field analysis shows that the shape of the accelerated fluid was elliptical. Furthermore, the height of the accelerated fluid layer decreased along the span. Taken together, these points explain the difference in the two-dimensional model and our three-dimensional model.

The decrease of the fluid-layer over the span of the wing also showed that the length of the wing is an important geometrical scaling parameter. Therefore, we proposed a geometrical scaling where we combine the second moment of area along the span, and the geometrical scaling S_{sedov}. The proposed geometrical scaling robustly makes our model independent of the wing morphology.

In the geometrical scaling, the wing length and the wing chord both play a equal role. This means that contrary to the original scaling a low-aspect ration and high-aspect ratio are both equally influenced by the stroke-accelerations.

In this study, we used a set of 15 rigid model wings. However, the wings of insects are deformable, which might influence the generation of forces. Based on the pressure distribution of the stroke-acceleration forces (figure 3.7) the center of pressure can be approximated at half the chord-length and 2/3 span. The location of the center of pressure lies close to the rotation axes, and therefore we expect that the wing deformations due to stroke-acceleration will not be as large as for instance the wing deformation due to pitch-based motions [4, 7, 8, 9]. However, the stroke-

accelerations often occur when the wing also has a large pitch rotation around its span. Therefore, more research on the effects of the deformation of the wing on the stroke-acceleration based forces is needed.

3.4.3 The interaction forces

The interaction forces F_{sr-sa} explicitly model the interaction between the stroke-rate forces F_{sr} and the stroke-acceleration forces F_{sr-sa}. It shows that large stroke-accelerations in combination with large stroke-rates reduce the leading-edge vortex (LEV) and therefore reduce the stroke-acceleration forces. This reduction of the LEV can be explained by a decrease in the pressure region on the top surface of the wing. This decrease in pressure region creates a steeper pressure gradient, which in turn reattaches the separated flow faster. This hypothesis should be further studied to better understand the effect of stroke-accelerations on the LEV.

The reduction of the stroke-acceleration forces is minimal for lower stroke rates and stroke accelerations. This can clearly be observed from figure 3.4*a*. It can also be seen from the application of the model to the kinematics of the fruit fly and mosquito (figure 3.13*a* and *b* respectively), where the interaction forces almost played no role compared to those from other aerodynamic mechanisms. Therefore, for insects with similar wingbeat kinematics as the fruit fly and mosquito the interaction forces can safely be ignored.

3.4.4 Importance for insect flight

The stroke-acceleration forces are often not taken into account when studying insect flight. For insects with a high-amplitude and a low frequency, like for instance the fruit fly, this might be appropriate for a first order approximation of the forces. However, for insects with a higher wing-beat frequency, such as the mosquito the instantaneous stroke-acceleration forces play a more prominent role.

For insect flight maneuverability, the stroke-acceleration forces might play a more prominent role than for weight support. Many adjustments of the wingbeat kinematics for maneuvering occur during stroke-reversal [17], which is the phase where the stroke-acceleration forces appear prominent in both the fruit fly and the mosquito.

The model proposed in this study is a new take on a known aerodynamic mechanisms, with the use of a systematic parametric study based on computational fluid dynamics. Furthermore, with the use of our two model species, the fruit fly and the

malaria mosquito, we showed that the stroke accelerations play an important role in the transient force generation of these insects. For high-frequency flappers, like the malaria mosquito, the stroke acceleration forces do influence the force required for weight support. This study is one of the first steps into a broader and more universal understanding in the flight of flapping insects.

3.5 References

[1] C. P. Ellington. "The aerodynamics of hovering insect flight. IV. aerodynamic mechanisms". In: *Philosophical transaction royal society London* 305 (1984), pp. 79–113. DOI: 10.1098/rstb.1984.0052.

[2] C. Zhang, T. L. Hedrick, and R. Mittal. "Centripetal acceleration reaction: An effective and robust mechanism for flapping flight in insects". In: *Plos One* (2015). DOI: 10.1371/journal.pone.0132093.

[3] C. P. Ellington, C. van den Berg, A. P. Willmott, and A. L. R. Thomas. "Leading-edge vortices in insect flight". In: *Nature* 384.6610 (1996), pp. 626–630. DOI: 10.1038/384626a0.

[4] M. H. Dickinson, F. Lehmann, and S. P. Sane. "Wing rotation and the aerodynamic basis of insect flight". In: *Science* 284.5422 (June 1999), pp. 1954–1960. DOI: 10.1126/science.284.5422.1954.

[5] J. M. Birch and M. H. Dickinson. "Spanwise flow and the attachment of the leading-edge vortex on insect wings". In: *Nature* 412 (2001), pp. 729–733. DOI: 10.1038/35089071.

[6] J. M. Birch, W. B. Dickson, and M. H. Dickinson. "Force production and flow structure of the leading edge vortex on flapping wings at high and low Reynolds numbers". In: *The Journal of Experimental Biology* 207 (2004), pp. 1063–1072. DOI: 10.1242/jeb.00848.

[7] T. Nakata, H. Liu, and R. J. Bomphrey. "A CFD-informed quasi-steady model of flapping-wing aerodynamics". In: *Journal of Fluid Mechanics* 783 (Nov. 2015), pp. 323–343. DOI: 10.1017/jfm.2015.537.

[8] R. J. Bomphrey, T. Nakata, N. Phillips, and S. M. Walker. "Smart wing rotation and trailing-edge vortices enable high frequency mosquito flight". In: *Nature* 554 (2017), pp. 92–95. DOI: 10.1038/nature21727.

[9] W. G. van Veen, J. L. van Leeuwen, and F. T. Muijres. “A chordwise offset of the wing-pitch axis enhances rotational aerodynamic forces on insect wings: a numerical study”. In: *Journal of The Royal Society Interface* 16.155 (2019), pp. 1–13. DOI: 10.1098/rsif.2019.0118.

[10] J. M. Birch and M. H. Dickinson. “The influence of wing–wake interactions on the production of aerodynamic forces in flapping flight”. In: *The Journal of Experimental Biology* 206 (2003), pp. 2257–2272. DOI: 10.1242/jeb.00381.

[11] F. Lehman. “When wings touch wakes: understanding locomotor force control by wake–wing interference in insect wings”. In: *The Journal of Experimental Biology* 211 (2008), pp. 224–233. DOI: 10.1242/jeb.007575.

[12] P. S. Sane and M. H. Dickinson. “The control of flight force by a flapping wing: lift and drag production”. In: *The journal of experimental biology* 204 (2001), pp. 2607–2626. ISSN: 0022-0949.

[13] M. H. Dickinson. “The effects of wing rotation on unsteady aerodynamic performance at low Reynolds numbers”. In: *The Journal of Experimental Biology* 192 (1994), pp. 179–206. ISSN: 0022-0949.

[14] J. A. Walker and M. W. Westneat. “Mechanical performance of aquatic rowing and flying”. In: *Proceedings of the royal society B* 267.1455 (2000), pp. 1875–1881. DOI: 10.1098/rspb.2000.1224.

[15] C. K Kang, H. Aono, C. E. S. Cesnik, and W. Shyy. “Effects of flexibility on the aerodynamic performance of flapping wings”. In: *AIAA* (2011).

[16] J.P. Whitney and R.J. Wood. “Aeromechanics of passive rotation in flapping flight”. In: *Journal of Fluid Mechanics* 660 (2010). DOI: 10.1017/S002211201000265X.

[17] M. H. Dickinson and F. T. Muijres. “The aerodynamics and control of free flight manoeuvres in Drosophila”. In: *Philosophical Transactions B* 371.1704 (2016). DOI: 10.1098/rstb.2015.0388.

[18] F.T. Muijres, S.W. Chang, W.G. Veen, J. Spitzen, B.T. Biemans, M.A.R. Koehl, and R. Dudley. “Escaping blood-fed malaria mosqtuitoes minimize tactile detection without compromising on take-off speed”. In: *Journal of Experimental Biology* 220.20 (2017), pp. 3751–3762. DOI: 10.1242/jeb.163402.

[19] T. Maxworthy. “Experiments on the Weis-Fogh mechanism of lift generation by insects in hovering flight. Part1. Dynamics of the ’fling’”. In: *Journal of Fluid Mechanics* 93 (1979), pp. 47–63.

[20] D. Lentink and M. H. Dickinson. “Rotational accelerations stabilize leading edge vortices on revolving fly wings”. In: *The Journal of Experimental Biology* (2009). DOI: 10.1242/jeb.022269.

[21] S. P. Sane. “The aerodynamics of insect flight”. In: *The Journal of Experimental Biology* 206 (2003), pp. 4191–4208. DOI: 10.1242/jeb.00663.

[22] T. L. Daniel. “Unsteady aspects of aquatic locomotion”. In: *American Zoologist* (1984).

[23] L. I. Sedov. *Two-Dimensional Problems in Hydrodynamics and Aerodynamics*. Interscience Publishers, 1965.

[24] G. J. Berman and Z. J. Wang. “Energy-minimzing kinematics in hovering insect flight”. In: *Journal of Fluid Mechanics* 582 (2007), pp. 153–168. DOI: 10.1017/S002211200700620.

[25] L. Liu and M. Sun. “The added mass forces in insect flapping wings”. In: *Journal of theoretical biology* 437 (Jan. 2017), pp. 45–50. DOI: 10.1016/j.jtbi.2017.10.014.

[26] M. Karasek, F. T. Muijres, C. De Wager, B. D. W. Remes, and G. C. H. E. Croon. “A tailless aerial robotic flapper reveals that flies use torque coupling in rapid banked turns”. In: *Science* 361 (2018). DOI: 10.1126/science.aat0350.

[27] A. P. S. Bhalla, R. Bale, B. E. Griffith, and N. A. Patankar. “A unified mathematical framework and an adaptive numerical method for fluid–structure interaction with rigid, deforming, and elastic bodies”. In: *Journal of Computational Physics* 250 (2013), pp. 446–476. DOI: 10.1016/j.jcp.2013.04.033.

3.6 Figures

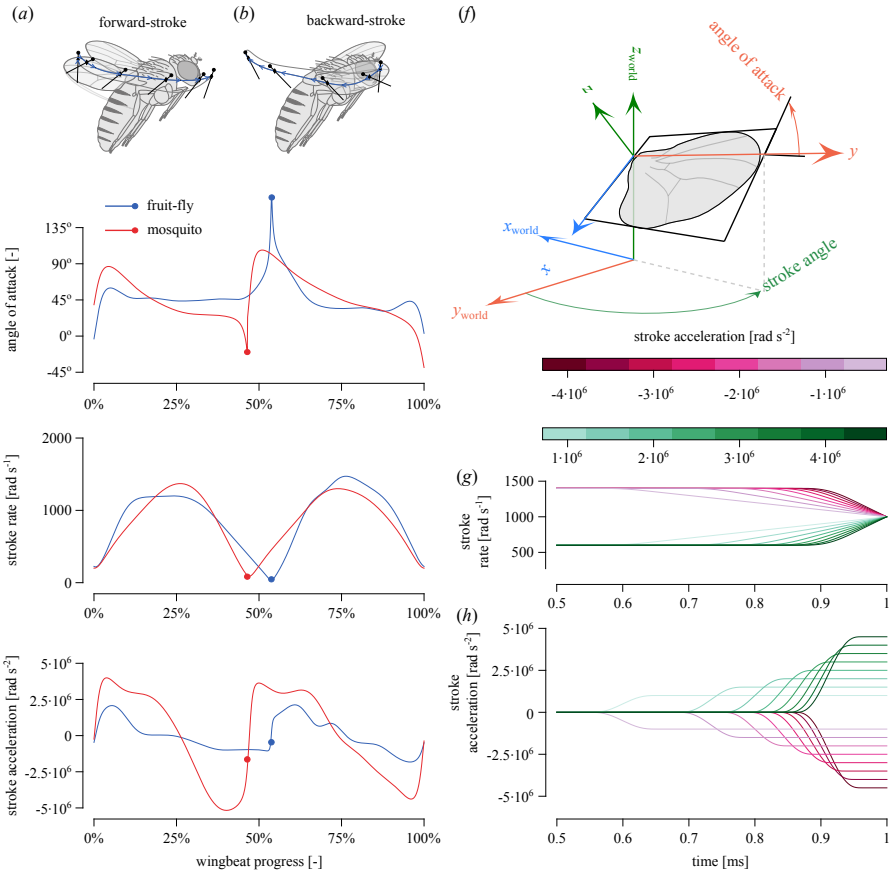

Figure 3.1: (*a*, *b*) Schematic representation of the wing motion of a fruit fly of the forward- and backward-stroke respectively. (*c*, *d*) Kinematics of a fruit fly (blue) [17] and mosquito [18] (red) where the dot indicates the stroke reversal, angle-of-attack, stroke-velocity and stroke-acceleration respectively. (*f*) Definition of the world-reference-frame, wing reference frame and the stroke angle and angle-of-attack. (*g*, *h*) Design of the kinematics used in this study, pink green colors are different stroke accelerations at the end of the simulation indicated by the color-bar, stroke rate and stroke acceleration respectively.

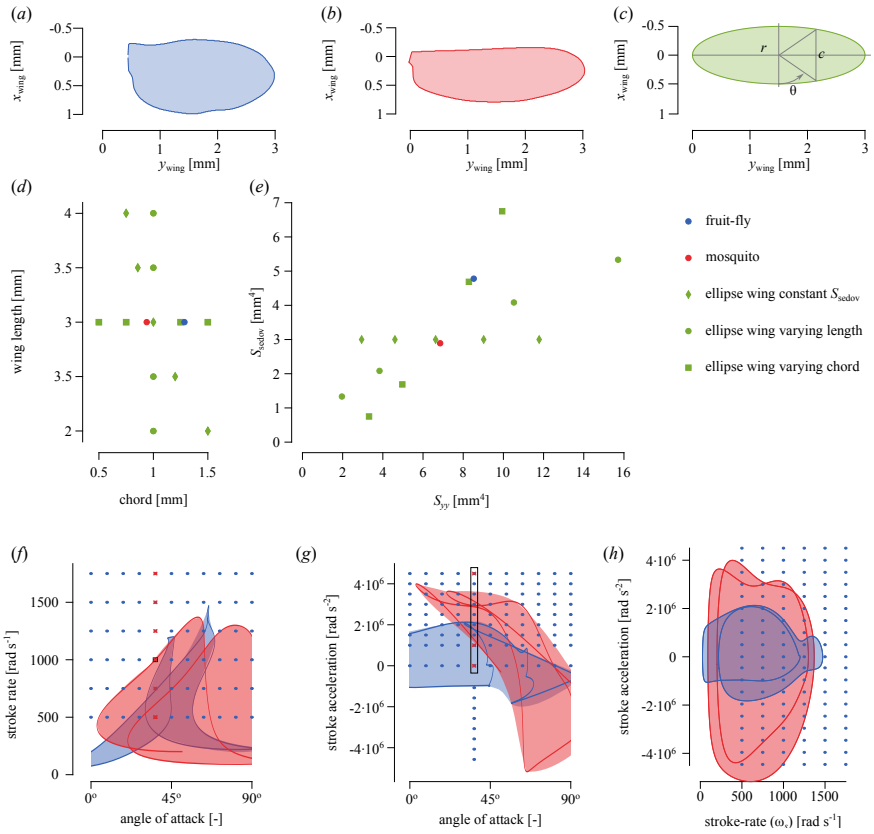

Figure 3.2: Description of the kinematic and morphological parametric space. (*a–c*) Wing morphology of the fruit fly, mosquito and *ellipse*-shaped wings. (*d*) Variation of the chord and wing length for the *ellipse*-shaped wings. (*e*) Morphological parametric space of for all the wing morphologies in this study, the span-wise second moment of area S_{yy} against the scaling parameter S_{sedov}. (*f*, *g*, *h*) Kinematic parametric space spanned by the fruit fly (blue) [17] and mosquito (red) [18], blue dots indicate the simulations for the fruit fly, crosses indicate the simulations for all the other morphologies (see table 3.1), box indicates the example discussed in section 3.2.5.

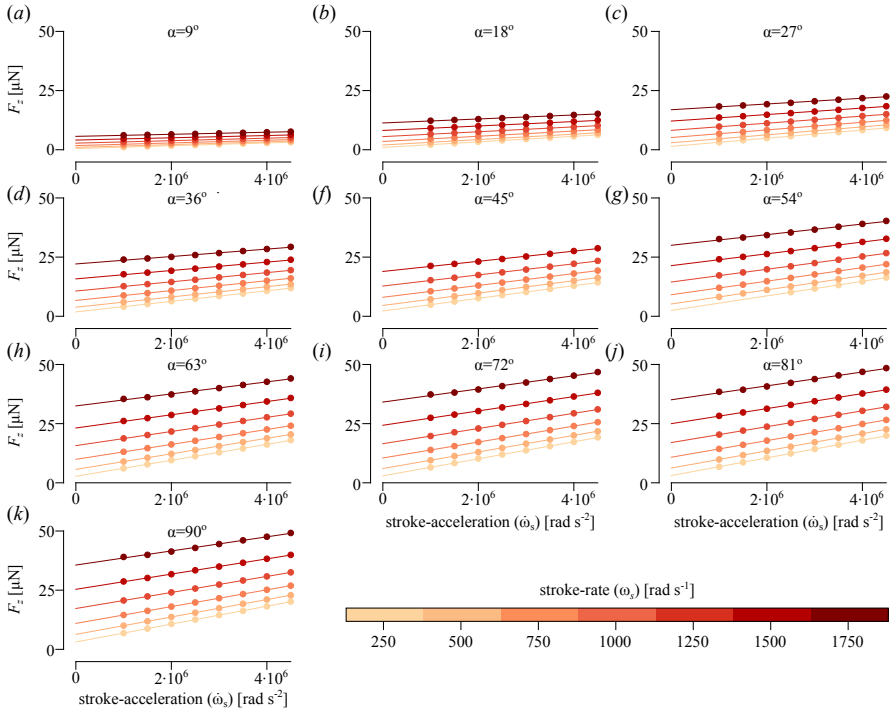

Figure 3.3: Forces for the fruit fly wing morphology as a function of the stroke-acceleration $\dot{\omega}_s$, colored by the stroke-rate ω_s (see colorbar), for different angles-of-attack α (*a*–*k*, 9° to 90° respectively).

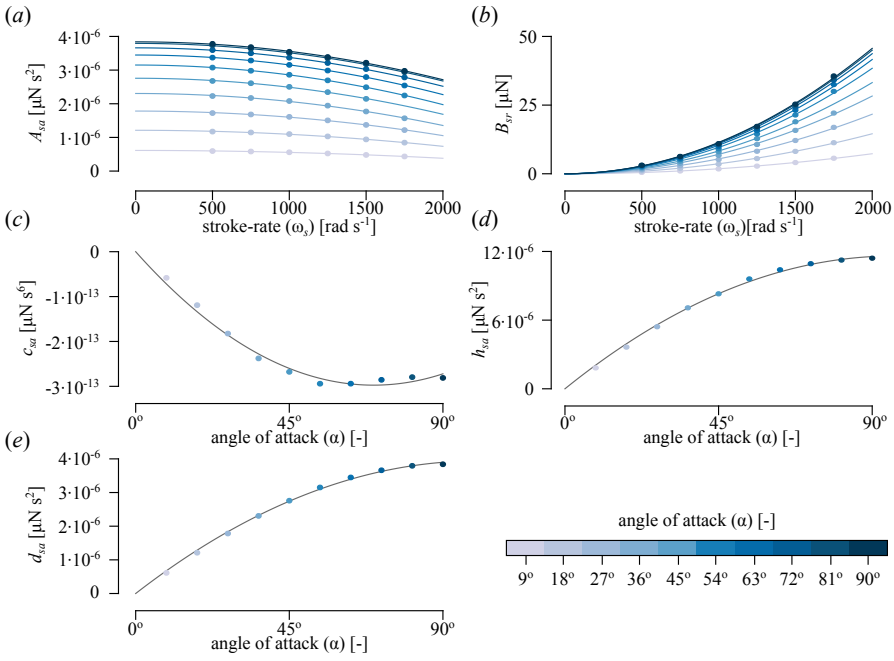

Figure 3.4: Coefficients of the stroke-based force model (equation (3.6)) for the fruit fly wing morphology. (*a*) The slope (A_{sa}) of the lines in figure 3.3 as a function of the stroke-rate ω_s colored by the angle-of-attack (α), curves are fits based on equation (3.7). Intercept B_{sr} of the lines in figure 3.3 as a function of the stroke-rate ω_s colored by the angle-of-attack, fits are based on equation (3.10). (*c*, *e*) Fitting parameters c_{sa} and d_{sa} as a function of the angle-of-attack, dark gray lines are the fits based on equation (3.8) and (3.9) respectively. (*d*) Fitting parameter h_{sr} as a function of the angle-of-attack, dark gray line is the fit based on equation (3.11).

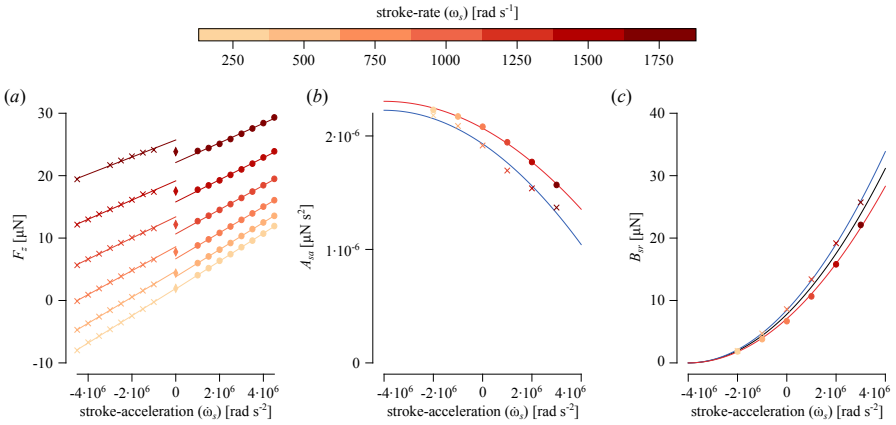

Figure 3.5: Comparison of a decelerating and accelerating fruit fly wing at an angle-of-attack $\alpha = 36°$. (*a*) Stroke-based forces as a function of the stroke-acceleration $\dot{\omega}_s$ for a negative (crosses) and positive (dots) stroke-acceleration. (*b*) The slope ($A_{s\dot{\alpha}}$) of the lines in panel *a*, for a decelerating wing (blue) and accelerating wing (red), fits are based on equation (3.7). (*c*) Intercept (B_{sr}) of the lines in panel *a*, for a decelerating wing (blue) and accelerating wing (red), fits are based on equation (3.10).

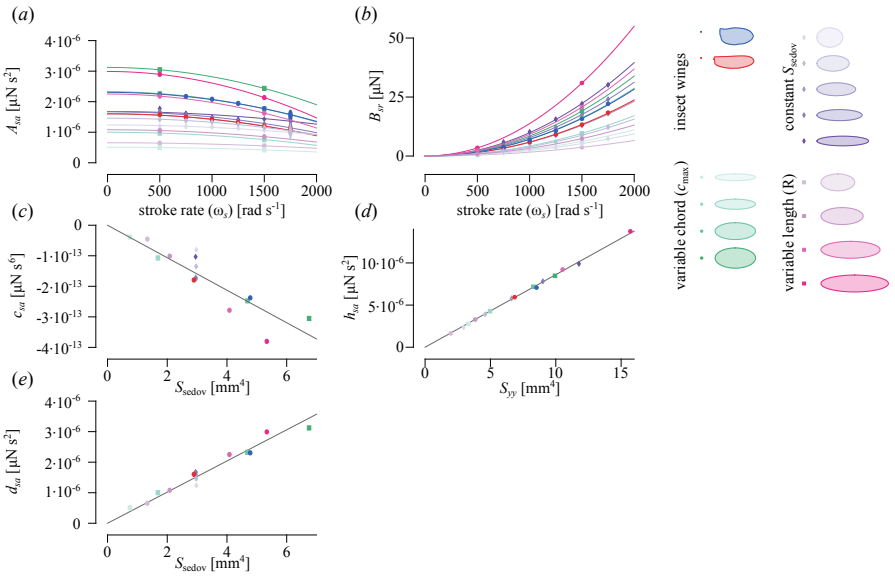

Figure 3.6: Scaling of the stroke-based forces for different wing morphologies. (*a*, *b*) Variation of the coefficients A_{sa} and B_{sr} respectively, with the stroke-rate ω_s colored by wing morphology (see legend). (*c*, *e*) Coefficients c_{sa} and d_{sa} respectively as a function of the geometrical scaling parameter S_{sedov} colored by the different wing morphologies, dark gray line is a simple linear fit. (*d*) Coefficients h_{sr} as a function of the span-wise second moment of area S_{yy} colored by the different wing morphologies, dark gray line is a simple linear fit.

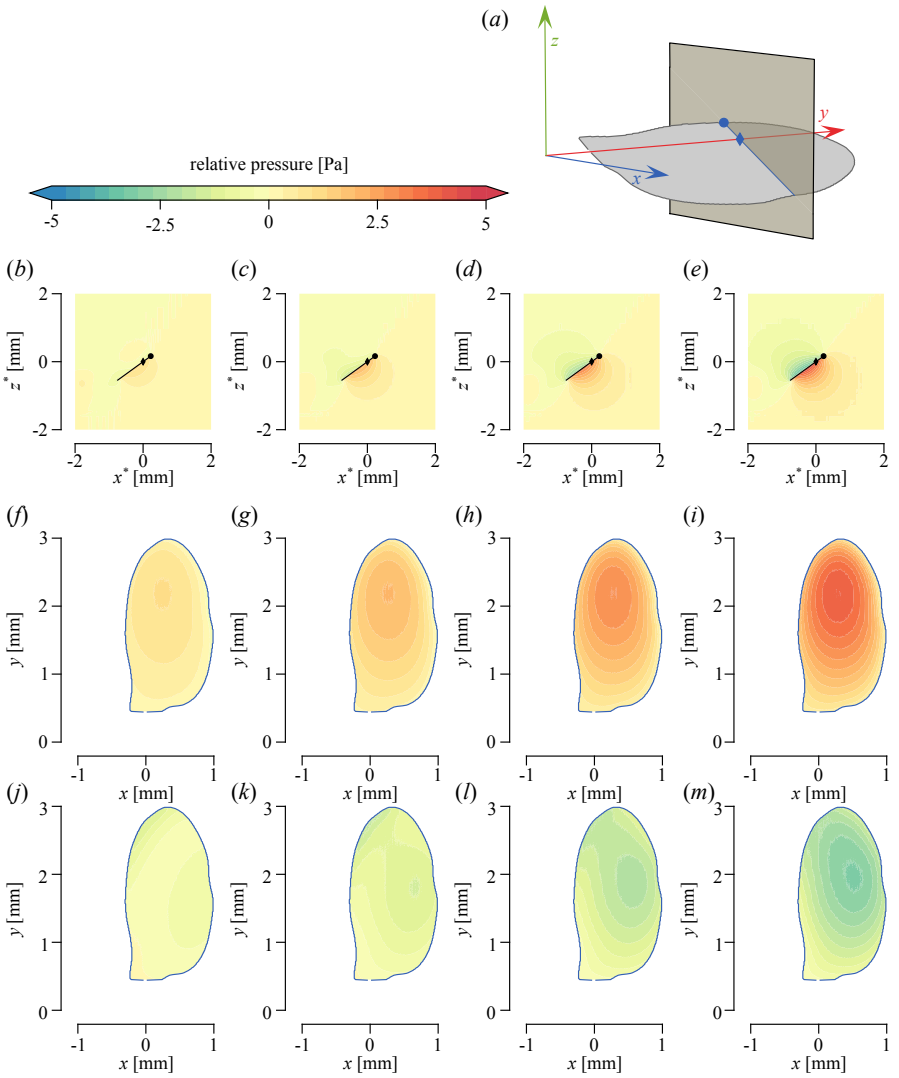

Figure 3.7: Effect of the stroke-acceleration on the pressure field for the fruit fly wing morphology. (*a*) Schematic representation of a fruit fly wing under and angle-of-attack of $\alpha = 36°$, square indicates the extraction plane used for panel *b–e*. (*b–e*) Pressure distribution due to the stroke-acceleration p_{sa} (equation (3.14)) for $1 \cdot 10^6$ rad s^{-2}, $2 \cdot 10^6$ rad s^{-2}, $3 \cdot 10^6$ rad s^{-2}, $4 \cdot 10^6$ rad s^{-2} respectively. (*f–i*) Pressure distribution p_{sa} on the bottom surface for a wing with a stroke-acceleration of $1 \cdot 10^6$ rad s^{-2}, $2 \cdot 10^6$ rad s^{-2}, $3 \cdot 10^6$ rad s^{-2}, $4 \cdot 10^6$ rad s^{-2} respectively. (*j–m*) Pressure distribution p_{sa} on the top surface for a wing with a stroke-acceleration of $1 \cdot 10^6$ rad s^{-2}, $2 \cdot 10^6$ rad s^{-2}, $3 \cdot 10^6$ rad s^{-2}, $4 \cdot 10^6$ rad s^{-2} respectively.

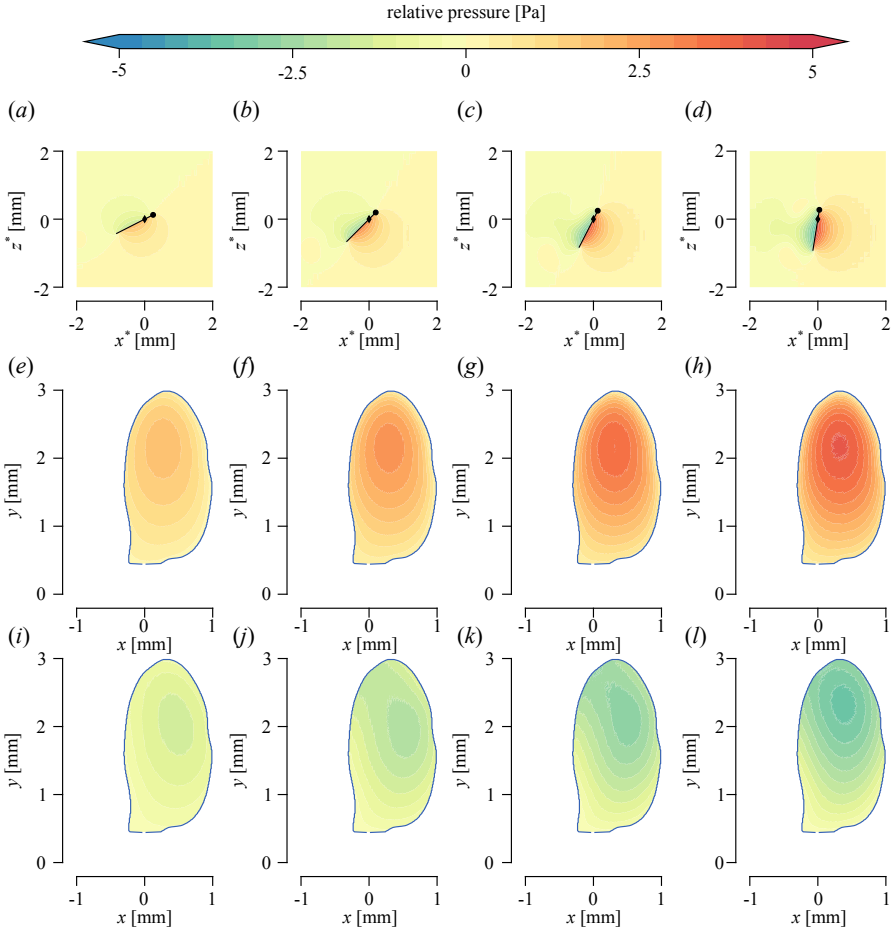

Figure 3.8: Effect of the angle-of-attack on the pressure field for the fruit fly wing morphology, $\omega_s = 500\,\mathrm{rad\,s^{-1}}$, $\dot{\omega}_s = 4 \cdot 10^6\,\mathrm{rad\,s^{-1}}$. (*a–d*) Pressure distribution due to the stroke-acceleration p_{sa} (equation (3.14)) for angles of attack 27°, 45°, 63° and 81° respectively, in a plane perpendicular to the span 2 mm from the root (figure 3.7 *a*). (*f–i*) Pressure distribution p_{sa} on the bottom surface for a wing with the angles of attack 27°, 45°, 63° and 81° respectively. (*i–l*) Pressure distribution p_{sa} on the top surface for a wing with the angles of attack 27°, 45°, 63° and 81° respectively.

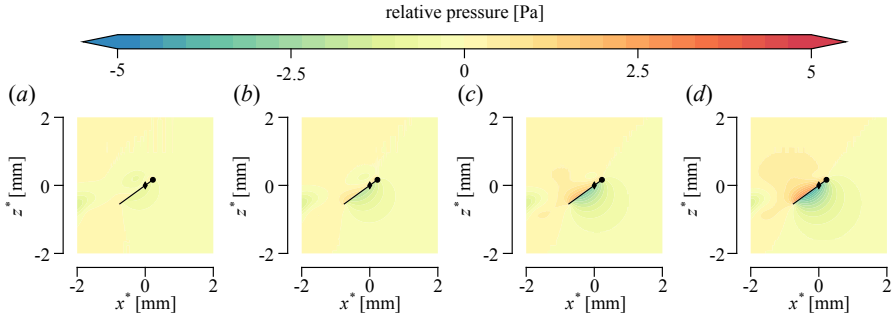

Figure 3.9: Effect of the stroke-deceleration on the pressure field for the fruit fly wing morphology. ($a - d$) Pressure distribution due to the stroke-acceleration p_{sa} (equation (3.14)) for stroke-accelerations $-1 \cdot 10^6$ rad s^{-2}, $-2 \cdot 10^6$ rad s^{-2}, $-3 \cdot 10^6$ rad s^{-2}, $-4 \cdot 10^6$ rad s^{-2} respectively, in a plane perpendicular to the span 2 mm from the root (figure 3.7*a*).

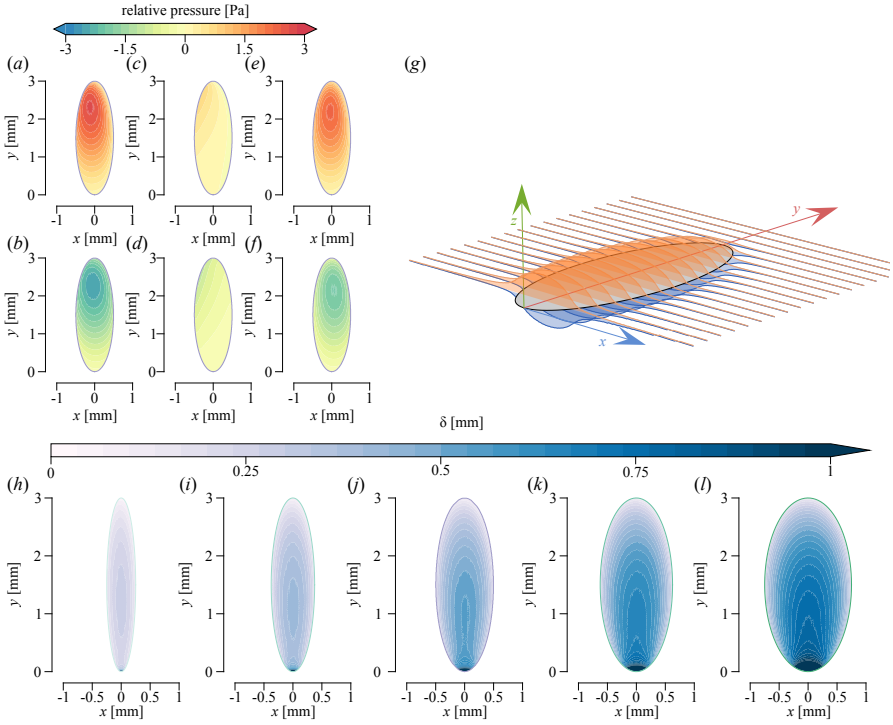

Figure 3.10: Effect of the geometry on the thickness of the accelerated fluid layer δ_{sa} (equation (3.19)) for an elliptical wing with varying chord. (*a*, *b*) Pressure distribution on the bottom and top surface of an elliptical wing ($\dot{\omega}_s = 4.5 \cdot 10^6\,\mathrm{rad\,s^{-2}}$, $\omega_s = 500\,\mathrm{rad\,s^{-1}}$ and $\alpha = 36°$). (*c*, *d*) Pressure distribtuion on the bottom and top surface of an elliptical wing ($\omega_s = 500\,\mathrm{rad\,s^{-1}}$ and $\alpha = 36°$). (*e*, *f*) Difference between the pressure distributions given in panels *a*, *b* and *c*, *d*. (*g*) Schematic representation of the thickness of the fluid-layer accelerated by an elliptical wing. (*h*–*l*) Thickness of the fluid-layer for an elliptical wing with increasing chord length.

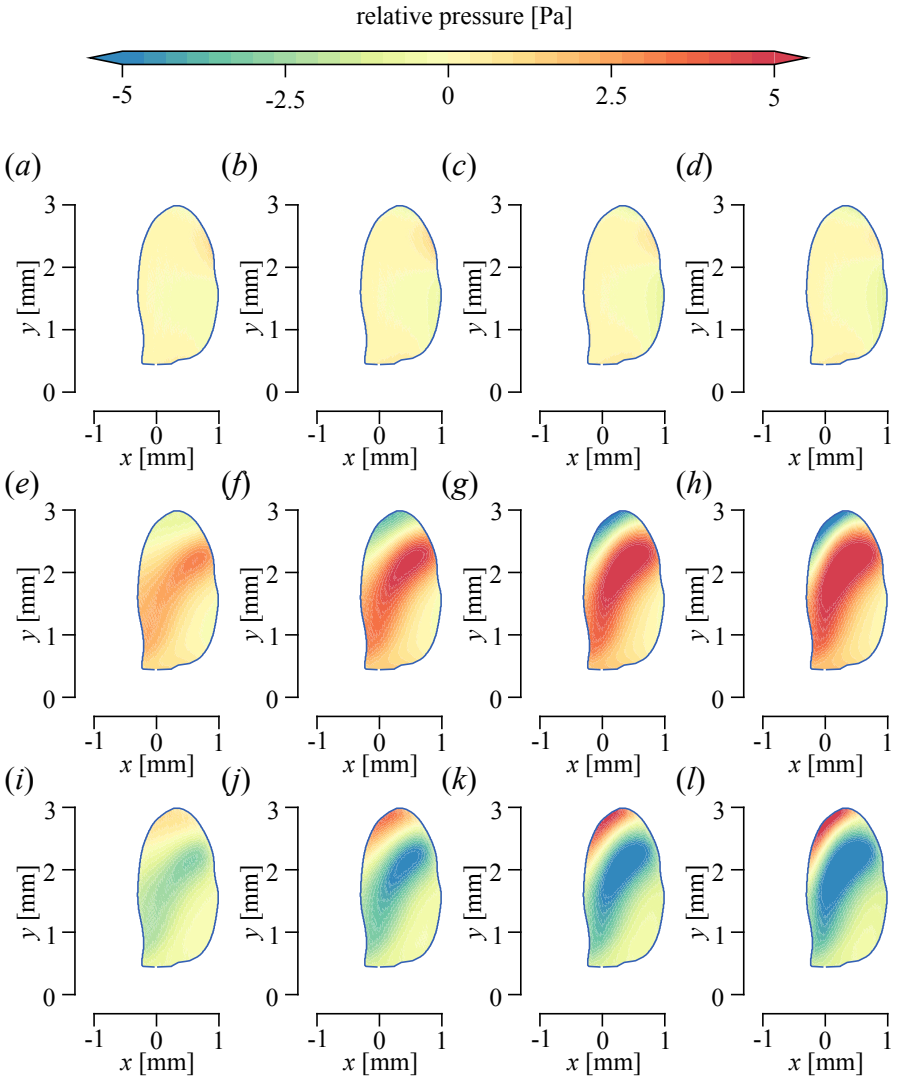

Figure 3.11: Effect of the stroke-acceleration on the pressure distribution due to the interaction for the fruit fly wing morphology at an angle-of-attack $\alpha = 36°$. (*a–d*) Interaction pressure distribution p_{sr-sa} (equation (3.20)) on the bottom surface of a wing moving with $\dot{\omega}_s = 1 \cdot 10^6\,\mathrm{rad\,s^{-2}}$, $\dot{\omega}_s = 2 \cdot 10^6\,\mathrm{rad\,s^{-2}}$, $\dot{\omega}_s = 3 \cdot 10^6\,\mathrm{rad\,s^{-2}}$ and $\dot{\omega}_s = 4 \cdot 10^6\,\mathrm{rad\,s^{-2}}$. (*e–h*) Interaction pressure distribution p_{sr-sa} (equation (3.20)) on the top surface of a wing moving with $\dot{\omega}_s = 1 \cdot 10^6\,\mathrm{rad\,s^{-2}}$, $\dot{\omega}_s = 2 \cdot 10^6\,\mathrm{rad\,s^{-2}}$, $\dot{\omega}_s = 3 \cdot 10^6\,\mathrm{rad\,s^{-2}}$ and $\dot{\omega}_s = 4 \cdot 10^6\,\mathrm{rad\,s^{-2}}$. (*i–l*) Difference between the bottom surface (*a–d*) and top surface (*e–h*).

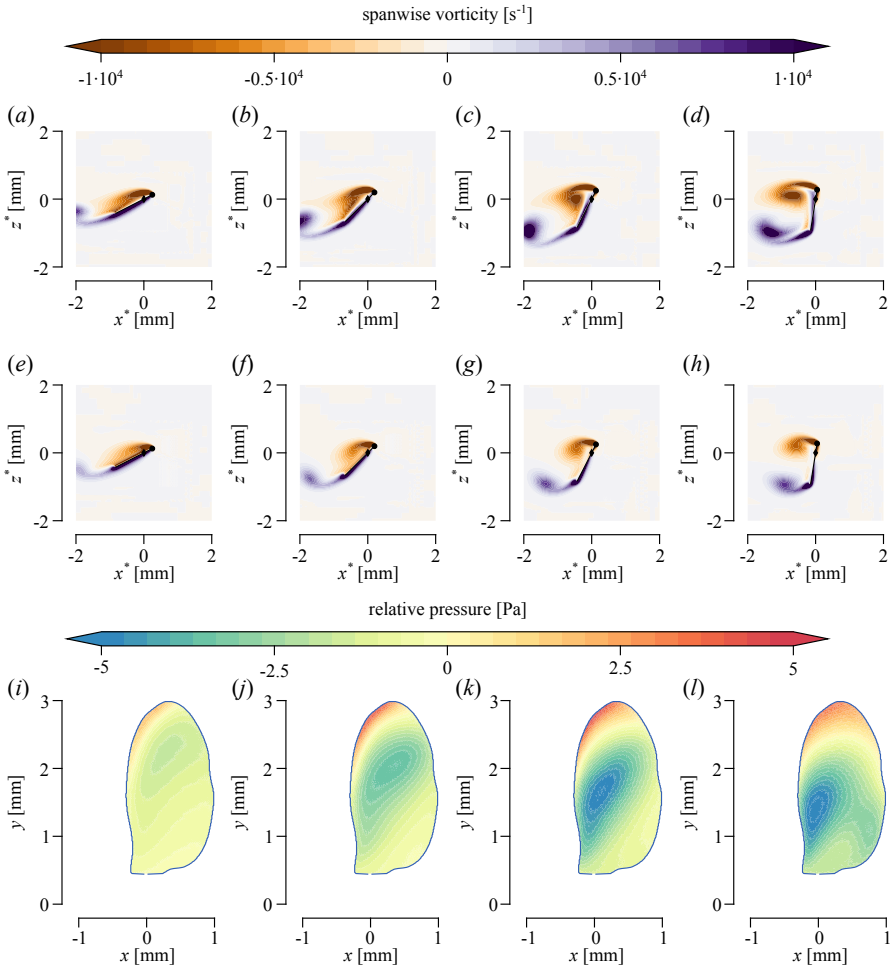

Figure 3.12: Effect of the angle-of-attack on the interaction pressure distribution (p_{sr-sa} (equation (3.20)) for the fruit fly wing morphology with $\alpha = 36°$, $\omega_s = 1250\,\mathrm{rad\,s^{-1}}$ and $\dot{\omega}_s = 4.5 \cdot 10^6\,\mathrm{rad\,s^{-2}}$. (*a–d*) Span-wise vorticity of a wing without stroke-acceleration for $\alpha = 27°$, $\alpha = 45°$, $\alpha = 63°$, $\alpha = 81°$ respectively. (*e–h*) Span-wise vorticity of a wing with stroke-acceleration for $\alpha = 27°$, $\alpha = 45°$, $\alpha = 63°$, $\alpha = 81°$ respectively. (*i–l*) Interaction pressure distribution (equation (3.20)) for $\alpha = 27°$, $\alpha = 45°$, $\alpha = 63°$, $\alpha = 81°$ respectively.

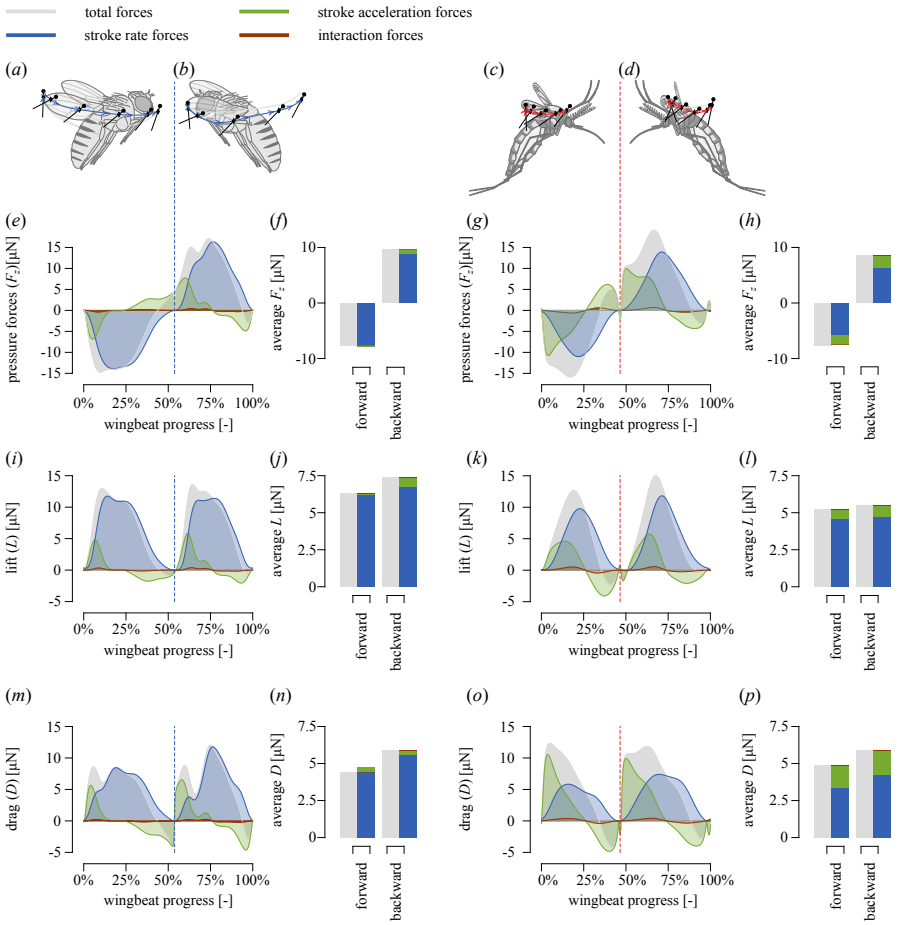

Figure 3.13: Application of the stroke-acceleration model to the wing motion of the (*a*, *b*) fruit fly [17] and (*c*, *d*) mosquito [18]. (*e*, *g*) Pressure forces in the wing reference frame, for the fruit fly and mosquito respectively. (*f*, *h*) Average pressure forces in the wing reference frame. (*i*, *k*) Lift forces perpendicular to the wing velocity vector for the fruit fly and mosquito respectively. (*j*, *l*) Average lift force for the fruit fly and mosquito respectively. (*m*, *o*) Drag forces, parallel to the wing velocity vector, for the fruit fly and mosquito respectively. (*n*, *p*) Average drag forces for the fruit fly and mosquito respectively. For the stroke rate contribution (blue), stroke-acceleration contribution (green), interaction contribution (brown) and total (grey). Vertical line indicates stroke-reversal.

Supplementary methods

3.7 List of symbols

Table 3.2: List of symbols

Symbol	unit	Description
α	-	angle-of-attack
A_{sa}	µN s^2 kg m^{-3}	Coefficient that relates the stroke acceleration to the stroke based forces
B_{sr}	µN kg m^{-3}	Offset of the stroke based forces uninfluenced by the stroke acceleration
c	mm	chord length
c_{max}	mm	maximum chord length
c_{sa}	µNs^6 kg/m^3	Coefficient that relates A_{sa} to the stroke rate
$c_{sa-\alpha a}$, $c_{sa-\alpha b}$	µNs^6 kg/m^3	Coefficients that relates the coefficient c_{sa} to the angle-of-attack α
$\vec{C}_{sr}$	-	stroke rate force coefficients
d_{sa}	µN s^2 kg m^{-3}	Offset of the coefficient A_{sa} independent of the stroke rate
$d_{sa-\alpha b}$, $d_{sa-\alpha b}$	µN s^2 kg m^{-3}	Coefficients that relates the coefficient d_{sa} to the angle-of-attack α.
δ_{sa}	mm	thickness of the accelerated fluid layer
$\vec{F}_{sr}$	µN	stroke rate forces
F_s	µN	stroke based forces
F_{sr}	µN	stroke rate forces
F_{sr-sa}	µN	stroke rate stroke acceleration interaction forces
F_{sa}	µN	stroke acceleration forces normal to the wing surface
$\vec{F}_{sa}$	µm	stroke acceleration forces
$\vec{F}_{sa,\text{2D}}$	µm	stroke acceleration forces estimate based on the blade element model
$F_{s,z}$	µN	stroke based forces normal to the wing surface
γ	-	stroke angle
h_{sr}	µNs^4 kg/m^3	Coefficient that relates the offset in B_{sr} to the stroke rate
$h_{sa-\alpha a}$, $h_{sa-\alpha b}$	µNs^4 kg/m^3	Coefficients that relates the coefficient h_{sr} to the angle-of-attack.
ω_s	rad s^{-1}	stroke rate
$\dot{\omega}_s$	rad s^{-2}	stroke acceleration
p_{sa}	Pa	pressure distribution due to the stroke accelerations
p_s	Pa	pressure distribution due to the stroke rate and stroke acceleration
p_{sr}	Pa	pressure distribution due to the stroke rate
p_{sr-sa}	Pa	pressure distribution due the to stroke rate stroke acceleration interaction
θ	-	deviation angle
ϕ	-	pitch angle
S_{yy}	mm^4	span-wise second moment of area
S_{sedov}	mm	second moment of area based on a cylinder of accelerated fluid
R	mm	distance from wing root to wing tip

Continued on next page

Continued from previous page

Symbol	unit	Description
ρ	kg m^{-3}	fluid density
V	m^3	volume of fluid accelerated with the wing
$\vec{v}$	m s^{-1}	velocity of the fluid
$[x, y, z]^T$	mm	position in the wing reference frame

3.8 Viscous forces

For the fruit fly wing geometry, we extracted the viscous forces along the chord (figure 3.14) and along the span (figure 3.15). We approximated the dependence of viscous forces on the stroke acceleration $\dot{\omega}_s$ with the same linear relation used to predict the dependence of the pressure forces on the stroke-acceleration (equation (3.6).

The viscous forces along the chord are mainly influenced by the stroke-acceleration for lower angles of attack (figure 3.14*a* – *d*). For the span-wise viscous forces an opp-site effect is observed (figure 3.15). However, both the chord- and span-wise forces are minimal compared to the forces normal to the wing surface (figure 3.3).

3.9 Stroke-rate forces

The stroke-rate forces (F_{sr} are the forces a function of the angle-of-attack α, stroke-rate ω_s and wing morphology (see equation (3.4)). In this study, we conducted a total of 76 simulations where we systematically varied the stroke-rate, angle-of-attack, and the wing morphology (see table 3.3)

Table 3.3: Stroke-rate kinematics overview

Geometry	α [-]	ω_s [rad s^{-1}]
fruit fly	9° to 90°	250 to 1750
mosquito	36°	500 to 1500
ellipse constant S_{sedov}	36°	500 to 1500
ellipse variable chord c_{max}	36°	250 to 1750
ellipse variable wing length R	36°	250 to 1750

The forces at the end of the simulation (1 ms) show a quadratic relation with the stroke-rate ω_s (figure 3.16 *a*–*c*). The viscous forces (F_x and F_y) are approximately 10 % of the total forces. The viscous force along the chord of the wing (F_x is dominant for lower angles of attack, and decreases with an increase in angle-of-attack.

Interestingly, this force switches sign around an angle-of-attack of 72°. Contrary to the chord-wise force, the span-wise force (F_y) increases with the angle-of-attack up to around 72°, after which it starts to decrease. For each angle-of-attack, the forces can be approximated by the function

$$\vec{F}_{sr} = \rho \begin{bmatrix} C_{sr-x\omega a}\omega_s^2 + C_{sr-x\omega b}\omega_s \\ C_{sr-y\omega a}\omega_s^2 + C_{sr-y\omega b}\omega_s \\ C_{sr-z\omega a}\omega_s^2 \end{bmatrix} S_{yy}, \tag{3.21}$$

where S_{yy} is the second moment of area along the span, and the coefficients $C_{sr-*\omega*}$ are determined from fitting equation (3.21) to the results of our simulations. The fitting coefficients are dependent on the angle-of-attack (figure 3.16 (*d–h*), and are approximated by a simple quadratic relation as

$$C_{sr-*\omega*} = C_{sr-*\alpha*a}\alpha^2 + C_{sr-*\alpha*b}\alpha + C_{sr-*\alpha*c}. \tag{3.22}$$

The resulting fitting coefficients are only valid for the fruit fly wing morphology and are presented in table 3.4

Table 3.4: Fitting parameters of equation (3.21) and (3.22)

	$C_{sr-*\alpha*a}$	$C_{sr-*\alpha*a}$	$C_{sr-*\alpha*a}$
$C_{sr-x\omega a}$	0.19	−0.39	0.14
$C_{sr-x\omega b}$	−29.96	−49.06	148.27
$C_{sr-y\omega a}$	−0.12	0.16	
$C_{sr-y\omega b}$	26.99	30.99	
$C_{sr_z\omega a}$	1.57		

To test the dependence of stroke-rate forces on the wing morphology, we included an additional 14 wing morphologies. Of each of these geometries, we determined the coefficients of equation (3.21), and compared these 14 geometries with the second moment of area along the span S_{yy} (see figure 3.17). We assumed that the relation of these 14 coefficients with the angle-of-attack is not dependent on the wing morphology. The quadratic component of both the span-wise viscous force (F_y) and the pressure force F_z show a linear relation with the span-wise second moment of area S_{yy} (figure 3.17 *b* and *c*). At first sight, the scaling of the quadratic term of the chord-wise viscous force F_x appears to be poor. However, the quadratic term is small, and the chord-wise viscous force scales almost linearly with the stroke-rate ω_s. There-

fore, we assume that the proposed scaling is still adequate for the chord-wise viscous forces. Indeed, the linear term of the chord-wise viscous force (figure 3.17 *d*) does scale with the span-wise second moment of area S_{yy}. The same can be said for the linear term of the span-wise viscous force F_y.

3.10 Quasi-steady model

To test how the stroke-acceleration forces influence the total force production of flapping insects, we developed a quasi-steady model. This model is only based on the forces generated due to a stroke-motion (see forces in equation (3.4). The kinematics used in this study where based on three angles; the stroke-angle γ, the deviation-angle θ and the pitch-angle ϕ. From these three angles the total rotation matrix is defined as

$$\boldsymbol{A} = \boldsymbol{A}_\gamma \boldsymbol{A}_\theta \boldsymbol{A}_\phi. \tag{3.23}$$

From the rotation matrix we determined the angular rotation of the wing in the *world reference frame*:

$$\boldsymbol{\omega} = \begin{bmatrix} 0 & \omega_z & \omega_y \\ \omega_z & 0 & -\omega_x \\ \omega_y & \omega_z & 0 \end{bmatrix} = \frac{d\boldsymbol{A}}{dt} A^T. \tag{3.24}$$

From the angular velocity matrix $\boldsymbol{\omega}$ the angular velocity vector $\vec{\omega} = [\omega_x, \omega_y, \omega_z]^T$ is determined. The angular velocity in the *world-reference frame* is then rotated to the *wing-reference frame* with

$$\vec{\omega}_{\text{wing}} = \boldsymbol{A}^T \vec{\omega}_{\text{world}}. \tag{3.25}$$

The angle-of-attack α is determined from the angular velocity in the wing reference frame as

$$\alpha = \tan^{-1}\left(\frac{\omega_x}{\omega_z}\right) \text{sign}\left(\omega_x\right). \tag{3.26}$$

The multiplication with the sign of the angular velocity ω_x in the wing reference frame is included to change the sign of the angle-of-attack according to the direction

of motion of the wing. The stroke rate ω_s is positive by definition and can easily be obtained with

$$\omega_s = \sqrt{\omega_x^2 + \omega_z^2}. \tag{3.27}$$

Finally, the stroke acceleration $\dot{\omega}_s$ is obtained by differentiating the stroke rate ω_s

$$\dot{\omega}_s = \frac{d}{dt}\left(\omega_s\right). \tag{3.28}$$

3.11 Supplementary figures

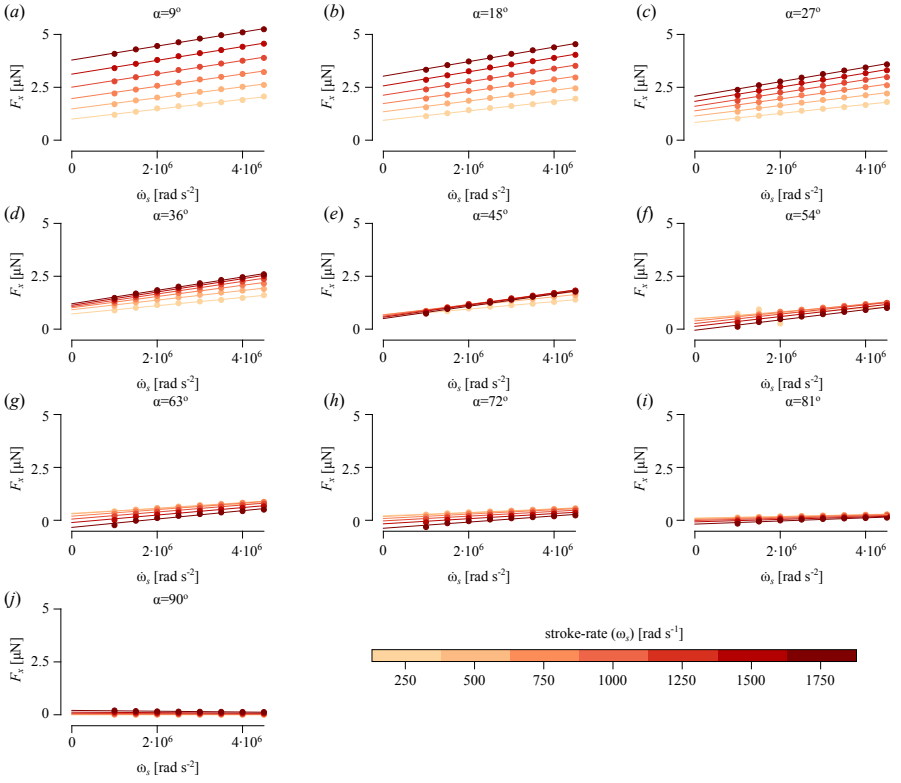

Figure 3.14: Viscous forces along the chord for the fruit fly wing morphology as a function of the stroke-acceleration $\dot{\omega}_s$, colored by the stroke-rate ω_s (see colorbar), for different angles of attack (*a–k*, 9° to 90° respectively).

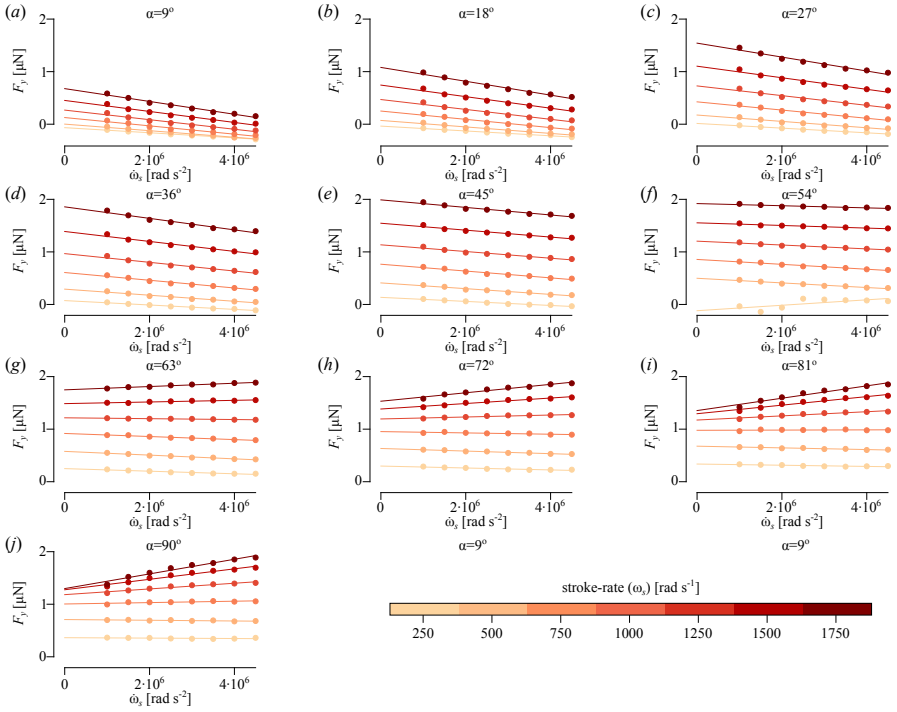

Figure 3.15: Viscous force salong the span for the fruit fly wing morphology as a function of the stroke-acceleration $\dot{\omega}_s$, colored by the stroke-rate ω_s (see colorbar), for different angles of attack (*a–k*, 9° to 90° respectively).

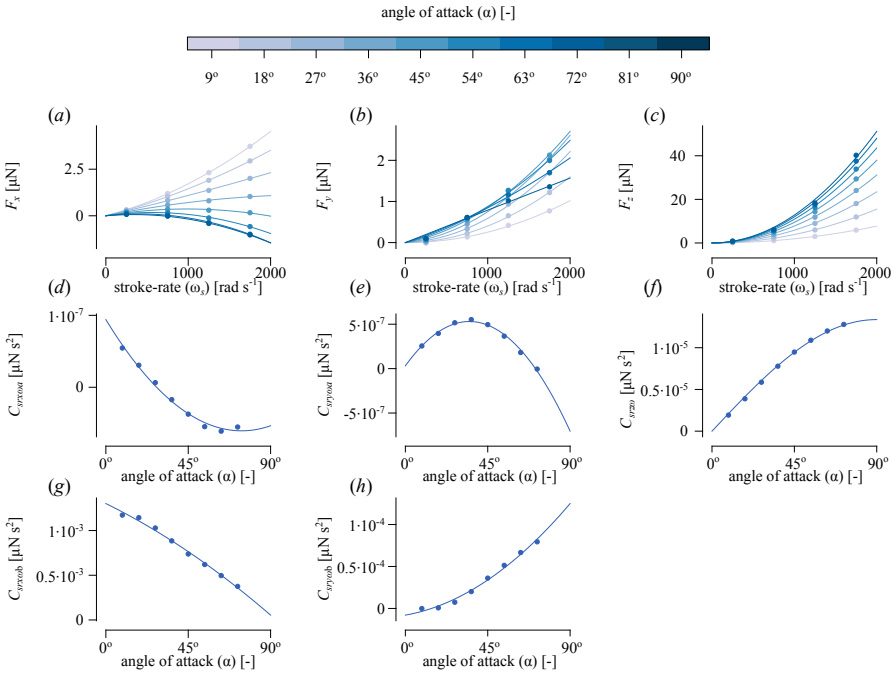

Figure 3.16: Stroke-rate forces for the fruit fly wing morphology in the *wing reference-frame*. (*a* – *c*) Stroke-rate forces as a function of the stroke-rate ω_s colors indicate different angles of attack (see colobar) for the force in the *x*-direction (F_x) *y*-direction (F_y) and *z*-direction (F_z) respectively. (*d–f*) Coefficients of the quadratic terms (equation (3.22)) as a function of the angle-of-attack (α) for F_x, F_y and F_z respectively. (*g*, *h*) Coefficients of the linear terms (equation (3.8) and (3.9)) as a function of the angle-of-attack α for F_x and F_y respectively.

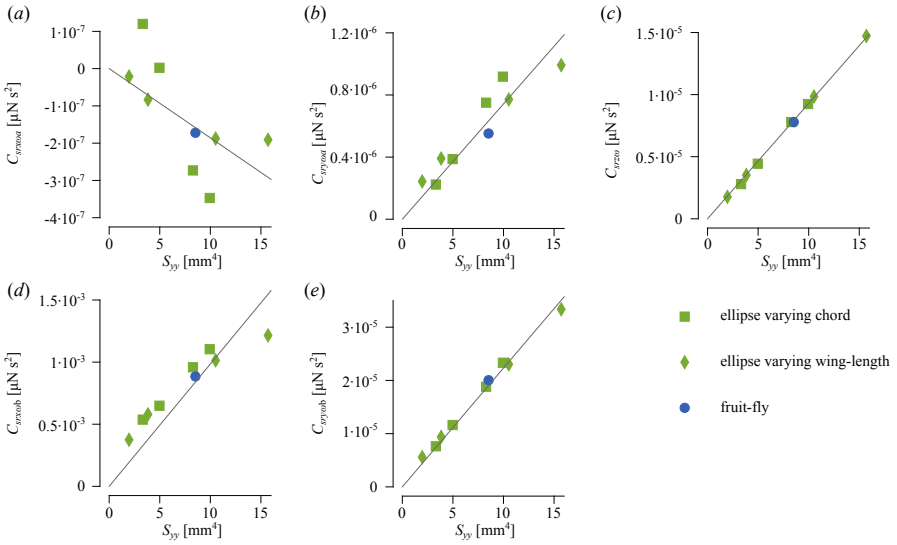

Figure 3.17: Scaling of the stroke-rate forces with the wing morphology. (a – c) Coefficients of the quadratic terms of the stroke-rate forces (equation (3.21)) as a function of the second moment of area along the span S_{yy} for different wing morphologies (see table 3.3). (d, e) Linear terms of the stroke-rate forces (equation (3.21) for the two viscous forces ($F_{sr,x}$ and $F_{sr,y}$) as a function of the second moment of area along the span (S_{yy}) .

Chapter 4

A new perspective on rotational forces in insect flight: a numerical study

Wouter G. van Veen, Johan L. van Leeuwen, Florian T. Muijres

Abstract

Flying insects flap their wings back and forth at high frequencies to generate the forces required for flight. At the end of each of each wing stroke, the insect rotates its wing around it span to prepare for the next stroke. Before and after this stroke-reversal, the angular accelerations of the wing around its span can become very big, and are expected to influence the forces acting on the wing. With the use of Computational Fluid Dynamics (CFD), we systematically studied how the pitch motion of the wing influences the aerodynamic force generation. Furthermore, we varied the wing morphology to study how the forces dependent on the shape of the wing. From these results, we developed a new phenomenological model for all the forces associated with the pitching motion of an insect wing. In this model, we also explicitly implemented the interaction between each aerodynamic mechanism present due to a stroke- and pitch-motion. This newly acquired model underlines the importance of the pitch acceleration forces for insect flight, specifically for high-frequency flappers such as the mosquito.

4.1 Introduction

Dipteran fliers flap their wings back and forth at high-frequencies to produce the required forces and torques to hover and maneuver [1]. During each back- and forth-motion (wing-beat) the wing has to be re-orientated for the next wing-beat (figure 4.1 *a*, *b*, example for the fruit fly)[2]. Apart from reversing the direction of motion of the wing, the wing is rotated around its span to attain a positive angle-of-attack for the next wing-beat. Before this reorientation the wing motion is dominated by extreme angular accelerations around its span-wise axis (figure 4.1 *i* for the fruit fly [2] and mosquito [3]). Previously, we observed that this angular acceleration has an big effect on the forces acting on the wing (chapter 2).

A systematic approach of linking the motion of the wing to the aerodynamic forces can be found in so called aerodynamic mechanisms [1], which are sometimes called phenomenology based models [4]. An aerodynamic mechanism is a link between a subset of the motion of the wing and a force generation. Aerodynamic mechanisms

are often combined into a single quasi-steady model that can be used to predict forces acting on the wing with only the use of the kinematics and wing morphology [1].

As an example of an aerodynamic mechanism, the angular velocity during mid-stroke and the high-angle-of-attack is linked to the so-called stroke-based forces (translational forces)[5]. The high-angle-of-attack in combination with the stroke rate separates the flow directly at the leading edge. The separated flow reattaches before the trailing edge, forming a leading-edge-vortex (LEV) [6]. This generation of the LEV is thought to be the main physical principle why insect can fly at such remarkably high-angles [5], [6]. A model for the stroke-based forces is based on the principle that the angular velocity of the wing causes a pressure difference between the top and bottom surface proportional to the stroke-velocity (ω_s) [5] and consequently can be written as

$$F_{sr} = \frac{1}{2}\rho C_{sr}\left(\alpha\right)\omega_s^2 \int_0^R y^2 c dy, \tag{4.1}$$

where ρ is the density of the surrounding fluid, $C_{sr}\left(\alpha\right)$ is the force coefficient as a function of the angle-of-attack α, y the coordinate along the wing span, c the local chord length, and R the length of the wing. The integral in equation (4.1) relates the wing morphology to the scaling of the forces and is known as the span-wise second moment of area S_{yy}.

Another aerodynamic mechanism links the rotation of the wing around its span at the end and start of the forward-stroke and backward-stroke (figure 4.1 *a*, *b*, *c*, *d*) to the generation an additional set of forces [7, 8, 9, 5]. These forces play an important role for maneuvering flight [2], but also play an important role for high-frequency flapping flight found in for instance mosquitoes [8]. The stroke motion of the wing in combination with the rotation around its span generates so-called stroke-pitch related forces, which can be seen as a result of an increase of circulation around the wing due to the pitching motion. Apart from this combination of the pitch-motion and stroke-motion, the pitch-motion alone also generates forces known as the pitch rate forces [7, 9]. Important for these pitch-related forces is the offset of the pitch axis with respect to the symmetry axis (chapter 2). A remarkably simple model is found to relate the forces to the kinematics and geometry of the wing is written as

$$F_p = \rho C_{pr}\left[\omega_p \omega_s \sqrt{S_{xx} S_{yy}} + \omega_p^2 S_{x|x|}\right], \tag{4.2}$$

where C_{pr}, is the rotational force coefficient, ω_p the pitch rate, S_{xx}, S_{yy} and $S_{x|x|}$ the second moment of areas (see supplementary methods, 4.7).

Even though the pitch related forces are relatively well understood, all models are based on the pitch up motion of the wing [2, 7]. The forces are assumed to behave similarly for a wing that is pitching up as it is for a wing that is pitching down. However, no systematic validation of this assumption has been carried out.

The two aforementioned models, or mechanisms, link the generation of the forces to the angular-rate, wing morphology and orientation of the wing. However, in reality the wing is not moving at a constant velocity, but is constantly changing the stroke rate and pitch rate. The effect of the change in velocity is often captured in the model known as the added mass or acceleration reaction forces. The first model already hints about the physical principle thought to be responsible for this mechanism, the acceleration of a mass of fluid around the wing [10]. This idea is captured in an equation as

$$\vec{F}_{am} = \rho V \frac{d\vec{v}}{dt}. \tag{4.3}$$

Here V is the volume of accelerated fluid and $\vec{v}$ is velocity of the fluid. A simple two dimensional model [11] is often integrated over the wing to find the effect of the wing acceleration [4, 12, 13, 14]. This integration results in

$$F_{\text{sedov},3D} = \frac{\rho\pi}{4}\left[\int_0^R \dot{\omega}_s y c(y)^2 dy + \int_0^R \Delta x \dot{\omega}_p c(y)^2 dy\right]. \tag{4.4}$$

In equation (4.4) the forces generated by the wing are again linked to the kinematics of the wing and the geometry and suggest a linear dependence of the forces on the stroke-acceleration (first term) and pitch-acceleration (second term). In this study, we focused on the pitch motion of the wing, and therefore ignored the first term in equation (4.4).

When we combine the model for the pitch rate forces (equation (4.2)) with the pitch acceleration forces (last term equation (4.4)) we should be able to predict all the forces associated with a pitching wing. However, it is unclear if these two aerodynamic mechanisms influence each other. Furthermore, to our knowledge no systematic validation of equation (4.4) is presented in literature. And lastly, there appears to be no convergence on the choice of geometrical scaling used for this model, for example in the scaling the offset Δx is sometimes ignored in favor of a scaling based

on the chord length [9].

In this study, we will limit our attention to all forces associated with a pitching motion of the wing. To accomplish this, we designed four distinct wing kinematics which enabled us to differentiate between a wing that is pitching up, and pitching down, accelerating and decelerating. With the use of computational fluid dynamics (CFD) solver based on the immersed boundary methods (IBAMR) [15], we systematically varied the kinematics over a large parametric space. The kinematics of the fruit fly (*Drosophila hydei*)[2] and malaria mosquito (*Anopheles coluzzii*)[3] largely fall within the simulated parametric space. Apart from systematically changing the wing kinematics, we also varied the wing morphology with the inclusion of seven different wing morphologies. Two of these wing morphologies are based on insects, and five wing morphologies are generic elliptical wings.

The inclusion of the four kinematic cases, and seven wing morphologies has the disadvantage of becoming complex and difficult to comprehend. Therefore, we included road map (see section 4.2.7 figure 4.4). The advantage of this approach is that we where able to explicitly test the interaction between different aerodynamic mechanisms, test the difference between a wing that is pitching up or down, test the difference between an accelerating and decelerating wing, and finally test the effect of the wing morphology on the forces. At the end of our study (section 4.3.3), we applied our newly constructed model to the kinematics of the fruit fly and mosquito. Especially for the mosquito, the forces due to the pitch motion of the wing play an important role in the generation of lift and drag.

4.2 Material & methods

4.2.1 Nomenclature

Here we will look at the effect of the pitch-acceleration on the other known aerodynamic mechanisms found in insect flight. In line with previous studies on pitch-rate aerodynamic mechanisms we will focus only on the forces perpendicular to the wing-surface [7, 9, 5]. We based the name of the aerodynamic mechanism on the motion to which it is related. For instance, stroke-rate forces is based on the ”stroke-rate” motion of the wing. Sometimes such a naming scheme is impractical, for instance when we want to discuss all the forces associated with a pitching moment. In such a case, we named the forces after the motion itself, e.g. pitch-based forces. The total

forces F_t are the sum of the stroke-based forces F_s and the pitch based forces F_p

$$F_t = F_s + F_p. \tag{4.5}$$

We defined a generic model that captures the influence of the stroke-rate ω_s, pitch-rate ω_p and pitch-acceleration $\dot{\omega}_p$ on the pitch-based forces F_p

$$F_p = F_{pr} + F_{pa} + F_{sr-pr} + F_{sr-pa} + F_{pr-pa} + F_{pr-sr-pa}, \tag{4.6}$$

where F_{pr} are the pitch-rate forces, F_{pa} the pitch-acceleration forces, F_{sr-pr} the stroke-pitch-rate interaction forces, F_{sr-pa} the stroke-rate pitch-acceleration interaction forces, F_{pr-pa} the pitch-rate interaction forces and $F_{pr-sr-pa}$ the pitch-stroke rate interaction forces.

4.2.2 Numerical setup

All the simulations in this study were carried out with the immersed boundary methods solver IBAMR [15], on a Cartesian grid with adaptive mesh refinement. We chose a domain of 5 cm x 5 cm x 5 cm with a periodic boundary conditions on the walls and on the wing we used a no-slip boundary condition. The mesh- and time-step were chosen at $\Delta x = 0.01$ mm and $\Delta t = 1 \cdot 10^{-7}$ s, which led to a mesh with approximately four million cells and twelve thousand time-steps. The solver was validated in a previous study [7].

4.2.3 Wing morphology

We varied the wing-morphology to determine the geometrical scaling parameter in our model. Two wing morphologies were based on insects, namely the wing of the fruit fly [2] and the mosquito [3]. The mosquito combines a high-frequency (600 s^{-1}), low-amplitude (40°) kinematics with a slender wing (figure 4.2 *f*), whereas the frequency of the fruit fly is considerable lower (190 s^{-1}), and its wing is less slender (figure 4.2 *g*).

In addition to the two insect wings, we designed a set of 5 elliptical wings where the offset of the pitch-axis with respect to the symmetry axis (Δx, equation (4.4)) was systematically varied from 0 mm to 0.4 mm. These elliptical wings where designed such that the parametric space of the geometrical scaling parameters S_{yy} and $S_{x|x|}$

completely enclosed the geometrical parameters of the fruit fly and mosquito wings (figure 1h).

4.2.4 Reference frames

The motion of the wing (kinematics) were defined in the right-handed world-reference-frame with the origin placed at the root of the wing(figure 4.1 *c*). The stroke-angle γ was defined around the *z*-axis of the world-reference-frame and the pitch-angle ϕ around the *y*-axis of the wing-reference-frame (figure 4.1 *c*, *y*). Because the kinematics (see section 4.2.5) did not have any out of plane motion the angle-of-attack and pitch-angle are the same, we therefore chose to name the pitch-angle as the angle-of-attack.

The forces were computed in the world-reference-frame and then transformed to the right-handed wing-reference-frame. The wing-reference-frame is attached a reference frame attached to the wing with the *x*-axis parallel to the wing surface, pointing from the leading-edge towards the trailing-edge. The *y*-axis is parallel to the wing surface pointing from the root of the wing towards the tip of the wing. The *z*-axis was defined perpendicular to the wing surface. As a result the forces along the *x*- and *y*-axis of the wing-reference frame are only viscous forces, the forces on the wing along the *z*-axis are only pressure forces.

4.2.5 Kinematic setup

We used four distinct cases: pitching up and accelerating up ($\omega_p > 0, \dot{\omega}_p > 0$), pitch up accelerating down ($\omega_p > 0, \dot{\omega}_p < 0$), pitching down and accelerating down ($\omega_p < 0, \dot{\omega}_p < 0$) and pitch-down and accelerating up ($\omega_p < 0, \dot{\omega}_p > 0$) (figure 4.3 *a–d*). For each of these different cases we designed the wing motion (kinematics) such that the force due to pitch-acceleration could be separated from the other forces.

The first case (I figure 4.3 *a*) requires the wing to have a positive pitch rate (ω_p) and positive pitch acceleration $\dot{\omega}_p$. The wing is first accelerated to a constant stroke-rate ω_s starting at a zero angle-of-attack. After this initial acceleration the wing is accelerated smoothly around its span to a constant pitch-acceleration (figure 4.3 *e*, *i* and *m*). The simulation is stopped if the pitch-rate became larger than 3000 rad s^{-1} or the angle-of-attack became larger than 70°.

The second case (II figure 4.3 *b*) requires the wing to have a positive pitch rate and a negative pitch acceleration. The first step is the same as in the first case. For

the second step, we increased the pitch rate to 3000 rad s^{-1} (figure 4.3 *j*). For the third step we smoothly decelerated the wing until the pitch rate became 0 rad s^{-1}.

The third case (III figure 4.3 *d*) was started at an angle-of-attack of 70°, such that the angle-of-attack remained constant throughout the wing motion (figure 4.3 *g*). After the wing reached a constant stroke rate, the pitch rate was decreased to a constant of −3000 rad/second. Finally, the wing was decelerated until it reached a pitch rate of 0 rad s^{-1} (figure 4.3 *k*).

For the forth and final case (IV figure 4.3 *c*), we started the wing at an angle-of-attack of 70°. After reaching a constant stroke rate the wing was pitched down with a constant pitch-acceleration (figure 4.3 *l*, *p*). The simulation was stopped when the wing reached a pitch rate of −3000 rad s^{-1}.

4.2.6 Parametric space

The four kinematic cases, described in the previous section, all had two input parameters that define the full kinematics: the stroke rate and the pitch acceleration. For each kinematic case we systematically varied these parameters (figure 4.1 *i*, *j*). We based the parametric space on the kinematics of the fruit fly and mosquito.

For the first kinematic case (pitch rate up, pitch acceleration up) we varied the stroke rate form 0 rad s^{-1} to 1750 rad s^{-1} with the step size 250 rad s^{-1}, and the pitch acceleration $4 \cdot 10^6$ rad s^{-2} to $2 \cdot 10^7$ rad s^{-2} with step size of $2 \cdot 10^6$ rad s^{-2}. The forces were extracted at the pitch rates in the range 500 rad s^{-1} to 2750 rad s^{-1} with a step size of 250 rad s^{-1} (see table 4.1, and figure 4.1 *i*, *j*). For this kinematic case we included all wing morphologies (see second 4.2.3, and figure 4.2).

For the second kinematic case (pitch rate up, pitch acceleration down) we used a similar parametric space as for the first case. The only difference being the pitch acceleration range, which we varied between $-2 \cdot 10^7$ rad s^{-2} to $-6 \cdot 10^6$ rad s^{-2} with a step size of $2 \cdot 10^6$ rad s^{-2} (see table 4.1, and figure 4.1 *i*, *j*). For this kinematic case we only included the fruit fly wing morphology.

For the last two cases (pitch down) we used the same range for the pitch acceleration as for case one and case two. The stroke rate is varied between 250 rad s^{-1} to 1750 rad s^{-1} with steps of 250 rad s^{-1}. We did not include the zero stroke rate, because for that kinematic there is not difference between pitch up and pitch down. For both cases the forces are extracted at pitch rates −3000 rad s^{-1} to −500 rad s^{-1} with a step size of 250 rad s^{-1} (see table 4.1, and figure 4.1 *i*, *j*).

Table 4.1: Parametric space of the four kinematic spaces.

case	geometries	ω_s [rad s^{-1}]	ω_p [rad s^{-1}]	$\dot{\omega}_p$[rad s^{-2}]
I	all	0 to 1750	500 to 2750	$4 \cdot 10^6$ to $2 \cdot 10^7$
II	fruit fly	0 to 1750	500 to 2750	$-2 \cdot 10^7$ to $-6 \cdot 10^6$
III	fruit fly	250 to 1750	−3000 to −500	$4 \cdot 10^6$ to $2 \cdot 10^7$
IV	fruit fy	250 to 1750	−3000 to −500	$-2 \cdot 10^7$ to $-6 \cdot 10^6$

4.2.7 Analysis

The four different kinematic cases in combination with seven different wing morphologies not only create a large data set, but also a complex one. To aid the reader through the rest of this study we created a road map (figure 4.4). As an input for analysis we start with the four kinematic cases for the fruit fly wing morphology. For each simulation in these kinematic cases we obtained the forces in the world reference frame (see section 4.2.4).

The goal of the first step of our analysis (i, figure 4.4)is to obtain the relation between the pitch based forces F_p and the stroke rate ω_s for both a wing pitching up and down. To accomplish this, we first rotated the forces of each simulation from the world reference frame to the wing reference frame. Then we subtracted the stroke based forces (F_{sr}), which where computed using a previously obtained model (see chapter 3). For each simulation, we then obtained the forces at specific pitch rates (see section 4.2.6). The forces of all simulations with the same pitch acceleration where grouped by the pitch rate and plotted against the stroke rate (see section 4.3.1).

In the second step (ii, figure 4.4, section 4.3.1), we wanted to obtain the relation between the pitch motion and the force generation in absence of a stroke motion. We did this in a similar way as our previous study on this subject [7], where we used the intercept of the relation between the stroke rate and the pitch based forces. In section 4.3.1 we used this intercept (B_{pr}) to find the pitch rate forces F_{pr} and the pitch acceleration forces F_{pa} (equation (4.6)).

In the third step (iii, figure 4.4 section 4.3.1), we quantified the interaction between the stroke motion and the pitch motion for a wing that was pitching up. For this we took the slope ($A_{pr,u}$) of the linear relation found between the pitch based forces and the stroke rate (see section 4.3.1). At the end of this step we obtained the stroke-pitch interaction forces F_{sr-pr}, stroke-pitch acceleration interaction forces F_{sr-pa}) and the interaction term $F_{sr-pr-pa}$ for a wing that is pitching up. We re-

peated this step for the wing that is pitching down in the fourth step (iv, figure 4.4, section 4.3.1) and obtained the same terms as for the third step.

In the fifth step, we included the effect of changing the wing morphology (v, figure 4.4, section 4.3.2). For this, we repeated all the steps of the first step for each wing morphology. From this additional set of simulations, we obtained the geometrical scaling for a wing that is pitching up and accelerating up.

4.3 Results

In this study, we looked at four different kinematic cases for the *fruit fly* wing morphology. For one of these kinematic cases we included a total of six additional wing morphologies (case I). In section 4.3.1 and section 4.3.2, we will uses these kinematic cases and different wing morphologies to derive a model for the pitch based forces. Figure 4.4 and section 4.2.7 serve as a road map throughout these two sections. In section 4.3.3 we will apply the newly found model for the pitch based forces to the kinematics and morphology of the fruit fly [2] and mosquito [3].

4.3.1 Forces

The total forces for each simulation consist of the summation of the forces of two aerodynamic mechanisms: the stroke-based forces and the pitch-based forces (equation (4.5)). The forces due to the stroke-motion in absence of pitch-motion was known from a previous study (see chapter 3). Therefore the forces were simply determined as

$$F_p = F_t - F_s. \tag{4.7}$$

The resulting pitch-based forces F_p are extracted at a range of given pitch-rates (see figure 4.5 *a* for an example). This step enabled us to compare the forces at the same pitch rate and stroke rate, but with different pitch-accelerations. The second step is to group the forces by the same pitch-rate and plot the forces against the stroke rate (figure 4.5 *b*, for an example). The example (figure 4.5 *b*) shows a clear linear relation of the pitch-based forces with the stroke rate. Furthermore, the higher the pitch-rate the higher the forces become, without violating this linear relation.

Effect of the stroke motion

We repeated the steps discussed in section 4.3.1 for all 4 kinematic cases for the fruit fly wing kinematics. The resulting forces due to a pitch-up acceleration are presented in figure 4.6 and due to a pitch-down acceleration in figure 4.7. This is step i, in figure 4.4.

The forces due to a pitch-up motion, all show a linear relation with the stroke rate, irrespective of the direction of the pitch-acceleration (pink lines in figure 4.6 and 4.7). However, when the wing is pitching down the relation is no longer linear (purple lines in figure 4.6 and 4.7). For lower stroke rates (up to $\omega_s = 1000\,\mathrm{rad\,s^{-1}}$) it appears that the pitch-based forces are suppressed. The decay of the pitch-based forces for a wing pitching down appears to be higher after $\omega_s = 1000\,\mathrm{rad\,s^{-1}}$. To capture the relation between the pitch-based forces and the stroke rate ω_s we moddeled the pitch-up and pitch-down separately

$$F_p = \begin{cases} \rho\left(A_{pr,u}\omega_s + B_{pr}\right) & \omega_p > 0 \\ \rho\left(A_{pr,d}\omega_s^2 + B_{pr}\right) & \omega_p < 0 \end{cases}, \tag{4.8}$$

where the three coefficients $A_{pr,u}$, $A_{pr,d}$ and B_{pr} are dependent on the pitch rate and pitch acceleration. The term B_{pr} models the force that is independent of the stroke motion of the wing.

Effect of the pitch motion

We are at step (ii) in our road map (figure 4.4). The coefficient B_{pr} is the intercept of the lines in figure 4.6 and figure 4.7. This intercepts B_{pr} increases with increasing pitch rate for a wing pitching down or up (figure 4.8 *a*). We grouped all the intercept which were based on simulations with the same pitch-acceleration (figure 4.8 *a*). In this last step the variation of the pitch-acceleration was removed within a subset, because each force is based on the same pitch acceleration. We estimated the dependence of B_{pr} on the pitch rate with a third order polynomial

$$B_{pr} = a_{pa}\omega_p^3 + b_{pa}\omega_p + c_{pa}. \tag{4.9}$$

The three coefficients a_{pa}, b_{pa} and c_{pa} are determined from fitting equation (4.9) to the data in figure 4.8 *a*. All three coefficients show a variation with the pitch acceleration

(figure 4.8 *b – d*).

It is difficult to asses the effect of this variation on the forces acting on the wing. Therefore, we computed the forces of each individual term in equation (4.9) based on the average, minimum and maximum coefficient (figure 4.8 *e–g*). The first two coefficients a_{pa} and b_{pa} show little variation in the forces between the minimum and maximum coefficient. Therefore, we assumed that the two coefficients are constant and took the value at the average. The last coefficient does show a large variation due to the change in pitch acceleration. We estimated the dependence of the coefficient c_{pa} with a simple linear function.

Turning to our generic model (equation (4.6)), we can identify the pitch rate forces F_{pr} and the pitch acceleration forces F_{pa}

$$F_{pr} = \rho \left(a_{pa} \omega_p^3 + b_{pa} \omega_p \right) \tag{4.10}$$

$$F_{pa} = \rho \left(\hat{c}_{pa} \dot{\omega}_p \right). \tag{4.11}$$

The pitch rate interaction forces F_{pr-pa} are zero because we assumed that the two coefficients a_{pa} and b_{pa} are not dependent on the pitch acceleration. For the fruit fly, we determined the coefficients $a_{pa} = 1.35 \cdot 10^{-16}\,\mathrm{N\,s^3\,m^3\,kg^{-1}}$, $b_{pa} = 2.01 \cdot 10^{-9}\,\mathrm{N\,s\,m^3\,kg^{-1}}$ and $\hat{c}_{pa} = 6.82 \cdot 10^{-13}\,\mathrm{N\,s^2\,m^3\,kg^{-1}}$ (see table 4.2).

Interaction with the stroke motion: pitch up

Now we will turn to step (iii) in our road map (figure 4.4). The interaction of the pitch based forces with the stroke rate motion is modeled with the terms $A_{pr,u}$ and $A_{pr,d}$ in equation (4.8). Because the pitch-up motion and the pitch-down motion both have a different interaction with the stroke rate we will discuss them separately. In this section, we will focus on the model for a wing that is pitching up, and in section 4.3.1 on a wing that is pitching down.

The dependence of the stroke interaction on the pitch rate for a wing pitching up is approximated with a second order polynomial (figure 4.9 *a*)

$$A_{pr,u} = d_{pr,u} \omega_p^2 + f_{pr,u} \omega_p + g_{pr,u}, \tag{4.12}$$

where the coefficients $d_{pr,u}$, $f_{pr,u}$ and $g_{pr,u}$ show a variation with the pitch acceleration (figure 4.9 *b–d*). For the first two coefficients $d_{pr,u}$ and $f_{pr,u}$ there appears to be a clear distinction between a accelerating wing and decelerating wing (disconti-

nuity around zero figure 4.9 *b*, *c*). For the last term there is a larger variation for a decelerating wing than for an accelerating wing (figure 4.9 *d*).

Like we did for the for the coefficient B_{pr} we estimated the contribution of each term in equation (4.12) to the total forces. Because equation (4.12) needs to be multiplied with the stroke rate to find the forces we chose a stroke rate of $\omega_s = 1000\,\mathrm{rad\,s^{-1}}$ as reference value. For the first coefficients we modeled the acceleration and deceleration separately (figure 4.9 *e*,*f*). When the acceleration and deceleration are modeled separately the two first coefficients show almost no variation with the pitch acceleration. Therefore, we estimated the two coefficients $d_{pr,u}$ and $f_{pr,u}$ to be constant. The last term $g_{pr,u}$ has an average value around zero (figure 4.9 *g*) and its variation has little effect on the forces. For these reasons we assumed that the last term of equation (4.12) can be ignored.

From the analysis given above, we may assume that the interaction with the stroke motion is only dependent on the pitch rate for a wing that is pitching up. This means that the only forces that model this interaction are the stroke pitch interaction forces F_{sr-pr} (equation (4.6)). Thus, all other forces that represent an interaction with the stroke motion are assumed to be zero: $F_{sr-pa} = 0$, $F_{sr-pr-pa} = 0$.

Interaction with the stroke motion: pitch down

Here we will discuss step (iv) from our road map (figure 4.4). The pitch-down motion of the wing (second part equation (4.8)) was analyzed similar to the pitch up motion. First the relation between the coefficient $A_{pr,d}$ and the pitch rate ω_p was estimated by a second order polynomial

$$A_{pr,d} = d_{pr,d}\omega_p^2 + f_{pr,d}\omega_p + g_{pr,d}, \tag{4.13}$$

where the coefficients $d_{pr,d}$, $f_{pr,d}$ and $g_{pr,d}$ are estimated from the fitting equation (4.13) to the data (figure 4.10 *a*, *b* for deceleration and acceleration respectively). All three coefficients vary with the pitch acceleration (figure 4.10 *c*–*e*).

We estimated the effect of this variation similar to what we did previously for the pitch-up motion. The only difference being that we took the first two terms of equation (4.13) together. We did this because part of the variation of one term is canceled by the other term. The variation of the first two terms ($d_{pr,d}\omega_p^2 + f_{pr,d}\omega_p$) was estimated for a stroke rate of $\omega_s = 1000\,\mathrm{rad\,s^{-1}}$ (figure 4.10 *f* acceleration, *g* deceleration). Both the acceleration and the deceleration show little variation with

pitch acceleration. Therefore, both the coefficients $d_{pr,d}$ and $f_{pr,d}$ are taken constant for acceleration and deceleration.

The last term $g_{pr,d}$ does show a big variation for the a decelerating wing (figure 4.10 *e* right side). In contrast, for an accelerating wing the pitch acceleration has little influence on this term (figure 4.10 *e* left side). Therefore, we assumed that $g_{pr,d}$ for an accelerating wing that is pitching down is zero. The relation between $g_{pr,d}$ for a decelerating wing was estimated with the a simple linear function (figure 4.10 *e*).

For a wing that is pitching down, the same interaction term as for a wing that is pitching up is identified (F_{sr-pr} equation (4.6)).

Summary of the pitch acceleration model for the fruit fly

In the previous two paragraphs, we obtained a model that describes the forces due to a pitch motion for the fruit fly wing morphology as

$$F_p = \begin{cases} \rho\left[\left(d_{pr,u}\omega_p^2 + f_{pr,u}\omega_p\right)\omega_s + a_{pa}\omega_p^3 + b_{pa}\omega_p + \hat{c}_{pa}\dot{\omega}_p\right] & \omega_p > 0 \\ \rho\left[\left(d_{pr,d}\omega_p^2 + f_{pr,d}\omega_p + \hat{g}_{pr,d}\dot{\omega}_p\right)\omega_s^2 + a_{pa}\omega_p^3 + b_{pa}\omega_p + \hat{c}_{pa}\dot{\omega}_p\right] & \omega_p < 0, \dot{\omega}_p > 0 \\ \rho\left[\left(d_{pr,d}\omega_p^2 + f_{pr,d}\omega_p\right)\omega_s^2 + a_{pa}\omega_p^3 + b_{pa}\omega_p + \hat{c}_{pa}\dot{\omega}_p\right] & \omega_p < 0, \dot{\omega}_p < 0 \end{cases}. \tag{4.14}$$

The coefficients for each of these equations are presented in table 4.2. Apart from the total representation of the forces we splitted the forces into their respective aerodynamic mechanism based on the wing kinematics they relate to based on equation (4.6). The forces that are purely dependent on the pitch motion are written as

$$F_{pr} = \rho\left[a_{pa}\omega_p^3 + b_{pa}\omega_p\right] \tag{4.15}$$

$$F_{pa} = \rho\hat{c}_{pa}\dot{\omega}_p. \tag{4.16}$$

Furthermore, the forces that are dependent on the interaction between the stroke rate and pitch rate are written as

$$F_{sr-pr} = \begin{cases} \rho\left[d_{pr,u}\omega_p^2\omega_s + f_{pr,u}\omega_p\omega_s\right] & \omega_p > 0 \\ \rho\left[d_{pr,d}\omega_p^2\omega_s^2 + f_{pr,d}\omega_p\omega_s^2\right] & \omega_p < 0 \end{cases}. \tag{4.17}$$

Lastly, an interaction between the stroke rate and the pitch acceleration is identi-

fied for a wing that is pitching down and decelerating that can be written as

$$F_{pa-sr} = \begin{cases} \rho \hat{g}_{pr,d} \dot{\omega}_p \omega_s^2 & \omega_p < 0, \dot{\omega}_p > 0 \\ 0 & \text{otherwise} \end{cases}. \tag{4.18}$$

Table 4.2: Coefficients of the pitch based model for the fruit fly wing morphology

	$\dot{\omega}_p < 0$	$\dot{\omega}_p > 0$	
a_{pa}			$1.35 \cdot 10^{-16}$ N s^3 m^3 kg^{-1}
b_{pa}			$2.01 \cdot 10^{-9}$ N s m^3 kg^{-1}
$\hat{c}_{pa}$			$6.82 \cdot 10^{-13}$ N s^2 m^3 kg^{-1}
pitch down $\omega_p < 0$			
$d_{pa,d}$	$3.58 \cdot 10^{-19}$ Ns^5 m^3/kg	$3.09 \cdot 10^{-20}$ Ns^5 m^3/kg	
$f_{pa,d}$	$2.45 \cdot 10^{-15}$ N s^2 m^3 kg^{-1}	$1.69 \cdot 10^{-15}$ N s^2 m^3 kg^{-1}	
$\hat{g}_{pa,d}$	$-1.83 \cdot 10^{-19}$ Ns^4 m^3/kg	-	
pitch up $\omega_p > 0$			
$d_{pa,u}$	$-1.55 \cdot 10^{-16}$ Ns^4 m^3/kg	$5.07 \cdot 10^{-16}$ Ns^4 m^3/kg	
$f_{pa,u}$)	$2.09 \cdot 10^{-12}$ N s^2 m^3 kg^{-1}	$5.21 \cdot 10^{-12}$ N s^2 m^3 kg^{-1}	

4.3.2 Geometrical scaling

We are now at the last step of our roadmap (step (v), figure 4.4). For a subset of the kinematic cases we included six additional wing morphologies (figure 4.2 *a*). We repeated the analysis we did for the fruit fly wing morphology for these wings. For a complete overview of the forces as a result of the simulation of these morphologies refer to appendix 4.8 and 4.9.

For each wing morphology, we extracted the two coefficients $A_{pr,u}$ and $B_{pr,u}$ (figure 4.11). The coefficient $A_{pr,u}$ shows a quadratic relation with the pitch rate, similar to the relation for the fruit fly (equation (4.12)). We assumed that the two fitting coefficients $d_{pr,u}$ and $f_{pr,u}$ are independent of the pitch acceleration for all wing morphologies. The coefficient $d_{pr,u}$ is scaled with the scaling parameter $S_{x|x|}\sqrt{S_{yy}}$ (figure 4.12 *a*) and the coefficient $f_{pr,u}$ with the span-wise second moment of area S_{yy} (figure 4.12 *b*).

The coefficient B_{pr} has a similar relation with the pitch rate as found before for the fruit fly (equation (4.9), figure 4.11 *h–n*). We assumed that the first two coefficients of equation (4.9) (a_{pa} and b_{pa}) are independent of the pitch acceleration. We scaled both of these coefficients with the asymmetric second moment of area $S_{x|x|}$ (figure 4.12 *c*,

d). We approximated the dependence of the coefficient c_{pa} on the pitch acceleration with a simple linear relation $c_{pa} = \hat{c}\dot{\omega}_p$. The fitting parameter $\hat{c}_p$ is scaled with the asymmetric second moment of area $S_{x|x|}$ (figure 4.12 *f*). Finally, the normalized values for c_{pa} all fall approximately on a single line (figure 4.12 *g*). We did omit the result for the symmetric wing, because $c_{pa} \approx 0$ and the asymmetric second moment of area $S_{x|x|} = 0\,\text{mm}^4$.

With this newly found geometrical scaling we are able to write the model for the fruit fly (section 4.3.1) independent of the wing shape

$$F_{sr-pr} = \rho \left[d^*_{pr,u} \omega_p^2 \omega_s S_{x|x|} \sqrt{S_{yy}} + f^*_{pr,u} \omega_p \omega_s S_{yy} \right] \quad \omega_p > 0 \quad \dot{\omega}_p > 0 \tag{4.19}$$

$$F_{pr} = \rho S_{x|x|} \left[a^*_{pa} \omega_p^3 + b^*_{pa} \omega_p \right] \quad \omega_p > 0 \quad \dot{\omega}_p > 0 \tag{4.20}$$

$$F_{pa} = \rho \left[\hat{c}^*_{pa} \dot{\omega}_p S_{x|x|} \right] \quad \omega_p > 0 \quad \dot{\omega}_p > 0. \tag{4.21}$$

However, the geometrical scaling is only computed for a wing that is pitching and accelerating up. Therefore, the geometrical scaling for the stoke pitch acceleration interaction F_{pa-sr} (equation (4.18)) could not be determined.

4.3.3 Application of the pitch-acceleration model

We applied the model found in section 4.3.1 to the wing kinematics of the fruit fly and mosquito (figure 4.13). Because we used equations that are discontinuous around zero for the stroke pitch interaction forces (F_{sr-pr}, equation (4.17)) and the stroke pitch acceleration interaction forces (F_{sr-pa}, equation (4.18)), the resulting forces also show discontinuities (figure 4.13 *e*, *g*).

We determined the lift and drag relative to the direction of motion of the wing. The lift is defined perpendicular to the velocity vector, and the drag parallel to the velocity vector. A negative drag therefore means that the drag and velocity are pointed in the same direction. The pitch rate ω_p and pitch acceleration $\dot{\omega}_p$ were also defined relative to the direction of motion.

For the fruit fly, the stroke rate forces dominate the pressure forces (figure 4.13 *e*). The wing-beat averaged forces show a similar pattern, where only a small part of the forces is generated due to the pitch motion (figure 4.13 *f*). For the lift and drag, a similar pattern is observed. However, for the mosquito the stroke rate forces play a less prominent role, contributing only half of the total forces (figure 4.13 *h*). This pattern is also observed for the lift and drag forces of the mosquito (figure 4.13 *k*, *l*,

o, *p*).

For both insects, the forces associated with the pitch rate of the wing cause a reduction in lift. This reduction of lift is related to the pitch down motion of the wing directly after stroke reversal. Interestingly, this pitch down motion also causes a negative contribution to the drag (figure 4.13 *m*, *o*). This negative drag can be seen as a "thrust" force, that aids the acceleration of the wing directly after stroke reversal.

The negative dip in lift due to the forces associated with the pitch rate (F_{pr} and F_{sr-pr}) is compensated by a positive contribution due to the pitch acceleration forces (F_{pa}). For the mosquito, the pitch acceleration forces remain present in the lift forces throughout the wingbeat (figure 4.13 *k*). For the fruit fly, the pitch acceleration forces are almost non-existent after mid-stroke of both the forward-stroke and backward-stroke (figure 4.13 *i*). Therefore, it will not come as a surprise that in the averaged lift forces this force component (F_{pa}) almost has no influence on the total forces for the fruit fly. On the other hand, for the mosquito these forces add up to approximately 40 % (figure 4.13 *l*). In the drag forces, the pitch acceleration component plays a smaller role (figure 4.13 *p*).

4.4 Discussion

4.4.1 Our model

From 612 simulations with four different kinematic cases and seven different wing morphologies, we obtained a new model for the forces associated with the pitch motion of the wing. This model is able to predict the forces associated with a pitching wing with non constant pitch rate.

Our model is the most complete description of the forces associated with the pitch motion of a flapping insect wing. We based our model of fully three-dimensional viscous flow, whereas other models often fall back to inviscid two-dimensional flow [11, 9, 13, 14]. Furthermore, we explicitly tested the interaction between aerodynamic mechanisms. Lastly, we tested the assumption that a wing that is pitching up behaves similar to a wing that is pitching down [5, 7, 9].

In our simulations, the wing had a constant pitch acceleration. This means that the pitch rate is constantly changing. We then grouped the results at certain pitch rates for different simulations together. The drawback of this analysis is that for each data point with the same pitch rate the angle-of-attack is different. In line with previous

study on this subject [5, 7], we assumed that the angle-of-attack did not have an effect on the pitch based forces. However, in future studies this assumption should be tested.

Furthermore, this analysis method also means that we assumed that the time that the flow needed to develop did not have an effect on the pitch based forces. However, it is know that the flow around a moving wing does change over time [16]. Therefore, it is unclear if in the final model the effect of flow development is implicitly modeled through the other parameters.

4.4.2 Geometrical scaling

We included an additional set of simulations to give an estimate of how the pitch based forces scale with the wing morphology. We showed that the wing asymmetry is an important factor for the generation of the pitch based forces. This result is in line with our previous study [7], where we showed the importance of the offset of the rotation axis for the pitch rate forces and stroke pitch interaction forces. In addition, the scaling of the pitch acceleration forces with this asymmetric second moment of area is in line with previous studies on added mass forces.

The geometrical scaling was obtained for simulations with a wing that was pitching up and accelerating up. For the application of our model (section 4.3.3), we assumed that this geometrical scaling could be extended towards a decelerating wing and a wing that is pitching down. Future studies should test this assumption directly by systematically varying the wing morphologies of wings that are decelerating or pitching down.

4.4.3 Stroke interaction forces: Pitch up is not pitch down

Other models that predict the forces based on a wing pitch motion often only included the effect of the stroke pitch interaction [5], or stroke pitch interaction and pitch rate forces [9] [7]. Some models that were based on a two dimensional inviscid model [11] were able to predict the pitch acceleration forces [14, 13]. However, our model is the first to explicitly study the interaction between the stroke rate, pitch rate and pitch acceleration. Furthermore, we based our model on fully three-dimensional viscous flow.

In addition, our model distinguishes between a wing that is pitching up, or pitching down. Previously it was assumed that simply mirroring the forces for a pitching up wing was enough [5, 9, 7, 2]. However, in section 4.3.1 we clearly showed that

the stroke pitch rate interaction forces do not scale linearly with the stroke rate for a wing that is pitching down, whereas for a wing that is pitching up it does. This difference mostly impacts the lower stroke rates ($\omega_s < 1000\,\mathrm{rad\,s^{-1}}$) where the forces are damped for a wing that is pitching down.

4.4.4 Pitch acceleration forces

More than anything our model underlines the importance of the pitch acceleration for insect flight. The pitch acceleration forces scale linear with the pitch accelerations, which is in accordance with the two-dimensional model [11, 13, 14, 9]. This leads to a significant contribution of the pitch acceleration forces to the transient force contribution of both the fruit fly and the mosquito. For the average of the forward-stroke and backward-stroke, the contribution of the pitch acceleration forces for the fruit fly is less pronounced. However, for the mosquito the pitch acceleration forces have a contribution almost as big as the stroke rate forces.

Surprisingly, the stroke pitch interaction forces for the fruit fly have a relative small contribution to the lift and drag forces (figure 4.13 *j*, *n*). Only for the backward stroke of the drag component the pitch stroke interaction forces have a substantial contribution compared to the pitch acceleration forces. This result is not in line with previous results [5], where the stroke pitch interaction was seen as the main contributor to the weight support after the stroke rate forces.

Something similar is observed for the mosquito, albeit more extreme. The pitch rate forces (rotational drag) was seen as the main contributor to the weight support of mosquitoes [8]. However, our results do not show the same result (figure 4.13 *l*, *p*), where the pitch rate forces almost have no contribution to the overall forces. The stroke pitch interaction forces and the pitch acceleration forces both have a major contribution to the lift and drag generation in mosquito flight.

The force generation of both the fruit fly and the mosquito clearly illustrate the importance of the pitch acceleration forces for insect flight. However, before we hail the pitch acceleration forces as the new king of aerodynamic mechanisms we should model all possible interactions and mechanism. Because, this study also shows the importance of quantifying all the aerodynamic mechanisms before pointing to a single mechanism as the ”enabler” of a insect flight.

4.5 References

[1] C. P. Ellington. “The aerodynamics of hovering insect flight. III. kinematics”. In: *Philosophical Transactions B* 305.1122 (1983), pp. 41–78. ISSN: 0080-4622.

[2] M. H. Dickinson and F. T. Muijres. “The aerodynamics and control of free flight manoeuvres in Drosophila”. In: *Philosophical Transactions B* 371.1704 (2016). DOI: 10.1098/rstb.2015.0388.

[3] F.T. Muijres, S.W. Chang, W.G. Veen, J. Spitzen, B.T. Biemans, M.A.R. Koehl, and R. Dudley. “Escaping blood-fed malaria mosqtuitoes minimize tactile detection without compromising on take-off speed”. In: *Journal of Experimental Biology* 220.20 (2017), pp. 3751–3762. DOI: 10.1242/jeb.163402.

[4] C. Zhang, T. L. Hedrick, and R. Mittal. “Centripetal acceleration reaction: An effective and robust mechanism for flapping flight in insects”. In: *Plos One* (2015). DOI: 10.1371/journal.pone.0132093.

[5] M. H. Dickinson, F. Lehmann, and S. P. Sane. “Wing rotation and the aerodynamic basis of insect flight”. In: *Science* 284.5422 (June 1999), pp. 1954–1960. DOI: 10.1126/science.284.5422.1954.

[6] C. P. Ellington, C. van den Berg, A. P. Willmott, and A. L. R. Thomas. “Leading-edge vortices in insect flight”. In: *Nature* 384.6610 (1996), pp. 626–630. DOI: 10.1038/384626a0.

[7] W. G. van Veen, J. L. van Leeuwen, and F. T. Muijres. “A chordwise offset of the wing-pitch axis enhances rotational aerodynamic forces on insect wings: a numerical study”. In: *Journal of The Royal Society Interface* 16.155 (2019), pp. 1–13. DOI: 10.1098/rsif.2019.0118.

[8] R. J. Bomphrey, T. Nakata, N. Phillips, and S. M. Walker. “Smart wing rotation and trailing-edge vortices enable high frequency mosquito flight”. In: *Nature* 554 (2017), pp. 92–95. DOI: 10.1038/nature21727.

[9] T. Nakata, H. Liu, and R. J. Bomphrey. “A CFD-informed quasi-steady model of flapping-wing aerodynamics”. In: *Journal of Fluid Mechanics* 783 (Nov. 2015), pp. 323–343. DOI: 10.1017/jfm.2015.537.

[10] T. L. Daniel. “Unsteady aspects of aquatic locomotion”. In: *American Zoologist* (1984).

[11] L. I. Sedov. *Two-Dimensional Problems in Hydrodynamics and Aerodynamics*. Interscience Publishers, 1965.

[12] L. Liu and M. Sun. "The added mass forces in insect flapping wings". In: *Journal of theoretical biology* 437 (Jan. 2017), pp. 45–50. DOI: 10.1016/j.jtbi.2017.10.014.

[13] C. K Kang, H. Aono, C. E. S. Cesnik, and W. Shyy. "Effects of flexibility on the aerodynamic performance of flapping wings". In: *AIAA* (2011).

[14] J.P. Whitney and R.J. Wood. "Aeromechanics of passive rotation in flapping flight". In: *Journal of Fluid Mechanics* 660 (2010). DOI: 10.1017/S002211201000265X.

[15] A. P. S. Bhalla, R. Bale, B. E. Griffith, and N. A. Patankar. "A unified mathematical framework and an adaptive numerical method for fluid–structure interaction with rigid, deforming, and elastic bodies". In: *Journal of Computational Physics* 250 (2013), pp. 446–476. DOI: 10.1016/j.jcp.2013.04.033.

[16] S. P. Sane. "The aerodynamics of insect flight". In: *The Journal of Experimental Biology* 206 (2003), pp. 4191–4208. DOI: 10.1242/jeb.00663.

4.6 Figures

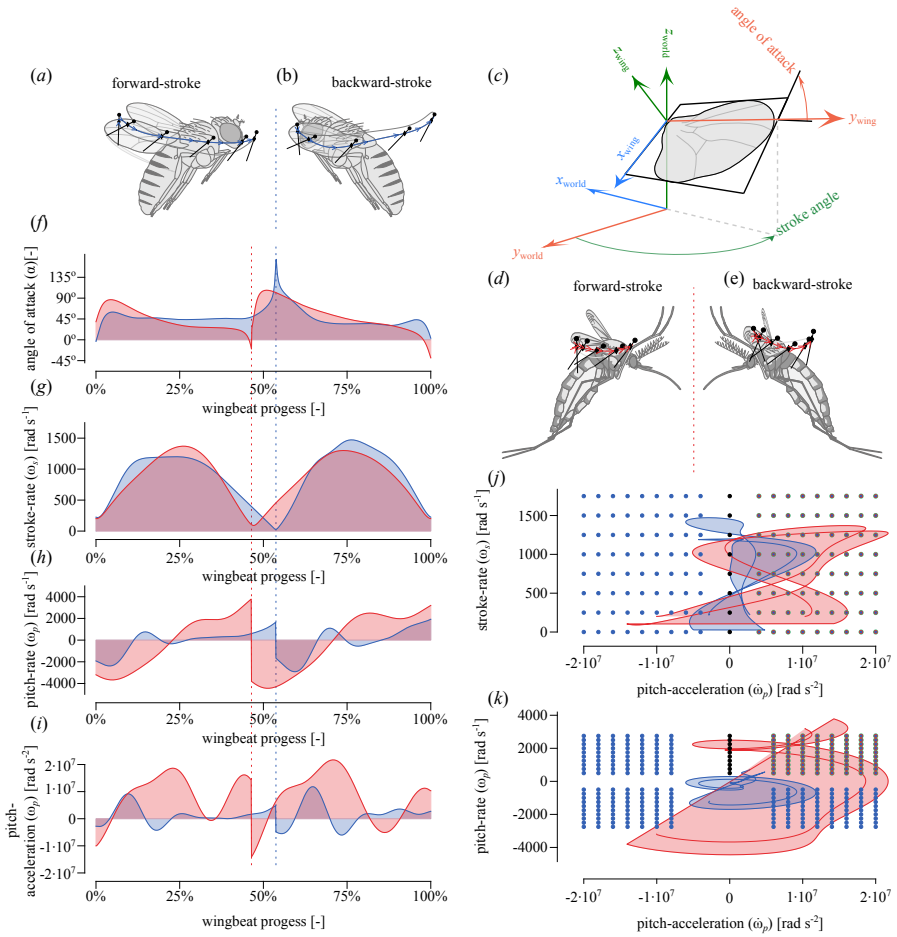

Figure 4.1: Kinematics of the fruit fly and mosquito and the parametric setup. (*a*, *b*, *d*, *e*) Schematic representation of the forward-stroke and backward-stroke of the fruit fly [2] and mosquito [3], dashed line indicates stroke-reversal. (*c*) Definition of the world-reference-frame, wing reference frame and the stroke angle and angle-of-attack. ($f-i$) Kinematics of the fruit fly (blue) and mosquito (red), angle-of-attack α, stroke-rate ω_s, pitch-rate ω_p and pitch-acceleration $\dot{\omega}_p$ respectively. (*j*, *k*) Parametric space for the fruit fly (blue shaded) and mosquito (red shaded), blue dots indicate simulations with fruit fly morphology, red dots for the mosquito morphology, green dots *ellipse* shaped morphology and black dots are results from previous study [7].

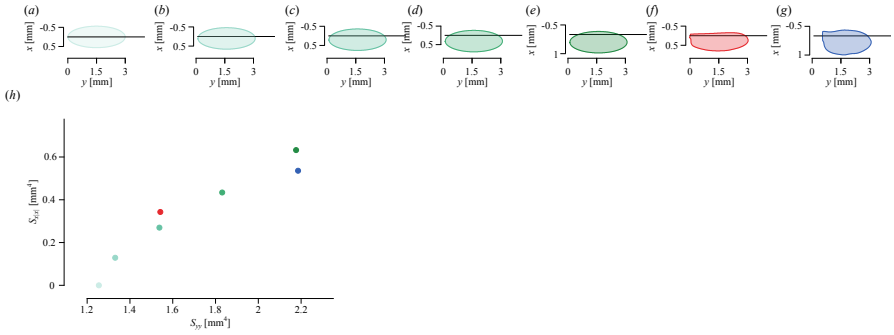

Figure 4.2: Different wing morphologies used in this study. (*a* – *e*) Elliptical wings with with a variation of the pitch axis (black line). (*f*, *g*) Wing morphology of the fruit fly [2] and mosquito [3]. (*h*) Span wise second moment of area S_{yy} against the asymmetric second moment of area ($S_{x|x|}$) for all the wings used in this study (panel *a*–*g*).

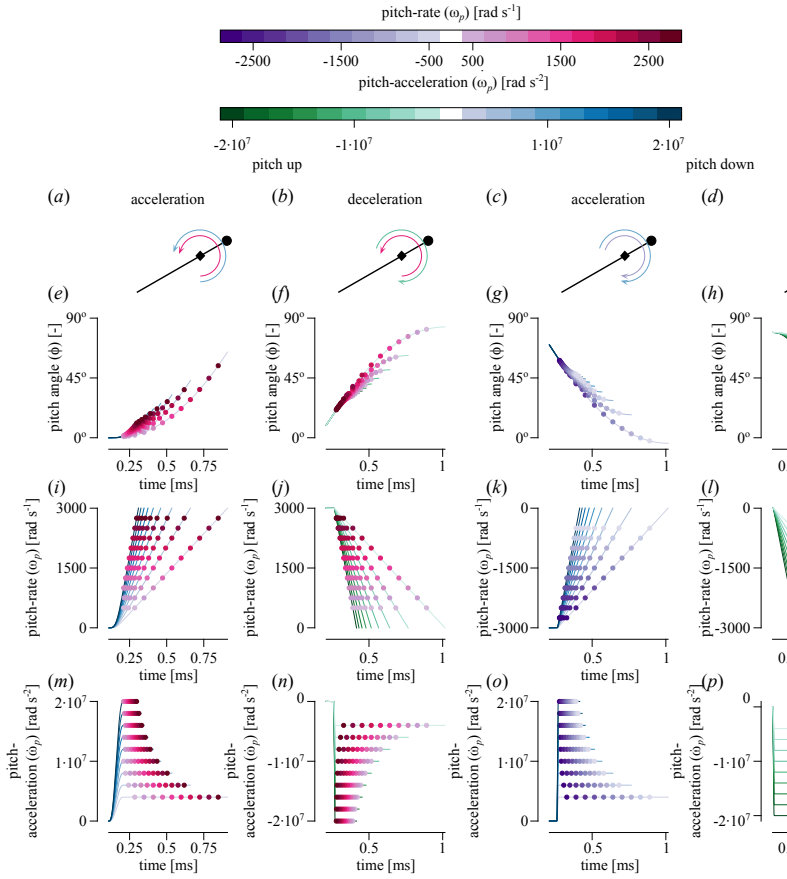

Figure 4.3: Kinematic setup divided in four different ”cases”: (*a*) pitch-up acceleration-up, (*b*) pitch-up acceleration-down, (*c*) pitch-down acceleration-up and (*d*) pitch-down acceleration-down, the dot indicates the leading-edge, diamond indicates rotation axis, outer arrow the pitch-acceleration and inner arrow the pitch-rate. (*e* – *h*) Pitch angle for each case respectively, dots indicate the extraction point. (*i* – *l*) Pitch-rate for each case respectively, dots indicate the extraction point. (*m*–*p*) Pitch-acceleration for each case respectively, dots indicate the extraction points.

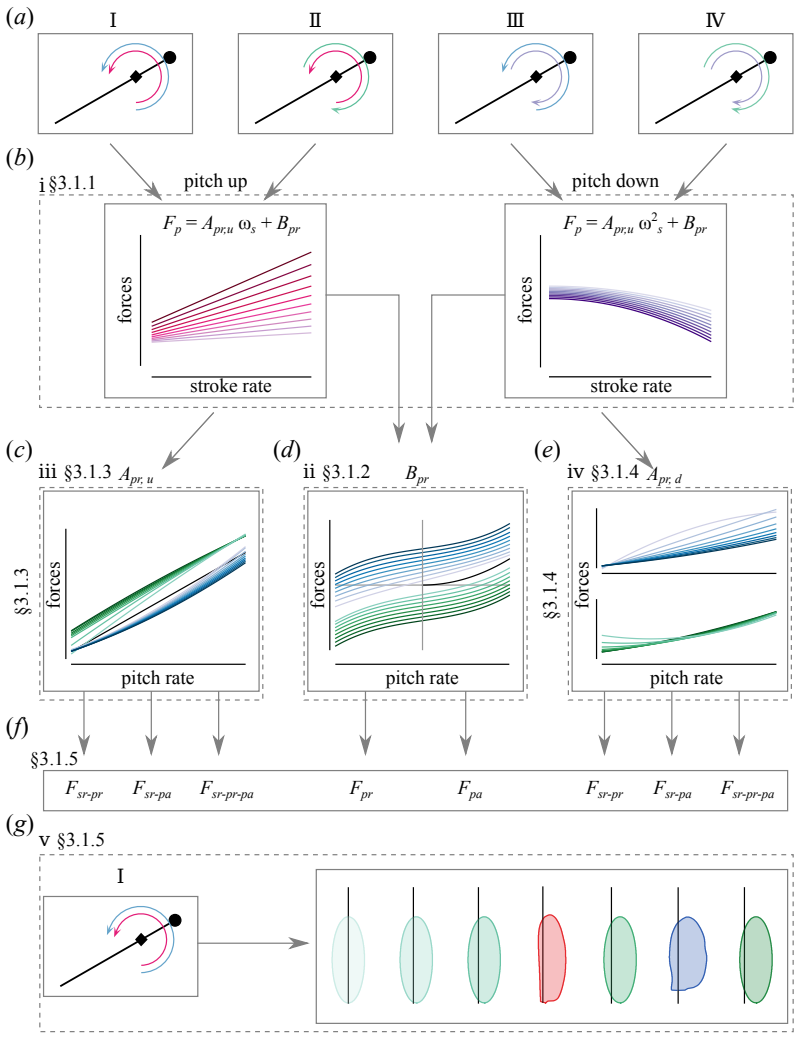

Figure 4.4: Road map for the analysis of the pitch based forces, each box has a schematic that is characteristic for the analysis step. (*a*) Setup of the four different kinematic cases (see section 4.2.5 and figure 4.3). (*b*) Analysis step to relate the pitch based forces to the stroke rate for a wing pitching up and down (see section 4.3.1, and figure 4.5, 4.6 and 4.7). (*c*) Analysis step that includes the influence of the pitch rate on the stroke pitch interaction forces for a wing that is pitching up (see section 4.3.1 and figure 4.9). (*d*) Analysis step that includes the effect of the pitch rate on the pitch based forces (see section 4.3.1 and figure 4.8). (*e*) Analysis step that includes the influence of the pitch rate on the stroke pitch interaction forces for a wing that is pitching down (see section 4.3.1 and figure 4.10). (*f*) Summary of the results for the fruit fly (see section 4.3.1). (*g*) Final step of the analysis, which includes the effect of the wing morphology variation (see section 4.3.2 and figures 4.11, 4.12).

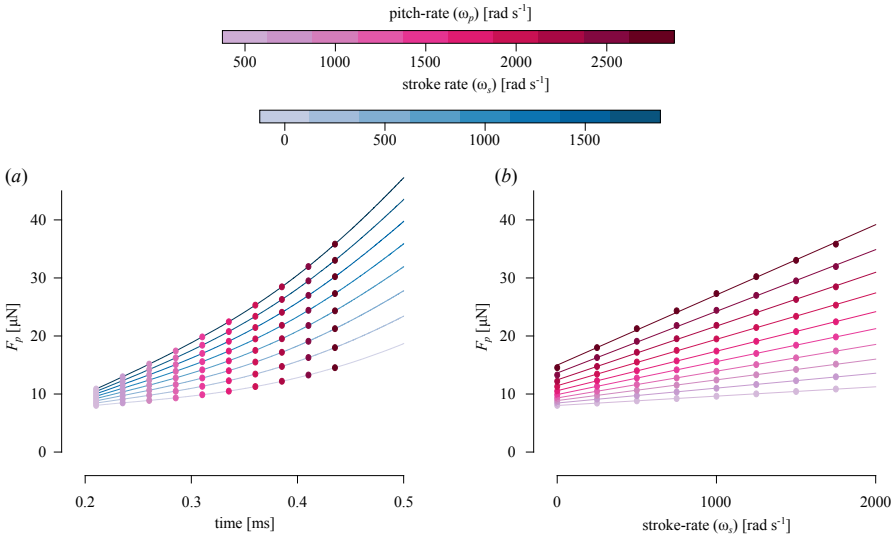

Figure 4.5: Example of the analysis with the stroke-rate $\omega_s = 0\,\mathrm{rad\,s^{-1}}$ to $1750\,\mathrm{rad\,s^{-1}}$, pitch-rate $\omega_p = 500\,\mathrm{rad\,s^{-1}}$ to $2750\,\mathrm{rad\,s^{-1}}$ and the pitch-acceleration $\dot{\omega}_p = 1 \cdot 10^7\,\mathrm{rad\,s^{-2}}$ for the fruit fly wing morphology. (*a*) Pitch-based forces F_p variation over time for a wing moving with different stroke-rates (blue), dots indicate extraction points where the pitch-rates are the same (pink). (*b*) Pitch-based forces F_p as a function of the stroke-rate ω_s for different pitch-rates (pink), lines are fits of equation (4.8).

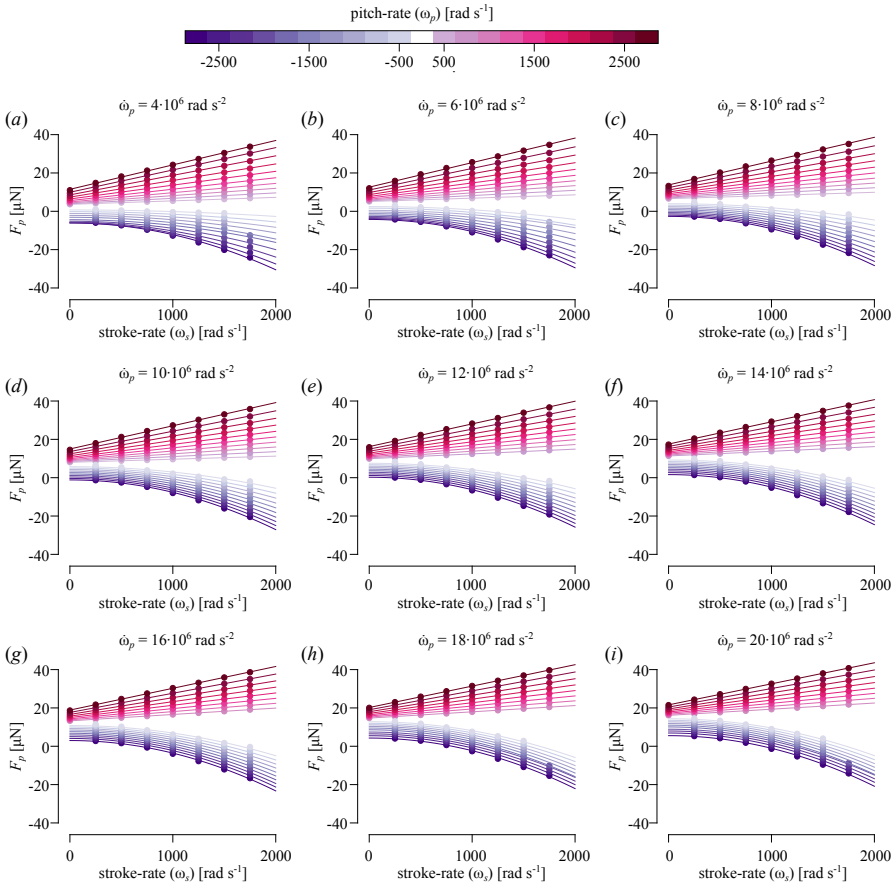

Figure 4.6: Variation of the pitch-based forces F_p for wings accelerating up while pitching up (pink dots) or down (purple dots). (*a*) $\dot{\omega}_p = 4 \cdot 10^6\,\mathrm{rad\,s^{-2}}$. (*b*) $\dot{\omega}_p = 6 \cdot 10^6\,\mathrm{rad\,s^{-2}}$. (*c*) $\dot{\omega}_p = 8 \cdot 10^6\,\mathrm{rad\,s^{-2}}$. (*d*) $\dot{\omega}_p = 1 \cdot 10^7\,\mathrm{rad\,s^{-2}}$. (*e*) $\dot{\omega}_p = 1.2 \cdot 10^7\,\mathrm{rad\,s^{-2}}$. (*f*) $\dot{\omega}_p = 1.4 \cdot 10^7\,\mathrm{rad\,s^{-2}}$. (*g*) $\dot{\omega}_p = 1.6 \cdot 10^7\,\mathrm{rad\,s^{-2}}$. (*h*) $\dot{\omega}_p = 1.8 \cdot 10^7\,\mathrm{rad\,s^{-2}}$. (*i*) $\dot{\omega}_p = 2 \cdot 10^7\,\mathrm{rad\,s^{-2}}$.

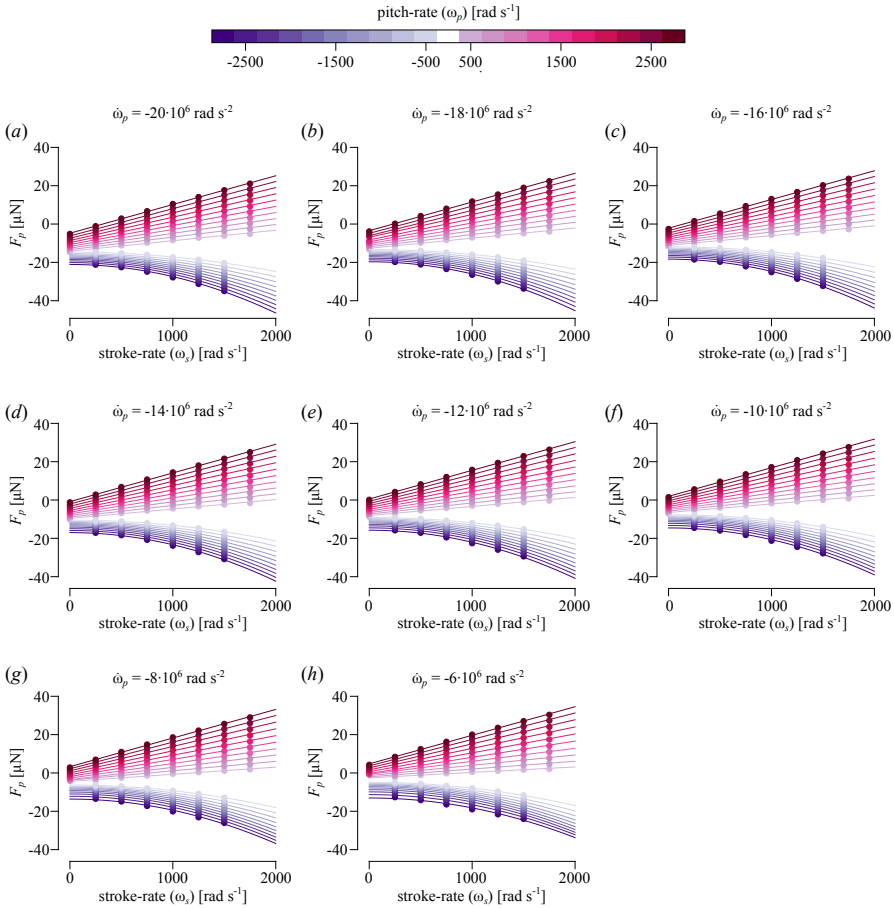

Figure 4.7: Variation of the pitch-based forces F_p for wings accelerating down while pitching up (pink dots) or down (purple dots). (*a*) $\dot{\omega}_p = -20 \cdot 10^6\,\mathrm{rad\,s^{-2}}$. (*b*) $\dot{\omega}_p = -18 \cdot 10^6\,\mathrm{rad\,s^{-2}}$. (*c*) $\dot{\omega}_p = -16 \cdot 10^6\,\mathrm{rad\,s^{-2}}$. (*d*) $\dot{\omega}_p = -14 \cdot 10^6\,\mathrm{rad\,s^{-2}}$. (*e*) $\dot{\omega}_p = -12 \cdot 10^6\,\mathrm{rad\,s^{-2}}$. (*f*) $\dot{\omega}_p = -10 \cdot 10^6\,\mathrm{rad\,s^{-2}}$. (*g*) $\dot{\omega}_p = -8 \cdot 10^6\,\mathrm{rad\,s^{-2}}$. (*h*) $\dot{\omega}_p = -6 \cdot 10^6\,\mathrm{rad\,s^{-2}}$.

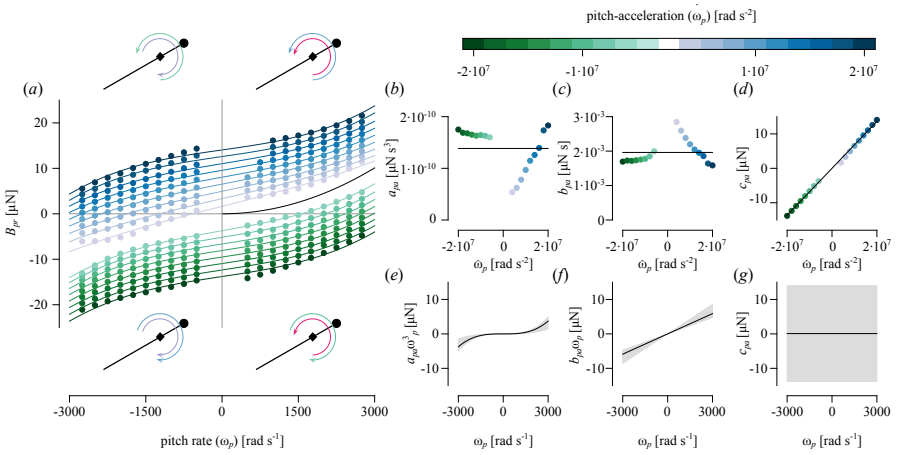

Figure 4.8: Variation of the coefficient B_{pr} with the pitch rate and pitch acceleration for the fruit fly wing morphology. (*a*) Variation of the coefficient B_{pr} of equation (4.8) with the pitch rate, curves are fitted functions (4.9), colors indicate the pitch acceleration (blue pitch-up, green pitch down), black line is the solution in absence of stroke acceleration [7]. (*b–d*) Fitting coefficients of equation (4.9) as a function of the pitch acceleration, black lines are the estimates used in our model (see section 4.3.1). (*e–g*) Amount of force generated by each term in equation (4.9), black line is based on the average coefficient, grey area is the area between the solution with the minimal and maximal coefficient.

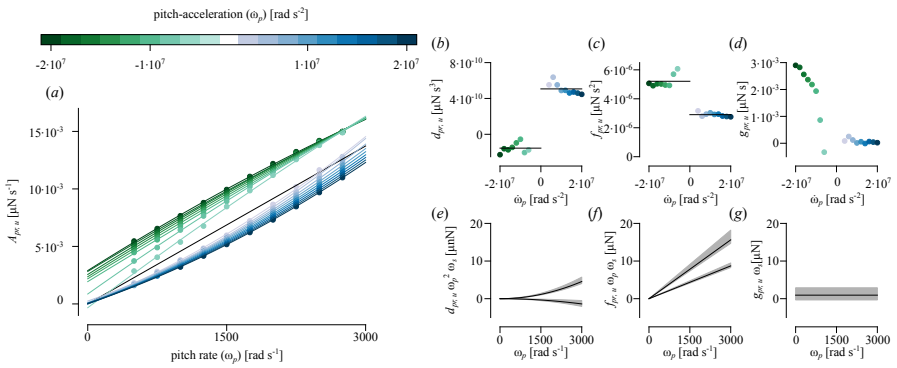

Figure 4.9: Variation of the coefficient $A_{pr,u}$ with the pitch rate, and pitch acceleration for the fruit fly wing morphology. (*a*) Variation of the coefficient $A_{pr,u}$ of equation (4.8) with the pitch rate, the lines are fits based on function (4.12), colored with the pitch acceleration. (*b–d*) Fitting coefficietns of equation (4.12) as a function of pitch acceleration, black lines are the estimates used in our model (see section 4.3.1). (*e–g*) Estimate of the forces generated by each term in equation (4.12), based on a stroke rate $\omega_s = 1000\,\mathrm{rad\,s^{-1}}$, black line is based on the average coefficient, grey area is the area between the solution with the minimal and maximal coefficient.

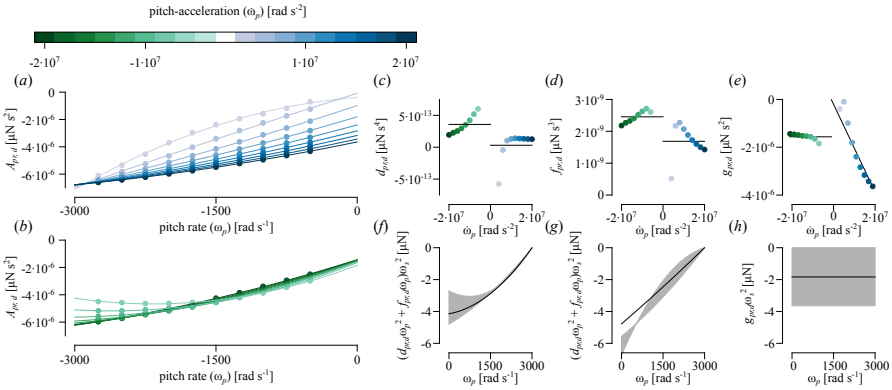

Figure 4.10: Variation of the coefficient $A_{pr,d}$ with the pitch rate, and pitch acceleration for the fruit fly wing morphology. (*a*, *b*) Variation of the coefficient $A_{pr,d}$ of equation (4.8) with the pitch rate, the lines are fits based on function (4.13), colored with the pitch acceleration for acceleration and deceleration respectively. (*c*–*e*) Fitting coefficients of equation (4.13) as a function of pitch acceleration, black lines are the estimates used in our model (see section 4.3.1). (*f*–*g*) Estimate of the first two terms in equation (4.13), for a decelerating and accelerating wing respectively, based on a stroke rate $\omega_s = 1000\,\mathrm{rad\,s^{-1}}$, black line is based on the average coefficient, grey area is the area between the solution with the minimal and maximal coefficient. (*h*) Estimate of the last term of equation (4.13), based on a stroke rate of $\omega_s = 1000\,\mathrm{rad\,s^{-1}}$, black line is based on the average coefficient, grey area is the area between the solution with the minimal and maximal coefficient.

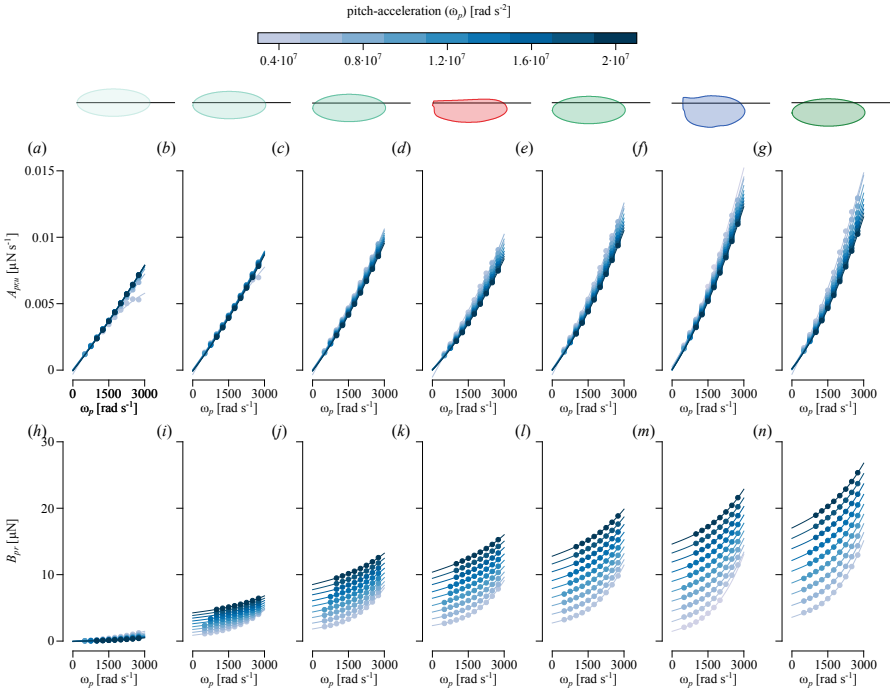

Figure 4.11: Variation of the $A_{pr,u}$ and B_{pr} coefficients for five elliptical wings, a mosquito wing and a fruit fly wing. (*a*–*g*) The coefficient $A_{pr,u}$ as a function of the pitch rate, for different pitch accelerations (blue colors) and different geometries (panels) the curves are fits based on equation (4.12). (*h*–*n*) The coefficient B_{pr} as a function of the pitch rate, for different pitch accelerations (blue colors) and different geometries (panels), the lines are fits based on equation (4.9).

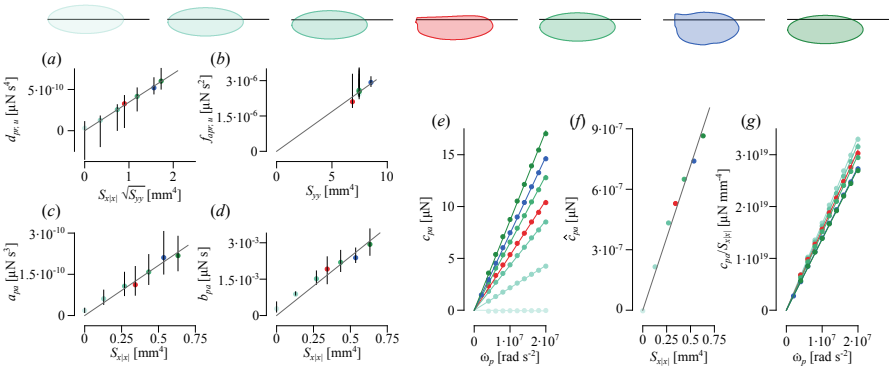

Figure 4.12: The fitting coefficients a_{pa}, b_{pa}, c_{pa} of equation (4.9), and $d_{pr,u}$, $f_{pr,u}$ of equation (4.12) for different wing morphologies (colors). (*a*) $d_{pr,u}$ as a function of the scaling parameter $S_{x|x|}\sqrt{S_{yy}}$, bars indicate minimum and maximum coefficient per wing morphology. (*b*) $f_{pr,u}$ as a function of the span-wide second moment of area S_{yy}, bars indicate the mimumum and maximum coefficient per morphology. (*c*, *d*) a_{pa} and b_{pa} as a function of the asymmetric second moment of area $S_{x|x|}$ bars indicate minimum and maximum coefficient per wing morphology. (*e*) Variation of c_{pa} with the pitch acceleration $\dot{\omega}_p$ for different wing morphologies (colors), lines are simple fits ($c_{pa} = \hat{c}_{pa}\dot{\omega}_p$). (*f*) The fitting parameter $\hat{c}_{pa}$ as a function of the asymmetric second moment of area $S_{x|x|}$. (*g*) The fitting parameter c_{pa} normalized with the asymmetric second moment of area $S_{x|x|}$ as a function of the pitch acceleration for different wing morphologies.

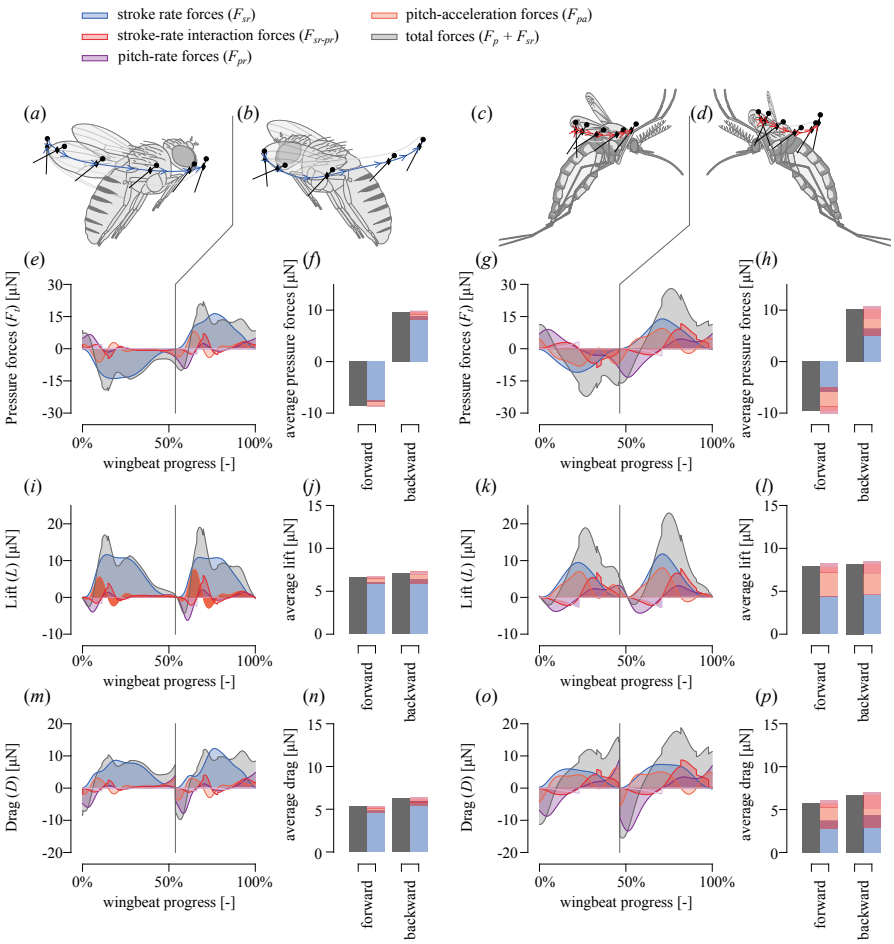

Figure 4.13: Application of the pitch-based forces to the wing-kinematics of the fruit fly [2] and mosquito [3], vertical lines are the stroke-reversal from forward-stroke to backward-stroke. (*a*, *b*) Schematic representation of the forward- and backward-stroke for the fruit fly, dot is leading edge, diamond rotation axis, blue line is path of the forward or backward stroke respectively (*c*, *d*) Schematic representation of the forward- and backward-stroke for the mosquito, diamond is rotation axis, red line is the path of the foward or backward-stroke respectively. (*e*, *g*) Predicted pressure forces based on the pitch acceleration model, forces in the wing reference frame for the fruit fly and mosquito respectively. (*f*, *h*) Wingbeat averaged pressure force components for the fruit fly and mosquito respectively. (*i*, *k*) Components of the lift forces of the fruit fly and mosquito respectively. (*j*, *l*) Wingbeat averaged lift components of the fruit fly and mosquito respectively. (*m*, *o*) Components of the drag forces of the fruit fly and mosquito respectively. (*n*, *p*) Wingbeat averaged drag components of the fruit fly and mosquito respectively.

Supplementary methods

4.7 Definitions

Table 4.3: List of symbols

Symbol	unit	Description
α	-	Angle-of-attack
a_{pa}, b_{pa}, c_{pa}	N m^3 kg^{-1}	Force coefficients relating the pitch rate to B_{pr}
a^*_{pa}, b^*_{pa}, $\hat{c}^*_{pa}$	s, s^{-1}, -	Equivallent of a_{pa}, b_{pa} and $\hat{c}_{pa}$ corrected for the wing morphology variation.
$A_{pr,u}$	N s	Interaction coefficient between the stroke rate and the pitch based forces for a wing that is pitching up
$A_{pr,d}$	N s^2 kg m^{-3}	Interaction coefficient between the stroke rate and the pitch based forces for a wing that is pitching down
B_{pr}	N	Force independent of the stroke rate
c	m	Chord length
$\hat{c}_{pa}$	N s^2 kg m^{-3}	Force coefficient relating the pitch acceleration to the pitch acceleration forces
C_{sr}	-	Force coefficient for the stroke rate forces
Δx_m	m	Space step for the mesh
Δx	m	Offset between the center of the chord and the pitch axis
$d_{pr,u}$, $f_{pr,u}$, $g_{pr,u}$	Ns^4 kg/m^3, N s^2 kg m^{-3} , N s kg m^{-3}	Force coefficients relating the pitch rate to the coefficient $A_{pr,u}$
$d_{pr,d}$, $f_{pr,d}$, $g_{pr,d}$	Ns^5 kg/m^3, N s^3 kg m^{-3}, N s^2 kg m^{-3}	Force coefficients relating the pitch rate to the coefficient $A_{pr,d}$
$d^*_{pr,u}$, $f^*_{pr,u}$	s^2 m^{-2}, -	Equivallent of $d_{pr,u}$ and $f_{pr,u}$ corrected for the wing morphology variation.
F_{am}	N	Added mass forces
$F_{\text{sedov},3D}$	N	Acceleration forces computed with the three-dimensional model based on [11]
$\dot{\omega}_s$	rad s^{-2}	Stroke acceleration
$\dot{\omega}_p$	rad s^{-2}	Pitch acceleration
F_p	N	Pitch based forces
F_{pr}	N	Pitch rate forces
F_{pa}	N	Pitch acceleration forces
F_{pr-pa}	N	Pitch rate interaction forces
$F_{pr-sr-pa}$	N	Pitch-stroke interaction forces
F_{sr}	N	Stroke rate forces
F_s	N	Stroke based forces
F_{sr-pr}	N	stroke pitch interaction forces
F_{sr-pa}	N	stroke rate pitch acceleration forces
F_t	N	Total aerodynamic forces
γ	-	Stroke angle

Continued on next page

Continued from previous page

Symbol	unit	Description
$\hat{g}_{pr,d}$	$Ns^4\ kg/m^3$	Force coefficient relating the pitch acceleration to the force coefficient $g_{pr,d}$
ϕ	-	Pitch angle
ρ	$kg\,m^{-3}$	Fluid density
R	m	Distance from the root of the wing to the tip of the wing
S_{xx}	m^4	Chord-wise second moment of area
$S_{x\|x\|}$	m^4	Assymmetric second moment of area
S_{yy}	m^4	Span-wise second moment of area
V	m^3	Volume of added mass
v	$m\,s^{-1}$	Velocity of the volume of the added mass
ω_p	$rad\,s^{-1}$	Pitch rate
ω_s	$rad\,s^{-1}$	Stroke rate
y	m	Location along the span of the wing

Throughout this study we used three second moments of area (S_{xx}, S_{yy} and $S_{x|x|}$, which are defined as:

$$S_{yy} = \int_0^R y^2 c \mathrm{d}y \tag{4.22}$$

$$S_{xx} = \int_{c_{te}}^{c_{le}} r x^2 dx \tag{4.23}$$

$$S_{x|x|} = \int_{c_{te}}^{c_{le}} x|x| r dx \tag{4.24}$$

4.8 Forces of the elliptical wings

In the our main study, we have only presented the forces as a function of the stroke rate for the fruit fly wing morphology. Throughout the rest of the study we only used the derived coefficients for the other geometries. Here, we present the pitch based forces for the symmetric elliptical wing (figure 4.14), the elliptical wing with a pitch axis offset of 0.1 mm (figure 4.15), the elliptical wing with a pitch axis offset of 0.2 mm (figure 4.16), the elliptical wing with a pitch axis offset of 0.3 mm (figure 4.17) and the elliptical wing with a pitch axis offset of 0.4 mm (figure 4.18).

4.9 Forces of the mosquito wing

In the our main study, we have only presented the forces as a function of the stroke rate for the fruit fly wing morphology. Throughout the rest of the study, we only used the derived coefficients for the other geometries. Here, we present the pitch based forces for the mosquito wing (figure 4.19).

4.10 Viscous forces

In this study, we only considered the pressure forces in our pitch motion model. We did this because the viscous forces along the chord (F_x) and the span (F_y) are considerable lower than the pressure forces. For the sake of completeness, we the viscous forces for the fruit fly wing morphology are presented in figure 4.20, 4.21, 4.22 and 4.23.

4.11 Quasi-steady model

To test how our newly constructed pitch forces model influence the total force production of flapping insects we developed a quasi-steady model. This model is only based on the forces generated due to a stroke rate motion and the pitch motion. The kinematics used in this study where based on three angles; the stroke-angle γ, the deviation-angle θ and the pitch-angle ϕ. From these three angles the total rotation matrix is defined assumed

$$\boldsymbol{A} = \boldsymbol{A}_\gamma \boldsymbol{A}_\theta \boldsymbol{A}_\phi. \tag{4.25}$$

From the rotation matrix we determined the angular rotation of the wing in the *world reference frame*:

$$\boldsymbol{\omega} = \begin{bmatrix} 0 & \omega_z & \omega_y \\ \omega_z & 0 & -\omega_x \\ \omega_y & \omega_z & 0 \end{bmatrix} = \frac{d\boldsymbol{A}}{dt} A^T. \tag{4.26}$$

From the angular velocity matrix $\boldsymbol{\omega}$ the angular velocity vector $\vec{\omega} = [\omega_x, \omega_y, \omega_z]^T$ is determined. The angular velocity in the *world-reference frame* is then rotated to the

wing-reference frame with

$$\vec{\omega}_{\text{wing}} = \boldsymbol{A}^T \vec{\omega}_{\text{world}}. \tag{4.27}$$

The angle-of-attack α is determined from the angular velocity in the wing reference frame

$$\alpha = \tan^{-1}\left(\frac{\omega_x}{\omega_z}\right) \text{sign}\left(\omega_x\right). \tag{4.28}$$

The multiplication with the sign of the angular velocity ω_x in the wing reference frame is included to change the sign of the angle-of-attack according to the direction of motion of the wing. The stroke rate ω_s is positive by definition and the pitch rate is based on the angular rate around the pitch axis (ω_y), but has to be corrected for the direction of stroke motion. This results in two equations to compute the stroke rate and pitch rate, which are written as

$$\omega_s = \sqrt{\omega_x^2 + \omega_z^2} \tag{4.29}$$

$$\omega_p = \omega_y \text{sign}\omega_x. \tag{4.30}$$

Finally the pitch acceleration is obtained by first taking the derivative of the angular rate around the pitch axis, and then correcting it for the direction of stroke motion, which is written as

$$\dot{\omega}_p = \frac{\mathrm{d}}{\mathrm{d}t}\left(\omega_y\right) \text{sign}(\omega_x). \tag{4.31}$$

4.12 Supplementary figures

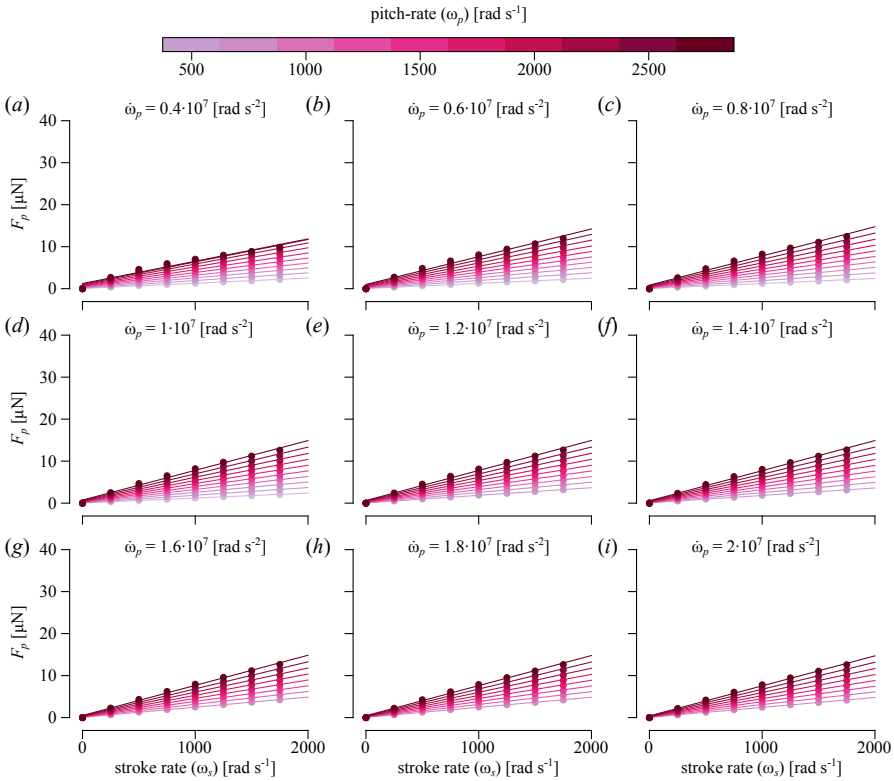

Figure 4.14: Variation of the pitch-based forces F_p for wings accelerating up while pitching up (pink dots) for the symmetric elliptical wing. (*a*) $\dot{\omega}_p = 4 \cdot 10^6\,\mathrm{rad\,s^{-2}}$. (*b*) $\dot{\omega}_p = 6 \cdot 10^6\,\mathrm{rad\,s^{-2}}$. (*c*) $\dot{\omega}_p = 8 \cdot 10^6\,\mathrm{rad\,s^{-2}}$. (*d*) $\dot{\omega}_p = 1 \cdot 10^7\,\mathrm{rad\,s^{-2}}$. (*e*) $\dot{\omega}_p = 1.2 \cdot 10^7\,\mathrm{rad\,s^{-2}}$. (*f*) $\dot{\omega}_p = 1.4 \cdot 10^7\,\mathrm{rad\,s^{-2}}$. (*g*) $\dot{\omega}_p = 1.6 \cdot 10^7\,\mathrm{rad\,s^{-2}}$. (*h*) $\dot{\omega}_p = 1.8 \cdot 10^7\,\mathrm{rad\,s^{-2}}$. (*i*) $\dot{\omega}_p = 2 \cdot 10^7\,\mathrm{rad\,s^{-2}}$.

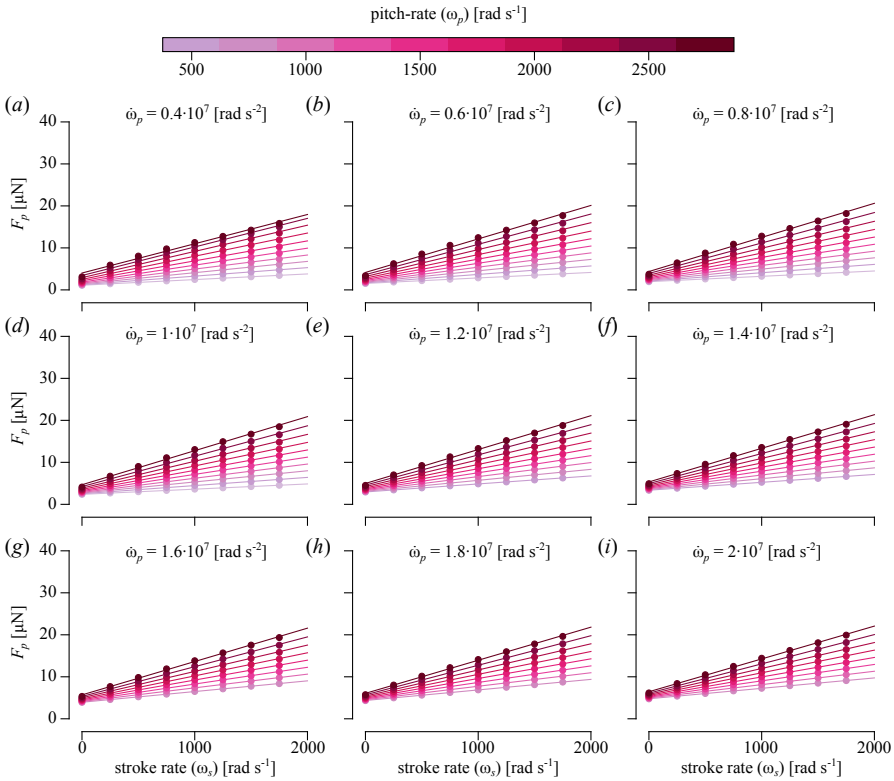

Figure 4.15: Variation of the pitch-based forces F_p for wings accelerating up while pitching up (pink dots) for the elliptical wing with a pitch axis offset of 0.1 mm. (*a*) $\dot{\omega}_p = 4 \cdot 10^6\,\mathrm{rad\,s^{-2}}$. (*b*) $\dot{\omega}_p = 6 \cdot 10^6\,\mathrm{rad\,s^{-2}}$. (*c*) $\dot{\omega}_p = 8 \cdot 10^6\,\mathrm{rad\,s^{-2}}$. (*d*) $\dot{\omega}_p = 1 \cdot 10^7\,\mathrm{rad\,s^{-2}}$. (*e*) $\dot{\omega}_p = 1.2 \cdot 10^7\,\mathrm{rad\,s^{-2}}$. (*f*) $\dot{\omega}_p = 1.4 \cdot 10^7\,\mathrm{rad\,s^{-2}}$. (*g*) $\dot{\omega}_p = 1.6 \cdot 10^7\,\mathrm{rad\,s^{-2}}$. (*h*) $\dot{\omega}_p = 1.8 \cdot 10^7\,\mathrm{rad\,s^{-2}}$. (*i*) $\dot{\omega}_p = 2 \cdot 10^7\,\mathrm{rad\,s^{-2}}$.

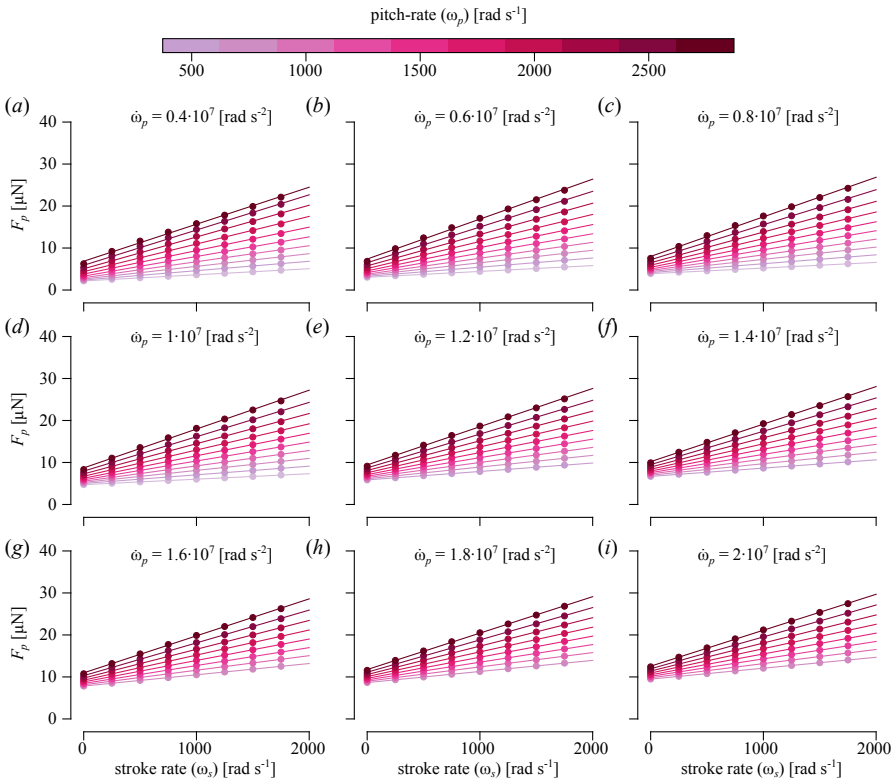

Figure 4.16: Variation of the pitch-based forces F_p for wings accelerating up while pitching up (pink dots) for the elliptical wing with a pitch axis offset of 0.2 mm. (*a*) $\dot{\omega}_p = 4 \cdot 10^6\,\mathrm{rad\,s^{-2}}$. (*b*) $\dot{\omega}_p = 6 \cdot 10^6\,\mathrm{rad\,s^{-2}}$. (*c*) $\dot{\omega}_p = 8 \cdot 10^6\,\mathrm{rad\,s^{-2}}$. (*d*) $\dot{\omega}_p = 1 \cdot 10^7\,\mathrm{rad\,s^{-2}}$. (*e*) $\dot{\omega}_p = 1.2 \cdot 10^7\,\mathrm{rad\,s^{-2}}$. (*f*) $\dot{\omega}_p = 1.4 \cdot 10^7\,\mathrm{rad\,s^{-2}}$. (*g*) $\dot{\omega}_p = 1.6 \cdot 10^7\,\mathrm{rad\,s^{-2}}$. (*h*) $\dot{\omega}_p = 1.8 \cdot 10^7\,\mathrm{rad\,s^{-2}}$. (*i*) $\dot{\omega}_p = 2 \cdot 10^7\,\mathrm{rad\,s^{-2}}$.

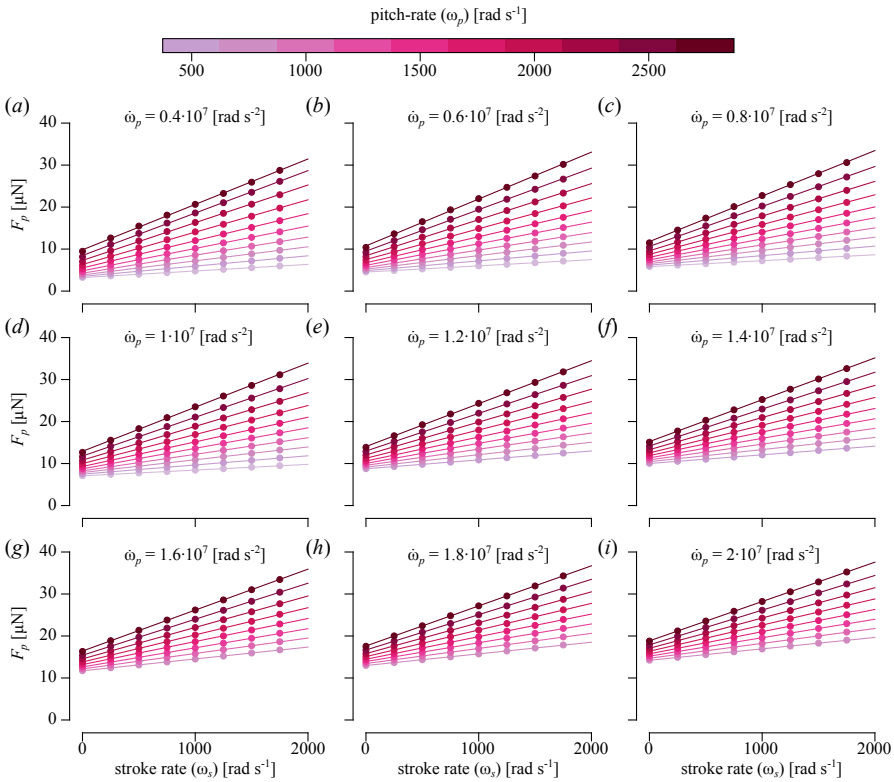

Figure 4.17: Variation of the pitch-based forces F_p for wings accelerating up while pitching up (pink dots) for the elliptical wing with a pitch axis offset of 0.3 mm. (*a*) $\dot{\omega}_p = 4 \cdot 10^6\,\mathrm{rad\,s^{-2}}$. (*b*) $\dot{\omega}_p = 6 \cdot 10^6\,\mathrm{rad\,s^{-2}}$. (*c*) $\dot{\omega}_p = 8 \cdot 10^6\,\mathrm{rad\,s^{-2}}$. (*d*) $\dot{\omega}_p = 1 \cdot 10^7\,\mathrm{rad\,s^{-2}}$. (*e*) $\dot{\omega}_p = 1.2 \cdot 10^7\,\mathrm{rad\,s^{-2}}$. (*f*) $\dot{\omega}_p = 1.4 \cdot 10^7\,\mathrm{rad\,s^{-2}}$. (*g*) $\dot{\omega}_p = 1.6 \cdot 10^7\,\mathrm{rad\,s^{-2}}$. (*h*) $\dot{\omega}_p = 1.8 \cdot 10^7\,\mathrm{rad\,s^{-2}}$. (*i*) $\dot{\omega}_p = 2 \cdot 10^7\,\mathrm{rad\,s^{-2}}$

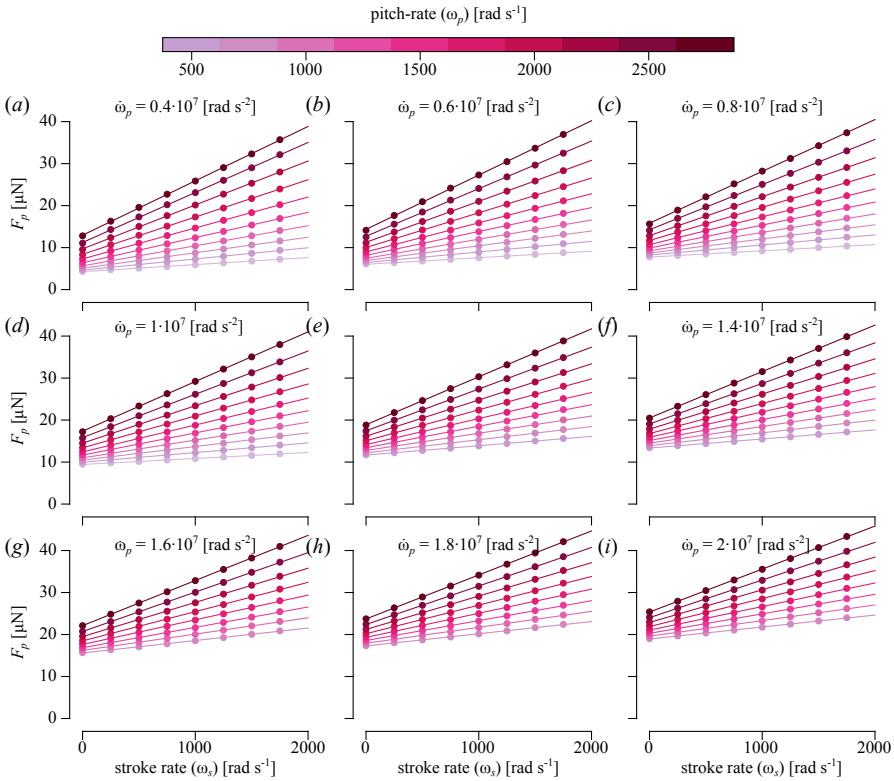

Figure 4.18: Variation of the pitch-based forces F_p for wings accelerating up while pitching up (pink dots) for the elliptical wing with a pitch axis offset of 0.4 mm. (*a*) $\dot{\omega}_p = 4 \cdot 10^6\,\mathrm{rad\,s^{-2}}$. (*b*) $\dot{\omega}_p = 6 \cdot 10^6\,\mathrm{rad\,s^{-2}}$. (*c*) $\dot{\omega}_p = 8 \cdot 10^6\,\mathrm{rad\,s^{-2}}$. (*d*) $\dot{\omega}_p = 1 \cdot 10^7\,\mathrm{rad\,s^{-2}}$. (*e*) $\dot{\omega}_p = 1.2 \cdot 10^7\,\mathrm{rad\,s^{-2}}$. (*f*) $\dot{\omega}_p = 1.4 \cdot 10^7\,\mathrm{rad\,s^{-2}}$. (*g*) $\dot{\omega}_p = 1.6 \cdot 10^7\,\mathrm{rad\,s^{-2}}$. (*h*) $\dot{\omega}_p = 1.8 \cdot 10^7\,\mathrm{rad\,s^{-2}}$. (*i*) $\dot{\omega}_p = 2 \cdot 10^7\,\mathrm{rad\,s^{-2}}$.

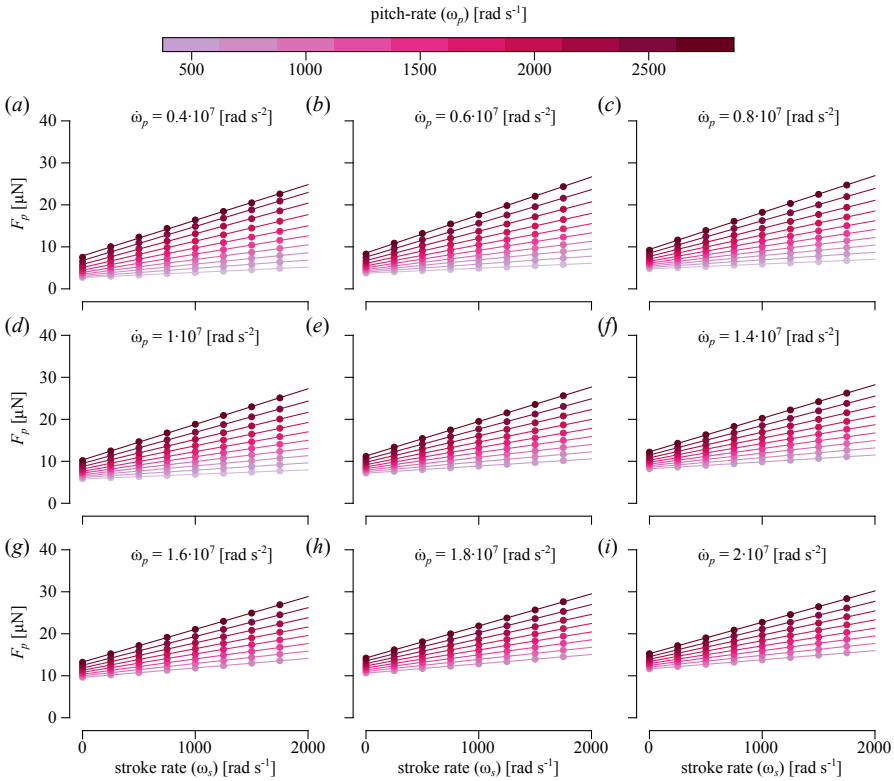

Figure 4.19: Variation of the pitch-based forces F_p for wings accelerating up while pitching up (pink dots) for the mosquito wing.(*a*) $\dot{\omega}_p = 4 \cdot 10^6\,\mathrm{rad\,s^{-2}}$. (*b*) $\dot{\omega}_p = 6 \cdot 10^6\,\mathrm{rad\,s^{-2}}$. (*c*) $\dot{\omega}_p = 8 \cdot 10^6\,\mathrm{rad\,s^{-2}}$. (*d*) $\dot{\omega}_p = 1 \cdot 10^7\,\mathrm{rad\,s^{-2}}$. (*e*) $\dot{\omega}_p = 1.2 \cdot 10^7\,\mathrm{rad\,s^{-2}}$(*f*). $\dot{\omega}_p = 1.4 \cdot 10^7\,\mathrm{rad\,s^{-2}}$. (*g*) $\dot{\omega}_p = 1.6 \cdot 10^7\,\mathrm{rad\,s^{-2}}$. (*h*) $\dot{\omega}_p = 1.8 \cdot 10^7\,\mathrm{rad\,s^{-2}}$ (*i*) $\dot{\omega}_p = 2 \cdot 10^7\,\mathrm{rad\,s^{-2}}$.

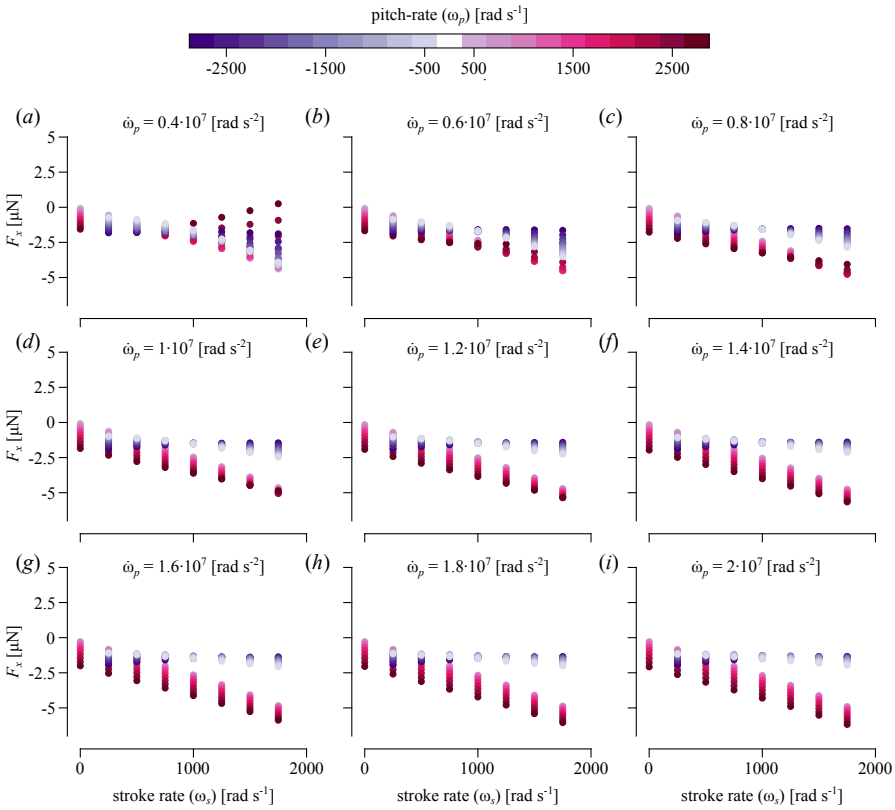

Figure 4.20: Variation of the viscous forces F_x for wings accelerating up while pitching up (pink dots) or down (purple dots) for the fruit fly wing morphology. (*a*) $\dot{\omega}_p = 4 \cdot 10^6\,\mathrm{rad\,s^{-2}}$. (*b*) $\dot{\omega}_p = 6 \cdot 10^6\,\mathrm{rad\,s^{-2}}$. (*c*) $\dot{\omega}_p = 8 \cdot 10^6\,\mathrm{rad\,s^{-2}}$. (*d*) $\dot{\omega}_p = 1 \cdot 10^7\,\mathrm{rad\,s^{-2}}$. (*e*) $\dot{\omega}_p = 1.2 \cdot 10^7\,\mathrm{rad\,s^{-2}}$. (*f*) $\dot{\omega}_p = 1.4 \cdot 10^7\,\mathrm{rad\,s^{-2}}$. (*g*) $\dot{\omega}_p = 1.6 \cdot 10^7\,\mathrm{rad\,s^{-2}}$. (*h*) $\dot{\omega}_p = 1.8 \cdot 10^7\,\mathrm{rad\,s^{-2}}$ (*i*) $\dot{\omega}_p = 2 \cdot 10^7\,\mathrm{rad\,s^{-2}}$.

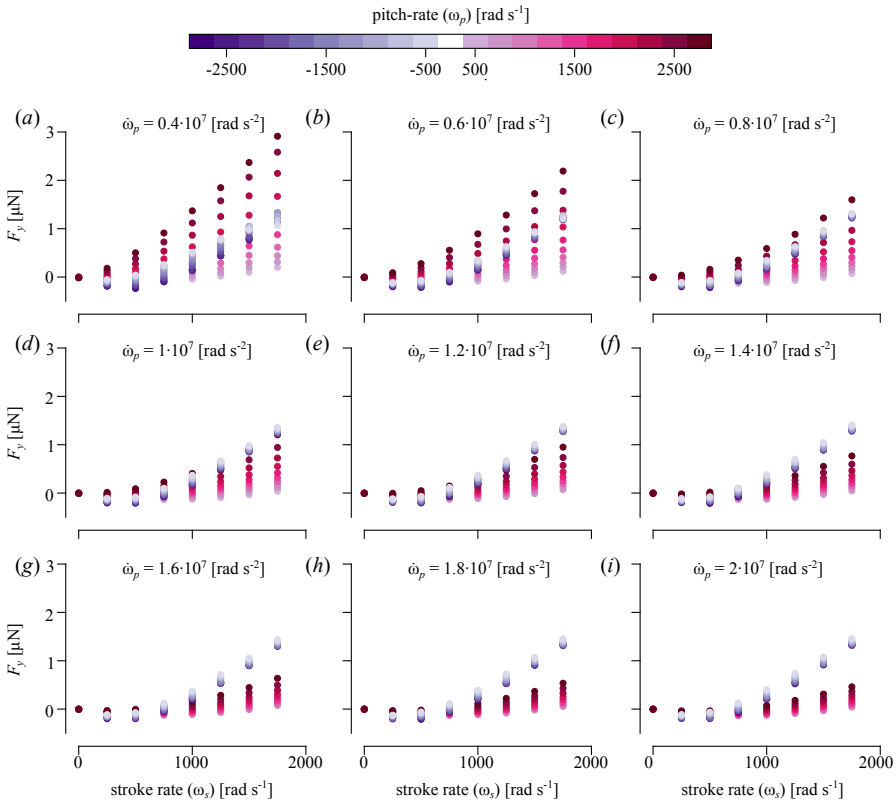

Figure 4.21: Variation of the viscous forces F_y for wings accelerating up while pitching up (pink dots) or down (purple dots) for the fruit fly wing morphology. (*a*) $\dot{\omega}_p = 4 \cdot 10^6\,\mathrm{rad\,s^{-2}}$. (*b*) $\dot{\omega}_p = 6 \cdot 10^6\,\mathrm{rad\,s^{-2}}$. (*c*) $\dot{\omega}_p = 8 \cdot 10^6\,\mathrm{rad\,s^{-2}}$. (*d*) $\dot{\omega}_p = 1 \cdot 10^7\,\mathrm{rad\,s^{-2}}$. (*e*) $\dot{\omega}_p = 1.2 \cdot 10^7\,\mathrm{rad\,s^{-2}}$. (*f*) $\dot{\omega}_p = 1.4 \cdot 10^7\,\mathrm{rad\,s^{-2}}$. (*g*) $\dot{\omega}_p = 1.6 \cdot 10^7\,\mathrm{rad\,s^{-2}}$. (*h*) $\dot{\omega}_p = 1.8 \cdot 10^7\,\mathrm{rad\,s^{-2}}$. (*i*) $\dot{\omega}_p = 2 \cdot 10^7\,\mathrm{rad\,s^{-2}}$.

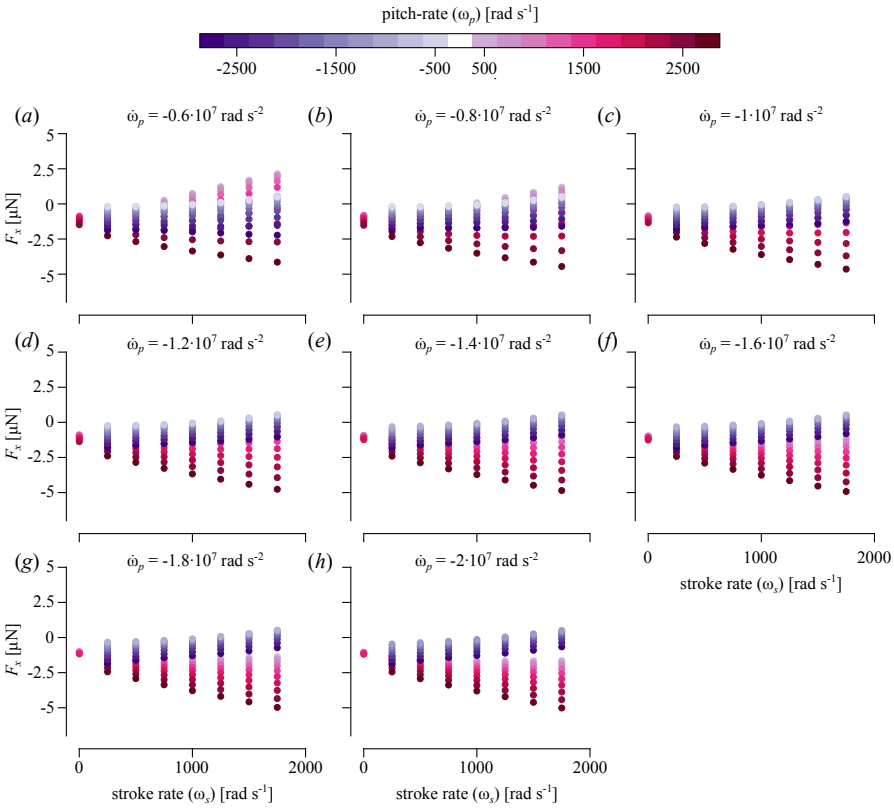

Figure 4.22: Variation of the viscous forces F_x for wings accelerating down while pitching up (pink dots) or down (purple dots). (*a*) $\dot{\omega}_p = -20 \cdot 10^6\,\mathrm{rad\,s^{-2}}$. (*b*) $\dot{\omega}_p = -18 \cdot 10^6\,\mathrm{rad\,s^{-2}}$. (*c*) $\dot{\omega}_p = -16 \cdot 10^6\,\mathrm{rad\,s^{-2}}$. (*d*) $\dot{\omega}_p = -14 \cdot 10^6\,\mathrm{rad\,s^{-2}}$ (*e*). $\dot{\omega}_p = -12 \cdot 10^6\,\mathrm{rad\,s^{-2}}$. (*f*) $\dot{\omega}_p = -10 \cdot 10^6\,\mathrm{rad\,s^{-2}}$. (*g*) $\dot{\omega}_p = -8 \cdot 10^6\,\mathrm{rad\,s^{-2}}$. (*h*) $\dot{\omega}_p = -6 \cdot 10^6\,\mathrm{rad\,s^{-2}}$.

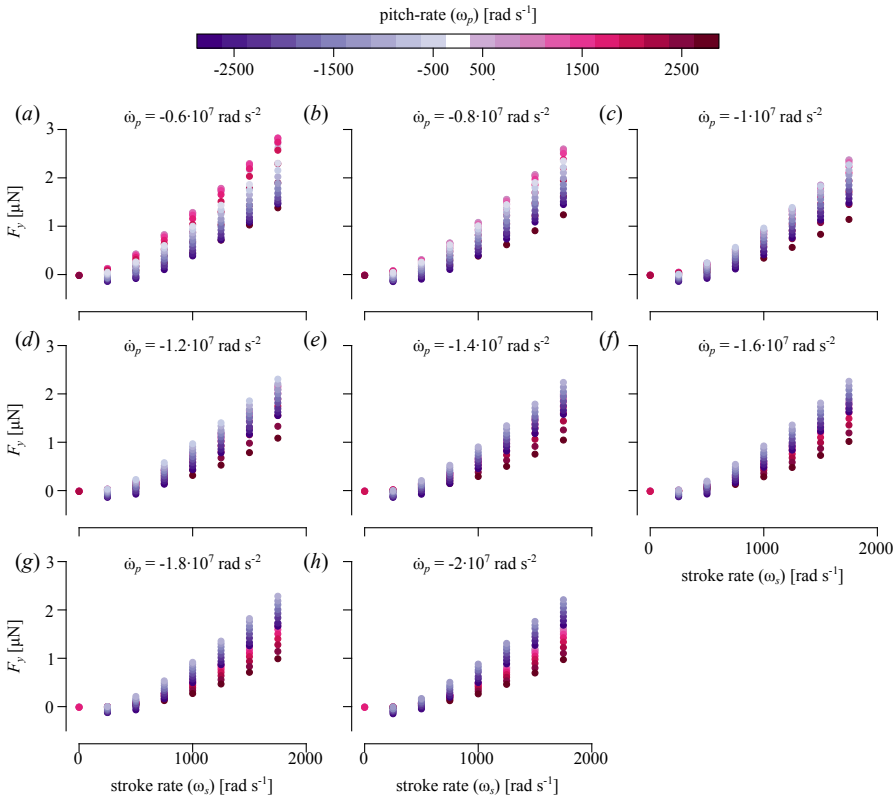

Figure 4.23: Variation of the viscous forces F_y for wings accelerating down while pitching up (pink dots) or down (purple dots). (*a*) $\dot{\omega}_p = -20 \cdot 10^6\,\mathrm{rad\,s^{-2}}$. (*b*) $\dot{\omega}_p = -18 \cdot 10^6\,\mathrm{rad\,s^{-2}}$. (*c*) $\dot{\omega}_p = -16 \cdot 10^6\,\mathrm{rad\,s^{-2}}$. (*d*) $\dot{\omega}_p = -14 \cdot 10^6\,\mathrm{rad\,s^{-2}}$. (*e*) $\dot{\omega}_p = -12 \cdot 10^6\,\mathrm{rad\,s^{-2}}$. (*f*) $\dot{\omega}_p = -10 \cdot 10^6\,\mathrm{rad\,s^{-2}}$. (*g*) $\dot{\omega}_p = -8 \cdot 10^6\,\mathrm{rad\,s^{-2}}$. (*h*) $\dot{\omega}_p = -6 \cdot 10^6\,\mathrm{rad\,s^{-2}}$

Chapter 5

Malaria mosquitoes use leg push-off forces to control body pitch during take-off

Wouter G. van Veen, Johan L. van Leeuwen, Florian T. Muijres

Journal of Experimental Zoology Part A: Ecological and Integrative Physiology Volume 333 Issue 1

Abstract

Escaping from a blood host with freshly acquired nutrition for her eggs is one of the most critical actions in the life of a female malaria mosquito. During this take-off she has to carry a large payload, up to three times her body weight, while avoiding tactile detection by the host. What separates the malaria mosquito from most other insects is that the mosquito pushes off gently with its legs whilst producing aerodynamic forces with its wings. Apart from generating the required forces, the malaria mosquito has to produce the correct torques to pitch up during the take-off. Furthermore, the fed mosquito has to alter the direction of its aerodynamic force vector to compensate for the higher body pitch angle due to its heavier abdomen. Whether the mosquito generates these torques and redirection of the forces with its wings or legs remains unknown. By combining rigid-body inverse dynamics analyses with computational fluid dynamics simulations, we show that mosquitoes use leg push-off to control pitch torques, and that the adaption of the aerodynamic force direction is synchronized with modulations in force magnitude. These results suggest that during the push-off phase of a take-off, mosquitoes use their flight-apparatus primarily as a motor system, and they use leg push-off forces for control.

5.1 Introduction

Females of most mosquito species depend on a blood-meal to acquire the needed nutrition for reproduction [1], however obtaining this blood-meal is not without risk [2]. The gravid mosquito has to find and land on a host, consume the blood and take-off all without being detected. The host-seeking behavior and the blood feeding has been studied in detail [1] [3], but less is known about the take-off [2].

To increase its chance to successfully fly away, a mosquito needs to maximize its escape velocity within the constraint of avoiding tactile detection by the host [4]. Maintaining a high escape velocity becomes particularly challenging for blood-fed mosquitoes, because a mosquito can triple in weight due to a blood-meal [1], [2], which in combination with the absence of large forces generated by the legs, puts even more strain on the flight apparatus. The escape velocity scales inversely with

the size of the blood-meal and consequently with the survival chance [2].

During the take-off of an insect, the flight-apparatus can either be started before take-off, during take-off, or after take-off [5]. Insects adopting the first take-off strategy, such as the butterfly [6] and the drone-fly [5], rely almost completely on the generation of aerodynamic forces with their wings. Insects adopting the last take-off mechanics rely on the forces generated by the legs to generate the upward acceleration, for instance found in the escape response of the fruit fly [7] and the take-off of the Locust [8]. Finally, many insects combine leg forces with aerodynamic forces to generate the upward acceleration, for example the voluntary take-off of the fruit fly [5], [7]. It has been suggested that mosquitoes avoid tactile detection by extending their legs whilst generating aerodynamic forces with their wings [4], [9], keeping the force on the substrate lower than the tactile detection threshold of mammalian skin ($F_{\text{threshold}} = 0.07$ mN) [10]. This may explain why the difference between a voluntary take-off and escape take-off in the fruit fly is not found in mosquitoes [4].

How the aerodynamic forces and torques required for take-off are generated by the mosquito remains unknown [4]. One of the possible explanations of the remarkable lifting capabilities of the mosquitoes may be caused by the interaction of wingbeat-induced air movement with the substrate from where the animal flies away, known as the ground effect. Although no ground effect has been found in similarly sized insects, such as the fruit fly [11], the mosquito does not jump in the air, but starts flapping its wings close to the ground. The closer proximity of the flapping mosquito wing to the substrate, may lead to ground reaction forces to aid in the mosquito's take-off.

Another explanation is the increase of the stroke amplitude during take-off, which is linked to an increase in force production [4]. Other insects that are able to carry large payloads employ a similar wingbeat kinematics as the mosquito [12], [13]; using a shallow stroke amplitude during steady hovering flight, enables the insect to increase its stroke amplitude when accelerating the body or carrying large payloads.

Apart from generating enough forces, the mosquito has to correct its body pitch angle, which is nose-down at the start of the take-off, to a nose-up orientation to ensure a more horizontal stroke-plane of the wingbeat [4]. The required pitch-up torque can be generated by the legs, as seen in the take-off of fruit-flies [5], or by adapting the wing kinematics as applied by maneuvering fruit flies in free flight [14], [15], [16]. It remains an open question how the mosquito controls its body pitch during the take-off.

In this study, we focused on the forces and torques generation during take-off of the malaria mosquito (*Anopheles coluzzii*)[4], clarified by combining rigid-body in-

verse dynamics analyses with state of the art computational fluid dynamics [17]. Our analysis suggests that the ground effect plays no role in aerodynamic force production during the take-off of the mosquito, despite the close proximity of the beating wings to the ground. Furthermore, the aerodynamic force vector aligns closer to the body with increasing total force to compensate for the pitch-up orientation due to the heavy abdomen of a blood-fed female mosquito. Lastly, the pitch-up body movement throughout the take-off is primarily controlled my modulating the leg push-off forces exerted on the ground, which in turn change the pitch-torques.

5.2 Materials & Methods

Experimental animals and conditions

Here, we combined rigid-body inverse dynamics analyses with computational fluid dynamics (CFD) to study the take-off dynamics of 13 female malaria mosquitoes (*Anopheles coluzzii*). Six take-off maneuvers were of non-blood-fed mosquitoes, and seven of blood-fed malaria mosquitoes; the kinematics of these maneuvers were previously published [4]. The inverse dynamics method provided us with total force and torque dynamics throughout each maneuver and the CFD simulations allowed us to determine the aerodynamic forces and torques produced by the flapping wings. By subtracting aerodynamic forces and torques from the total forces and torques, we estimated the contribution of the leg push-off to force and torque production.

For one take-off of a lean mosquito and one of a blood-fed mosquito, we performed CFD simulations both with and without a take-off platform to evaluate the effect of the presence of the ground on the aerodynamic forces and torques acting on the mosquitoes.

Computational fluid dynamics solver

We used computational fluid dynamics (CFD) based on the immersed boundary methods [17] to simulate the forces, torques and the flow-field as a result of the wing and body motion of the mosquito during take-off. The immersed boundary method enabled us to simulate the complex movement of the mosquito, without having to take complex mesh deformations of traditional CFD methods into account [18].

The simulations were conducted on a domain of size 140mm on all sides (figure 5.1 *b*). The domain size was chosen such that negligible interaction between the

airflow generated by the mosquito and the domain boundaries occurred, except for the bottom boundary, because we simulated a mosquito taking-off from the ground. On all boundaries, a no-slip boundary is enforced, such that all boundaries act as an impenetrable wall. On the body of the mosquito, a no-slip boundary condition was enforced using the forcing function of the immersed boundary method [17].

Both the motion and the shape of the mosquito were prescribed during the simulation. The motion of the body and wings arises from the measured kinematics, the shape of the mosquito comes from the combined shape of the body and wings (figure 5.1 *c*, *d*). Wing geometry scale isometrically with wing length and all wings had a thickness of 0.03mm (1% of the wing length). All mosquitoes had a body length of 4.7mm, and the shape of the body was kept constant for all lean mosquitoes and blood-fed mosquitoes; for the computation of the center of mass it is assumed that the mass is homogeneous distributed in the mosquito.

To accurately compute the complex fluid dynamics close to the mosquito, we used an adaptive mesh refinement (AMR) algorithm that refines the mesh based on areas in the flow-field with high-vorticity. This resulted effectively in a refinement close to the body and in the wake. At the finest refinement level a refinement of $\Delta x = 0.0304$ mm was used, which led to a mesh-size of approximately 4 million cells. After the choice of the refinement level a corresponding time-step was chosen of $\Delta t = 1{\cdot}10^{-7}$s. We validated the solver using the wingbeat kinematics of a hovering fruit fly and the corresponding aerodynamic forces, determined using a robotic flapper experiment [14]. The forces simulated by our method are similar to the forces predicted in the robotic experiment (see Supplementary methods for more detail).

Reference frames

In this study, two reference frames were used; the world-reference frame, and the stroke-plane reference frame. The world-reference frame is a right-handed orthogonal reference frame with its origin at the center of the domain at ground level (figure 5.1 *b*). To simulate a take-off without a ground present, the start of the take-off was placed 70mm above the bottom of the simulation domain.

The stroke-plane reference frame is a right-handed orthogonal reference frame attached to the center of mass of the body of the mosquito (figure 1e—g) and aligned with the stroke plane of an average wingbeat. Its y-axis is pointing to the right-side of the animal, the x-axis pointing forward in the direction of the head, and pitched down

relative to the body axis with a constant stroke-plane angle $\beta = 47.5^{\text{o}}$ (figure 5.1 *f*); the z-axis pointing down towards the ventral side of the mosquito (figure 5.1 *e*–*g*).

Kinematics

The body and wing motion of the mosquito take-offs were obtained from a previous study [4]. The rotation and location of the body were prescribed in the world-reference frame (figure 5.1 *b*). The motion of the wings was described in the stroke-plane reference frame (figure 5.1 *e*), using three Euler angles; the stroke angle, the deviation angle and the wing rotation angle. First, the stroke angle (γ, figure 5.1 *e*) describes the forward and backward motion within the stroke-plane of the wing, where for a zero stroke angle the wing is aligned with the y-axis. Secondly, the deviation angle (θ, figure 5.1 *g*) describes the wing angle out of the stroke-plane, where for positive deviation angles the wing is pointing towards the dorsal side of the body. Finally, the wing rotation angle (ϕ, figure 5.1 *f*) describes the rotation of the wing along its longitudinal axis, where a zero angle defines a vertical wing with the leading edge pointing upwards.

Force analysis

Throughout a take-off, the total force acting on a mosquito, $\vec{F}_{\text{total}}$, consist of the aerodynamic force, $\vec{F}_{\text{aero}}$, and the ground reaction forces from the legs, $\vec{F}_{\text{leg}}$. The total forces were computed in the world-reference frame from the kinematics using inverse rigid-body dynamics as

$$\left(\vec{F}_{\text{total}}\right)_{\text{world}} = m_{\text{mosq}} \frac{d}{dt}\left(\vec{V}_{\text{world}}\right) - \vec{W}, \tag{5.1}$$

where m_{mosq} is the mass of the mosquito, $\vec{V}_{\text{world}}$ the velocity vector of the body in the world-reference frame and $\vec{W}$ the weight of the mosquito ($\vec{W} = [0; 0; -m_{\text{mosq}}g]$, where $g = 9.81$ m s^{-2}).

The aerodynamic forces computed by the CFD solver were also determined in the world-reference frame. These aerodynamic forces fluctuate highly throughout each wingbeat, and therefore we estimated the wingbeat-average aerodynamic forces, $\vec{F}_{\text{aero}}$, using a fifth order Butterworth filter ($f_{\text{low}} = 1 \cdot 10^{-6}$ Hz and $f_{\text{high}} = 200$ Hz). The leg-derived forces were estimated as the difference between the total aerodynamic forces and the wingbeat-average aerodynamic forces as $\vec{F}_{\text{leg}} = \vec{F}_{\text{total}} - \vec{F}_{\text{aero}}$.

To compute the angle between the aerodynamic force vector and the stroke-plane, the forces derived from the CFD solver $\vec{F}_{\text{aero}}$ were first transformed to the stroke-plane reference frame by

$$\left(\vec{F}_{\text{aero}}\right)_{\text{stroke}} = \boldsymbol{A}^{T}_{\text{stroke}}\boldsymbol{A}^{T}_{\text{body}}\left(\vec{F}_{\text{aero}}\right)_{\text{world}}, \tag{5.2}$$

where $\boldsymbol{A}_{\text{stroke}}$ is the rotation matrix from the body-reference frame to the stroke-plane reference frame and $\boldsymbol{A}_{\text{body}}$ the rotation matrix that describes the motion of the body in the world reference frame.

From the forces in the stroke-reference frame, the angle between the force and the stroke-plane (figure 5.1 *f*) was computed as

$$\xi = \tan^{-1}\left(\frac{(F_z)_{\text{stroke}}}{\text{sign}(F_x)_{\text{stroke}}\sqrt{(F_x)^2_{\text{stroke}} + (F_y)^2_{\text{stroke}}}}\right). \tag{5.3}$$

All forces were either normalized with the weight of the animal as $\vec{F}^{*} = \vec{F}/(m_{\text{mosq}}g)$, or with a generic weight $\vec{F}^{**} = \vec{F}/(m_{\text{gen}}g)$, with $m_{\text{gen}} = 1\text{mg}$.

Torque analysis

Similar to the forces, the torques produced by the mosquito were also expressed in the stroke-plane reference frame, using the reference frame transformation described in equation (5.2). The resulting stroke-plane-based torques consist of roll torque about the x-axis, pitch torque about the y-axis, and yaw torque about the z-axis.

The total torques produced by the mosquito were computed based on the kinematics using rigid-body inverse dynamics in two steps: first, we computed the angular momentum of the mosquito in the stroke-plane reference frame as

$$\left(\vec{\mathcal{L}}_{\text{total}}\right)_{\text{stroke}} = \boldsymbol{I}\vec{\omega}_{\text{stroke}}, \tag{5.4}$$

where $\boldsymbol{I}$ is the moment of inertia matrix of the mosquito, and $\vec{\omega}_{\text{stroke}}$ the angular velocity of the mosquito in the stroke-plane reference frame. Secondly, the total torque produced by the mosquito was computed as

$$\left(\vec{T}_{\text{total}}\right)_{\text{stroke}} = \frac{d}{dt}\left(\vec{\mathcal{L}}_{\text{total}}\right)_{\text{stroke}}. \tag{5.5}$$

The equivalent aerodynamic torques produced by the beating wings were esti-

mated using CFD. Like the forces, these torques vary highly throughout each wingbeat, and therefore we estimated the wingbeat-average aerodynamic torques using a fifth order Butterworth filter ($f_{\text{low}} = 1 \cdot 10^{-6}$ Hz and $f_{\text{high}} = 200$ Hz [19]). The angular momentum that would result from aerodynamic torque production alone, was estimated by numerically integrating the aerodynamic torques throughout each take-off maneuver.

The corresponding torques and angular momentum produced by leg push-off were consequently estimated as $\vec{T}_{\text{leg}} = \vec{T}_{\text{total}} - \vec{T}_{\text{aero}}$ and $\vec{\mathcal{L}}_{\text{leg}} = \vec{\mathcal{L}}_{\text{total}} - \vec{\mathcal{L}}_{\text{aero}}$, respectively. All torques were then normalized with the product of body length and body weight of the animal $\vec{T}^* = \vec{T}/(m_{\text{mosq}} g l_{\text{mosq}})$.

Throughout a take-off, a mosquito primarily pitches up, and thus we primarily focused on pitch torque production. To study the effect of the different pitch torque components on this pitch dynamics, we defined the contribution of pitch torque on pitch angle change $\varepsilon_{\text{pitch}}$. This parameter can be calculated by integrating the angular momentum throughout the push-off phase of the take-off as

$$\varepsilon_{\text{pitch}} = \boldsymbol{I}^{-1} \sum_{i=0}^{n_{\text{lift-off}}} \left(\vec{\mathcal{L}}_i\right)_{\text{pitch}}, \tag{5.6}$$

whereby $\boldsymbol{I}^{-1}$ is the inverse of the moment of inertia, $n_{\text{lift-off}}$ is the time-step at which the last leg leaves the ground, and $\vec{\mathcal{L}}_i$ either the total, aerodynamic or leg contribution to the angular momentum at time-step i.

5.3 Results

Ground effect

The ground effect was studied by conducting two identical simulations, the only difference being the presence or absence of the ground. We conducted this dual simulation for both a lean mosquito and a blood-fed mosquito.

A patch of the ground surface (2cm x 2cm) was extracted when the air pressure acting on the ground was maximum (figure 5.2 *a–d*). The maximum air pressure planes with the ground present (figure 5.2 *a*, *c*) show larger pressure fluctuations when compared with the planes without ground present (figure 5.2 *b*, *d*). The air pressure acting on the ground surface of 2cm x 2cm was extracted for all the time-steps during the push-off phase and integrated over the surface. The resulting forces fluctuate

during the take-off, but for all simulated lean mosquitoes the average maximum force ($F_{\text{substrate}} = 0.05 \pm 0.01$ mN, $n = 6$) remain below the force detection threshold of mammalian skin ($F_{\text{threshold}} = 0.07$ mN, figure 5.2 *i*) [10]. The average maximum forces for the blood-fed mosquitoes is equal to the detection threshold ($F_{\text{substrate}} = 0.07 \pm 0.01$ mN, $n = 7$). The averaged pressure forces are considerable lower than the forces generated by the legs, and only alter the total averaged forces acting on the substrate slightly (figure 5.2 *i*, *j*).

Interestingly, the large differences in ground pressure between the simulations with and without ground do not lead to large differences in the wake structure (figure 5.2 *e–h*). For the case with ground present, the wake is interacting with the ground but no large change is propagated further towards the insect (figure 5.2 *e*, *g*). Furthermore, no difference can be observed in the forces on the body and wings of the mosquitoes, for both the lean and blood-fed mosquitoes (figure 5.2 *i*, *j*; lean mosquito with ground: $F^*_{\text{aero},z} = 0.69 \pm 2.45$; lean mosquito without ground: $F^*_{\text{aero},z} = 0.69 \pm 2.45$; fed mosquito with ground: $F^*_{\text{aero},z} = 0.69 \pm 1.35$; fed mosquito without ground:$F^*_{\text{aero},z} = 0.69 \pm 1.35$). This suggests that throughout the take-off, the mosquito does affect the pressure distribution on the ground, but that the presence of the ground has no effect on the aerodynamic forces on the mosquito.

Vertical forces

At the start of a take-off, mosquitoes are often pitched head down (figure 5.3 *a*, *b*) and during the take-off they make a rapid pitch-up movement. As a consequence, the stroke-plane is oriented almost vertically at the start of the take-off and rotates towards a horizontal orientation near the end of the push-off phase. The path of the blood-fed mosquito has a larger horizontal component compared to the lean mosquitoes (figure 5.3 *a*, *b* and figure 5.4 *a*).

Comparing the computed aerodynamic force opposing the gravity vector $F_{z,\text{aero}}$ with the total vertical forces $F_{z,\text{total}}$ needed for the measured body accelerations (figure 5.3 *c*, *e*) show that the large force fluctuation during the push-off originate from the ground forces on the legs and not from the aerodynamic forces acting on the wing. After push-off, the difference between the computed aerodynamic forces and the required aerodynamic forces are minimal and not significantly different from zero (one sample t-test, $p = 0.0034$), except for a short phase directly after lift-off in the case of the lean mosquito. This might originate from the filtering of the aerodynamic forces.

The average total force, aerodynamic force and leg force during take-off (figure 5.4 *c*) shows that both the legs and the wings make a contribution to force production throughout the push-off. The ratio between aerodynamic forces and leg-induced push-off forces are not significantly different between lean and fed mosquitoes (figure 5.4 *d*, independent t-test, $p = 0.087$). For both lean and blood-fed mosquitoes the wings contribute $25.9\% \pm 6.9\%$ ($n = 13$) to vertical force production throughout the push-off phase of a take-off.

The angle between the resultant force vector and the stroke-plane, known as the force angle ξ, was computed when the aerodynamic resultant force is larger than half of the body weight. In the case of the lean mosquito (figure 5.3 *d*), the force angle starts high at take-off and gradually decreases to around 90^{o}. The blood-fed mosquito starts with a force vector more aligned to the body of the mosquito (figure 5.3 *f*). The average force angle during take-off for the fed mosquitoes is significantly lower than the lean mosquitoes (figure 5.4 *b*; fed mosquitoes: $\xi = 82.93^{\text{o}} \pm 8.81^{\text{o}}$, $n = 7$; lean mosquitoes: $\xi = 94.62^{\text{o}} \pm 8.30^{\text{o}}$, $n = 6$; independent t-test, $p = 0.038$) [19].

The resultant force, normalized with a standard mass of 1mg, per wingbeat for both the lean and fed mosquitoes scales with the stroke amplitude (figure 5.4 *e*), and shows a significant positive correlation (simple linear regression, $p < 0.0001$). The deviation angle amplitude, the difference between the maximum and minimum deviation angle per wingbeat, also scales positively with the stroke amplitude (figure 5.4 *f*, simple linear regression, $p < 0.0001$). Finally, in the blood-fed mosquitoes the force angle ξ scales negatively with the resultant force (figure 5.4 *g*, $p < 0.0029$), whereas this correlation is absent in the lean mosquitoes ($p = 0.36$).

Pitch torques

During the take-off, all the measured mosquitoes are pitching up [4]. To initiate this pitch-up maneuver a mosquito needs to produce pitch-up torque, and to stop this pitch-up rotation the animal should produce a pitch-down torque. To test how the mosquitoes produce these torques, we compared total pitch torques and the aerodynamic pitch torques throughout the take-off (figure 5.5 *a*, *c*). During the flight phase of the take-off, the wingbeat-average aerodynamic pitch torques do not significantly differ from the total torques ($\Delta T^*_{\text{pitch}} = -0.017 \pm 0.049$, $n = 12$, one sample t-test, $p = 0.28$). This shows that our CFD method captures the aerodynamic torques well, allowing us to estimate pitch torques from leg push-off as the difference between total

torque and aerodynamic torque. During the push-off phase, largest differences occur between total pitch torques and the aerodynamic pitch torques, suggesting that the leg push-off forces contribute to pitch-torque production.

During the push-off phase, the total body pitch-torque shows a positive pitch-up peak for both lean and blood-fed mosquitoes (figure 5.5*a*, *c*). In the case of the lean mosquito, part of this torque is generated by the wings, but the aerodynamic torques are always lower than the total torques. The total torques produced by the blood-fed mosquito reveals a more dramatic dynamics, with a large pitch-up total torque followed by a pitch-down torque, which is not found in the corresponding aerodynamic torques (figure 5.5/c/).

The pitch-up torque peaks at the start of the push-off phase are not different between the lean and blood-fed mosquitoes ($p = 0.208$ independent t-test, figure 5.5*b*), whereas the following pitch-down torque peaks are on average 2.16 times higher in the blood-fed mosquitoes, compared to the lean mosquitoes ($p = 0.0022$ independent t-test, figure 5.5*b*).

Based on the temporal dynamics of torque production, we determined the relative contribution of total pitch torque, leg-induced torque and wing-induced torque to the pitch-up body reorientation (equation (5.6), figure 5.5*d*). The contribution of the total torques to the pitch angle ($\varepsilon_{\text{total}}$) is similar for both the lean and the fed mosquitoes (figure 5.5 *d*). The contribution of the aerodynamic torques to the pitch angle $\varepsilon_{\text{aero}}$ is higher for the fed mosquitoes than for the lean mosquitoes, most likely due to a blood-load induced backward shift of the center of mass relative to the aerodynamic center (figure 5.5*d*). As a result, the blood-fed mosquitoes have a lower contribution of the legs to the pitch up torque production ε_{leg} than the lean mosquitoes. In fact, on average, leg push-off in blood-fed mosquitoes even contribute negatively to the pitch-up maneuver (fed mosquitoes: $\varepsilon_{\text{leg}} = -4.66^{\text{o}} \pm 29.70^{\text{o}}$, $n = 7$), whereas for the lean mosquitoes the average leg-induced pitch-up contribution was positive (lean mosquitoes: $\varepsilon_{\text{leg}} = 30.96^{\text{o}} \pm 33.05^{\text{o}}$, $n = 6$).

Comparing the contribution of aerodynamic torques and leg push-off torques to the pitch-up movement within the push-off phase (figure 5.5*e*) shows that the positive contribution of aerodynamic torques, mostly present in the blood-fed mosquitoes, is compensated by a reduced (or even negative) pitch-up contribution from the legs.

5.4 Discussion

Force production

During take-off, a mosquito has to produce high enough forces to reach an escape velocity that maximizes the chance to escape a predator or a defensive blood-host [2]. These forces are generated by a combination of the aerodynamic forces produced by the flapping wings and ground push-off forces from the legs [4], [9]. In our simulations, we compared the required forces needed to perform the measured take-off with the aerodynamic forces generated by the wings. Our results show that during the push-off phase of a take-off, the aerodynamic force indeed represents $25.9\% \pm 6.90\%$ of the total take-off force ($n = 13$, figure 5.4*c*). Interestingly, this fraction does not differ significantly between fed mosquitoes and lean mosquitoes ($p = 0.087$), which suggests that the aerodynamic and leg forces scale both with the body mass of the animal.

Forces acting on the substrate

The take-off poses a large demand on the flight-apparatus of particularly a blood-fed mosquito, because during a take-off the animal has to generate a high enough escape velocity while carrying a considerable payload. We explored whether the interaction of the wake with the substrate enhances the force generation of the wing, aiding in the take-off.

For this, we conducted two computational experiments; one for a lean and one for a fed mosquito. Both experiments consisted of two simulations; one with ground present, and one without ground present. Surprisingly the ground had no effect on the forces on the mosquito, even though the wake had a clear interaction with the substrate (figure 5.2*i–l*). The change in the wake did not seem to propagate upstream to the flapping mosquito, which resulted in a similar airflow around the wings compared to the case without substrate present. This result is in line with a previous study on fruit flies [11].

However, our result do show that the presence of the substrate increases the local pressure compared to equivalent plane at the same location in free air. This means that the wake has an effect on the substrate, which is in line with previous hypotheses [4]. For the blood-fed mosquitoes, the force on the platform resulting from this air

pressure increase is equal to the detection threshold for mammalian skin, which might suggest that blood-fed mosquitoes can be detected during take-off. However, this force does not act on a single point as it is distributed over an surface of 2cm x 2cm (figure 5.2*c*). This spreading may cause that the peak force on the skin surface remains below the detection limit of a mammalian host, which is in line with the hypothesis that escaping hematophagous insects can use wing-induced aerodynamic forces to reduce the chance of being detected [4].

Adaptation of the wingbeat kinematics

Our second hypothesis was that the mosquito increases its shallow stroke amplitude in order to increase the aerodynamic force production. The stroke amplitude is strongly correlated with the wingbeat-average aerodynamic resultant forces (figure 5.4*e*). Furthermore, the stroke amplitude is correlated positively with the deviation angle amplitude (figure 5.4*f*), which implies that both the stroke angle and the deviation angle are adapted simultaneously. This combined adjustment of the stroke and deviation angle amplitude suggests that a relatively simple mechanism is used to increase the resultant forces. A similar mechanism to increase the aerodynamic forces was found in honeybees [12].

Force angle alignment

Due to the higher weight of the abdomen during take-off, the pitch angle of a fed mosquito is in general higher than for unfed mosquitoes [4]. This higher pitch-angle of the body leads to a higher angle between the stroke-plane and the ground, because the stroke-plane is fixed to the body-axis of the animal (figure 5.1*e*–*g*). The force angle (ξ) of blood-fed mosquitoes, the pitch angle between the force vector and the stroke-plane, is reduced significantly compared with lean mosquitoes (figure 5.4*b*).

For the blood-fed mosquitoes, the decrease in force angle, aligning the force vector closer to the body axis, is correlated with the increase in aerodynamic force production (figure 5.4*g*). At the same time, to increasing this aerodynamic force, blood-fed mosquitoes not only increase stroke amplitude (figure 5.4*e*), but they also increase the deviation angle amplitude (figure 5.4*f*). A recent study showed that such change in deviation angle amplitude causes a pitch down rotation of the force vector [4]. This suggests that blood-fed mosquitoes synchronize re-alignment of the force vector with increase in force magnitude. This allows them to simultaneously compensate

for both the weight increase and the higher body pitch angle as a result of flying with a blood-load in their abdomen.

Pitch control via leg push-off

During take-off, the mosquito has to pitch-up rapidly to reorient its stroke-plane parallel to the ground, such that the force vector opposes the gravity vector [4]. This pitch-up motion occurs when the legs are still touching the ground. We have found that both lean and fed mosquitoes use their legs for pitch-up control (figure 5.5*d*). Interestingly, the lean mosquitoes achieve this pitch control via a positive contribution of leg torques to the pitch-up movement, whereas in fed mosquitoes the legs contribute on average negatively to the pitch-up movement (figure 5.5*e*). This is most likely caused by a backward shift of the center of mass as a result of blood feeding (figure 1c). Due to this, a blood-fed mosquito generates larger aerodynamic pitch-up torques, which need to be compensated by pitch-down torques produced by the legs at push-off (figure 5.5*b*, *c*).

Fruit flies also generate a large pitch-up torque during take-off, where they rely solely on their legs. When the fruit fly is airborne it uses its wings to generate a counter torque to stop the pitch up rotation of the body [5]. On the other hand, mosquitoes produce pitch torques with both their legs and wings throughout the complete push-off phase. The pitch torque produced by the wings remains relatively constant throughout the take-off maneuver. For blood-fed mosquitoes the leg-induced torques vary from positive when initiating the pitch-up maneuver, to negative when stopping the pitch up rotation (figure 5.5*b*–*c*).

This suggests that that malaria mosquitoes use their flight-apparatus primarily as a motor system, whereas they use their legs to control the body pitch movements throughout take-off maneuvers. Together with the apparent co-regulation of aerodynamic force magnitude and force angle, this suggests that malaria mosquitoes possess a robust control system that allows them to perform rapid take-off maneuvers both with and without a blood-load in their abdomen.

Data, code and materials. The datasets supporting this article are available in an online repository.

Funding. F.T.M. was supported by a grant from The Netherlands Organization for Scientific Research (NWO/VENI-863-14-007).

Competing interests We declare we have no competing interests.

Authors' contributions W.G.v.V. developed the computational system, carried out the simulations, analyzed the data, and drafted the manuscript. F.T.M. provided the mosquito data, coordinated the study and helped to draft the manuscript. All authors were involved in conceiving and designing the study, contributed critical to writing the manuscript and gave final approval for publication.

Acknowledgment. We thank Cees Voesenek for his help and feedback during the analysis, Antoine Cribellier and Pulkit Goyal for the useful discussions, Sophia Chang and Jeroen Spitzen for the data measurements, Annelieke Wentzel and Steven ten Hoff for helping with the statistical analysis, and Henk Schipper for helping with organizing the computational resources.

5.5 References

[1] *The biology of mosquitoes, volume 3 Transmission of viruses and interactions with bacteria*. 2011.

[2] B. D. Roitberg, E. B. Mondor, and J. G. A. Tyerman. "Pouncing spider, flying mosquito: Blood acquisition increases predation risk in mosquitoes". In: *Behavioral ecology* (2003).

[3] W. Takken. "The role of olifaction in host-seeking of mosqtuioes: a review". In: *Insect science application* 12.1/2/3 (1990), pp. 287–295.

[4] F.T. Muijres, S.W. Chang, W.G. Veen, J. Spitzen, B.T. Biemans, M.A.R. Koehl, and R. Dudley. "Escaping blood-fed malaria mosqtuitoes minimize tactile detection without compromising on take-off speed". In: *Journal of Experimental Biology* 220.20 (2017), pp. 3751–3762. DOI: 10.1242/jeb.163402.

[5] M. Chen and M. Sun. "Wing/body kinematics measurement and force and moment analyses of the takeoff of fruitlfies". In: *Acta Mechanica Sinica* 30.4 (2014), pp. 495–506.

[6] S. Sunada, K. K. Wtanabe, and A. Azuma. "Performance of a butterfly in take-off flight". In: *Journal of experimental biology* 183 (1993), pp. 249–277.

[7] G. Card and M. Dickinson. "Performace trade-off in the flight initiation of Drosophila". In: *The Journal of Experimental Biology* (2008).

[8] C. M. Pond. "The initation of flight in unrestrained locusts, Schistocera gregaria". In: *Journal of comparative physiology* 80.2 (1972), pp. 163–178.

[9] N. M. Smith, G. V. Clayton, H. A. Khan, and A. K. Dickerson. “Mosquitoes modulate leg dynamics at takeoff to accomodate surface roughness”. In: *Bioinspiration & Biomimetics* 14.1 (2018). DOI: 10.1088/1748-3190/aaed87.

[10] L. Li, V. E. Rutlin, C. Cassidy, L. Kus, S. Gong, M. P. Jankowski, W. Luo, N. Heintz, H. R. Koerber, C. J. Woodburry, and D. D. Ginty. “The functional organization of cutaneous low-threshold mechanosensory neurons”. In: *Cell* 147 (2011), pp. 1615–1627.

[11] D. Kolomenskiy, M. Maeda, T. Engels, H. Liu, K. Schneider, and J. Nave. “Aerodynamic ground effect in fruitfly sized insect takeoff”. In: *PLoS ONE* (2016). DOI: 10.1371/journal.pone.0152072.

[12] D. L. Altshuler, W. B. Dickson, J. T. Vance, S. P. Roberts, and M. H. Dickinson. “Short-amplitude high-frequency wing strokes determine the aerodynamics of honeybee flight”. In: *PNAS* 102.50 (2005), pp. 18213–18218.

[13] R. J. Bomphrey, T. Nakata, N. Phillips, and S. M. Walker. “Smart wing rotation and trailing-edge vortices enable high frequency mosquito flight”. In: *Nature* 554 (2017), pp. 92–95. DOI: 10.1038/nature21727.

[14] F. T. Muijres, M. J. Elzinga, J. M. Melis, and M. H. Dickinson. “Flies evade looming targets by executing rapid visually directed banked turns”. In: *Science* 344 (2014), pp. 172–177. DOI: 10.1126/science.1248955.

[15] M. H. Dickinson and F. T. Muijres. “The aerodynamics and control of free flight manoeuvres in Drosophila”. In: *Philosophical Transactions B* 371.1704 (2016). DOI: 10.1098/rstb.2015.0388.

[16] M. Karasek, F. T. Muijres, C. De Wager, B. D. W. Remes, and G. C. H. E. Croon. “A tailless aerial robotic flapper reveals that flies use torque coupling in rapid banked turns”. In: *Science* 361 (2018). DOI: 10.1126/science.aat0350.

[17] A. P. S. Bhalla, R. Bale, B. E. Griffith, and N. A. Patankar. “A unified mathematical framework and an adaptive numerical method for fluid–structure interaction with rigid, deforming, and elastic bodies”. In: *Journal of Computational Physics* 250 (2013), pp. 446–476. DOI: 10.1016/j.jcp.2013.04.033.

[18] R. Mittal and G. Iaccarino. “Immersed boundary methods”. In: *Annual Review Fluid Mechanics* 37 (2005), pp. 239–261.

[19] Jones E., T. Oliphant, P. Peterson, et al. *SciPy: Open source scientific tools for Python*. 2001. URL: `http://www.scipy.org/`.

[20] F. T. Muijres, J. Elzinga, N. A. Iwasaki, and M. H. Dickinson. “Body saccades of Drosophila consist of stereotyped banked turns”. In: *The Journal of Experimental Biology* 218 (2015), pp. 864–875. DOI: `10.1242/jeb.114280`.

5.6 Figures

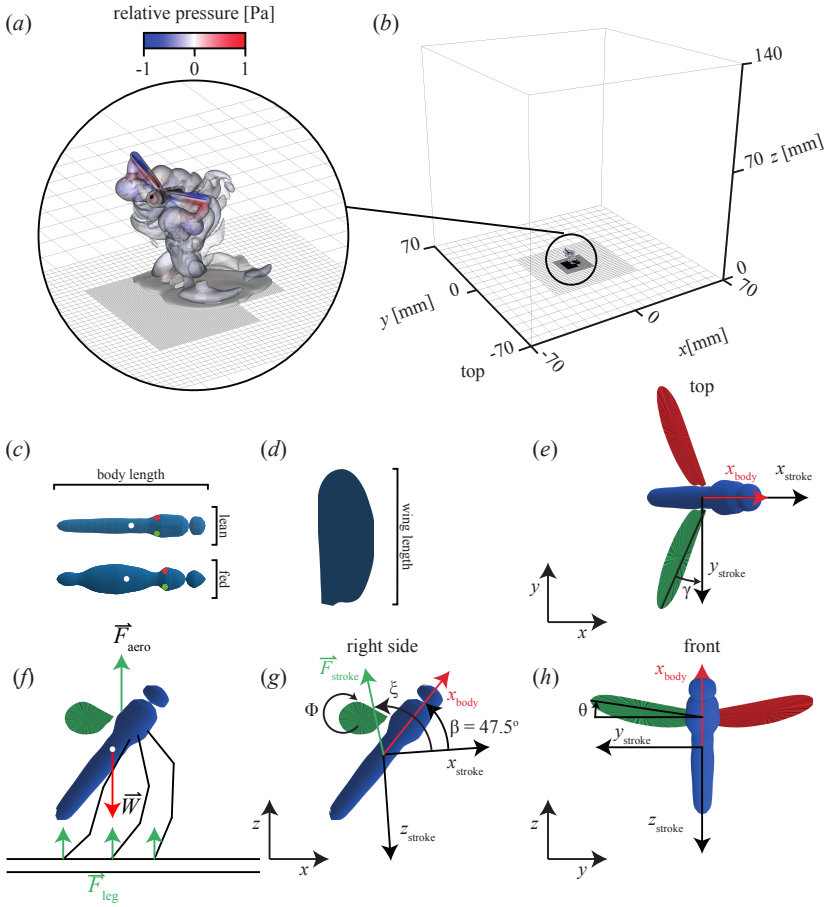

Figure 5.1: (*a*) Wake structure visualization using an iso-surface with a vorticity threshold of 1000 1/s, colored by relative pressure. (*b*) Domain setup, with in the center the solution of a take-off (see (*a*)). (*c*) – (*d*) Body and wing geometries used for the simulations, wing are isometrically scaled with length. (*e*)–(*g*) Definition of the stroke-reference frame, with in right wing (green), the left wing (red). Within in the lower-left corner the world-reference frame is shown, assuming the body is only pitched (*e*) top view, with stroke angle γ (*f*) right side view, with stroke plane angle β the force angle ξ and the wing pitch angle ϕ (*g*) front view, with the deviation angle θ.

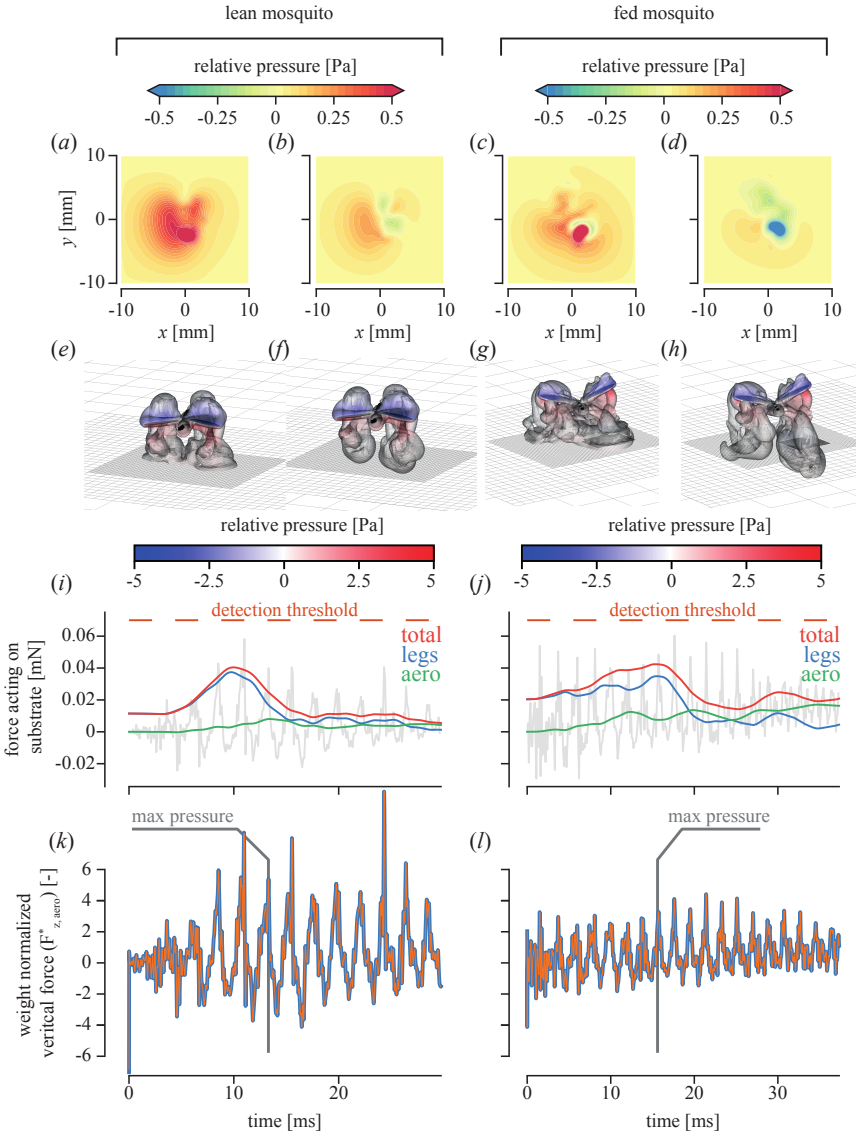

Figure 5.2: (*a*)–(*d*) Maximal pressure on the ground surface (see (*k*)–(*l*) for time) (*a*),(*c*) with ground. (*b*),(*d*) without ground. (*a*),(*b*) lean mosquito. (*c*),(*d*) fed mosquito. (*e*)–(*h*) Wake structure visualization at the point of maximum pressure on the ground, with iso-surface at the vorticity level of 1000 1/s (*e*) lean, ground (*f*)/ lean, no ground (*g*) fed, ground (*h*) fed, no ground (*i*)–(*j*) Integrated pressure over a patch of 2 cmx2 cm, light-gray line are the aerodynamic forces, orange line the filtered aerodynamic forces, blue line are the forces exerted by the legs on the ground and green line the sum of the leg and filtered aerodynamic forces (*i*) lean mosquito (*j*) fed mosquito (*k*)–(*l*) Normalized vertical forces of the lean (*m*) and fed (*n*) mosquitoes, blue no ground, red with ground.

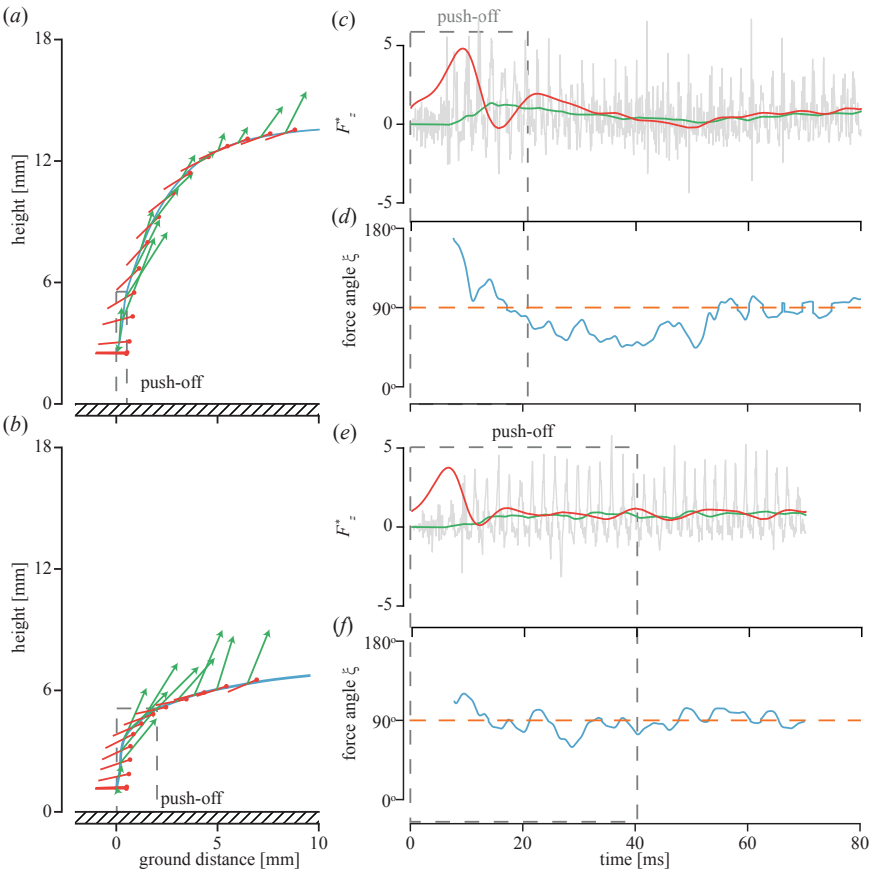

Figure 5.3: (*a*)–(*b*) Take-off dynamics of a lean and fed mosquito, respectively. The trajectory is shown by the blue curve, red lollipops indicate the body-axis at intervals of 5 ms, green arrows indicate the aerodynamic force vector at each time interval, and the dashed gray body indicates the interval when at least one leg is still on the ground. (*c*), (*e*) Normalized vertical forces for the lean and fed mosquito respectively, where total vertical forces based on the body acceleration are in red, aerodynamic forces throughout the wing-beats are in light-gray, and the Butterworth filtered aerodynamic forces in green. (*d*),(*f*) Angle ξ between the mean aerodynamic force vector and the stroke-plane (equation (5.3)) for the lean and fed mosquito respectively; crossings with the horizontal dashed line indicates where the force vector is perpendicular to the stroke-plane.

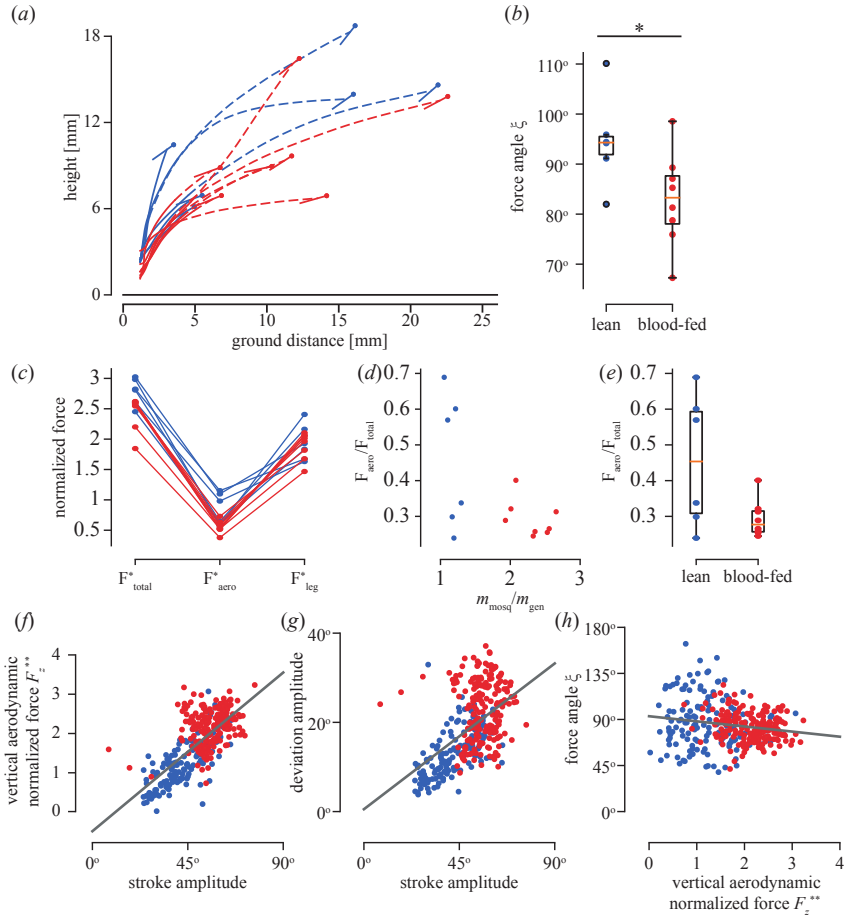

Figure 5.4: (*a*) Tracks of all the simulated mosquitoes; solid line segment: push-off phase, dashed line figment after lift-off; lollipops show body position and orientation at the end of the track for, lean (blue),and fed (red) mosquitoes. (*b*) Average force angle ξ during the take-off. Star indicates significant difference ($p = 0.038$). (*c*) Mean normalized force magnitude throughout the push-off phase of the take-off for all lean (blue) and fed red) mosquitoes, separated into total force, aerodynamic force, and leg force. (*d*) Ratio between the mean aerodynamic force and mean leg force during lift-off phase against the norm body weight, of each lean (blue dots) and fed (red dots) mosquito. (*e*) Average force ratio for the lean and the blood-fed mosquitoes (*f*) Stroke amplitude against the aerodynamic normalized forces. Gray line shows a simple linear regression fit with $p < 0.0001$ (*g*) Stroke angle amplitude against the deviation angle amplitude. Gray line shows a simple linear regression fit with $p < 0.0001$ (*h*) resultant normalized force against the force angle ξ, equation (5.3), gray line is simple linear regression with $p = 0.0007$.

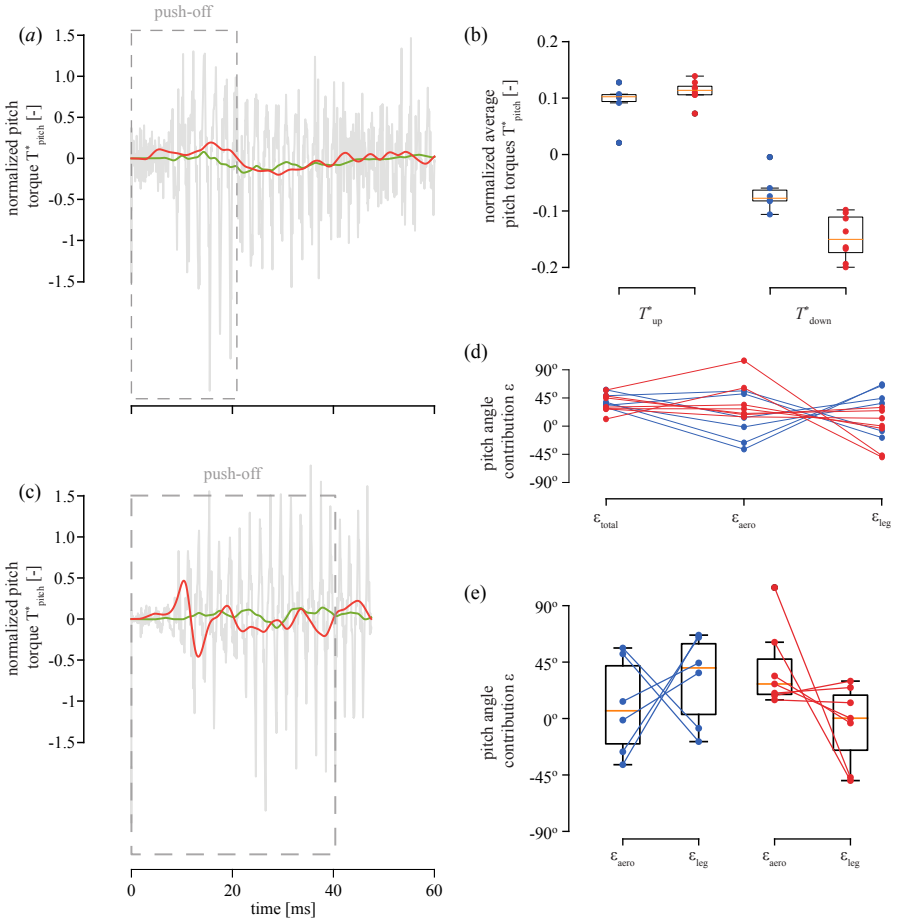

Figure 5.5: (*a*), (*c*) Pitch torques normalized by the body length and body mass for the lean and fed mosquito respectively. Aerodynamic pitch torques throughout each wing-beat are in light-gray, the equivalent Butterworth filtered aerodynamic torques are in green, required torques in red. The dashed box indicates the interval when the legs still touch the ground. (*b*) Normalized average pitch-up and pitch-down torques during take-off, blue dots indicate lean mosquitoes, red dots fed mosquitoes. (*d*) Total pitch-angle (ε_{total}, equation (5.6)), aerodynamic pitch angle (ε_{aero}) and leg pitch angle (ε_{leg}) contribution at the point of lift-off for all lean mosquitoes (blue), fed mosquitoes (red). (*e*) Pitch angle contribution for either the wings and legs for all lean mosquitoes (blue) and fed mosquitoes (red). All torques and angular momentum were normalized with the product of body weight and body length of the mosquito.

Supplementary methods

5.7 List of symbols

Table 5.1: List of symbols

Variable	*units*	*description*
$\boldsymbol{A}_{\text{stroke}}$		Rotation matrix from the body reference frame to the stroke reference frame
$\boldsymbol{A}_{\text{body}}$		Rotation matrix from the world-reference frame to the body reference frame
β		Angle between the stroke-plane and the body axis
$\vec{\varepsilon}$		Angle produced by a torque around a single axis during the push-off phase
$\varepsilon_{\text{aero}}$		Angle produced by the aerodynamic torque around the pitch axis during the push-off phase
ε_{leg}		Angle produced by the leg torque around the pitch axis during the push-off phase
$\vec{F}_{\text{total}}$	N	Forces derived from the body accelerations
$\vec{F}_{\text{leg}}$	N	Forces exerted by the legs
$\vec{F}_{\text{aero}}$	N	Aerodynamic forces produced by the mosquito
$F_{\text{substrate}}$	mN	Force acting perpendicular to the substrate caused by the interaction of the wake with the substrate
$\vec{F}^*$		Specific weight normalized forces $\vec{F}^* = \vec{F}/(m_{\text{mosq}}g)$
$\vec{F}^{**}$		Generic weight normalized forces $\vec{F}^{**} = \vec{F}/(m_{\text{gen}}g)$
γ		Stroke angle
$\boldsymbol{I}$	kg m^2	Mass moment of inertia
l_{mosq}	mm	Specific body length of the mosquito
$\vec{\mathcal{L}}_{\text{total}}$	kg m^2 s^{-1}	Angular momentum derived from the body rotation
m_{mosq}	mg	Specific body mass of the mosquito
m_{gen}	mg	Generic body mass of 1mg
$\vec{\omega}$	s^{-1}	Angular velocity
ϕ		Rotation angle
θ		Deviation angle
$\vec{T}_{\text{total}}$	Nm	Torques derived from the total angular momentum $\mathcal{L}_{\text{total}}$
$\vec{T}_{\text{leg}}$	Nm	Torques produced by the legs
$\vec{T}_{\text{aero}}$	Nm	Aerodynamic torques produced by the mosquito
T_{pitch}		Normalized pitch torque
$\vec{T}^*$		Specific weight and body length normalized torques $\vec{T}^* = \vec{T}/(m_{\text{mosq}}g l_{\text{mosq}})$
$\vec{V}$	ms^{-1}	Velocity of the mosquito in the world reference frame, derived from the kinematics
$\vec{W}$	N	Weight vector in the world reference frame
ξ		Angle between the force vector and the stroke-plane

5.8 CFD

The spatial and time resolutions were chosen after performing a mesh and time-step study. The mesh-study was performed first using a wing that pitches up ($\omega_{\text{pitch}} = 3000\,\text{rad}\,\text{s}^{-1}$) whilst moving forward ($\omega_{\text{stroke}} = 1750\,\text{rad}\,\text{s}^{-1}$), for a range of mesh sizes (Figure 5.6c) with a time-step of $\Delta t = 1 \cdot 10^{-7}$ s. The effect of the mesh size on the force at the extraction point (Figure 5.6 a, c) is small but decreasing mesh size comes

at a vast increase in the amount of cells. We have chosen the mesh-size of $\Delta x = 3.04 \cdot 10^{-5}$ mm, which falls within a small error from the finer mesh; in contrast the computation time increases steeply due to the large number of cells needed. Choosing this mesh-size led to an average use of 4 million cells for each simulation. After choosing the mesh-size, the time-step was chosen in a similar fashion. For the same simulation as used for the mesh study ($\omega_{\text{pitch}} = 3000\,\text{rad}\,\text{s}^{-1}$,$\omega_{\text{stroke}} = 1750\,\text{rad}\,\text{s}^{-1}$), a range of time-steps where tested (Figure 5.6d). The effect of the time-step (Figure 5.6b, d) is larger than that of the mesh-size. We chose a time step $\Delta t = 1 \cdot 10^{-7}$ s, because further refinement has little effect on the solution, but the number of steps needed does increase drastically.

The computational fluid dynamics solver is validated using the kinematics of a steady hovering fruit fly and the resulting forces published earlier [20]. The forces predicted by the solver on the third wing-beat show a good match with the forces found by the robotic flapper (see Figure 5.6f) [17].

The wake-structure for both the lean mosquito and the fed mosquito are shown in Figure 5.7 and 5.8 respectively. Both figures show a front view (a), perspective view (b), top view (c) and side view (d). Both figures show the complex flow-field around a mosquito during take-off.

5.9 Supplementary figures

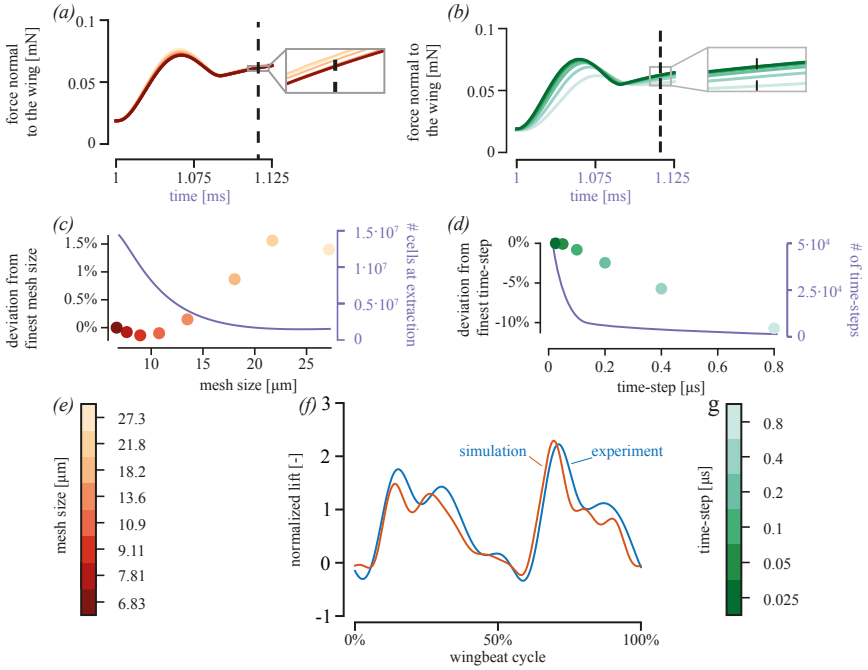

Figure 5.6: Mesh-study, time-step study and solver validation. (a) Forces for a pitching fruit fly wing ($\omega_{\text{pitch}} = 3000\,\text{rad}\,\text{s}^{-1}$, $\omega_{\text{stroke}} = 1750\,\text{rad}\,\text{s}^{-1}$) for several mesh sizes (see Figure 5.6 e). (b) Forces for a pitching fruit fly wing ($\omega_{\text{pitch}} = 3000\,\text{rad}\,\text{s}^{-1}$, $\omega_{\text{stroke}} = 1750\,\text{rad}\,\text{s}^{-1}$) for several time-steps (see Figure 5.6g). (c) Force deviation from finest mesh at extraction point (pitch angle$= 45^{\text{o}}$) for several mesh sizes (see Figure 5.6e), in purple an estimate of the number of cells at extraction. (d) Force deviation from finest time-step at extraction point ($\omega_{\text{pitch}} = 45^{\text{o}}$) for several time-steps (see figure 5.6g). (e) Color-legend for all the mesh sizes used in panel (a) and (c). (f) Solver validation using the kinematics of a hovering fruit fly [20], red shows simulation results, and blue shows robotic experiment results [20] . (g) Color-legend for all time-steps used in panel (b) and (d).

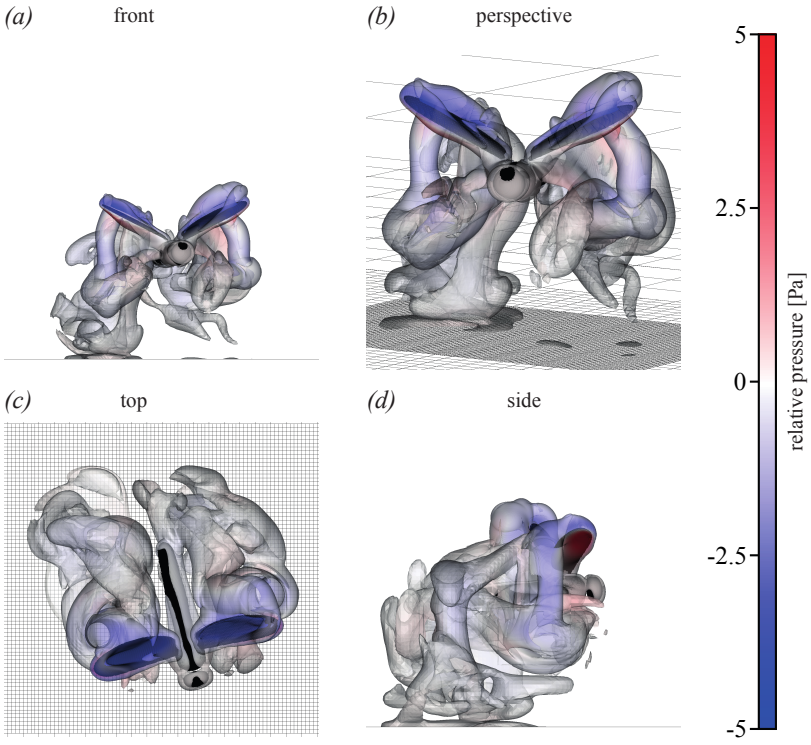

Figure 5.7: Wake-structure visualisation around a lean mosquito during the take-off. The iso-surface was chosen at a vorticity threshold of 2000 s^{-1}. (a) front view (b) perspective view (c) top view (d) side view.

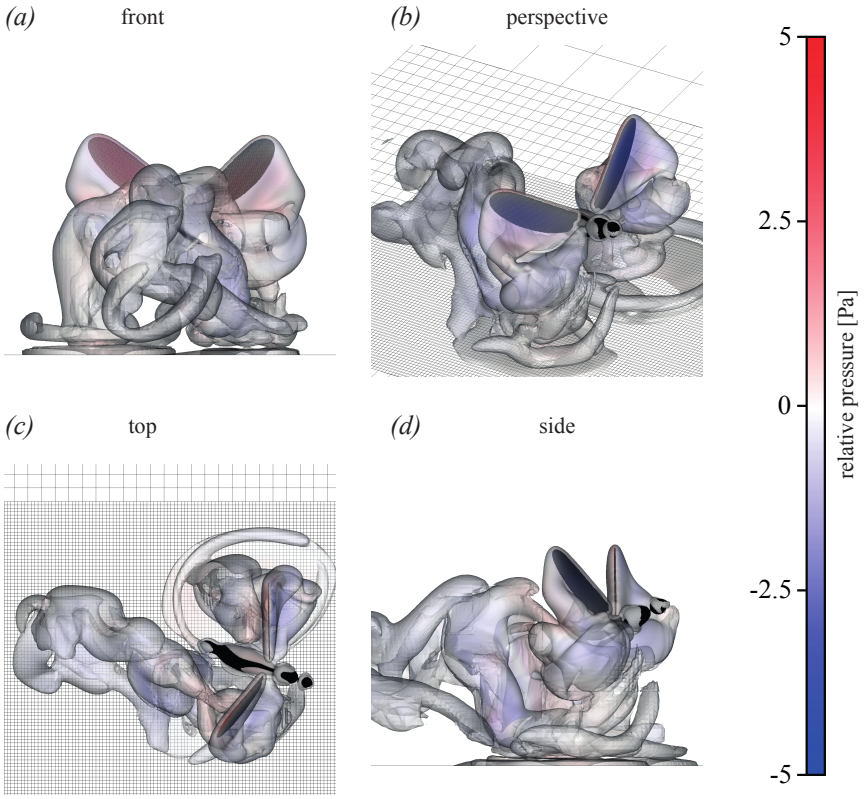

Figure 5.8: Wake-structure visualisation around a blood-fed mosquito during the take-off. The iso-surface was chosen at a vorticity threshold of 2000 s^{-1}. (a) front view (b) perspective view (c) top view (d) side view.

5.10 Supplementary legends

Database The forces, torques and kinematics of all the simulations used in this study are provided in the electronic supplementary file "`database_S1.h5`". This is an open-source HDF5 database file format that can be read with commonly-used scripting languages such as Matlab and Python. The database consists of three groups: "Lean mosquitoes", "Blood-fed mosquitoes" and "Ground effect". These groups have more groups inside which conincide with the data-set per simulation. In this set the following data can be found: the forces from CFD in the world reference frame, the torques from CFD in the stroke-plane reference frame, the forces from inverse dynamics, the torques from inverse dynamics, and the geometry used in the simulations. The

sequence name consists of the date and the sequence number used in the study from which we got the kinematics [4].

Movie S1 Movie of the CFD simulation results of the take-off of the lean mosquito shown in Figure 5.7. The movie shows the mosquito and iso-surfaces at a vorticity threshold of 2000 s^{-1}, colored according to Figure 5.7. Playback is slowed down approximately 900 times.

Movie S2 Movie of the CFD simulation results of the take-off of the fed mosquito shown in Figure 5.8. The movie shows the mosquito and iso-surfaces at a vorticity threshold of 2000 s^{-1}, colored according to Figure 5.8. Playback is slowed down approximately 900 times.

Chapter 6

General discussion

Wouter G. van Veen

6.1 Introduction

I started this thesis with a simple and seemingly humble question: *How do insects fly?* In the first three chapters, I used large parametric studies to uncover the aerodynamics behind a constant pitch rate motion, a stroke acceleration motion and a pitch acceleration motion. In my last research project, I studied the take-off maneuver of several lean and blood fed mosquitoes to find the effect of the interaction with the substrate, of both the fluid and the legs of the animal.

In this chapter, I will use the aerodynamic mechanisms found in the first three chapters to study hovering flight of the fruit fly (*Drosophila hydei*) [1] and the malaria mosquito (*Anopheles coluzzii*) [2]. To do this, I developed a quasi-steady aerodynamic model, which I applied step by step to the kinematics of the two insects. Furthermore, I used computational fluid dynamics (CFD) [3] to find the total forces of the flying insects. The forces computed by the quasi-steady model were compared with these total forces and data from literature.

At the end of this chapter, I used the quasi-steady model on the kinematics of the take-off of the lean and fed mosquitoes. The forces I found in chapter 5 served as a comparison for the output of the quasi-steady model.

6.2 Forces of hovering flight

With the use of computational fluid dynamics simulations, I calculated the aerodynamic forces of a fruit fly and a mosquito during hovering flight. The force output of these two simulations were used as a comparison for the quasi-steady model that I developed in section 6.3. In section 6.2.1, I will briefly introduce the setup I used for these simulations. In section 6.2.2, I will discuss the outcome of these simulations.

6.2.1 Setup

Reference frames and kinematics

I used four reference frames of which three were right-handed reference frames: the world reference frame, the stroke plane reference frame and the wing reference frame,

and one aerodynamic reference frame. The forces were computed in the world reference frame, with the *z*-axis opposing the gravity vector (figure 6.1 *a*). The stroke plane reference frame was defined to the body of the animal with the *z*-axis pointing down and the *x*-axis pointing forward and the *y*-axis pointing to the tip of the right wing at mid-stroke (figure 6.1 *a–c*). Finally, the wing reference frame was defined with respect to the stroke plane reference frame with three Euler angles: the stroke-angle γ, the deviation angle θ and the pitch angle ϕ.

The wing was first rotated with the stroke-angle around the *z*-axis of the stroke plane reference frame, with a positive stroke angle being a rotation towards the ventral side of the animal (figure 6.1 *f*). Secondly, the wing is rotated around the *x*-axis of the intermediate reference frame with the deviation angle (figure 6.1 *d*). Finally, the wing is rotated around its span with the pitch angle ϕ (figure 6.1 *e*). The three Euler angles for the fruit fly and mosquito for hovering flight were based on previous results [1, 2] (figure 6.3 *a–c*).

In addition, to the three reference frames, I included an aerodynamic reference frame which depends on the direction of motion of the wing (figure 6.2). The lift was defined perpendicular to the direction of motion of the wing. The drag was defined parallel to the direction of motion of the wing. This reference frame was also used to define the angle-of-attack, stroke rate, stroke acceleration, pitch rate, and the pitch acceleration.

Computational setup

I used an immersed boundary method solver (IBAMR) [3] to simulate the forces acting on a wing of a hovering fruit fly and mosquito. I used the same setup as I did throughout this thesis, with a domain of 5 cm x 5 cm x 5 cm, a time-step of $\Delta t = 1 \cdot 10^{-7}$ s, and adaptive mesh refinement with the finest grid size $\Delta x = 0.01$ mm. This resulted in a mesh of approximately four million cells and for the fruit fly 53 000 time-steps per wingbeat and for the mosquito 17 000 time-steps per wingbeat. For a verification and validation of the solver refer to the appendix of chapter 2.

6.2.2 Results

The forces normal to the wing surface of the fruit fly and the mosquito (figure 6.3 *f*) are presiding over the viscous forces (figure 6.3 *d*, *e*). The force along the chord (figure 6.3 *a*) has a small contribution to the overall forces. The chord-wise force

points towards the trailing edge throughout the wingbeat, which reduces the lift and increases the drag.

The lift and drag components (figure 6.3 *g*, *h* respectively) are computed based only on the pressure force. The resulting lift and drag will be higher throughout the wingbeat if the viscous forces were included. I chose to remove the effect of the viscous forces, because almost all models I developed in this thesis are only based on the forces normal to the wing surface. Obviously, figure 6.3 *a* shows the importance of models that explicitly model the viscous force component.

The drag (figure 6.3 *h*) shows a large discontinuity at stroke-reversal. This discontinuity is actually caused by the definition of the aerodynamic reference frame, that makes the drag dependent on the direction of motion of the wing. This discontinuity is not present in the forces in the wing reference frame (figure 6.3 *d–f*). However, this jump in forces is not some mathematical oddity. The mosquito, and in lesser amount the fruit fly, are both experiencing a negative drag directly after stroke reversal (around 50 % wingbeat progress). This negative drag means that the insect is actually aided in the acceleration of its wing at the start of the stroke. The lift of the fruit fly reaches a maximum after stroke reversal for the backward stroke. For the mosquito, this maximum is reached mid-stroke for the forward stroke (figure 6.3 *g*).

6.3 From wing motion to force production

In this section, I will gradually develop a quasi-steady model based on the aerodynamic mechanisms I found in this thesis. I will compare the quasi-steady model with the results of the CFD found in section 6.2.2. In each section, I will compare the sum of all aerodynamic mechanism up to that point with the sum of all aerodynamic mechanisms before that point. I will start with the stroke rate forces in section 6.3.1. In section 6.3.2, I will add the stroke pitch interaction forces to the model. Then I will add the pitch rate forces in section 6.3.3. After adding the stroke rate and pitch rate to the model, I will add the stroke acceleration in section 6.3.4. Finally, in section 6.3.5 I will add the pitch acceleration forces and the stroke pitch acceleration interaction forces. In this last step, the quasi-steady model based on the aerodynamic mechanisms described in this thesis is complete. I will end this section with a discussion on the roles which the quasi-steady model has in section 6.3.7.

6.3.1 The stroke motion: setting a baseline

The forces associated with the stroke motion of the wing with a constant stroke rate and constant angle-of-attack are generally correlated with the presence of the leading edge vortex (LEV) [4, 5, 6]. In the appendix of chapter 3, I computed the stroke rate forces based on a relative simple model, which can be written as

$$F_{sr} = \rho C_{sr} \sin(\alpha)\, \omega_s^2 S_{yy} \text{sign}(\omega_x), \tag{6.1}$$

where, ρ is the fluid density, C_{sr} the stroke rate force coefficient, α the angle-of-attack, ω_s the stroke rate, S_{yy} the span-wise second moment of area and ω_x the angular rate around the *x*-axis in the wing reference frame. The stroke rate and angle-of-attack both depend on the direction of motion of the wing. To robustly quantify in which direction the wing is moving, I chose to use the sign of the angular rate in the wing reference frame around the *x*-axis (ω_x). From the definition of the stroke rate (ω_s and the angle-of-attack α in figure 6.2 *b*, and *d*), I derived the following two equations:

$$\omega_s = \sqrt{\omega_x^2 + \omega_z^2}, \tag{6.2}$$

$$\alpha = \tan^{-1}\left(\frac{\omega_x}{\omega_z}\right) \text{sign}(\omega_x). \tag{6.3}$$

The force coefficient was determined in chapter 3 (appendix D) as $C_{sr} = 1.56$. I used this coefficient in combination with the model (equation (6.1)) to compute the lift and drag for the fruit fly and mosquito (figure 6.4).

For both the fruit fly and the mosquito, the stroke rate forces produce a strictly positive lift and drag (figure 6.4), by definition. Around mid-stroke both force components reach their maximum. For the fruit fly, it appears that both components are reasonably well predicted by the stroke rate forces alone, but for the mosquito the stroke rate forces lead to an under-prediction of the lift and drag (figure 6.4 *b*, *d*). This under-prediction of the forces by the stroke rate forces is in line with previous studies for the fruit fly [1] and for the mosquito [7].

The model for the stroke rate forces F_{sr} (equation (6.1)) resembles the normal force model found previously [8] (figure 6.5). If I only compare the results at a single angle-of-attack ($\alpha = 46°$), the model presented here is close to earlier found models [9]. Interestingly, some models based on the results of robotic flappers lead to a higher estimation of the coefficient of lift and the coefficient of drag [5, 10, 11, 12].

The model developed for mosquito flight used interpolation to find the dependence of the coefficient on the angle-of-attack [7]. Therefore, I took the coefficient of lift and the coefficient of drag at an angle-of-attack of 45°, which resulted in $C_l \approx 1 - 1.05$ and $C_d \approx 1.1 - 1.5$ (figure 9, in Bomphrey 2017 [7]). These results are considerable lower than the coefficient of lift and drag I find at an angle-of-attack of 45° ($C_l = 1.56$). Partially, this might be explained by the fact that in the former study the lift is measured after three revolutions of the wing, which means that the wing is rotated through its own wake. However, the wake from continuous revolutions has a velocity moving with the wing due to the spin-up of the fluid, whereas for a reciprocal movement of the wing the velocity of the previous stroke moves against the movement of the wing. Therefore, I consider the method I discuss in this thesis more accurate than the method presented in literature.

6.3.2 The combined stroke & pitch motion: stroke pitch interaction

The forces as a result of a pitching wing and a wing that has a stroke motion is modeled as

$$F_{sr-pr} = \begin{cases} \rho \left(d^*_{pr,u} \omega_p^2 \omega_s S_{x|x|} \sqrt{S_{yy}} + f^*_{pr,u} \omega_p \omega_s S_{yy} \right) \text{sign}\left(\omega_x\right) & \omega_p > 0 \\ \rho \left(d^*_{pr,d} \omega_p^2 \omega_s^2 S_{x|x|} \sqrt{S_{yy}} + f^*_{pr,d} \omega_p \omega_s^2 S_{yy} \right) \text{sign}\left(\omega_x\right) & \omega_p < 0, \end{cases} \tag{6.4}$$

where ω_p is the pitch rate, $S_{x|x|}$ the asymmetric second moment of area, and $d^*_{pr,u}$, $f^*_{pr,u}$, $d^*_{pr,d}$ and $f^*_{pr,d}$ the coefficients that link the kinematics to the force generation (see chapter 4).

Here, I do make a big assumption, namely that the geometrical scaling for a wing pitching down is the same as for a wing pitching up. I chose to use the model that differentiates between pitch up and pitch down in favor of the model discussed in chapter 2, because I consider the later model an advancement of the earlier one.

The pitch rate ω_p coincides with the pitch rate around the span in the wing reference frame. Because the pitch rate changes definition as the wing changes its direction after stroke reversal (figure 6.2 *b* and *d*), I included the sign of the angular rate around the x axis, which results in a simple equation for the pitch rate, which is written as

$$\omega_p = \omega_y \text{sign}\left(\omega_x\right), \tag{6.5}$$

where ω_y is the angular rate around the pitch axis in the wing reference frame. For both insects, the inclusion of the stroke pitch interaction results in a higher peak force for the lift (figure 6.6 *a*, *b*). The lift and drag are predicted reasonably well with the combination of the stroke rate model, and the stroke pitch interaction model. Notably absent are the large negative peaks in the drag of the mosquito (figure 6.6 *d*).

The prediction of the stroke pitch interaction forces introduces a discontinuity when the wing is changing from pitch up to a pitch down motion and visa-versa. I assumed that this change from models happens instantaneously. However, in reality a smoother transition from one model to the other is probably present. More research is needed to uncover how the transition from a pitch up to a pitch down motion occurs and how the forces are influenced.

The model found in the second chapter did not discriminate between a wing that is pitching up or down. Actually, the assumption that a wing that pitches up produces the same forces as a wing that pitches down is commonly applied [5, 1, 13, 14, 15]. The model from chapter 2 indeed does include these negative peaks in both the lift and drag (figure 6.7 *a*, *b* and *c*, *d* respectively). These negative peaks are often associated with the hypothesis that Dipteran flappers use delayed wing rotation to generate torques required for maneuvering [6, 1]. This delayed wing rotation happens around stroke reversal, where the wing is pitching down. This new model shows that the stroke pitch interaction forces due to a wing that is pitching down is impaired compared to a wing that is pitching up. Therefore, it might be that other aerodynamic mechanisms are more relevant for predicting the torque production around stroke-reversal.

There are several models present in literature that model the stroke pitch interaction forces as a function of the kinematics and wing morphology [15, 14, 13]. Each of these models use the same scaling for the wing morphology, namely:

$$S_{xy} = \int_{c_{te}}^{c_{le}} yx^2 dx. \tag{6.6}$$

Because the model presented in equation (6.4) is dependent on the direction of rotation and the coefficients in equation (6.4) on the direction of the acceleration (see chapter 4, table 4.2), I decided to use the much simpler model presented in chapter 2 for the comparison with literature. This simpler model shows good agreement with the more complex model for a wing pitching up (figure 6.7).

The model presented in chapter 2 used a different morphological scaling than presented in equation (6.6). For the sake of comparison I recomputed the coefficients

found in literature by multiplying them with the fraction $S_{xy}/\sqrt{S_{xx}S_{yy}}$ for both the fruit fly and the mosquito.

The rotational lift coefficient based on the scaling parameter S_{xy} (equation (6.6)) reported in literature is $C_{sr-pr} = 1.55$ [15, 13, 14]. Here I assume that the reported value of $C_{sr-pr} = 0.55$ in Nakata 2015 is actually a typo and should be 1.55[14]. When I multiply this coefficient with the scaling fraction discussed earlier I come to a coefficient for the fruit fly of $C_{sr-pr} = 1.02$ and for the mosquito of $C_{sr-pr} = 1.06$. The coefficient found in chapter 2 was $C_{sr-pr} = 2.08$,which means that the model discussed in this thesis will result in stroke pitch interaction forces that are almost a factor two higher than the forces predicted previously in literature.

6.3.3 The pitch motion: pitch rate

The forces as a result of a wing pitching up or down can be modeled as (see chapter 4)

$$F_{pr} = \rho a^*_{pa} \omega_p^3 S_{x|x|} + \rho b^*_{pa} \omega_p S_{x|x|}, \tag{6.7}$$

where the pitch rate was obtained in the previous section (section 6.3.2, equation (6.5)), $S_{x|x|}$ is the asymmetric second moment of area, and a^*_{pa}, b^*_{pa} are coefficients that describe the relation between the pitch rate and the pitch rate forces. For the fruit fly, the pitch rate forces cause a dip in the lift forces directly after stroke reversal (figure 6.8 *a*). For the mosquito, the pitch rate forces also show a dip in the lift directly after stroke reversal for the forward stroke (figure 6.8 *b* at $\approx 10\,\%$). However, for the backward stroke the pitch rate forces are first positive, and then become negative. At around mid-stroke of both the forward stroke and backward stroke, the pitch rate forces have a positive contribution to the lift.

The contribution of the pitch rate forces to the drag of the fruit fly and the mosquito are negative after stroke reversal (figure 6.8 *c*, *d*). A negative drag means that the force vector is pointed towards the direction of motion of the wing. Therefore, the pitch rate forces contribute to the acceleration of the wing at the start of the forward stroke and backward stroke. In addition, the contribution of the pitch based forces to the drag becomes positive around mid-stroke for both insects. A positive drag is acting in the opposite direction to the wing motion. This means that the pitch rate forces also aid in the deceleration of the wing at the end of the stroke, which might reduce

the cost of flight.

The model proposed in equation (6.7) is similar to other models in literature [14]. As before, the main difference is the geometrical scaling with the asymmetric scaling parameter $S_{x|x|}$ compared to the previously used scaling parameter S_{xy}. To compare the coefficient directly, I multiplied the coefficient from literature with the factor $S_{xy}/S_{x|x|}$. The coefficient from literature is actually based on the maximum coefficient of drag [14], which is found at 3.2 [16]. If I multiply this value with the factor of scaling parameters, I find for the fruit fly a coefficient of 8.59 and for the mosquito 9.60. Both these values are considerably higher than the coefficient 2.08 I found in chapter 2 and in chapter 4.

Apart from the difference in coefficients the geometrical scaling is also different. The geometrical scaling proposed in this thesis ($S_{x|x|}$) takes into account that a symmetrical wing does not generate pitch rate forces. Whereas the geometrical scaling S_{xy} does not take this into account, and clearly overlooks the importance of the asymmetrical placement of the wing pitch axis with respect to the symmetry axis.

6.3.4 Wing accelerations: stroke acceleration

In chapter 3, I showed that the stroke acceleration influence the aerodynamic forces. The influence of the stroke motion on the aerodynamic forces consists of an interaction term F_{sr-sa} and an independent term F_{sa}. The influence of the interaction term on the forces is minimal and therefore I ignore this term here. The stroke acceleration forces can be modeled as

$$F_{sa} = \rho \left(d^*_{sa-\alpha a} \alpha^2 + d^*_{sa-\alpha b} \alpha \right) \dot{\omega}_s \sqrt{S_{sedov} S_{yy}}. \tag{6.8}$$

Where $\dot{\omega}_s$ are the stroke accelerations, S_{sedov} a geometrical scaling parameter based on the two-dimensional model developed by (Sedov 1965)[17], and $d^*_{sa-\alpha a}$, $d^*_{sa\alpha b}$ are coefficients that describe the relation between the angle-of-attack and the stroke acceleration forces. I obtained the angle-of-attack in a previous section (section 6.3.1, equation (6.3)), and the stroke acceleration is derived from the stroke rate (equation (6.2)) as

$$\dot{\omega}_s = \frac{d}{dt} \left(\sqrt{\omega_x^2 + \omega_z^2} \right). \tag{6.9}$$

The stroke acceleration forces have a positive contribution to the lift at the start of the stroke, directly after stroke reversal (figure 6.9 *a*, *b*). At the end of the forward stroke and backward stroke, the contribution to the lift becomes negative due to the deceleration of the wing.

The contribution to the drag is positive at the start of the forward and the backward stroke (figure 6.9 *c*, *d*). At mid-stroke, the contribution becomes negative, working in opposite direction of the wing acceleration. The stroke accelerations on average have a positive contribution to the drag (6.12). Thus, the hypothesis posed in literature, that the stroke acceleration forces are irrelevant for the wingbeat averaged forces, is not valid [18].

Overall, the prediction of the lift and drag of the fruit fly appears to be quite good after the addition of the stroke acceleration forces. Especially the lift component only shows a small overshoot for the fruit fly, but for the mosquito it is almost equal. However, this does not mean that with the use of the models up to now we can explain insect flight. I will discuss this in more detail in section 6.3.7.

Others also have included the stroke accelerations (added mass) in their models, based on a two-dimensional model [17, 19, 20, 15, 21, 22]. These models are similar to the model presented in equation (6.8), with two noticeable differences: the dependence on the angle-of-attack, and the morphological scaling. The dependence of the angle-of-attack in these other models is based on the acceleration normal to the wing surface (e.g. $\dot{\omega}_s \sin\alpha$), whereas the model I present here uses a quadratic relation with the angle-of-attack. Actually these two methods of scaling with the angle-of-attack are not all that different.

What is different is the morphological scaling through the parameter $\sqrt{S_{yy} S_{\text{sedov}}}$ in the model presented here, and S_{sedov} in the other models. In the model presented here, the variation of the wing along the *y*-axis is an important scaling parameter for the stroke acceleration forces.

I evaluated the model presented here at an angle-of-attack $\alpha = 45°$ for both the fruit fly and the mosquito. For both species, the results from this model compared with literature is similar for the fruit fly:
$\left(d^*_{sa-\alpha a}\alpha^2 + d^*_{sa-alphab}\alpha\right)\sqrt{S_{\text{sedov}} S_{yy}} = 2.74 \cdot 10^{-12}\,\text{m}^4$ against $\pi/4 \sin(\alpha)\, S_{\text{sedov}} = 2.65 \cdot 10^{-12}\,\text{m}^4$ and for the mosquito:
$\left(d^*_{sa-\alpha a}\alpha^2 + d^*_{sa-alphab}\alpha\right)\sqrt{S_{\text{sedov}} S_{yy}} = 1.87 \cdot 10^{-12}\,\text{m}^4$ against $\pi/4 \sin(\alpha)\, S_{\text{sedov}} = 1.6 \cdot 10^{-12}\,\text{m}^4$. This means that the approximation based on the two-dimensional

model is capable of predicting the stroke acceleration forces quite well.

6.3.5 Wing accelerations: pitch-acceleration

The contribution of the pitch-acceleration to the overall forces consists of two terms: the pitch acceleration forces F_{pa} and the stroke-pitch acceleration forces F_{sr-pa}. I will first discuss the pitch acceleration forces and end the development of the model with the stroke-pitch acceleration interaction forces.

The pitch acceleration forces are linear dependent on the pitch acceleration, and can simply be modeled as

$$F_{pa} = \rho \hat{c}^*_{pa} \dot{\omega}_p S_{x|x|}, \tag{6.10}$$

where $\hat{c}^*_{pa}$ is a coefficient that describes the relation between the pitch acceleration $\dot{\omega}_p$ and the pitch acceleration forces. The pitch acceleration $\dot{\omega}_p$ needs to be determined before the direction of the pitch motion is determined. This can be done by taking the angular rate around the span and taking the derivative, which results in

$$\dot{\omega}_p = \frac{d}{dt} \left(\omega_y \right) \text{sign} \left(\omega_x \right). \tag{6.11}$$

The pitch acceleration forces affect lift around the start of the forward and backward stroke the most (figure 6.10 *a*, *b*). The fruit fly generates a small amount of pitch acceleration forces at the start of each stroke. However, the lift of the mosquito is largely impacted by the pitch acceleration forces.

The drag shows a similar trend as the lift, where the largest influence is at the start of the forward stroke and backward stroke (figure 6.10 *c*, *d*). Directly after stroke-reversal a negative contribution to the drag is provided for both the fruit fly and mosquito. This negative contribution means that the pitch acceleration forces actually provide a thrust, instead of a drag. At around $\approx$ 10 % after stroke reversal, the contribution to the drag becomes positive.

The linear scaling of the pitch acceleration forces with the pitch acceleration is in line with previous results [19, 20]. These previous models where based on a two-dimensional model [17]. The difference between these models and the model presented here is the geometrical scaling. Therefore, I recomputed the coefficient used in the models of the previous studies by multiplying them with a factor of the different scaling factors $S_{\text{sedov}} S_{x|x|}$. For the fruit fly, this results in a coefficient of 2.77 and

for the mosquito of 2.63. For both insects, the "old" coefficient is considerable larger than the coefficient $\hat{c}^*_{pa} = 1.27$ discussed in this section.

The last term of the quasi-steady model are the stroke pitch acceleration forces. These forces model the interaction between the stroke rate and the pitch acceleration of the wing. In chapter 4, I proposed a model for these forces as

$$F_{sr-pa} = \begin{cases} \rho \hat{g}_{pr,d} \dot{\omega}_p \omega_s^2 & \omega_p < 0, \dot{\omega}_p > 0 \\ 0 & \text{otherwise.} \end{cases} \tag{6.12}$$

Shining in its absence is the geometrical scaling. Because I only varied the wing morphology for the wings that are pitching up, I was unable to determine the geometrical scaling of the stroke pitch acceleration forces. Therefore, I assumed that the geometrical scaling of the stroke pitch acceleration forces is the same as the geometrical scaling for the pitch acceleration forces, namely: $S_{x|x|}$.

For the fruit fly, the stroke pitch acceleration forces barely have an effect on the lift and drag (figure 6.11 *a*, *c*). For the mosquito, a slight reduction of the lift and the drag is found at the start of the forward and backward stroke around $\approx 20\,\%$ after stroke reversal (figure 6.11 *b*, *d*). However, even for the mosquito the effect on the forces due to the interaction between the stroke rate and the pitch acceleration is minimal.

6.3.6 The total forces: fruit fly vs mosquito

In the previous section, I finished the quasi-steady model based on the aerodynamic mechanisms found in this thesis. Throughout each section, I applied each aerodynamic mechanism to the kinematics of the fruit fly and the mosquito. Here, I took the average of the lift and the drag for the forward and the backward stroke (figure 6.12). For the fruit fly, the lift and drag are mostly influenced by the stroke rate motion of the wing. The lift of the forward stroke is the component that is influenced the most by the other aerodynamic mechanisms (figure 6.12 *d*).

For the mosquito, the stroke rate motion remains a large influence. However, the other components take up to half of the total forces (figure 6.12). Especially the pitch acceleration forces play a huge role in the lift of the mosquito, and in lesser amount in the drag. Interestingly, the pitch rate forces play almost no role in the average lift forces, which is not in line with previous research [7]. However, the pitch rate forces

do have a big contribution to the drag forces.

To summarize, the stroke rate motion appears to be of great importance for both flappers. However, for low-amplitude high-frequency flappers it appears that the other aerodynamic mechanisms greatly influence the aerodynamic forces.

6.3.7 Bringing it all together: explanatory or predictive?

The final quasi-steady model presented at the end of the previous section seems to be a poor model in predicting the forces of either the fruit fly or the mosquito (section 6.3.5, figure 6.11). One could even argue that if we left out the last two steps, and took the model in figure 6.9, that the model would perform better. Before I will dive into the reasons why the prediction might deviate from the actual forces, I want to start with a more philosophical question: What kind of role does the model have?

I see the two roles being used mixed together throughout literature: explanatory and predictive. The predictive role is straightforward: Do the forces predicted by the quasi-steady model overlap with forces generated by the actual insect? However, the explanatory role has the goal to understand insect flight by linking part of the motion of the wing to the forces that are being generated [23]. By mixing the two goals one can easily come to the conclusion that if the model predicts the forces correctly, then it must also be able to explain the forces correctly.

For instance, when the rotational forces were described for the fruit fly, the model led to a better prediction of the forces [5, 13]. Actually, if we look at a quasi-steady model where only the stroke rate forces and the stroke pitch rate forces are present the prediction is rather good for the lift of the fruit fly (see section 6.3.1 and 6.3.2, figure 6.6 *a*). However, this does not mean that the fruit fly is not influenced by the other aerodynamic mechanisms found in this thesis. Actually, the aerodynamic mechanism that is "important" for the fruit fly is chosen through the order to which we apply the models to the kinematics. For instance, if we would have started with the pitch acceleration forces and ended with the stroke rate forces the latter would seem to be the cause of the over prediction of the quasi-steady model.

Another example is found in a recent discovery that the pitch rate forces are the key mechanism behind mosquito flight (rotational drag, see section 6.3.3) [7, 14]. A simple quasi-steady model based on the stroke rate forces and the stroke acceleration forces, was compared to the results from computational fluid dynamics. The difference between the aerodynamic forces computed by the quasi-steady model and the

CFD results were ascribed to the rotation of the wing. However, in this thesis I have shown that a direct computation of the pitch rate forces does not improve the predictive capabilities of the quasi-steady model for either the lift or drag of the mosquito (figure 6.8 *b*, *d*). Furthermore, the mix between the predictive and explanatory role is used to come to this conclusion; if the stroke rate forces are not enough to predict to lift generation there must be another aerodynamic mechanism that does.

These two examples both have a understandable flaw in reasoning, that if the predicted forces are correct that the aerodynamic mechanisms responsible for this prediction must be the explanation of insect flight. However, I believe that this reasoning should be turned around. All the aerodynamic mechanisms and their interactions should be understood thoroughly before we can asses their contribution to the force generation of a certain insect.

Considering the final model presented in figure 6.11. As mentioned before, the model is unable to accurately predict the forces during hovering flight of a fruit fly and mosquito. For both the fruit fly and the mosquito, the combination of all the models lead to an overestimation of the lift forces at the start of both the forward stroke and backward stroke. In this thesis, I ignored two unsteady aerodynamic mechanisms: the Wagner effect [24] and wake-capture [25, 26]. Both these models are strongly dependent on the history of the flow. This makes the development of these models, based on the kinematics alone, difficult or even impossible. Nonetheless, further research into the role of these two aerodynamic mechanisms might play a crucial part towards a deeper understanding of insect flight.

6.4 Let's stretch it: What can we learn from these aerodynamic models?

Up until this point, I have developed a quasi-steady model and applied it to the hovering flight of the fruit fly and mosquito. In this section, I will put the model through its paces and apply it to the take-off of the malaria mosquito in section 6.4.1. Finally, in section 6.4.2 I will look into the load carrying capabilities of the malaria mosquito.

6.4.1 Mosquito take-off

In chapter 5, I used CFD to find the forces and torques of 13 mosquitoes during take-off. The set consisted of a group of mosquitoes that where lean and a group

of mosquitoes that where blood-fed. Here I applied the quasi-steady model to the kinematics of these take-offs [2]. I used a moving average filter with a width of three wingbeats to minimize the large fluctuations. Because I computed the forces on two wings simultaneously the lift and drag were diffucult to asses and interpet. Furthermore, from the CFD results from chapter 5 only the forces of two wings where available. Therefore, I use the forward force (x-axis in the stroke reference frame figure 6.1) and the upward force (inverted z-axis in the stroke reference frame shown in figure 6.1).

I took one example sequence for the lean mosquito and one for the fed mosquito. In the lean mosquito, the forward force shows a minimum after ten wingbeats and then stabilizes from 20 wingbeats on (figure 6.13 *a*). The quasi-steady model follows this pattern rather well, but falls short in the exact prediction of the forces. A similar pattern is observed in the upward force for the lean mosquito (figure 6.13 *c*), where the model shows a similar pattern, but overshoots the prediction of the forces. For the blood-fed mosquito, the forward force is predicted rather poorly (figure 6.13 *b*), where neither the overall trend nor the forces itself are predicted correctly. In the upward force of the blood-fed mosquito (figure 6.13 *d*), a peak is observed in the quasi-steady model that is absent in the results from CFD.

To asses the contribution of each aerodynamic mechanism during the take-off, I took the average of the forces from the start until the point where the legs leave the ground (figure 6.13 *e*–*h*). In both the fed and lean mosquito, the stroke rate forces are dominant during in the upward direction, leading to an over-prediction of the forces of $\approx 150\,\%$ and $\approx 200\,\%$ for the lean and fed mosquitoes respectively. Interestingly, this trend is not persistent for the forward force component, where the stroke-pitch rate forces and the stroke acceleration forces are dominant (figure 6.13 *e*, *g*). The pitch rate forces have a negative contribution to the forward force, reducing the forward acceleration.

When applying the quasi-steady model to the take-off of the mosquitoes, I implicitly assumed that the motion of the insect has no influence on the forces. However, the forward velocity will change the lift and drag throughout the stroke [18]. This might explain part of the discrepancies between the quasi-steady model and the CFD results.

6.4.2 Blood fed mosquitoes vs lean mosquitoes

The take-off kinematics used for chapter 5 also led to the development of a generic wingbeat for load carrying in mosquitoes [2]. These kinematics can be obtained from the original wing kinematics in combination with a modified wing kinematics as (equation 9 from [2])

$$k = k_{\text{steady}} + \text{MOD}_k \left(F/mg_{\text{unfed}} - F/mg_{\text{unfed, steady}} \right), \tag{6.13}$$

where k is one of the Euler angles that describe the motion of the wing, and MOD_k the modification of the same angle. Equation (6.13) enabled me to vary the wingbeat kinematics of a mosquito gradually from a lean mosquito to a fed mosquito (figure 6.14). As second step, I computed the contribution of each component of the quasi-steady model to the drag and lift (figure 6.15 and figure 6.16). Finally, I computed the wingbeat averaged lift and drag (figure 6.17 *a* and *b* respectively).

The stroke-rate forces are a big part of both the drag and lift at any weight support (figure 6.17). Interestingly, the drag is only increased during the backward stroke, but remains almost unaffected during the forward stroke (figure 6.15 *a*). However, the lift is increased throughout the wingbeat (figure 6.16 *a*).

Actually, all the other aerodynamic mechanisms also only show an increase in drag during the backward stroke (figure 6.15). However, these aerodynamic mechanisms hardly influence the wingbeat averaged drag (figure 6.17 *a*), with the notable exception of the stroke acceleration forces.

The rise in lift found in the stroke rate forces is not found in the other aerodynamic mechanisms (figure 6.16 *b* – *f*). The stroke pitch rate forces and the pitch based forces mainly change during the backward stroke. However, these changes seem to balance each other, because in the wingbeat averaged forces little change is observed for these mechanisms (figure 6.17 *b*). The stroke acceleration forces show an increase at the start of the forward stroke, which is balanced at the start of the backward stroke (figure 6.16 *b*. The pitch acceleration forces do show an increase during the first part of the stroke (figure 6.16 *e*, which leads to a gradual increase of the averaged lift forces with increasing weight support (figure 6.17 *b*).

6.5 Concluding remarks

In this thesis, I used systematic parametric studies to uncover the aerodynamics of flapping insect flight. I started with a simple question: *How do insects fly?*. Coupling the motion of the wing to the generation of aerodynamic forces with the use of aerodynamic mechanisms gave a good framework for answering this question. Often these aerodynamic mechanisms were combined into a quasi-steady model.

I started out with revising the known aerodynamic mechanisms of stroke pitch rate interaction forces and pitch rate forces in chapter 2. Here I showed that the offset of the pitch axis and the symmetry axis of the wing influenced the generation of pitch rate forces greatly. Furthermore, I showed that the stroke rate forces, pitch rate forced and stroke pitch rate forces could all be linear added to form the total forces, if the wing is moving at a constant stroke rate and pitch rate.

In chapter 2 the systemically parametric study based on CFD was again used to uncover the relation to the stroke acceleration and the aerodynamic forces. With the use of a large parametric study I identified that there is an interaction between the stroke rate forces and the stroke acceleration forces. However, this interaction proved to be small enough to be ignored when applied to the kinematics of the fruit fly and mosquito. Furthermore, the stroke acceleration forces are particular important for the flight of high-frequency flappers such as the mosquito.

In chapter 4, I took another look at the pitch motion of the wing. However, this time the pitch rate was varying. The pitch motion model that followed showed that a wing that is pitching up does not generate the mirrored forces of a wing that is pitching down. Furthermore, the pitch acceleration influenced the pitch rate forces. In this model, the offset of the pitch axis and the symmetry axis again influenced the aerodynamic forces, strengthening its importance for insect flight.

In chapter 5, I studied the effect of the substrate on the take-off of a malaria mosquito. Here I showed that the aerodynamic ground effect was irrelevant. However, the insects do heavily rely on the ground for take-off by using their legs both for the generation of take-off forces, but also uses their legs to generate the required pitch torques for take-off.

In this general discussion, I combined all the aerodynamic mechanisms in a single quasi-steady model. With this model, I showed that the predictive capabilities based on the aerodynamic mechanisms described in this thesis is not adequate. However,

the model does give an insight in what mechanisms were responsible for lift and drag production in the hovering flight of a fruit fly and mosquito. Interestingly, the pitch rate forces, stroke acceleration forces and the pitch acceleration forces generated a thrust at the start of the forward stroke.

Even though, I explicitly tested the interaction between different components of the quasi-steady model, I was unable to test all the interactions. For instance, the interaction between the stroke acceleration and pitch acceleration. Some of these interactions might be large enough to influence the aerodynamic forces, and eventually lead to a better predictive capability of the quasi-steady model, and a better understanding of insect flight. Furthermore, the unsteady aerodynamic mechanisms, such as the Wagner effect and the wake-capture effect, might also have a large effect on the aerodynamic forces. These unsteady aerodynamic mechanisms, and the additional interaction terms, require a revision such that their effects can be known. Lastly, in this thesis I ignored derivatives higher than the acceleration, such as the jerk. It is unclear how a non-constant pitch or stroke acceleration will influence the aerodynamic forces.

When the aerodynamic mechanisms were applied to the take-off of the mosquito it was hard to predict the correct aerodynamic forces. The differences could not be ascribed to the ground effect, because I showed in chapter 5 that the ground effect is not present. Another possibility, apart from missing aerodynamic mechanisms, is the motion of the insect, which might also influence the aerodynamic forces. Similar parametric studies I conducted in this thesis could be fruitful to uncover the interaction between the aerodynamic mechanisms and the motion of the body.

Because the quasi-steady model has such poor predictive capabilities it appears that it is not useful to further pursue the missing aerodynamic mechanisms. Why not simply use computational fluid dynamics? With computing power becoming (relative) cheap one is capable to compute the aerodynamic torques and forces of complex maneuvers, such as I did in chapter 5. However, providing insight into the aerodynamics of flapping flight based on CFD simulations alone is not straightforward. I see the value of identifying the different aerodynamic mechanisms in conjunction with CFD to improve the understanding of insect flight.

6.6 References

[1] M. H. Dickinson and F. T. Muijres. “The aerodynamics and control of free flight manoeuvres in Drosophila”. In: *Philosophical Transactions B* 371.1704 (2016). DOI: 10.1098/rstb.2015.0388.

[2] F.T. Muijres, S.W. Chang, W.G. Veen, J. Spitzen, B.T. Biemans, M.A.R. Koehl, and R. Dudley. “Escaping blood-fed malaria mosqtuitoes minimize tactile detection without compromising on take-off speed”. In: *Journal of Experimental Biology* 220.20 (2017), pp. 3751–3762. DOI: 10.1242/jeb.163402.

[3] A. P. S. Bhalla, R. Bale, B. E. Griffith, and N. A. Patankar. “A unified mathematical framework and an adaptive numerical method for fluid–structure interaction with rigid, deforming, and elastic bodies”. In: *Journal of Computational Physics* 250 (2013), pp. 446–476. DOI: 10.1016/j.jcp.2013.04.033.

[4] J. M. Birch and M. H. Dickinson. “Spanwise flow and the attachment of the leading-edge vortex on insect wings”. In: *Nature* 412 (2001), pp. 729–733. DOI: 10.1038/35089071.

[5] M. H. Dickinson, F. Lehmann, and S. P. Sane. “Wing rotation and the aerodynamic basis of insect flight”. In: *Science* 284.5422 (June 1999), pp. 1954–1960. DOI: 10.1126/science.284.5422.1954.

[6] M. H. Dickinson, F. Lehmann, and K. G. Götz. “The active control of wing rotation by *Drosophila*”. In: *The Journal of Experimental Biology* 182 (1993), pp. 173–189.

[7] R. J. Bomphrey, T. Nakata, N. Phillips, and S. M. Walker. “Smart wing rotation and trailing-edge vortices enable high frequency mosquito flight”. In: *Nature* 554 (2017), pp. 92–95. DOI: 10.1038/nature21727.

[8] M. R. A. Nabawy and W. J. Crowther. “The role of the leading edge vortex in lift augmentation of steadily revolving wings: a change in perspective”. In: *Journal of the Royal Society Interfact* 14 (2017), pp. 1–9. DOI: 10.1098/rsif.2017.0159.

[9] S. Mao and D. Gang. “Lift and power requirements of hovering insect flight”. In: *The Chinese Society of Theoretical and Aplied Mechanics* 19.5 (2003), pp. 458–469. ISSN: 0567-7718.

[10] Z. J. Wang. “Dissecting Insect Flight”. In: *Annual Reviews in Fluid Mechanics* 37 (2005), pp. 183–210. DOI: 10.1146/annurev.fluid.36.050802.121940.

[11] Z. J. Wang, J. M. Birch, and M. H. Dickinson. “Unsteady forces and flows in low Reynolds number hovering flight: two-dimensional computations vs robotic wing experiments”. In: *The Journal of Experimental Biology* 207 (2003), pp. 449–460. DOI: 10.1242/jeb.00739.

[12] P. S. Sane and M. H. Dickinson. “The control of flight force by a flapping wing: lift and drag production”. In: *The journal of experimental biology* 204 (2001), pp. 2607–2626. ISSN: 0022-0949.

[13] S. P. Sane and M. H. Dickinson. “The aerodynamic effects of wing rotation and a revised quasi-steady model of flapping flight”. In: *The Journal of Experimental Biology* 205.8 (2002), pp. 1087–1096.

[14] T. Nakata, H. Liu, and R. J. Bomphrey. “A CFD-informed quasi-steady model of flapping-wing aerodynamics”. In: *Journal of Fluid Mechanics* 783 (Nov. 2015), pp. 323–343. DOI: 10.1017/jfm.2015.537.

[15] L. Zheng, T. L. Hedrick, and R. Mittal. “A multi-fidelity modelling approach for evalutation and optimization of wing stroke aerodynamics in flapping flight”. In: *The Journal of Fluid Mechanics* 721 (2013), pp. 118–154. DOI: 10.1017/jfm.2013.46.

[16] J. R. Usherwood and C. P. Ellington. “The aerodynamcis of revolving wings”. In: *The Journal of Experimental Biology* 205.11 (2002), pp. 1547–1564. ISSN: 0022-0949.

[17] L. I. Sedov. *Two-Dimensional Problems in Hydrodynamics and Aerodynamics*. Interscience Publishers, 1965.

[18] W. B. Dickson and M. H. Dickinson. “The effect of advance ratio on the aerodynamics of revolving wings”. In: *The Journal of Experimental Biology* 207 (2004), pp. 4269–4281. DOI: 10.1242/jeb.01266.

[19] J.P. Whitney and R.J. Wood. “Aeromechanics of passive rotation in flapping flight”. In: *Journal of Fluid Mechanics* 660 (2010). DOI: 10.1017/S002211201000265X.

[20] C. K Kang, H. Aono, C. E. S. Cesnik, and W. Shyy. “Effects of flexibility on the aerodynamic performance of flapping wings”. In: *AIAA* (2011).

[21] S. P. Sane. “The aerodynamics of insect flight”. In: *The Journal of Experimental Biology* 206 (2003), pp. 4191–4208. DOI: 10.1242/jeb.00663.

[22] T. L. Hedrick and T. L. Daniel. “Flight control in the hawkmoth *Manduca sexta*: the inverse problem of hovering”. In: *The Journal of Experimental Biology* 209 (2006), pp. 3114–3130. DOI: 10.1242/jeb.02363.

[23] C. P. Ellington. “The aerodynamics of hovering insect flight. IV. aerodynamic mechanisms”. In: *Philosophical transaction royal society London* 305 (1984), pp. 79–113. DOI: 10.1098/rstb.1984.0052.

[24] H. Wagner. “Flight performance and visual control of flight of the free-flying housefly”. In: *Philosphical transactions Royal Society of London* (1980).

[25] J. M. Birch and M. H. Dickinson. “The influence of wing–wake interactions on the production of aerodynamic forces in flapping flight”. In: *The Journal of Experimental Biology* 206 (2003), pp. 2257–2272. DOI: 10.1242/jeb.00381.

[26] D. Lentink, F. T. Muijres, F. J. Donker-Duyvis, and J. L. van Leeuwen. “Vortex-wake interactions of a flapping foil that models animal swimming and flight”. In: *The Journal of Experimental Biology* 211 (2007), pp. 267–273. DOI: 10.1242/jeb.006155.

6.7 Figures

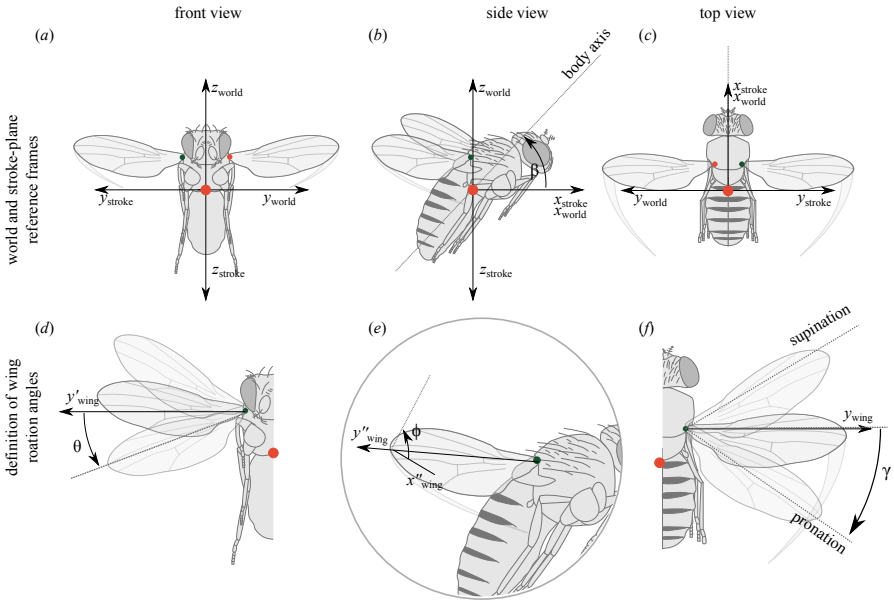

Figure 6.1: Defintion of the world reference frame, stroke reference frame and wind reference frame. $(a-c)$ Schematic representation of the front view, side view and top view of a fruit fly, large red dot is estimation of the center of mass, small green dot and red dot are the root of the right and left wing respectively. $(d-f)$ Definition of the deviation angle θ, pitch angle ϕ and stroke angle γ with respect to the stroke reference frame.

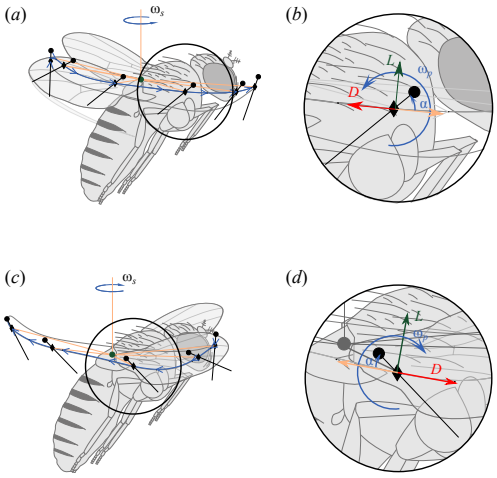

Figure 6.2: Definition of the aerodynamic reference frame, fruit fly kinematics added for reference. (*a*, *c*) Forward stroke and backward stroke respectively, in blue moving from the dorsal to the ventral side (forward) or visa-versa for the backward stroke, black lines indicate the location of the chord at 2 mm from the root of the wing, diamond indicates the rotation axis, black dot indicates the leading edge, large circle is the enlargement shown in panel *b*, *d*. (*b*, *d*) Enlargement of panel *a* and *c* around a single wing chord, blue arrows indicate the definition of a positve angle-of-attack α and positive pitch rate ω_p, green and red arrow indicate the definition of the lift and drag with respectively.

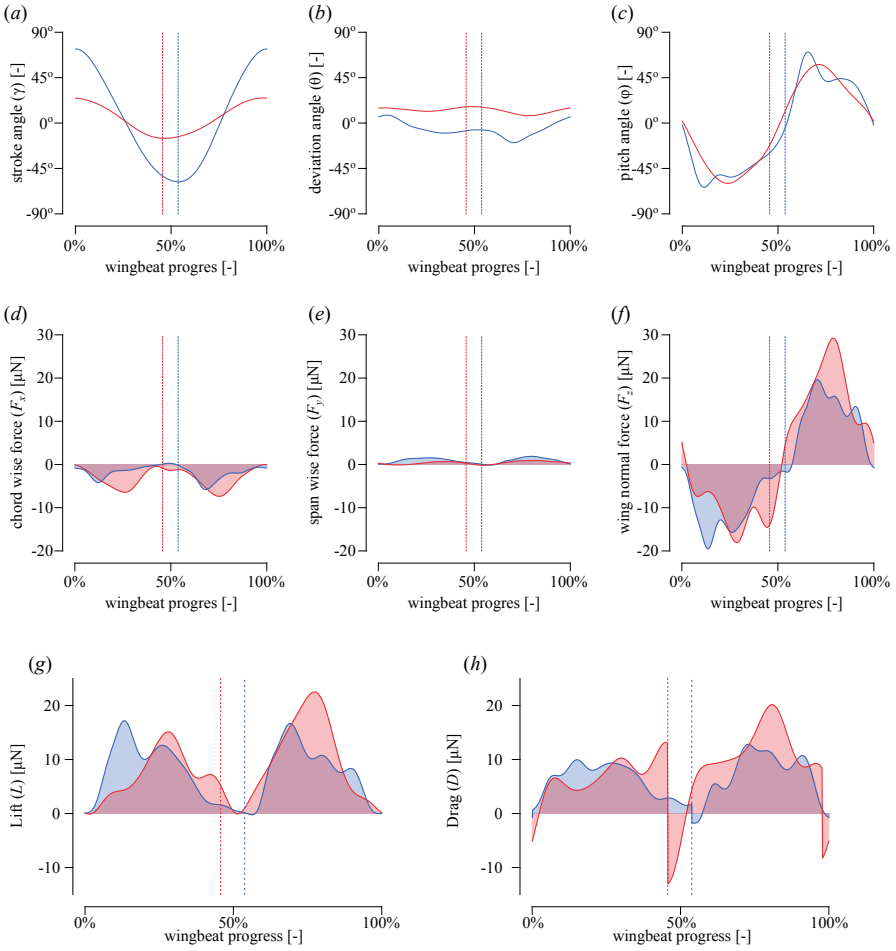

Figure 6.3: Kinematics and aerodynamic forces computed with CFD of the fruit fly (blue) and mosquito (red), vertical dashed lines indicate the location of stroke reversal. (*a* – *c*) Kinematics of the fruit fly (blue) [1] and mosquito (red) [2], stroke angle, deviation angle and pitch angle respectively. (*d* – *f*) Chord-wise, span-wise and wing normal forces of the fruit fly and mosquito. (*g*, *h*) Lift and drag based on the pressure forces only, for the fruit fly and mosquito based on the definition of the aerodynamic reference frame (see figure 6.2, and section 6.2.1).

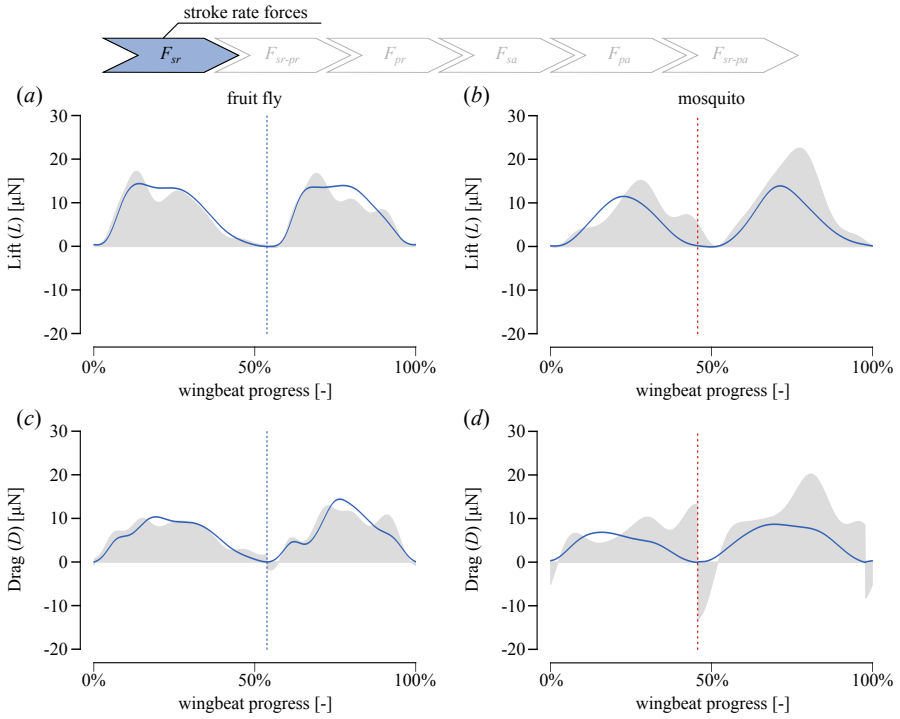

Figure 6.4: Application of the stroke rate force model (blue line, see chapter 3) for the fruit fly and mosquito wing kinematics, light gray shaded area are the forces computed with CFD (see section 6.2.2). (*a*, *b*) Lift component for the fruit fly and mosquito respectively. (*c*, *d*) Drag component for the fruit fly and mosquito respectively.

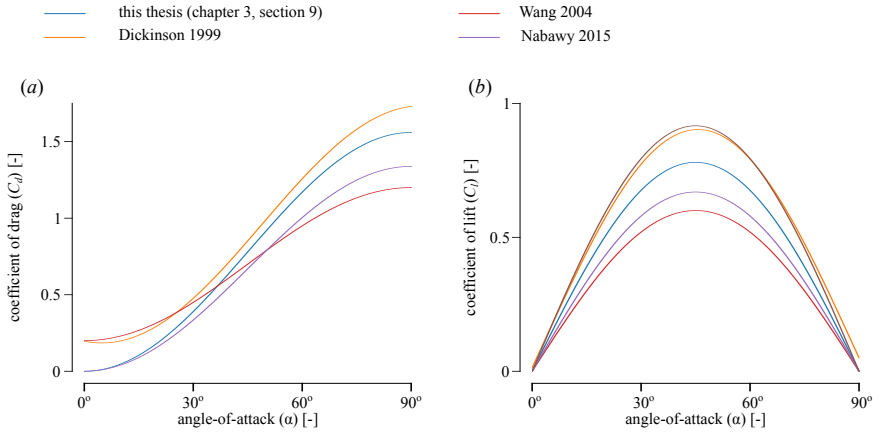

Figure 6.5: Comparison of the coefficient of drag (C_d) and the coefficient of lift (C_l) with different studies: Dickinson 1999 [5, 12], Wang 2003 [11], Nabawy 2017 [8]

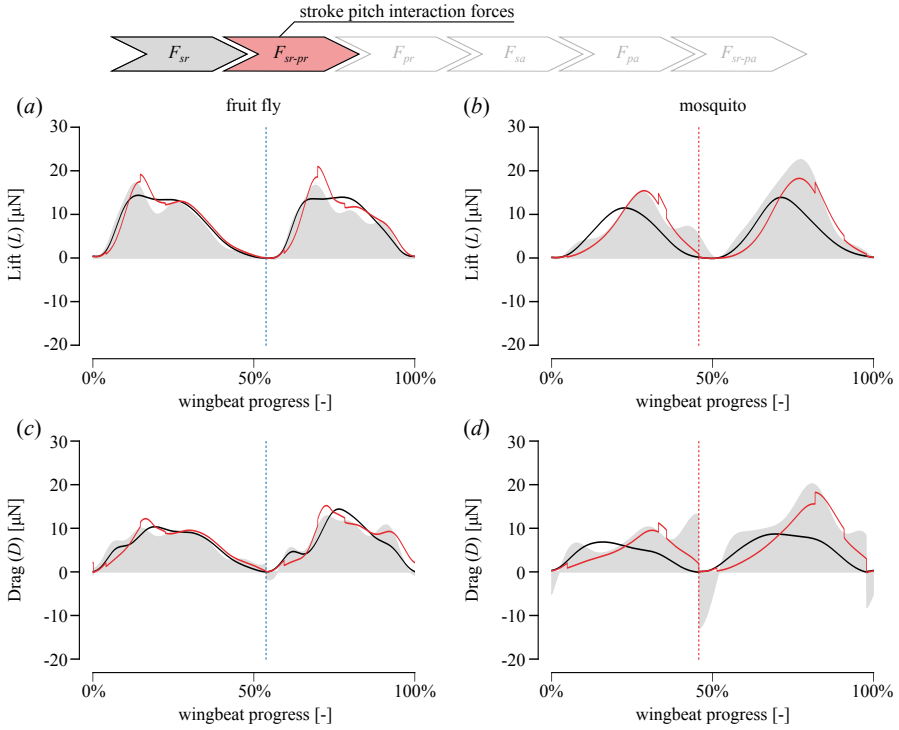

Figure 6.6: Application of the stroke pitch rate interaction force model (red line, see chapter 2), black line are the forces of the stroke rate force model for the fruit fly and mosquito wing kinematics, light gray shaded area are the forces computed with CFD (see section 6.2.2). (*a*, *b*) Lift component for the fruit fly and mosquito respectively. (*c*, *d*) Drag component for the fruit fly and mosquito respectively.

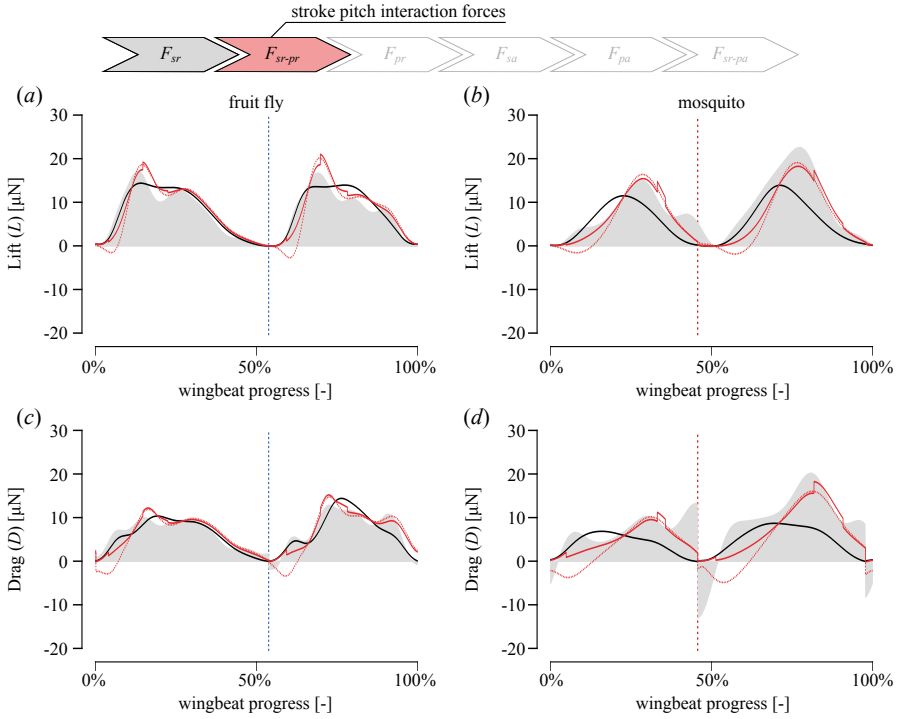

Figure 6.7: Comparison of the model stroke pitch interaction model from chapter 2 (red, dashed) and the stroke pitch interaction model from chapter 4 (red, solid), black line are the forces of the stroke rate force model for the fruit fly and mosquito wing kinematics, light gray shaded area are the forces computed with CFD (see section 6.2.2). (*a*, *b*) Lift component for the fruit fly and mosquito respectively. (*c*, *d*) Drag component for the fruit fly and mosquito respectively.

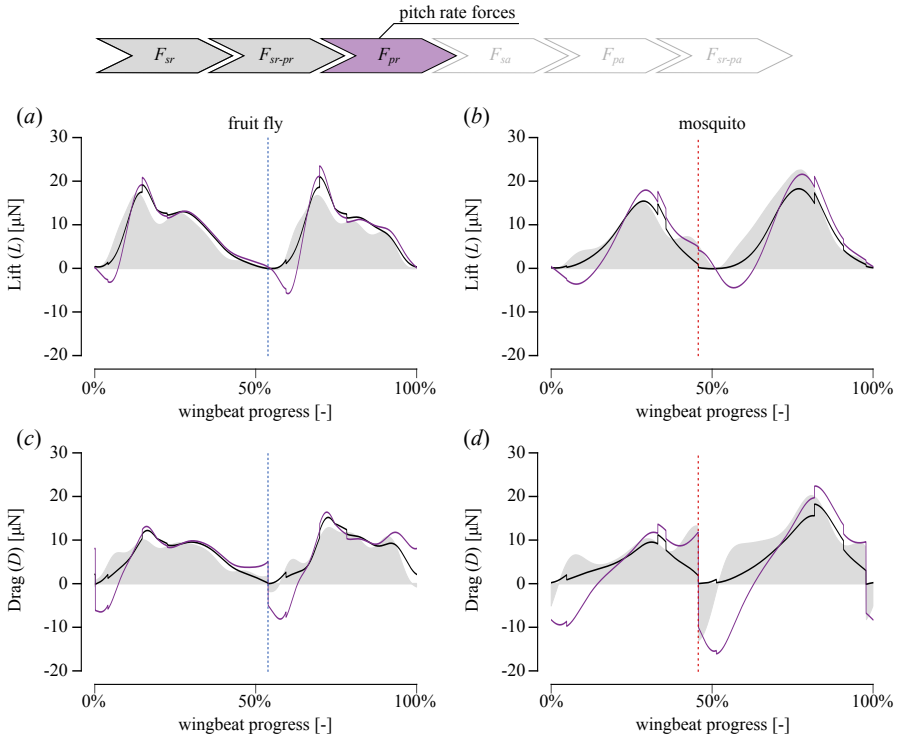

Figure 6.8: Application of the pitch rate force model (purple line, see chapter 2), black line are the sum of the stroke rate forces and the stroke pitch interaction forces, for the fruit fly and mosquito wing kinematics, light gray shaded area are the forces computed with CFD (see section 6.2.2), vertical dashed lines indicate stroke reversal. (*a*, *b*) Lift component for the fruit fly and mosquito respectively. (*c*, *d*) Drag component for the fruit fly and mosquito respectively.

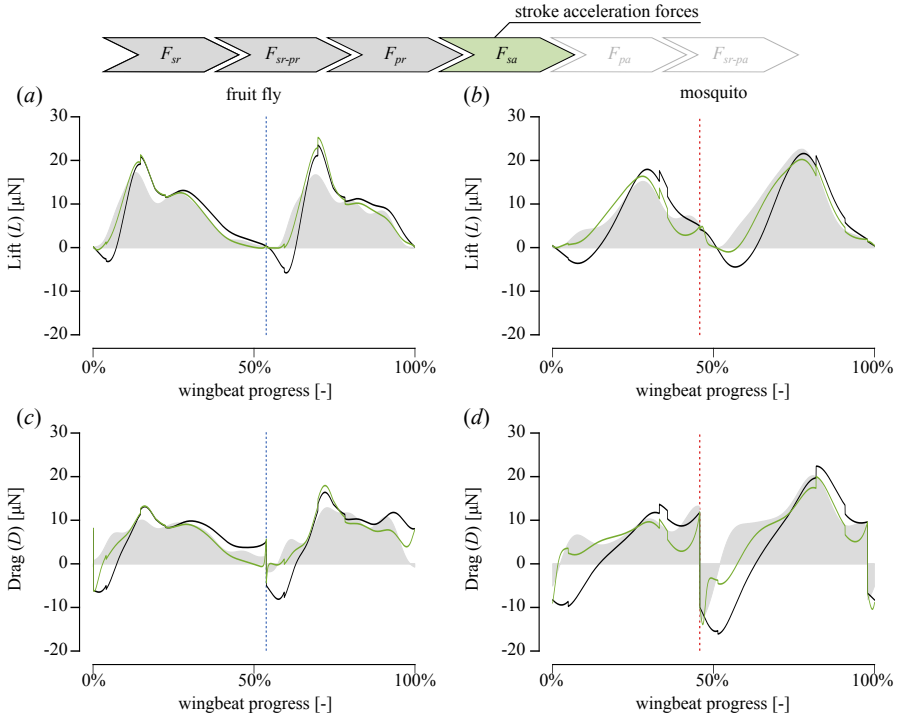

Figure 6.9: Application of the stroke acceleration force model (green line, see chapter 3), black line are the sum of the stroke rate forces, the stroke pitch interaction forces, and the pitch rate forces, for the fruit fly and mosquito wing kinematics, light gray shaded area are the forces computed with CFD (see section 6.2.2), vertical dashed lines indicate stroke reversal. (*a*, *b*) Lift component for the fruit fly and mosquito respectively. (*c*, *d*) Drag component for the fruit fly and mosquito respectively.

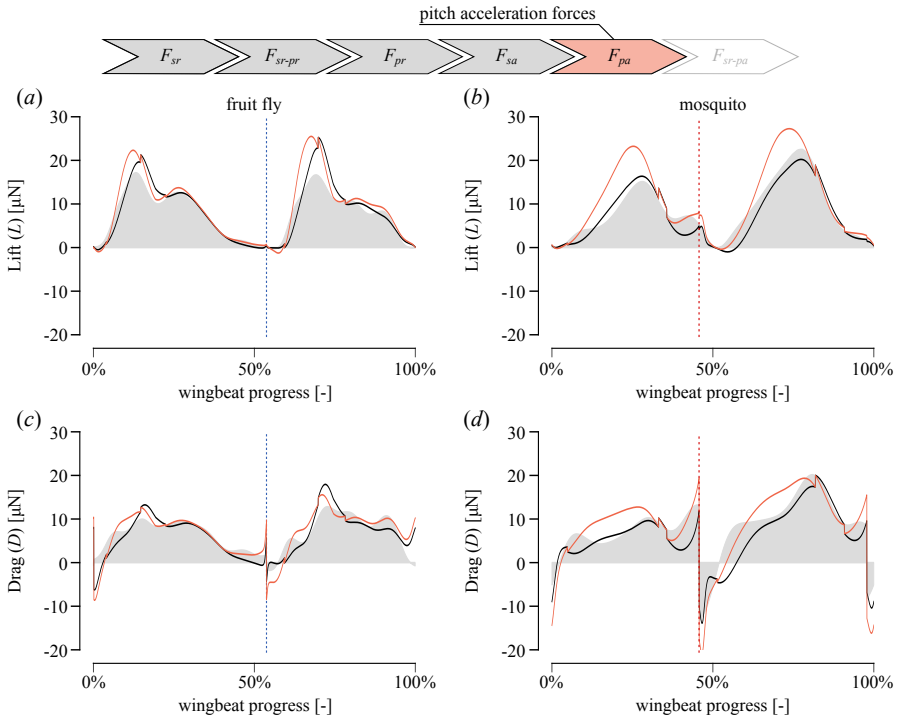

Figure 6.10: Application of the pitch acceleration force model (orange line, see chapter 4), black line are the sum of the stroke rate forces, the stroke pitch interaction forces, pitch rate forces, and the stroke acceleration forces, for the fruit fly and mosquito wing kinematics, light gray shaded area are the forces computed with CFD (see section 6.2.2), vertical dashed lines indicate stroke reversal. (*a*, *b*) Lift component for the fruit fly and mosquito respectively. (*c*, *d*) Drag component for the fruit fly and mosquito respectively.

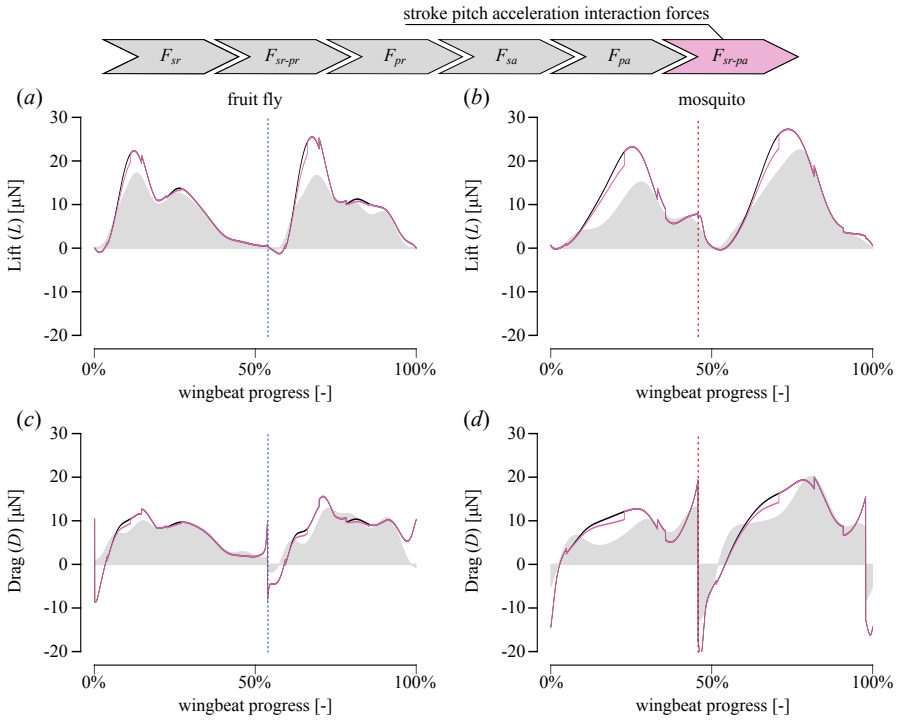

Figure 6.11: Application of the stroke pitch acceleration force model (pink line, see chapter 4), black line are the sum of the stroke rate forces, the stroke pitch interaction forces, pitch rate forces, stroke acceleration forces, and the pitch acceleration forces, for the fruit fly and mosquito wing kinematics, light gray shaded area are the forces computed with CFD (see section 6.2.2), vertical dashed lines indicate stroke reversal. (*a*, *b*) Lift component for the fruit fly and mosquito respectively. (*c*, *d*) Drag component for the fruit fly and mosquito respectively.

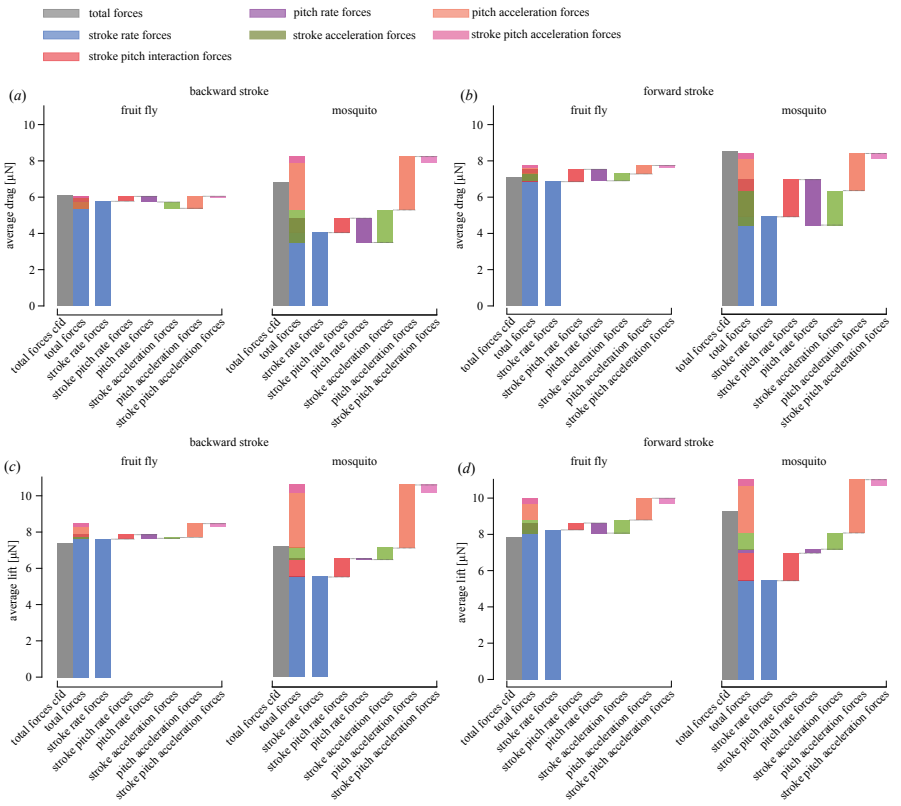

Figure 6.12: Average contribution of each aerodynamic mechanism discussed in this thesis, compared with the average forces computed with CFD. (*a*) Average force of the backward stroke. (*b*) Average drag of the forward stroke. (*c*) Average lift of the backward stroke. (*d*) Average lift of the foward stroke.

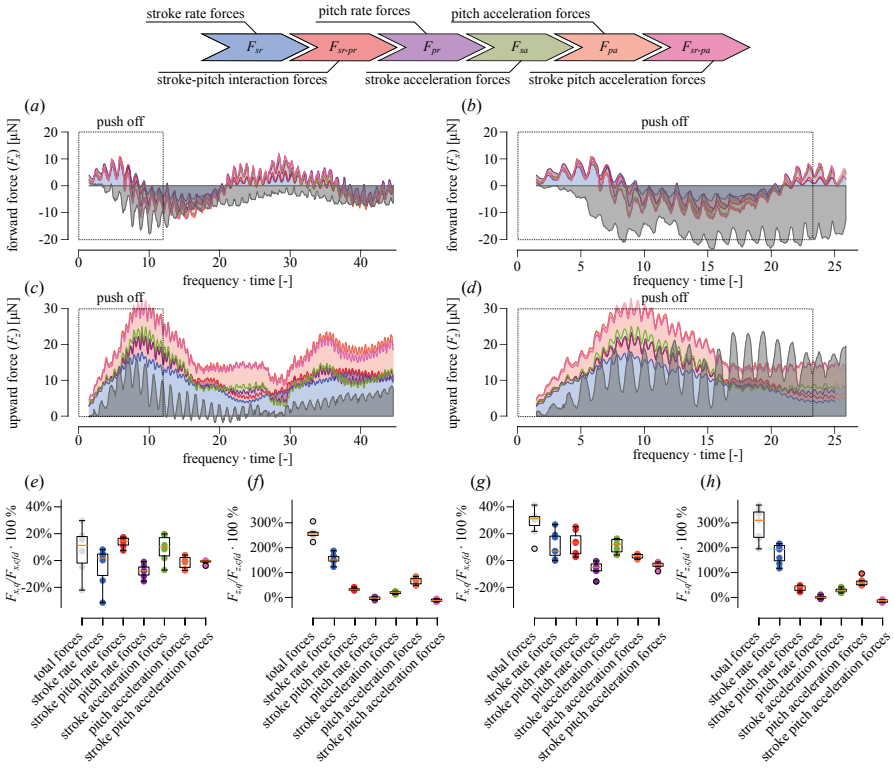

Figure 6.13: Application of the quasi-steady model to the take-off of lean and fed malaria mosquitoes. (*a*, *b*) Sum of the quasi-steady components of the forward force component of a lean and fed mosquito during take-off respectively, in grey the forces computed with CFD (see chapter 5) (*c*, *d*) Sum of the quasi-steady components of the upward force component of a lean and fed mosquito during take-off respectively, in grey the forces computed with CFD (see chapter 5). (*e*, *f*) Average percentage of each quasi-steady component with respect to the total forces computed with CFD before the legs leave the ground, for the forward and upward direction respectively for lean mosquitoes. (*g*, *h*) Average percentage of each quasi-steady component with respect to the total forces computed with CFD before the legs leave the ground, for the forward and upward direction respectively for fed mosquitoes.

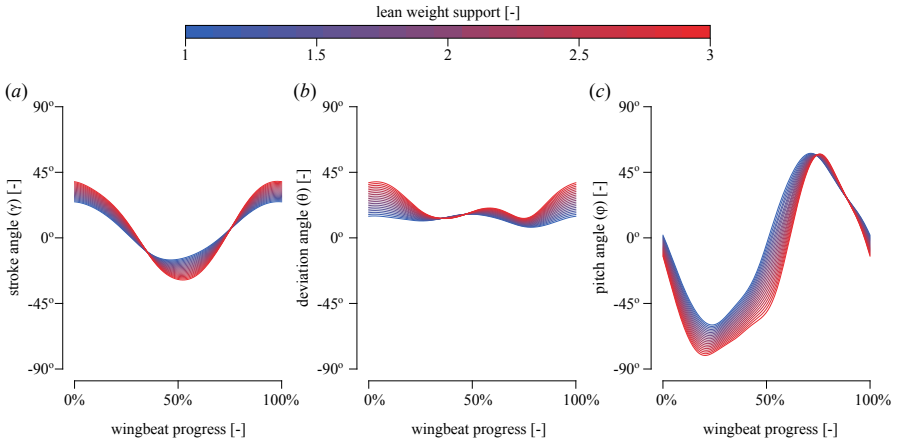

Figure 6.14: Kinematics of the mosquito under for different lean weight supports [2]. (*a*) Stroke angle. (*b*) Deviation angle. (*c*) Pitch angle.

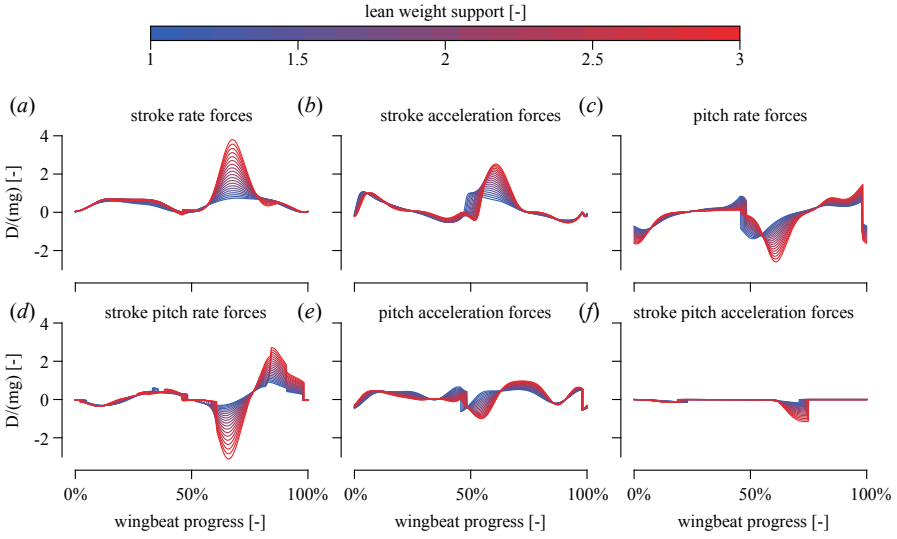

Figure 6.15: Drag of each quasi-steady component for the wingbeat kinematics of a mosquito with different weight support ratio's [2]. (*a*) Stroke rate forces. (*b*) Stroke acceleration forces. (*c*) Pitch rate forces. (*d*) Stroke pitch rate forces. (*e*) Pitch acceleration forces. (*f*) Stroke pitch acceleration forces.

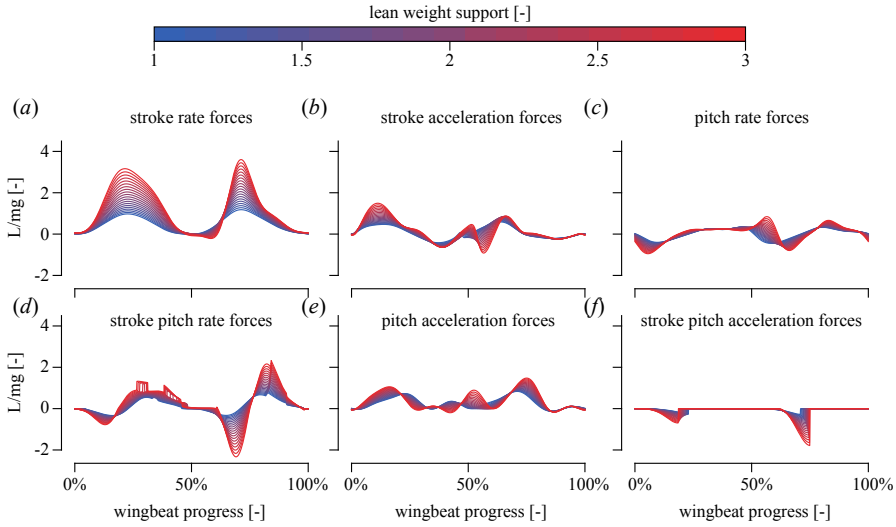

Figure 6.16: Lift of each quasi-steady component for the wingbeat kinematics of a mosquito with different weight support ratio's [2]. (*a*) Stroke rate forces. (*b*) Stroke acceleration forces. (*c*) Pitch rate forces. (*d*) Stroke pitch rate forces. (*e*) Pitch acceleration forces. (*f*) Stroke pitch acceleration forces.

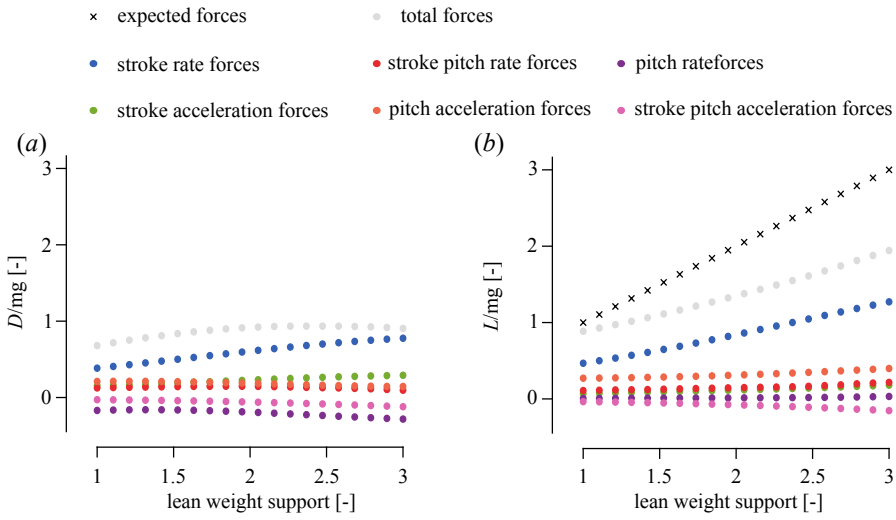

Figure 6.17: Wingbeat averaged drag and lift of each quasi-steady component for the wingbeat kinematics of a mosquito with different weight support ratio's [2]. (*a*) Drag (*b*) Lift

Chapter 7

Summary

7.1 Summary

Insects are flying all around us. However, answering the question: *How do insects fly?* is difficult. In this thesis, we set out to uncover the relation between the movement of the wing of an insect and the aerodynamic forces. For this we used two Dipteran species as model organisms for low frequency high amplitude and high frequency low amplitude fliers.

In **chapter 2**, we revisited the two aerodynamic mechanisms based on the pitch rate motion of the wing: the stroke pitch interactions and the pitch rate forces. We used a large parametric study based on computational fluid dynamics to uncover the relation between the kinematics and the aerodynamic forces. The aerodynamic forces as a result of the pitch motion with constant angular rate broke up into two components. The first component is only dependent on the pitch rate of the wing. The second component is an interaction component between the stroke rate and the pitch rate. To assess the influence of the wing morphology we included seven additional wing morphologies. The inclusion of these additional wing morphologies showed that the stroke interaction forces are related to both the spanwise and chordwise second moment of area. Furthermore, the pitch rate forces where dependent on the offset between the pitch axis and the symmetry axis of the wing.

We used a similar approach for **chapter 3** as we used in chapter **chapter 2**. With this parametric study we set out to uncover the relation between the aerodynamic forces and the stroke motion of the wing for a non-constant stroke rate. We designed a set of wing kinematics such that the aerodynamic forces due to the stroke rate, stroke acceleration and the interaction between the two, could be found. We included an additional set of wing morphologies to explicitly test the dependence of these forces on the wing morphology. The stroke acceleration forces depend on a scaling parameter that scales with the chord length and the length of the wing. At the end of this chapter we used a quasi-steady model to apply our model to the kinematics of the fruit fly and the mosquito. With the use of this model we were able to show that the stroke acceleration forces become more prominent for high-frequency, low-amplitude flappers, such as mosquitoes.

In **chapter 4**, we took another look at the pitch motion of the wing. Unlike we did

in **chapter 2**, we did not use a constant pitch rate. We again used a systematic parametric study based on computational fluid dynamics to uncover the relation between the stroke rate forces, pitch rate forces, pitch acceleration forces, and the interactions between each component. Here, we tested the validity of the two-dimensional model often used to model the pitch acceleration forces in flapping flight. Furthermore, we included a set of four different kinematic cases, which enabled us to explicitly test the dependence of the forces on the direction of motion of the wing. From this we learned that the forces generated by an accelerating pitch up wing cannot be simply translated into a model for an accelerating pitch down wing. With the inclusion of several additional wing morphologies we showed that the offset between the pitch axis and the symmetry axis is not only important for the pitch rate forces, but also for the pitch acceleration forces.

In **chapter 5**, we used the take-off of the mosquito to test the influence of the substrate on the generation of aerodynamic forces. We simulated several lean and blood fed mosquitoes taking off from a substrate using computational fluid dynamics. From these simulations we showed that the ground did not have any effect on the aerodynamic forces acting on the wings of the animal. However, the substrate did have an important effect on the generation of the forces of the insect. The mosquitoes used a combination of leg push-off forces and aerodynamic forces to take-off. Furthermore, the insect used its legs to generate pitch up torques during take-off.

In **chapter 6**, we gathered the knowledge gained in the previous chapters and build a quasi-steady model. In addition, we simulated the aerodynamic forces of a hovering fruit fly and mosquito, which gave us a comparison for the quasi-steady model. From this comparison, we learned that the quasi-steady model based on the aerodynamic mechanisms found in this thesis led to a poor predictive model. However, the model did uncover that mosquitoes rely more other aerodynamic mechanisms apart from the stroke rate forces. At the end of **chapter 6**, we applied the quasi-steady model to the take-off kinematics we used in **chapter 5**. This time the quasi-steady model showed even a bigger difference, mainly over-predicting the aerodynamic forces. This led us to hypothesize that the body motion of the insect also has a large interaction with the aerodynamic forces. Lastly, we used the kinematics of a lean mosquito and gradually changed these kinematics to that of a fed mosquito. Here, we showed that the lift is altered through a change in mainly the stroke rate forces.

7.2 Samenvatting

Insecten vliegen overal om ons heen. Desalniettemin, is het beantwoorden van de vraag "*Hoe vliegen insecten?*" lastig. In deze dissertatie zijn we vertrokken met de taak om de relatie tussen de beweging van de vleugel van een insect en de aerodynamische krachten te vinden. Hiervoor hebben we gebruik gemaakt van twee Diptera soorten as model organisme voor laag frequent hoge amplitude vliegen en hoog frequent lage amplitude vliegen.

In **hoofdstuk 2**, hebben we twee aerodynamische modellen gebaseerd op de pitch beweging van de vleugel herzien: de "stroke pitch interacties" en de "pitch rate" krachten. We hebben gebruik gemaakt van een grote parametrische studie gebaseerd op "computational fluid dynamics" (CFD) om de relatie tussen de kinetica en de aerodynamische krachten te achterhalen. De aerodynamische kracht als een resultaat van de pitch beweging met een constante hoeksnelheid viel uiteen in twee verschillende componenten. De eerste component is alleen afhankelijk van de pitch hoeksnelheid van de vleugel. De tweede component is een interactie tussen de "stroke" hoeksnelheid en de "pitch" hoeksnelheid. Om de invloed van de vleugelvorm te onderzoeken hebben we zeven extra vleugelvormen toegevoegd. De toevoeging van deze extra vleugelvormen lied zien dat de "stroke" interactie krachten allemaal gerelateerd zijn aan de spanwijze en koordwijze tweede oppervlakte moment. Verder waren de "pitch rate" krachten afhankelijk van de afstand tussen de "pitch" as en de symmetrie as van de vleugel.

Voor **hoofdstuk 3** hebben we een soortgelijke methode als voor **hoofdstuk 2** toegepast. Met deze parametrische studie hebben we de relatie tussen de aerodynamische krachten en de "stroke" beweging van de vleugel onderzocht voor een vleugel die beweegt met een niet constante "stroke" hoeksnelheid. We hebben een set vleugel bewegingen ontworpen zodat de aerodynamische krachten als resultaat van de "stroke" snelheid, "stroke" acceleratie en de interactie tussen deze twee bewegingen gevonden konden worden. We hebben een set extra vleugelvormen toegevoegd om expliciet te testen hoe de krachten afhangen van de vorm van de vleugel. De "stroke" acceleratie krachten hangen af van een schaling parameter die afhangt van de koorde en de lengte van de vleugel. Aan het einde van dit hoofdstuk hebben we gebruik gemaakt van een "quasi-steady" model om ons model toe te passen op de kinetica van een fruit vlieg en een mug. Met dit model hebben we kunnen aantonen dat

de stroke acceleratie prominent worden voor vliegers met een hoge frequentie, zoals muggen.

In **hoofdstuk 4**, zijn we nogmaal terug gegaan naar de "pitch" beweging van de vleugel. Deze keer, in tegenstelling tot in **hoofdstuk 2**, hebben we de "pitch" hoeksnelheid niet constant gehouden. We hebben wederom gebruik gemaakt van een systematische parametrische studie gebasseerd op "computational fluid dynamics" om de relatie tussen de "stroke rate" krachten, de "pitch rate" krachten, de "pitch" acceleratie krachten en de interactie tussen deze componenten te achterhalen. We hebben de validiteit van het twee-dimensionale model getest die vaak gebruikt wordt om de "pitch" acceleratie krachten te modeleren in flappend vliegen. Verder hebben we een set van vier verschillende vleugel bewegingen toegevoegd, die ons in staat stelde om expliciet de afhankelijkheid tussen de krachten en de richting van de beweging van de vleugel te testen. Hiervan hebben we geleerd dat de krachten gegenereerd door een accelererende vleugel die ook omhoog draait niet simpel te vertalen zijn naar een model voor een vleugel die naar beneden accelereert. Met de toevoeging van zeven extra vleugel vormen hebben we laten zien dat de afstand tussen de "pitch" as en de symmetry as niet alleen van belang is voor de "pitch rate" krachten, maar ook voor de "pitch acceleration" krachten.

In **hoofdstuk 5** hebben we het opstijgen van een mug gebruikt om te testen wat de invloed van het substraat is op de aerodynamische krachten. We hebben verscheidene ongevoede muggen en verscheidene gevoede muggen gesimuleerd die opstijgen van een substraat met gebruik van "computational fluid dynamics". Met gebruik van deze simulaties hebben we kunnen aantonen dat de grond geen effect had op de aerodynamische krachten. De muggen gebruikte een combinatie van hun poot afzet krachten en de aerodynamische krachten om op te stijgen. Verder gebruikte het insect zijn poten om de "pitch" omhoog momenten te genereren tijdens het opstijgen.

In **hoofdstuk 6** hebben we de kennis van de vorige hoofdstukken gebruikt en een "quasi-steady" model ontwikkeld. Verder hebben we de aerodynamische krachten van een stilhangende fruit vlieg en mug gesimuleerd, wat ons een vergelijking verschafte voor het "quasi-steady" model. Van deze vergelijking hebben we geleerd dat het "quasi-steady" model gebasseerd op de aerodynamische mechanismes beschreven in deze dissertatie leidde tot een slechte voorspelling van de krachten. Het model lied echter wel zien dat muggen meer vertrouwen op andere aerodynamische mechanisme dan de "stroke rate" krachten. Aan het einde van hoofdstuk **hoofdstuk 6** hebben we het "quasi-steady" model toegepast op de kinetica van opstijgende muggen die we

eerder gebruikt hebben in **hoofdstuk 5**. Deze keer liet het “quasi-steady” model een nog groter verschil zien met d voorspelde het model de krachten. Dit heeft ons tot de hypothese geleid dat de beweging van het lichaam van het insect ook een grote interactie heeft met de aerodynamische krachten. Als laatste hebben we de kinetica van niet gevoede en bloed gevoede muggen gebruikt. De kinetica werd langzaam veranderd van een ongevoede mug naar een bloed gevoede mug. In dit geval werd de “lift” vooral veranderd door de “stroke rate” krachten.

7.3 About the author

Wouter Gerben van Veen was born on the 17th of February 1988 in Hoorn, the Netherlands. In his childhood he was always curious how things worked, especially technical stuff. His teachers in primary school described him as a cheerful child, but too much talking. He needed a challenge. This need for challenge was expressed in secondary school (College Hageveld in Heemstede) by making and launching a water rocket, which unfortunately pierced a new roof of the schoolbuilding when coming down with enormous power.

After secondary school he started his study Aerospace Engineering at the TU Delft. During his bachelor period he followed a minor Software developing. His bachelor project contained the development of a hypersonic re-entry vehicle, the Hyperion-3. His internship was at Institut de Mécanique des Fluides de Toulouse, where he independently executed calculations of Computational Fluid Dynamics. In 2015 he completed his Master of Aerospace Engineering, specialization Aerodynamics. His thesis: Reynolds averaged Navier-Stokes modeling of schock wave boundary-layer interactions.

During his study Wouter participated at Proteus Eretes in Delft as a race rower and coach. He was also a Member of the Board. During his time here he developed a sensorsystem, which provided coaches with information of the rowers during the training, to increase the results of the team. For this, he won the Pinewood Innovation Price and he co-operated with the Vrije Universiteit in Amsterdam during his PhD to improve the system and with the purpose to test it on rowers of Olympic level.

After finishing his Master degree, he was ready for another challenge. He joined the team of Florian Muijres to study the aerodynamics of insect flight. Together with a colleague, he filled a room with computers that were able to put the best heaters to shame. The result of the calculations of these computers can be seen throughout this thesis. After his career in science, he will start a new life in Jena in Germany, where he will devote his time to become a better software developer.

7.3.1 List of publications

[1] D. Szubert, **van Veen, Wouter G.**, F. Grossi, Hoarau Y, Braza M., Giepman Rogier, Ferry Schrijer, and Bas van Oudheusden. “Physics and modelling of the transonic and supersonic shock wave boundary layer interaction of oblique and normal shock at high Reynolds number.” In: (10th International ERCO).

[2] **van Veen, Wouter G.**, Rogier Giepman, Ferry Schrijer, and Bas van Oudheusden. “RANS modeling of shock wave-boundary layer interactions”. In: (3rd ECCOMAS Young Investigators Conference, Aachen, Germany; 07/2015).

[3] F T Muijres, S W Chang, **van Veen, W G**, J Spitzen, B T Biemans, M A R Koehl, and R Dudley. “Escaping blood-fed malaria mosqtuitoes minimize tactile detection without compromising on take-off speed”. In: *Journal of Experimental Biology* (2017).

[4] **van Veen, Wouter G.**, Johan L. van Leeuwen, and Florian T. Muijres. “A chordwise offset of the wing-pitch axis enhances rotational aerodynamic forces on insect wings: a numerical study”. In: *Journal of The Royal Society Interface* 16.155 (2019), p. 20190118. DOI: 10.1098/rsif.2019.0118.

[5] **van Veen, Wouter G.**, Johan L. van Leeuwen, and Florian T. Muijres. “Malaria mosquitoes use leg push-off forces to control body pitch during take-off”. In: *Journal of Experimental Zoology Part A: Ecological and Integrative Physiology* 333.1 (2020), pp. 38–49. DOI: 10.1002/jez.2308.

[6] Annelieke S. Wentzel, Joëlle J. E. Janssen, Vincent C. J. de Boer, **van Veen, Wouter G.**, Maria Forlenza, and Geert F. Wiegertjes. “Fish Macrophages Show Distinct Metabolic Signatures Upon Polarization”. In: *Frontiers in Immunology* 11 (2020), p. 152. DOI: 10.3389/fimmu.2020.00152.

[7] Annelieke S. Wentzel, Jules Petit, **van Veen, Wouter G.**, Inge Rosenbek Fink, Marleen H. Scheer, M. Carla Piazzon, Maria Forlenza, Herman P. Spaink, and Geert F. Wiegertjes. “Transcriptome sequencing supports a conservation of macrophage polarization in fish”. In: *Scientific Reports* 10 (2020). DOI: 10.1038/s41598-020-70248-y.

7.4 Training Supervision Plan

A. The Basic Package	year	credits
WIAS Introduction Day	2015	0.3
Course on philosophy of science and or ethics	2016	1.5
Course on essential skills	2015	1.2
B. Disciplinary Competences		
Proposal	2016	6.0
Introduction course into programming using GPU CUDA	2017	1.2
WIAS Course Statistics for the life sciences	2017	2.0
C Programming with Linux	2019	5.0
C. Professional Competences		
Supervising Master students	2016	0.6
Efficient writing strategies	2019	1.3
Scientific writing	2018-2019	1.8
D. Presentation Skills		
(poster) "Aerodynamics of high-frequency flapping flight of mosquito's" New Orleans workshop Neuroscience and Locomotion 20-01-2016	2016	1.0
(Oral presentation) "The aerodynamics of rapid wing pitch movements of flapping insect wings, a numerical study" SEB	2018	1.0
(Oral presentation) "Offset in rotation axis increases rotational lift production in insect wings: a numerical study" Burgers dag	2018	1.0
E. Teaching competences		
Supervising bachelor student	2017	1.0
Supervising functional zoology	2015	0.5
Supervising functional zoology	2016	0.5
Supervising modeling biological systems	2016	4.0
Supervising modeling biological systems	2017	(4)
Supervising modeling biological systems	2018-2019	(4)
Education and Training Total		**30**

Colofon

Financial support from Wageningen University for printing this thesis is gratefully acknowledged.

Cover design by Wouter G. van Veen
Layout by Wouter G. van Veen
Printed by ProefschriftMaken.nl || www.proefschriftmaken.nl